

OFFICE OF CIVILIAN RADIOACTIVE WASTE MANAGEMENT
SPECIAL INSTRUCTION SHEET

1. QA: QA
Page: 1 of: 1

Complete Only Applicable Items

This is a placeholder page for records that cannot be scanned or microfilmed

2. Record Date
01/23/2001

3. Accession Number

MOL. 20010214.0031

4. Author Name(s)
YUEYING DENG

5. Author Organization
N/A

6. Title
WATER DISTRIBUTION AND REMOVAL MODEL

7. Document Number(s)
ANL-EBS-MD-000032

8. Version
REV 01

9. Document Type
REPORT

10. Medium
OPTIC/PAPER

11. Access Control Code
PUB

12. Traceability Designator
DC #26386

13. Comments
THIS IS A ONE-OF-A-KIND DOCUMENT DUE TO THE COLORED GRAPHS ENCLOSED AND CAN BE LOCATED THROUGH THE RPC

**OFFICE OF CIVILIAN RADIOACTIVE WASTE MANAGEMENT
ANALYSIS/MODEL COVER SHEET**

1. QA: QA

Page: 1 of 177

Complete Only Applicable Items

<p>2. <input checked="" type="checkbox"/> Analysis Check all that apply</p> <table border="1" style="width:100%; border-collapse: collapse;"> <tr> <td style="width:20%;">Type of Analysis</td> <td><input checked="" type="checkbox"/> Engineering</td> </tr> <tr> <td></td> <td><input type="checkbox"/> Performance Assessment</td> </tr> <tr> <td></td> <td><input type="checkbox"/> Scientific</td> </tr> </table> <table border="1" style="width:100%; border-collapse: collapse;"> <tr> <td style="width:20%;">Intended Use of Analysis</td> <td><input type="checkbox"/> Input to Calculation</td> </tr> <tr> <td></td> <td><input type="checkbox"/> Input to another Analysis or Model</td> </tr> <tr> <td></td> <td><input checked="" type="checkbox"/> Input to Technical Document</td> </tr> <tr> <td></td> <td><input type="checkbox"/> Input to other Technical Products</td> </tr> </table> <p>Describe use:</p> <p>This analysis/model report will support the development of the Engineered Barrier System Degradation, Flow and Transport Process Model Report</p>	Type of Analysis	<input checked="" type="checkbox"/> Engineering		<input type="checkbox"/> Performance Assessment		<input type="checkbox"/> Scientific	Intended Use of Analysis	<input type="checkbox"/> Input to Calculation		<input type="checkbox"/> Input to another Analysis or Model		<input checked="" type="checkbox"/> Input to Technical Document		<input type="checkbox"/> Input to other Technical Products	<p>3. <input checked="" type="checkbox"/> Model Check all that apply</p> <table border="1" style="width:100%; border-collapse: collapse;"> <tr> <td style="width:20%;">Type of Model</td> <td><input checked="" type="checkbox"/> Conceptual Model</td> <td><input type="checkbox"/> Abstraction Model</td> </tr> <tr> <td></td> <td><input checked="" type="checkbox"/> Mathematical Model</td> <td><input type="checkbox"/> System Model</td> </tr> <tr> <td></td> <td colspan="2"><input type="checkbox"/> Process Model</td> </tr> </table> <table border="1" style="width:100%; border-collapse: collapse;"> <tr> <td style="width:20%;">Intended Use of Model</td> <td><input type="checkbox"/> Input to Calculation</td> </tr> <tr> <td></td> <td><input type="checkbox"/> Input to another Model or Analysis</td> </tr> <tr> <td></td> <td><input checked="" type="checkbox"/> Input to Technical Document</td> </tr> <tr> <td></td> <td><input type="checkbox"/> Input to other Technical Products</td> </tr> </table> <p>Describe use:</p> <p>This analysis/model report will support the development of the Engineered Barrier System Degradation, Flow and Transport Process Model Report</p>	Type of Model	<input checked="" type="checkbox"/> Conceptual Model	<input type="checkbox"/> Abstraction Model		<input checked="" type="checkbox"/> Mathematical Model	<input type="checkbox"/> System Model		<input type="checkbox"/> Process Model		Intended Use of Model	<input type="checkbox"/> Input to Calculation		<input type="checkbox"/> Input to another Model or Analysis		<input checked="" type="checkbox"/> Input to Technical Document		<input type="checkbox"/> Input to other Technical Products
Type of Analysis	<input checked="" type="checkbox"/> Engineering																															
	<input type="checkbox"/> Performance Assessment																															
	<input type="checkbox"/> Scientific																															
Intended Use of Analysis	<input type="checkbox"/> Input to Calculation																															
	<input type="checkbox"/> Input to another Analysis or Model																															
	<input checked="" type="checkbox"/> Input to Technical Document																															
	<input type="checkbox"/> Input to other Technical Products																															
Type of Model	<input checked="" type="checkbox"/> Conceptual Model	<input type="checkbox"/> Abstraction Model																														
	<input checked="" type="checkbox"/> Mathematical Model	<input type="checkbox"/> System Model																														
	<input type="checkbox"/> Process Model																															
Intended Use of Model	<input type="checkbox"/> Input to Calculation																															
	<input type="checkbox"/> Input to another Model or Analysis																															
	<input checked="" type="checkbox"/> Input to Technical Document																															
	<input type="checkbox"/> Input to other Technical Products																															

4. Title:
Water Distribution and Removal Model

5. Document Identifier (including Rev. No. and Change No., if applicable):
ANL-EBS-MD-000032 REV 01

6. Total Attachments: Sixteen	7. Attachment Numbers - No. of Pages in Each: 1-3,II-4,III-9,IV-4,V-6,VI-3,VII-3,VIII-2,IX-3,X-8,XI-3,XII-15,XIII-3,XIV-15,XV-5,XVI-2*(includes 1 CD) <i>17 pgs 11/30/00</i>
----------------------------------	--

	Printed Name	Signature	Date
8. Originator	<i>for</i> Yueying Deng	<i>EL Hardin</i>	11/30/00
9. Checker	<i>for</i> Veraun Chipman	<i>Charles Mick</i>	11/30/00
10. Lead/Supervisor	Ernest L. Hardin	<i>EL Hardin</i>	11/30/00
11. Responsible Manager	Ernest L. Hardin	<i>EL Hardin</i>	11/30/00

12. Remarks:

Ernest Hardin was primary responsible for the planning and supervising, and Yueying Deng was responsible for the development of this water distribution and removal model;

Yueying Deng and John Case were responsible for the development of the water diversion submodel;

John Case, Dwayne Kicker, Ming Lin, Sean Vincent, Mason Pillow, Nina Rosenberg, Charles Carrigan, Kenrick Lee, James Gansemer, and Mary Gokoffski developed and contributed to the water drainage submodel.

Tom Buscheck, Yunwei Sun, Wunan Lin, and Paul Harding developed and contributed to the thermohydrologic submodel; and

James Kam developed the drip shield condensation submodel.

Ernest Hardin provided the FEPs screening arguments and addressed the IRSR acceptance criteria.

OFFICE OF CIVILIAN RADIOACTIVE WASTE MANAGEMENT
ANALYSIS/MODEL REVISION RECORD

Complete Only Applicable Items

1. Page: 2 of 177

2. Analysis or Model Title:

Water Distribution and Removal Model

3. Document Identifier (including Rev. No. and Change No., if applicable):

ANL-EBS-MD-000032 REV 01

4. Revision/Change No.

5. Description of Revision/Change

00

Initial issue.

00/01

Provide clarification and changes in response to DOE's acceptance review. Three references were added in Section 6.2.3. The technical content and the resulting conclusions have not changed.

01

Analysis and modeling for the previous revisions were performed for the baseline design with backfill in the waste emplacement drift. The main purposes were to investigate the water saturation levels, capillary pressures, and water fluxes in the host rock, backfill material, and the invert. Thirteen scenarios were examined to evaluate the impacts of infiltration rates, focused fracture flow, heat loading, and drift floor fracture plugging.

Revision 01 performs calculations, analyses, and modeling to reflect the repository baseline design without backfill. This revision is arranged to include four components: (1) water diversion; (2) water drainage; (3) thermal hydrology; and (4) drip shield condensation. Components (1), (2), and (3) were formerly developed and documented for the backfill case in three separate AMRs which will not be revised for the No-Backfill case. Component (4) is newly developed for this document. The backfill case for component (2) is used for the No-Backfill case and is justified in this document.

CONTENTS

ACRONYMS

1.	PURPOSE	13
1.1	OBJECTIVES	14
1.2	SCOPE OF WORK	14
1.3	ANALYSIS/MODEL APPLICABILITY	14
2.	QUALITY ASSURANCE	15
3.	COMPUTER SOFTWARE AND MODEL USAGE	16
3.1	WATER DIVERSION MODEL	16
3.2	WATER DRAINAGE MODEL	16
3.2.1	Description of Software Used	16
3.2.2	Description of Routines Used	20
3.2.3	Other Software	22
3.3	THERMOHYDROLOGIC MODEL	22
3.3.1	Description of TH Software Used	34
3.3.2	Description of TH Routines Used	34
3.4	DRIP SHIELD CONDENSATION MODEL	34
4.	INPUTS	35
4.1	DATA AND PARAMETERS	35
4.1.1	Water Diversion Model	35
4.1.2	Water Drainage Model	35
4.1.3	Thermohydrologic Model	40
4.1.4	Drip Shield Condensation Model	41
4.1.5	Miscellaneous	41
4.2	CRITERIA	41
4.2.1	Drip Shield Material	41
4.2.2	Emplacement Drift System	41
4.2.3	System Closure	42
4.2.4	Maximum Heat Load for Line Loading of Waste Packages	42
4.2.5	Water Drainage	42
4.2.6	Invert Ballast Material	42
4.2.7	Drip Shield Life	42
4.2.8	Water Diversion from Drip Shield	42
4.2.9	Emplacement Drift Wall Temperature	42
4.2.10	Heat Removal During Preclosure	42
4.2.11	Waste Package Spacing	43
4.2.12	Emplacement Drift Spacing	43
4.2.13	Emplacement Drift Diameter	43
4.2.14	Closure and Heat Removal	43
4.2.15	Invert Material	43
4.3	CODES AND STANDARDS	43

5.	ASSUMPTIONS	44
5.1	WATER DIVERSION MODEL.....	44
5.1.1	Drip Site	44
5.1.2	Drip Falling Distance	44
5.1.3	Drip Water Redistribution on Drip Shield	44
5.1.4	Drip Shield Dimensions	44
5.1.5	Viscosity.....	45
5.1.6	Maximum Percolation Rate at the Repository Horizon	45
5.1.7	Parallel Plates	45
5.1.8	Water Ponding on Drip Shield	45
5.1.9	Impact Time	45
5.1.10	Fracture Property of Rock in the Repository Horizon	46
5.1.11	Water Evaporation.....	46
5.2	WATER DRAINAGE MODEL.....	46
5.2.1	Drip Shield	46
5.2.2	Hydrologic Properties of Drip Shield.....	46
5.2.3	Backfill Material and Invert Placement.....	46
5.2.4	Tortuosity Factors.....	47
5.2.5	Thermal-Hydrological-Chemical and Thermal-Hydrological-Mechanical Effects.....	47
5.2.6	Location of Model.....	47
5.2.7	Steady State Two Dimensional Model at Isothermal Temperature	47
5.2.8	Thermal Conductivity of Stationary Components.....	47
5.2.9	Model for the Center of the Repository with Reflective Side Boundaries....	48
5.2.10	Modeling of the Rock Mass as a Dual Permeability Medium	48
5.2.11	Potential Field Theory for Closed Form Analytical Solution	48
5.2.12	Water Flux Rate under Steady-State Conditions for a Deep Water Table....	48
5.2.13	Infiltration.....	48
5.2.14	Model Geometry for the NBS and EBS	49
5.2.15	Temperature and Pressure Boundary conditions.....	49
5.3	THERMOHYDROLOGIC MODEL	49
5.3.1	Effective Tortuosity Factor	49
5.3.2	Homogeneous Fracture Continuum.....	49
5.3.3	Component Properties	50
5.3.4	Zero Dispersion Coefficients.....	51
5.3.5	Preclosure Ventilation Effects.....	51
5.3.6	Thermal Loading and Aging of Waste Inventory	51
5.3.7	Thermal and Hydrologic Properties for EBS Materials	52
5.3.8	Geometry of the Drift and Drip Shield and Waste Package.....	52
5.3.9	Properties of the Waste Package	52
5.3.10	Thermal Conductivity, the Lower and Upper Invert Layer.....	53
5.3.11	Mass Density of the Waste-Package/Drip Shield Monolith.....	53
5.3.12	Thermal Conductivity and Density for the Active Fracture Model	53
5.3.13	Hydrostratigraphic Unit Thickness, Contact Elevations, and Extents	54
5.3.14	Temperature and Total Pressure Boundary Conditions	54
5.3.15	(Not Used).....	55

5.3.16	Effective Thermal Conductivity of Cavities Inside Drifts	55
5.3.17	Heat Generation Rate	55
5.3.18	Net Infiltration Boundary Conditions.....	56
5.4	DRIP SHIELD CONDENSATION MODEL.....	57
6.	ANALYSIS/MODEL.....	58
6.1	WATER DIVERSION MODEL.....	59
6.1.1	Model Processes	59
6.1.2	Drop Size, Drip Site Density and Drip Rate.....	63
6.1.3	Impulsive Force, Impact Time and Splashing.....	64
6.1.4	Crevice Water Holding Capacity at Equilibrium	65
6.1.5	Crevice Flow By Interception of Film Flow	67
6.1.6	Crevice Flow by Impulsive Force	70
6.1.7	Thin Film Flow by Adsorptive Condensation.....	73
6.1.8	Model Validation.....	81
6.2	WATER DRAINAGE MODEL	82
6.2.1	Methodology	82
6.2.2	Model Domain and Grids	83
6.2.3	Boundary Conditions.....	88
6.2.4	Hydrologic and Thermal Properties	88
6.2.5	Simulations and Case Studies.....	88
6.2.6	Impact of Backfill to Drainage.....	101
6.2.7	Model Validation.....	104
6.3	THERMOHYDROLOGIC MODEL	105
6.3.1	Background for the LDTH-Model Calculations Using NUFT.....	105
6.3.2	Prescribing Drift Seepage in the LDTH Models	107
6.3.3	LDTH-Model Results.....	109
6.3.4	Thermohydrologic Model Validation.....	113
6.3.5	Alternative Models and Approaches	114
6.4	DRIP SHIELD CONDENSATION MODEL.....	139
6.4.1	Model Validation.....	140
6.5	INCLUSION AND EXCLUSION OF FEPS	143
6.6	IRSR ACCEPTANCE CRITERIA.....	143
7.	CONCLUSIONS.....	162
7.1	WATER DIVERSION MODEL.....	162
7.2	WATER DRAINAGE MODEL	163
7.3	THERMOHYDROLOGIC MODEL	164
7.4	DRIP SHIELD CONDENSATION MODEL.....	165
7.5	UNCERTAINTY ASSESSMENT.....	165
7.6	DISCUSSION OF DTNS AND TBVS.....	166
8.	REFERENCES.....	167
8.1	DOCUMENTS CITED.....	167
8.2	CODES, STANDARDS, REGULATIONS, AND PROCEDURES.....	174
8.3	SOURCE DATA BY DATA TRACKING NUMBER	175

9. ATTACHMENTS 177

FIGURES

Figure 3-1. Input Data Manipulation Flowchart	18
Figure 6-1. Drip Shield Connection Configuration	60
Figure 6-2. A Pendant Drop Formed at Fracture Intersection with Drift Roof	61
Figure 6-3. Contact Angle in a Crevice (a) Less Than 90° and (b) Greater Than 90°	62
Figure 6-4. Drip Rate vs. Drip Site Density	64
Figure 6-5. Film Flow as the Source of a Pendant Drop in an Unsaturated Crevice.....	67
Figure 6-6. Control Volume for Force-Momentum Balance for Thin Film Flow down the Cylindrical Drip Shield Surface.....	68
Figure 6-7. Volumetric Flow Rate vs. Crevice Location.....	70
Figure 6-8. Film Thickness vs. Crevice Location.....	70
Figure 6-9. Force Balances (a) Prior to the Impact of a Falling Drop (b) When Contact Angle Reaches 180°	71
Figure 6-10. Crevice Flow Induced by a Drop	73
Figure 6-11. Thin Film Flow due to Adsorptive Condensation.....	74
Figure 6-12. Film Thickness as a Function of Relative Humidity.....	79
Figure 6-13. Mass Flow Rate as a Function of Relative Humidity	79
Figure 6-14. Volumetric Flow Rate as a Function of Relative Humidity.....	80
Figure 6-15. Average Velocity as a Function of Relative Humidity	80
Figure 6-16. Model Domain and Boundary Conditions	86
Figure 6-17. Engineered Barrier Segment Block Model	87
Figure 6-18. Absolute Matrix Capillary Pressure Near the Repository Horizon at Steady State (Case 1).....	90
Figure 6-19. Fracture Saturation Levels Near the Repository Horizon at Steady State (Case1).....	91
Figure 6-20. Matrix Saturation Levels Near the Repository Horizon at Steady State (Case1).....	91
Figure 6-21. Fracture Mass Flux Rates (kg/m ² -s) and Direction of Flow Near the Repository Horizon at Steady State (Case 1).....	92
Figure 6-22. Absolute Matrix Capillary Pressure Near the Repository Horizon for Plugged Fractures at Steady State (Case 2)	94
Figure 6-23. Fracture Saturation Near the Repository Horizon for Plugged Fractures at Steady State (Case 2)	95
Figure 6-24. Matrix Saturation Levels Near the Repository Horizon for Plugged Fractures at Steady State (Case 2)	95
Figure 6-25. Fracture Mass Flux Rates (kg/m ² -s) and Direction of Near the Repository Horizon for Plugged Fractures at Steady State (Case 2)	96
Figure 6-26. Absolute Matrix Capillary Near the Repository Horizon for Plugged Fractures with a Sand Drain (Case 3)	98
Figure 6-27. Fracture Saturation Near the Repository Horizon for Plugged Fractures with a Sand Drain (Case 3)	99
Figure 6-28. Matrix Saturation Near the Repository Horizon for Plugged Fractures with a Sand Drain (Case 3).....	99
Figure 6-29. Fracture Mass Flux Rates (kg/m ² -s) and Direction of Flow Near the Repository Horizon for Plugged Fractures with a Sand Drain (Case 3).....	100

Figure 6-30. Fracture Pore Water Velocity Vectors in the Invert for Case 1	102
Figure 6-31. Matrix Pore Water Velocity Vectors in the Invert for Case 1.....	102
Figure 6-32. Fracture Pore Water Velocity Vectors in the Invert for Case 3	103
Figure 6-33. Matrix Pore Water Velocity Vectors in the Invert for Case 3.....	103
Figure 6-34. Temperature (a) and Relative Humidity (b) Histories on the Drip Shield for the 14c4 Location, an AML of 56 MTU/acres, and the Mean Infiltration-Flux Distribution Are Plotted for the 0%, 3%, and 30% Seepage Cases.....	115
Figure 6-35. Temperature (a) and relative humidity (b) histories on the drip shield for the 14c4 location, an AML of 56 MTU/acres, and the "lower" infiltration-flux distribution are plotted for the 0%, 3%, and 30% seepage cases.....	116
Figure 6-36. Temperature (a) and relative humidity (b) histories on the drip shield for the 14c4 location, an AML of 56 MTU/acres, and the "upper" infiltration-flux distribution are plotted for the 0%, 3%, and 30% seepage cases.....	117
Figure 6-37. Temperature (a) and relative humidity (b) histories on the drip shield for the 14c1 location, an AML of 34 MTU/acres, and the mean infiltration-flux distribution are plotted for the 0%, 3%, and 30% seepage cases.....	118
Figure 6-38. Temperature (a) and relative humidity (b) histories on the drip shield for the 14c1 location, an AML of 34 MTU/acres, and the "lower" infiltration-flux distribution are plotted for the 0%, 3%, and 30% seepage cases.....	119
Figure 6-39. Temperature (a) and relative humidity (b) histories on the drip shield for the 14c1 location, an AML of 34 MTU/acres, and the "upper" infiltration-flux distribution are plotted for the 0%, 3%, and 30% seepage cases.....	120
Figure 6-40. Temperature (a) and relative humidity (b) histories in the upper invert below the WP for the 14c4 location, an AML of 56 MTU/acres, and the mean infiltration-flux distribution are plotted for the 0%, 3%, and 30% seepage cases.....	121
Figure 6-41. Temperature (a) and relative humidity (b) histories in the upper invert below the WP for the 14c4 location, an AML of 56 MTU/acres, and the "lower" infiltration-flux distribution are plotted for the 0%, 3%, and 30% seepage cases.....	122
Figure 6-42. Temperature (a) and relative humidity (b) histories in the upper invert below the WP for the 14c4 location, an AML of 56 MTU/acres, and the "upper" infiltration-flux distribution are plotted for the 0%, 3%, and 30% seepage cases.....	123
Figure 6-43. Temperature (a) and relative humidity (b) histories in the upper invert below the WP for the 14c1 location, an AML of 34 MTU/acres, and the mean infiltration-flux distribution are plotted for the 0%, 3%, and 30% seepage cases.....	124
Figure 6-44. Temperature (a) and relative humidity (b) histories in the upper invert below the WP for the 14c1 location, an AML of 34 MTU/acres, and the "lower" infiltration-flux distribution are plotted for the 0%, 3%, and 30% seepage cases.....	125
Figure 6-45. Temperature (a) and relative humidity (b) histories in the upper invert below the WP for the 14c1 location, an AML of 34 MTU/acres, and the "upper" infiltration-flux distribution are plotted for the 0%, 3%, and 30% seepage cases.....	126
Figure 6-46. (a) Drip-shield temperature versus drip-shield relative humidity for the 14c4 location, an AML of 56 MTU/acres, and the mean infiltration-flux distribution is plotted for the 0%, 3%, and 30% seepage cases. (b) The same is plotted for the 14c1 location and an AML of 34 MTU/acre	127
Figure 6-47. (a) Drip-shield temperature versus drip-shield relative humidity for the 14c4 location, an AML of 56 MTU/acres, and the "lower" infiltration-flux distribution	

is plotted for the 0%, 3%, and 30% seepage cases. (b) The same is plotted for the l4c1 location and an AML of 34 MTU/acre	128
Figure 6-48. (a) Drip-shield temperature versus drip-shield relative humidity for the l4c4 location, an AML of 56 MTU/acres; and the "upper" infiltration-flux distribution is plotted for the 0%, 3%, and 30% seepage cases. (b) The same is plotted for the l4c1 location and an AML of 34 MTU/acre	129
Figure 6-49. (a) Drip-shield temperature versus drip-shield relative humidity for the l4c4 location, an AML of 56 MTU/acres, and the 0% seepage case is plotted for "lower", mean, and "upper" infiltration-flux distributions. (b) The same is plotted for the l4c1 location and an AML of 34 MTU/acre.....	130
Figure 6-50. (a) Drip-shield temperature versus drip-shield relative humidity for the l4c4 location, an AML of 56 MTU/acres, and the 3% seepage case is plotted for "lower", mean, and "upper" infiltration-flux distributions. (b) The same is plotted for the l4c1 location and an AML of 34 MTU/acre.....	131
Figure 6-51. (a) Drip-shield temperature versus drip-shield relative humidity for the l4c4 location, an AML of 56 MTU/acres, and the 30% seepage case is plotted for "lower", mean, and "upper" infiltration-flux distributions. (b) The same is plotted for the l4c1 location and an AML of 34 MTU/acre.....	132
Figure 6-52. Drip-shield temperature versus drip-shield relative humidity is plotted for three geographic locations and two WP types, resulting in four combinations of locations and WP types. These plots are obtained from the Multiscale Thermohydrologic Model calculations (CRWMS M&O 2000i) for the mean-infiltration-flux no-backfill case (DTN LLL000509112312.003; file: TSPA_SR00nbf_mean_Infiltration.ext)	133
Figure 6-53. Liquid saturation at (a) the top of the invert and (b) the bottom of the invert at the centerline of the drift for the l4c4 location, an AML of 56 MTU/acres, and the mean infiltration-flux distribution is plotted for the 0%, 3%, and 30% seepage cases	134
Figure 6-54. Liquid saturation at (a) the top of the invert and (b) the bottom of the invert at the centerline of the drift for the l4c1 location, an AML of 34 MTU/acres, and the mean infiltration-flux distribution is plotted for the 0%, 3%, and 30% seepage cases	135
Figure 6-55. (a) Liquid-phase flux at the bottom of the invert at the centerline of the drift for the l4c4 location, an AML of 56 MTU/acres, and the mean infiltration-flux distribution is plotted for the 0%, 3%, and 30% seepage cases. (b) The same is plotted for the l4c1 location and an AML of 34 MTU/acre.....	136
Figure 6-56. Evaporation Rate at the Invert for l4c4 Location with Mean Infiltration Distribution	137
Figure 6-57. Comparisons of Drift Crown (a) Temperature (b) Relative Humidity for the Various Infiltration Rate Distributions	138
Figure 6-58. Repository Area Used in the MSTHM.....	141
Figure 6-59. Condensation Index vs. Time for Upper Infiltration (No Seepage Imposed).....	142
Figure 6-60. Condensation Index R vs. Time for Mean Infiltration (No Seepage Imposed)	142

TABLES

Table 3-1. Software and Routine Usage	17
Table 3-2. Software Codes and Routines Used for Thermohydrologic Calculations.....	23
Table 3-3. Software Execution	23
Table 3-4. NUFT Input Files for Calculations Described in the Thermohydrologic Model	24
Table 4-1. Selected Water and Water Vapor Properties at 60 °C ⁽¹⁾	35
Table 4-2. Matrix Hydrologic Parameters for NBS (DTN: LB990861233129.001).....	36
Table 4-3. Fracture Hydrologic Parameters for NBS (DTN: LB990861233129.001)	37
Table 4-4. Hydrologic Parameters for Fracture-Matrix Interaction for NBS (DTN: LB990861233129.001)	38
Table 4-5. Thermal Parameters and Tortuosity Factor for NBS (DTN: LB990861233129.001)	39
Table 5-1. Additional EBS Dimensional Details (CRWMS M&O 2000u, Table 2).....	49
Table 5-2. Temperature and Total Pressure Boundary Conditions	54
Table 5-3. Air Mass-Fraction Boundary Conditions	55
Table 5-4. Infiltration Values for Model Locations.....	56
Table 5-5. Average Flux Values for Model Locations	56
Table 6-1. Contact Angle and Water Holding Capacity as a Function of Crevice Width.....	66
Table 6-2. Hydrostatigraphy for 14c4.....	85
Table 6-3. Ground Surface and Water Table Conditions	88
Table 6-4. Summary of Case Studies for the Water Drainage Model	89
Table 6-5. Fracture Mass Flux Rate.....	93
Table 6-6. Matrix Mass Flux Rate.....	93
Table 6-7. Summary of Invert Flow Characteristics.....	101
Table 6-8. Summary of Figures and Associated Source Files (Attachment XVI)	109
Table 6-9. Inclusion and Exclusion of Features, Events, and Processes Related to the WD&R Model.....	144
Table 6-10. Key Technical Issue Acceptance Criteria Addressed by the WD&R Model.....	157

ACRONYMS

ACC	Records Processing Center accession number
AFC	Active Fracture Concept
AMR	Analysis/Model Report
AP	Administrative Procedure
CRWMS M&O	Civilian Radioactive Waste Management System Management and Operating Contractor
CSNF	Commercial Spent Nuclear Fuel
DHLW	Defense High-Level Waste
DKM	Dual Permeability Model
DOE	U.S. Department of Energy
DTN	Data Tracking Number
EBS	Engineered Barrier System
EDA	Enhanced Design Alternative
FEPs	Features, Events, and Processes
IRSRs	Issue Resolution Status Report
LADS	License Application Design Selection
LLNL	Lawrence Livermore National Laboratory
NBS	Natural Barrier System
NRC	Nuclear Regulatory Commission
NUFT	Non-isothermal Unsaturated -saturated Flow and Transport
PMR	Process Model Report
QA	Quality Assurance
QAP	Quality Administrative Procedure
SAN	Software Activity Number
STN	Software Tracking Number
TBM	Tunnel Boring Machine
TBV	To Be Verified
THC	Thermal-Hydrological-Chemical
THM	Thermal-Hydrological-Mechanical
TIC	Technical Information Center
Tptpll	Topopah Spring Tuff crystal poor lower lithophysal zone
TSPA	Total System Performance Assessment
Tptpmn	Topopah Spring Tuff crystal poor middle nonlithophysal zone

TSw	Topopah Spring welded tuff
UZ	unsaturated zone
WP	waste package

1. PURPOSE

The design of the Yucca Mountain high level radioactive waste repository depends on the performance of the engineered barrier system (EBS). To support the total system performance assessment (TSPA), the *Engineered Barrier System Degradation, Flow, and Transport Process Model Report* (EBS PMR) is developed to describe the thermal, mechanical, chemical, hydrological, biological, and radionuclide transport processes within the emplacement drifts, which includes the following major analysis/model reports (AMRs):

- EBS Water Distribution and Removal (WD&R) Model
- EBS Physical and Chemical Environment (P&CE) Model
- EBS Radionuclide Transport (EBS RNT) Model
- EBS Multiscale Thermohydrologic (TH) Model

Technical information, including data, analyses, models, software, and supporting documents will be provided to defend the applicability of these models for their intended purpose of evaluating the post-closure performance of the Yucca Mountain repository system. The WD&R model ARM is important to the site recommendation.

Water distribution and removal represents one component of the overall EBS. Under some conditions, liquid water will seep into emplacement drifts through fractures in the host rock and move generally downward, potentially contacting waste packages. After waste packages are breached by corrosion, some of this seepage water will contact the waste, dissolve or suspend radionuclides, and ultimately carry radionuclides through the EBS to the near-field host rock.

Lateral diversion of liquid water within the drift will occur at the inner drift surface, and more significantly from the operation of engineered structures such as drip shields and the outer surface of waste packages. If most of the seepage flux can be diverted laterally and removed from the drifts before contacting the wastes, the release of radionuclides from the EBS can be controlled, resulting in a proportional reduction in dose release at the accessible environment.

The purposes of this WD&R model (CRWMS M&O 2000b) are to quantify and evaluate the distribution and drainage of seepage water within emplacement drifts during the period of compliance for post-closure performance. The model bounds the fraction of water entering the drift that will be prevented from contacting the waste by the combined effects of engineered controls on water distribution and on water removal. For example, water can be removed during pre-closure operation by ventilation and after closure by natural drainage into the fractured rock. Engineered drains could be used, if demonstrated to be necessary and effective, to ensure that adequate drainage capacity is provided.

This report provides the screening arguments for certain Features, Events, and Processes (FEPs) that are related to water distribution and removal in the EBS. Applicable acceptance criteria from the Issue Resolution Status Reports (IRSRs) developed by the U.S. Nuclear Regulatory Commission (NRC 1999a; 1999b; 1999c; and 1999d) are also addressed in this document.

1.1 OBJECTIVES

The specific objectives of this AMR (CRWMS M&O 2000b) are to:

- estimate the leakage of seepage water through drip shields that are degraded because of general corrosion, stress-corrosion cracking, or dislocation of the drip shield segments;
- predict liquid flux and saturation in the invert, and their dependence on seepage during and after the thermal period;
- evaluate the dependence of temperature and relative humidity in the emplacement drifts on seepage during the thermal period;
- identify thermal-hydrologic conditions that could produce condensation on the underside of the drip shields;
- provide screening arguments for relevant FEPs; and
- address the IRSR technical issue acceptance criteria.

1.2 SCOPE OF WORK

The WD&R model Revision 01 performs calculations, analyses, and modeling to reflect the repository baseline design without backfill (CRWMS M&O 2000b). It is developed to evaluate the water distribution and removal aspects of the EBS. The model consists of a set of submodels (models and submodels are interchangeable hereafter) that describe: (1) water diversion through drip shield; (2) water drainage on the drift floor; (3) thermohydrologic conditions within the drift; and (4) condensation on the underside of drip shield. Submodels (1), (2), and (3) were formerly developed and documented for the backfill case in three separate AMRs which will not be revised for the no-backfill case. Submodel (4) is newly developed for this document. The appropriateness of using backfill for submodel (2) is justified in Section 6.2 in this report.

1.3 ANALYSIS/MODEL APPLICABILITY

The WD&R model results are applicable for the Total System Performance Assessment. General guidance on the selection of materials was provided by the *Emplacement Drift System Description Document* (CRWMS M&O 2000r, Section 2) on the basis of thermal, hydrological, and geochemical consequences. The guidance included selection of a ballast material for the invert, and a drip shield. Any significant change to these basic parameters would require an assessment of the subsequent impacts to this analysis/model. It should be noted that the footprint that delineates the area of repository heating in this report (CRWMS M&O 1999c) is slightly larger than the one in the new baseline design (CRWMS M&O 2000x) due to small differences in the representation of the northwestern and southwestern repository boundaries. However, the total heat loading is the same, and the area difference is negligible, so the areal heat loading is basically unaffected. Also, the use of 14c4 and 14c1 locations for the representation of repository center and repository edge, respectively, is unaffected.

2. QUALITY ASSURANCE

This document has been prepared in accordance with AP-3.10Q, *Analyses and Models*, and the *Technical Work Plan for Subsurface Process Modeling FY 01 Work Activities* (CRWMS M&O 2000b) which includes the Water Distribution and Removal Model. The technical work plan was developed in accordance with AP-2.21Q, *Quality Determinations and Planning for Scientific, Engineering, and Regulatory Compliance Activities*.

The applicability of the QA program is documented in an activity evaluation per AP-2.21Q. The activity evaluation (CRWMS M&O 2000b) has concluded that this document is quality-affecting and subject to the QA controls of the Quality Assurance Requirements and Description (DOE 2000).

The design analysis, *Classification of the MGR Ex-Container System* (CRWMS M&O 1999b), was performed in accordance with QAP-2-3, *Classification of Permanent Items*. The drip shield is part of the Ex-Container System identified on the Q-list (YMP 2000, p.II-11), which is identified as Quality Level 1 (QL1). Water distribution and removal, which affect the physical and chemical environment, is not specifically addressed by the Q-list but is a characteristic of the ex-container system. For this document, it is assumed that the classification of features affecting the physical and chemical environment is Quality Level 1, which states that the structure, system, or components whose failure could directly result in a condition adversely affect public safety. These items have a high safety or waste isolation significance.

Qualified and accepted input data and references have been identified. All electronic data used in the preparation of this AMR were obtained from the Technical Data Management System as appropriate. Electronic data were controlled and managed per the technical work plan in accordance with AP-SV.1Q, *Control of the Electronic Management of Information*. Unqualified data used in this report are tracked in accordance with AP-3.15Q, *Managing Technical Product Inputs*. Computer software and model usage are discussed in Section 3 of this report.

As per Section 5.9 of AP-3.10Q, the results of this analysis/model will be submitted to the Technical Data Management System in accordance with AP-SIII.3Q, *Submittal and Incorporation of Data to the Technical Data Management System*. DTNs of any associated developed data, as well as decisions and recommendations based on the analysis and modeling activity are summarized in Section 7.6.

3. COMPUTER SOFTWARE AND MODEL USAGE

Per AP-3.10Q and AP-SI.1Q, electronic files developed for this report are discussed in the following sections and provided in the attached CD (Attachment XVI). A complete list of files is saved as "directory_listing.doc" and provided in the CD.

3.1 WATER DIVERSION MODEL

Mathcad 7 is an all-purpose, commercially available software that has many built-in functions for performing and documenting mathematical calculations. Mathcad 7 is used in the water diversion model to solve the equations for the crevice flow by interception of film flow in Attachment I (crevice_flow_f.mcd), the crevice flow by impulsive force in Attachment II (crevice_flow_p.mcd), and the thin film flow by adsorptive condensation in Attachment III (adsorptive_film.mcd). Accuracy of the Mathcad calculations were checked by comparing with hand calculations as shown in the Attachments. Electronic files are provided in the attached CD under the "diversion" directory. Computer execution was performed at U.S. DOE/YMP CRWMS M&O 112831, which is physically located at cubicle 1022C.

3.2 WATER DRAINAGE MODEL

The computer software and routines used in the water drainage model are identified in this section. All the computer files associated with this model are identified in Attachment XI and in the attached CD (Attachment XVI) under the "drainage" directory. This model is validated and documented in Section 6.2.7. Table 3-1 shows the sources of inputs and the actual file names of the input and output files for the various routines and software packages used in this model. Figure 3-1 further illustrates the path of data through routines and software packages. Software tracking numbers (STNs) are provided where applicable. Computer execution of the software and routines were performed at machines listed in Table 3-3.

3.2.1 Description of Software Used

The NUFT V3.0s (Nitao, 1998) software code was obtained from the software configuration management (CM) and was used within the range of validation in accordance with AP-SI.1Q. The software was applied to solve the simultaneous heat and water flows appropriately in this document. NUFT is classified as a qualified software program per AP-SI.1Q, *Software Management*, and is under configuration management (STN: 10088-3.0s-00) in Table 3-1. NUFT was run on a Sun Ultra 10 workstation with SunOS 5.6 operating system at locations listed in Table 3-3.

NUFT, specifically the USNT module of NUFT, was used in this model to simulate flow through a fractured porous media. NUFT solves the non-isothermal problem by solving a coupled set of balance equations for transported component. NUFT is based on the numerical technique called the integrated finite difference method or the finite volume method. This method allows for arbitrary polyhedral shapes. This method reduces to the standard finite difference method for a standard rectangular mesh. Because of the high degree of non-linearity in the van Genuchten constitutive relation for relative permeability for the fluid phase, NUFT uses various weighting approaches. The saturated permeability of a fluid phase between two adjacent cells is

harmonically weighted, while the relative permeability is upstream weighted. This approach is used throughout the model domain.

The key options used for the NUFT simulations include the dual permeability model (DKM) and the active fracture concept (AFC). These modeling methods are NUFT options selected in the NUFT input files (see Attachment XI, files: *.in).

Table 3-1. Software and Routine Usage

Name/ Number	Description	Software Identifiers (STN) or Validation Location	Input source	Input File name	Output File Name
NUFT V3.0s	Qualified Software	10088-3.0s-00	Intermediate file	*.in	*.ext
			Supporting Input file	vtough.pkg dkm-afc-EBS-Rev10-WDR Dkm-afc-NBS-WDR	
rme6 V1.1	Validated Routine	Attachment VIII	LB99EBS1233129.001 Attachment V	Tspa99_primary_mesh UZ99_3.grd	LBL99-YMESH
XTOOL V10.1	Qualified Software Routine	10208-10.1-00	Intermediate file	*.ext	*.ps
YMESH V1.53	Qualified Software Routine	10172-1.53-00	Intermediate file	LBL99-YMESH l4c4.dat	l4c4.col.units
Chim_Surf_TP V1.0	Validated Routine	Attachment VI	LB99EBS1233129.001 LB99EBS1233129.003	Tspa99_primary_mesh Bcs_99.dat	outpt, outpt_wt
Cover V1.1	Validated Routine	Attachment IV	MO9911MWDEBSWD. 000	dft1.dat	shape1.dat
CONVERTCOORDS V1.1	Qualified Software Routine	10209-1.1-00	MO9911MWDEBSWD. 000	*.inf	*.NV
ColumnInfiltration V1.1	Validated Routine	Attachment VII	Intermediate files Table V-3	*.NV Column.data	*.out (infiltration rates)
RETC V1.1	Validated Routine	10099-1.1-00	Attachment XV	Identified in Attachment XV	Attachment XV

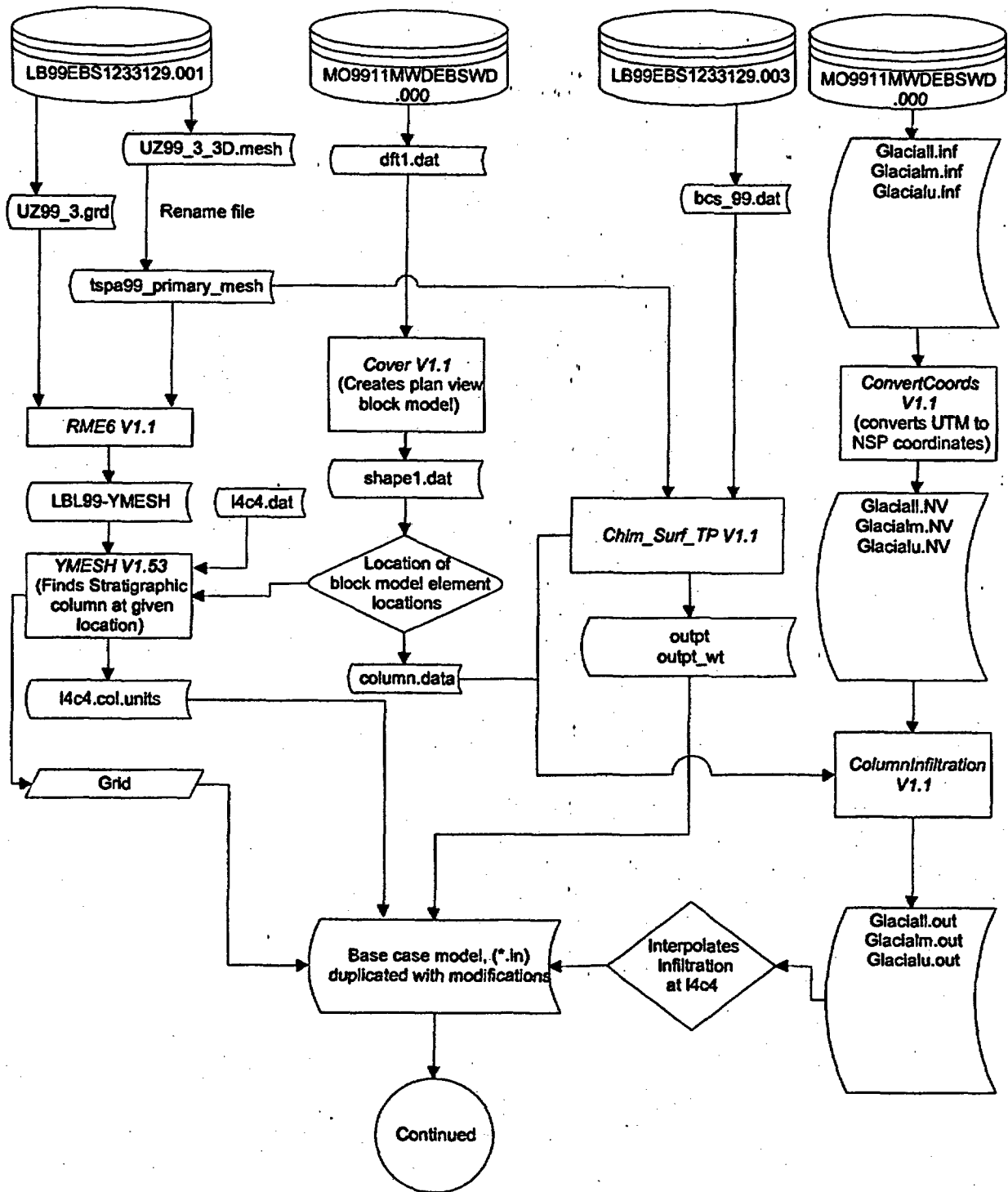


Figure 3-1. Input Data Manipulation Flowchart

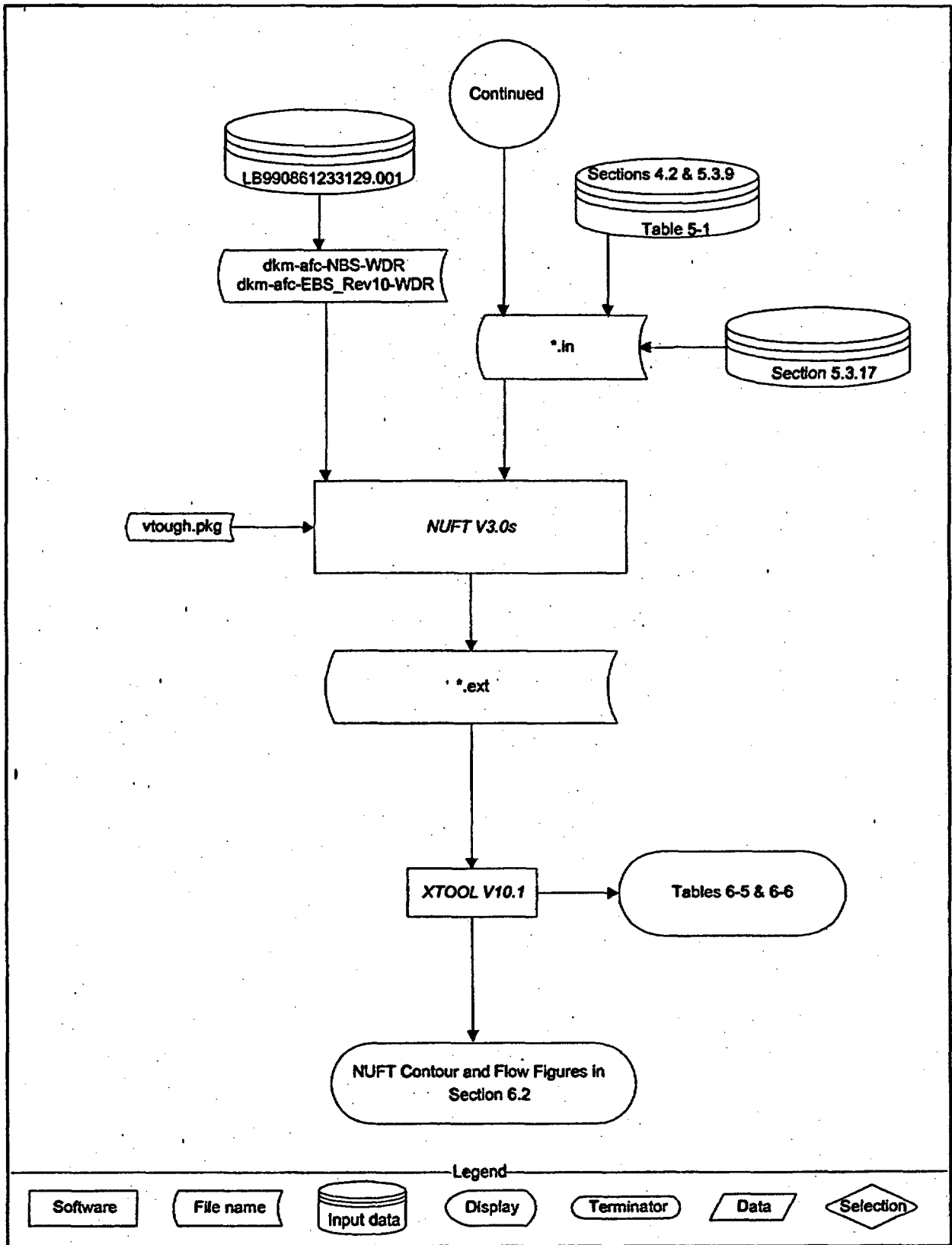


Figure 3-1. Input Data Manipulation Flowchart (Continued)

The DKM conceptualizes the fractured rock as having two interacting materials, one representing the matrix and one representing the fractures. The interaction between the fractures and the matrix is explicitly calculated from the local temperature and pressure differences, thus allowing transient behavior to be predicted. The DKM underestimates the fracture-matrix interaction for steep temperature and pressure gradients (Birkholzer and Tsang 1998, p.2). Simulations in this model are at isothermal, so there are no steep temperature or pressure gradients simulated in this model. Therefore, the DKM is appropriate for the model developed in this document.

The active fracture concept accounts for the contact area between the fracture and the matrix, as well as the frequency of fractures. The AFC is that fracture flow only occurs through some of the fractures. This is more conservative than assuming the influx flows evenly through all fractures. The flux through a fracture is greater when it has higher saturation and, therefore, focusing flow through a portion of the fractures (i.e., to active fractures) maximizes flux and results in fast pathways for flux through the mountain.

The rock properties in DTN: LB990861233129.001 were calibrated using an inverse modeling technique that assumes the properties will only be used in DKM employing AFC. Therefore, the DKM and AFC are appropriate NUFT options.

The RETC (REtention and Conductivity fitting) Version 1.1 (Software Tracking Number (STN) 10099-1.1-00) computer program was acquired from the software configuration management and used for curve fitting to estimate the saturated hydraulic conductivity for the invert as contained in Attachment XIV. RETC is appropriate for the application used in this task, and was used within the range of its validation.

3.2.2 Description of Routines Used

Three routines used in the preparation of this model are qualified through software routine reports in accordance with AP-SI.1Q Section 5.1.2, including XTOOL V10.1, CONVERT COORDS V1.1, and YMESH V1.53. All other routines used in the preparation of this document are qualified in accordance with AP-SI.1Q Section 5.1.1 and documented as follows: Chim_Surf_TP V1.0 is qualified in Attachment VI, ColumnInfiltration V1.1 is qualified in Attachment VII, Cover V1.1 is qualified in Attachment IV, and rme6 V1.1 is qualified in Attachment VIII.

3.2.2.1 XTOOL V10.1

XTOOL is classified as a qualified software routine (STN: 10208-10.1-00) per AP-SI.1Q (Table 3-1). The routine was acquired from the software configuration management and used within the range of validation. The routine was applied to produce graphical presentations appropriately in this document. The output from XTOOL is graphical (no actual data is produced with XTOOL). XTOOL is qualified and tracked in accordance with AP-SI.1Q because it is not commercial off the shelf software. XTOOL was used to develop graphical representations of the results in the NUFT output files (Attachment XI-files: *.ext). XTOOL is appropriate for the application used in this task. XTOOL was run on a Sun Ultra 10 workstation with SunOS 5.6 operating system at locations listed in Table 3-3.

3.2.2.2 CONVERTCOORDS V1.1

CONVERTCOORDS V1.1 is classified as a qualified software routine (STN: 10209-1.1-00) per AP-SI.1Q (Table 3-1). The routine was acquired from the software configuration management and was appropriately used within the range of validation. CONVERTCOORDS was used to convert from Universal Transverse Mercator coordinates to Nevada State Plane coordinates, as well as to reformat the data (see Attachment VIII, files: *.inf). The desired format is columns of data, with the input files in a matrix format. CONVERTCOORDS is appropriate for the application used in this task. CONVERTCOORDS was run on a Sun Ultra 2 workstation with SunOS 5.5.1 operating system at locations listed in Table 3-3.

3.2.2.3 YMESH V1.53

YMESH V1.53 is classified as a qualified software routine (STN: 10172-1.53-00) per AP-SI.1Q (Table 3-1). The routine was acquired from the software configuration management and was appropriately used within the range of validation. YMESH was used in this model to interpolate the thickness of the stratigraphic units as described in the flow chart of Figure 3-1. YMESH is appropriate for the application used in this task. YMESH was run on a Sun Ultra 2 workstation with SunOS 5.5.1 operating system at locations listed in Table 3-3.

3.2.2.4 Chim_Surf_TP V1.0

Chim_Surf_TP V1.0 is classified as routines per AP-SI.1Q, and is qualified in Attachment VI. The purpose of Chim_Surf_TP V1.0 was to interpolate the temperature and pressure at the ground surface and at the water table, respectively, for a given X-Y location using the inverse distance method (Isaaks and Srivastava 1989, p.258). The routine executes the expected mathematical operations accurately (see Attachment VI), and are therefore appropriate for the application in this task. Chim_Surf_TP V1.0 was run on a Sun Ultra 2 workstation with SunOS 5.5.1 operating system at locations listed in Table 3-3.

3.2.2.5 ColumnInfiltration V1.1

ColumnInfiltration V1.1 is classified as a routine per AP-SI.1Q, and is qualified in Attachment VII. The purpose of ColumnInfiltration V1.1 was to interpolate the infiltration at a given X-Y location using a Gaussian weighting function (Isaaks and Srivastava 1989, p.208 and Kitanidis 1997, p.54). This routine executes the required mathematical operations accurately (see Attachment VII), and is therefore appropriate for the application in this task. ColumnInfiltration V1.1 was run on a Sun Ultra 2 workstation with SunOS 5.5.1 operating system at locations listed in Table 3-3.

3.2.2.6 Cover V1.1

Cover V1.1 is classified as a routine per AP-SI.1Q, and is qualified in Attachment IV. The purpose of Cover V1.1 is to develop a block model based on the plan view of the repository that approximates the area and location of emplacement. The results of this routine meet these objectives (see Attachment VII). The routine is, therefore, appropriate for the application

in this task. Cover V1.1 was run on a Sun Ultra 2 workstation with SunOS 5.5.1 operating system at locations listed in Table 3-3.

3.2.2.7 rme6 V1.1

The routine rme6 V1.1 is classified as such per AP-SI.1Q, and is qualified in Attachment VIII. The purpose of rme6 was to reformat and combine specific files (Attachment XI files: tspa99_primary_mesh, UZ99_3.grd, l4c4.dat). The resulting file, LBL99-YMESH was used by a subsequent software program, YMESH V1 (Table 3-1 and Figure 3-1). The results of this routine meet the objectives (see Attachment VIII) and, therefore, the routine is appropriate. The routine rme6 V1.1 was run on a Sun Ultra 10 workstation with SunOS 5.6 operating system at locations listed in Table 3-3.

3.2.3 Other Software

In addition to the above listed items, both Microsoft Excel 97 and Mathcad 7 Professional were used. These software items were used to perform support calculations as described in Section 6.2 and Attachments V and XI. Computer execution of these programs were performed at machines listed in Table 3-3. To provide documentation of the analysis in sufficient detail to allow independent repetition of the software in accordance with AP-3.10Q Attachment I, and to ensure compliance with AP-SI.1Q, the minimum information required by AP-SI.1Q Section 5.1.1.2 has been provided:

- Identification of Excel and Mathcad files, including the version of the file, are provided in Section 6.2, Attachment V, and Attachment XI.
- The name and version of the commercial software are provided as described above.
- The inputs, spreadsheet cell contents and equations, and results are provided in attached CD (Attachment XVI). This provides sufficient documentation that these standard mathematical calculations provide correct results for the specified range of input parameters.

3.3 THERMOHYDROLOGIC MODEL

Software and software routines are used for the Thermohydrologic (TH) Model portion of the WD&R model (Table 3-2). Table 3-3 contains a list of the CPU's where these programs were executed. For the models described in this report, thermohydrologic software is used within the range of validation, where such constraint information is available, or within the range of standard practice, where such information is unavailable.

The following subsections describe these codes and routines in more detail. Documentation and validation of the software routines are summarized in Table 3-2. Table 3-4 lists the input files used for all NUFT V3.0s runs discussed in this report. Discussion of the output files is provided in Table 6-8.

All input and output files and software routine sources files have been saved electronically in the attached CD (Attachment XVI) under "thermo" directory.

Table 3-2. Software Codes and Routines Used for Thermohydrologic Calculations

Software Name	Type	STN	Attachment
Codes (qualified per AP-SI.1Q Section 5.1.2)			
NUFT V3.0s	Simulation Code	1088-3.0s-00	N/A
Routines (qualified per AP-SI.1Q Section 5.1.2)			
YMESH V1.53	NUFT preprocessor	10172-1.53-00	N/A
XTOOL 10.1	NUFT postprocessor	10208-10.1-00	N/A
CONVERTCOORDS V1.1	NUFT preprocessor	10209-1.1-00	N/A
Routines (see Attachments for Qualification/Validation Documentation)			
RME6 V1.1	NUFT preprocessor	N/A	VIII
COVER V1.1	NUFT preprocessor	N/A	IV
COLUMNINFILTRATION V1.1	NUFT preprocessor	N/A	VII
CHIM_SURF_TP V1.0	NUFT preprocessors	N/A	VI

Table 3-3. Software Execution

Workstation/PC Name	Physical Location
s139	LLNL, T1487 Rm 150A
s89	LLNL, T1487 Rm 150
s116	LLNL, T1401 Rm 1119
s117	LLNL, T1487 Rm 112
s187	LLNL, T1487 Rm 153
s70	LLNL, T1487 Rm 149
s11	LLNL, T1487 Rm 146
s08	LLNL, T1487 Rm 145
s28	LLNL, T1487 Rm 154
s13	LLNL, T1487 Rm 124
s188	LLNL, T1487 Rm 138
s175	LLNL, T1487 Rm 114
Dell PowerEdge 2200 #112524	Las Vegas, Rm 611
Dell Optiplex #116400	Las Vegas, Rm 1031F

Table 3-4. NUFT Input Files for Calculations Described in the Thermohydrologic Model

File Type	Filename
I4c4 location; mean infiltration; 56 MTU/acre 0% Seepage onto Drip Shield	
NUFT input (.in) file	I4c4-LDTH56-mi.00.in
Restart file from preclosure run	I4c4-LDTH56-1Dds_mc-mi-a.res
Rock properties file	dkm_afc-1Dds-mc-mi-00
EBS properties file	dkm-afc-EBS_Rev21
Thermal conductivity "modification" file	modprop_dr-20
Heat generation file	LDTH-SDT-0.3Qheat-1e6y_vent-20
Solver control file	vtough.pkg
Run control file	run_control_param_LDTH-v09
Genmsh grid file	I4c4-LDTH56-5pt.xz
Flux output control file	fluxOutput100
Enthalpy history file for seepage flux	enthalpyWater56Med.nft
Time steps for ext file output	output.times-56-20a
I4c4 location; mean infiltration; 56 MTU/acre 3% Seepage onto Drip Shield	
NUFT input (.in) file	I4c4-LDTH56-mi.03.in
Restart file from preclosure run	I4c4-LDTH56-1Dds_mc-mi-a.res
Rock properties file	dkm_afc-1Dds-mc-mi-00
EBS properties file	dkm-afc-EBS_Rev21
Thermal conductivity "modification" file	modprop_dr-20
Heat generation file	LDTH-SDT-0.3Qheat-1e6y_vent-20
Solver control file	vtough.pkg
Run control file	run_control_param_LDTH-v09
Genmsh grid file	I4c4-LDTH56-5pt.xz
Flux output control file	fluxOutput100
Enthalpy history file for seepage flux	enthalpyWater56Med.nft
Time steps for ext file output	output.times-56-20a
I4c4 location; mean infiltration; 56 MTU/acre 30% Seepage onto Drip Shield	
NUFT input (.in) file	I4c4-LDTH56-mi.30.in
Restart file from preclosure run	I4c4-LDTH56-1Dds_mc-mi-a.res
Rock properties file	dkm_afc-1Dds-mc-mi-00
EBS properties file	dkm-afc-EBS_Rev21
Thermal conductivity "modification" file	modprop_dr-20
Heat generation file	LDTH-SDT-0.3Qheat-1e6y_vent-20
Solver control file	vtough.pkg
Run control file	run_control_param_LDTH-v09
Genmsh grid file	I4c4-LDTH56-5pt.xz
Flux output control file	fluxOutput100
Enthalpy history file for seepage flux	enthalpyWater56Med.nft
Time steps for ext file output	output.times-56-20a

File Type	Filename
I4c4 location; "lower" infiltration; 56 MTU/acre 0% Seepage onto Drip Shield	
NUFT input (.in) file	I4c4-LDTH56-li.00.in
Restart file from preclosure run	I4c4-LDTH56-1Dds_mc-li-a.res
Rock properties file	dkm_afc-1Dds-mc-li-00
EBS properties file	dkm-afc-EBS_Rev21
Thermal conductivity "modification" file	modprop_dr-20
Heat generation file	LDTH-SDT-0.3Qheat-1e6y_vent-20
Solver control file	vtough.pkg
Run control file	run_control_param_LDTH-v09
Genmsh grid file	I4c4-LDTH56-5pt.xz
Flux output control file	fluxOutput100
Enthalpy history file for seepage flux	enthalpyWater56Low.nft
Time steps for ext file output	output.times-56-20a
I4c4 location; "lower" infiltration; 56 MTU/acre 3% Seepage onto Drip Shield	
NUFT input (.in) file	I4c4-LDTH56-li.03.in
Restart file from preclosure run	I4c4-LDTH56-1Dds_mc-li-a.res
Rock properties file	dkm_afc-1Dds-mc-li-00
EBS properties file	dkm-afc-EBS_Rev21
Thermal conductivity "modification" file	modprop_dr-20
Heat generation file	LDTH-SDT-0.3Qheat-1e6y_vent-20
Solver control file	vtough.pkg
Run control file	run_control_param_LDTH-v09
Genmsh grid file	I4c4-LDTH56-5pt.xz
Flux output control file	fluxOutput100
Enthalpy history file for seepage flux	enthalpyWater56Low.nft
Time steps for ext file output	output.times-56-20a
I4c4 location; "lower" infiltration; 56 MTU/acre 30% Seepage onto Drip Shield	
NUFT input (.in) file	I4c4-LDTH56-li.30.in
Restart file from preclosure run	I4c4-LDTH56-1Dds_mc-li-a.res
Rock properties file	dkm_afc-1Dds-mc-li-00
EBS properties file	dkm-afc-EBS_Rev21
Thermal conductivity "modification" file	modprop_dr-20
Heat generation file	LDTH-SDT-0.3Qheat-1e6y_vent-20
Solver control file	vtough.pkg
Run control file	run_control_param_LDTH-v09
Genmsh grid file	I4c4-LDTH56-5pt.xz
Flux output control file	fluxOutput100
Enthalpy history file for seepage flux	enthalpyWater56Low.nft
Time steps for ext file output	output.times-56-20a

File Type	Filename
I4c4 location; "upper" infiltration; 56 MTU/acre 0% Seepage onto Drip Shield	
NUFT input (.in) file	I4c4-LDTH56-ui.00.in
Restart file from preclosure run	I4c4-LDTH56-1Dds_mc-ui-a.res
Rock properties file	dkm_afc-1Dds-mc-ui-00
EBS properties file	dkm-afc-EBS_Rev21
Thermal conductivity "modification" file	modprop_dr-20
Heat generation file	LDTH-SDT-0.3Qheat-1e6y_vent-20
Solver control file	vtough.pkg
Run control file	run_control_param_LDTH-v09
Genmsh grid file	I4c4-LDTH56-5pt.xz
Flux output control file	fluxOutput100
Enthalpy history file for seepage flux	enthalpyWater56Upp.nft
Time steps for ext file output	output.times-56-20a
I4c4 location; "upper" infiltration; 56 MTU/acre 3% Seepage onto Drip Shield	
NUFT input (.in) file	I4c4-LDTH56-ui.03.in
Restart file from preclosure run	I4c4-LDTH56-1Dds_mc-ui-a.res
Rock properties file	dkm_afc-1Dds-mc-ui-00
EBS properties file	dkm-afc-EBS_Rev21
Thermal conductivity "modification" file	modprop_dr-20
Heat generation file	LDTH-SDT-0.3Qheat-1e6y_vent-20
Solver control file	vtough.pkg
Run control file	run_control_param_LDTH-v09
Genmsh grid file	I4c4-LDTH56-5pt.xz
Flux output control file	fluxOutput100
Enthalpy history file for seepage flux	enthalpyWater56Upp.nft
Time steps for ext file output	output.times-56-20a
I4c4 location; "upper" infiltration; 56 MTU/acre 30% Seepage onto Drip Shield	
NUFT input (.in) file	I4c4-LDTH56-ui.30.in
Restart file from preclosure run	I4c4-LDTH56-1Dds_mc-ui-a.res
Rock properties file	dkm_afc-1Dds-mc-ui-00
EBS properties file	dkm-afc-EBS_Rev21
Thermal conductivity "modification" file	modprop_dr-20
Heat generation file	LDTH-SDT-0.3Qheat-1e6y_vent-20
Solver control file	vtough.pkg
Run control file	run_control_param_LDTH-v09
Genmsh grid file	I4c4-LDTH56-5pt.xz
Flux output control file	fluxOutput100
Enthalpy history file for seepage flux	enthalpyWater56Upp.nft
Time steps for ext file output	output.times-56-20a

File Type	Filename
I4c1 location; mean infiltration; 34 MTU/acre 0% Seepage onto Drip Shield	
NUFT input (.in) file	I4c1-LDTH34-mi.00.in
Restart file from preclosure run	I4c1-LDTH34-1Dds_mc-mi-a.res
Rock properties file	dkm_afc-1Dds-mc-mi-00
EBS properties file	dkm-afc-EBS_Rev21
Thermal conductivity "modification" file	modprop_dr-20
Heat generation file	LDTH-SDT-0.3Qheat-1e6y_vent-20
Solver control file	vtough.pkg
Run control file	run_control_param_LDTH-v09
Genmsh grid file	I4c1-LDTH34-5pt.xz
Flux output control file	fluxOutput100
Enthalpy history file for seepage flux	enthalpyWater34Med.nft
Time steps for ext file output	output.times-34-20a
I4c1 location; mean infiltration; 34 MTU/acre 3% Seepage onto Drip Shield	
NUFT input (.in) file	I4c1-LDTH34-mi.03.in
Restart file from preclosure run	I4c1-LDTH34-1Dds_mc-mi-a.res
Rock properties file	dkm_afc-1Dds-mc-mi-00
EBS properties file	dkm-afc-EBS_Rev21
Thermal conductivity "modification" file	modprop_dr-20
Heat generation file	LDTH-SDT-0.3Qheat-1e6y_vent-20
Solver control file	vtough.pkg
Run control file	run_control_param_LDTH-v09
Genmsh grid file	I4c1-LDTH34-5pt.xz
Flux output control file	fluxOutput100
Enthalpy history file for seepage flux	enthalpyWater34Med.nft
Time steps for ext file output	output.times-34-20a
I4c1 location; mean infiltration; 34 MTU/acre 30% Seepage onto Drip Shield	
NUFT input (.in) file	I4c1-LDTH34-mi.30.in
Restart file from preclosure run	I4c1-LDTH34-1Dds_mc-mi-a.res
Rock properties file	dkm_afc-1Dds-mc-mi-00
EBS properties file	dkm-afc-EBS_Rev21
Thermal conductivity "modification" file	modprop_dr-20
Heat generation file	LDTH-SDT-0.3Qheat-1e6y_vent-20
Solver control file	vtough.pkg
Run control file	run_control_param_LDTH-v09
Genmsh grid file	I4c1-LDTH34-5pt.xz
Flux output control file	fluxOutput100
Enthalpy history file for seepage flux	enthalpyWater34Med.nft
Time steps for ext file output	output.times-34-20a

File Type	Filename
I4c1 location; "lower" infiltration; 34 MTU/acre 0% Seepage onto Drip Shield	
NUFT input (.in) file	I4c1-LDTH34-li.00.in
Restart file from preclosure run	I4c1-LDTH34-1Dds_mc-li-a.res
Rock properties file	dkm_afc-1Dds-mc-li-00
EBS properties file	dkm-afc-EBS_Rev21
Thermal conductivity "modification" file	modprop_dr-20
Heat generation file	LDTH-SDT-0.3Qheat-1e6y_vent-20
Solver control file	vtough.pkg
Run control file	run_control_param_LDTH-v09
Genmsh grid file	I4c1-LDTH34-5pt.xz
Flux output control file	fluxOutput100
Enthalpy history file for seepage flux	enthalpyWater34Low.nft
Time steps for ext file output	output.times-34-20a
I4c1 location; "lower" infiltration; 34 MTU/acre 3% Seepage onto Drip Shield	
NUFT input (.in) file	I4c1-LDTH34-li.03.in
Restart file from preclosure run	I4c1-LDTH34-1Dds_mc-li-a.res
Rock properties file	dkm_afc-1Dds-mc-li-00
EBS properties file	dkm-afc-EBS_Rev21
Thermal conductivity "modification" file	modprop_dr-20
Heat generation file	LDTH-SDT-0.3Qheat-1e6y_vent-20
Solver control file	vtough.pkg
Run control file	run_control_param_LDTH-v09
Genmsh grid file	I4c1-LDTH34-5pt.xz
Flux output control file	fluxOutput100
Enthalpy history file for seepage flux	enthalpyWater34Low.nft
Time steps for ext file output	output.times-34-20a
I4c1 location; "lower" infiltration; 34 MTU/acre 30% Seepage onto Drip Shield	
NUFT input (.in) file	I4c1-LDTH34-li.30.in
Restart file from preclosure run	I4c1-LDTH34-1Dds_mc-li-a.res
Rock properties file	dkm_afc-1Dds-mc-li-00
EBS properties file	dkm-afc-EBS_Rev21
Thermal conductivity "modification" file	modprop_dr-20
Heat generation file	LDTH-SDT-0.3Qheat-1e6y_vent-20
Solver control file	vtough.pkg
Run control file	run_control_param_LDTH-v09
Genmsh grid file	I4c1-LDTH34-5pt.xz
Flux output control file	fluxOutput100
Enthalpy history file for seepage flux	enthalpyWater34Low.nft
Time steps for ext file output	output.times-34-20a

File Type	Filename
I4c1 location; "upper" Infiltration; 34 MTU/acre 0% Seepage onto Drip Shield	
NUFT input (.in) file	I4c1-LDTH34-ui.00.in
Restart file from preclosure run	I4c1-LDTH34-1Dds_mc-ui-a.res
Rock properties file	dkm_afc-1Dds-mc-ui-00
EBS properties file	dkm-afc-EBS_Rev21
Thermal conductivity "modification" file	modprop_dr-20
Heat generation file	LDTH-SDT-0.3Qheat-1e6y_vent-20
Solver control file	vtough.pkg
Run control file	run_control_param_LDTH-v09
Genmsh grid file	I4c1-LDTH34-5pt.xz
Flux output control file	fluxOutput100
Enthalpy history file for seepage flux	enthalpyWater34Upp.nft
Time steps for ext file output	output.times-34-20a
I4c1 location; "upper" Infiltration; 34 MTU/acre 3% Seepage onto Drip Shield	
NUFT input (.in) file	I4c1-LDTH34-ui.03.in
Restart file from preclosure run	I4c1-LDTH34-1Dds_mc-ui-a.res
Rock properties file	dkm_afc-1Dds-mc-ui-00
EBS properties file	dkm-afc-EBS_Rev21
Thermal conductivity "modification" file	modprop_dr-20
Heat generation file	LDTH-SDT-0.3Qheat-1e6y_vent-20
Solver control file	vtough.pkg
Run control file	run_control_param_LDTH-v09
Genmsh grid file	I4c1-LDTH34-5pt.xz
Flux output control file	fluxOutput100
Enthalpy history file for seepage flux	enthalpyWater34Upp.nft
Time steps for ext file output	output.times-34-20a
I4c1 location; "upper" Infiltration; 34 MTU/acre 30% Seepage onto Drip Shield	
NUFT input (.in) file	I4c1-LDTH34-ui.30.in
Restart file from preclosure run	I4c1-LDTH34-1Dds_mc-ui-a.res
Rock properties file	dkm_afc-1Dds-mc-ui-00
EBS properties file	dkm-afc-EBS_Rev21
Thermal conductivity "modification" file	modprop_dr-20
Heat generation file	LDTH-SDT-0.3Qheat-1e6y_vent-20
Solver control file	vtough.pkg
Run control file	run_control_param_LDTH-v09
Genmsh grid file	I4c1-LDTH34-5pt.xz
Flux output control file	fluxOutput100
Enthalpy history file for seepage flux	enthalpyWater34Upp.nft
Time steps for ext file output	output.times-34-20a

File Type	Filename
I4c4 location; mean infiltration; 56 MTU/acre 3% Seepage onto Invert	
NUFT input (.in) file	I4c4-LDTH56-mi-inv.03.in
Restart file from preclosure run	I4c4-LDTH56-1Dds_mc-mi-a.res
Rock properties file	dkm_afc-1Dds-mc-mi-00
EBS properties file	dkm-afc-EBS_Rev21
Thermal conductivity "modification" file	modprop_dr-20
Heat generation file	LDTH-SDT-0.3Qheat-1e6y_vent-20
Solver control file	vtough.pkg
Run control file	run_control_param_LDTH-v09
Genrsh grid file	I4c4-LDTH56-5pt.xz
Flux output control file	fluxOutput100
Enthalpy history file for seepage flux	enthalpyWater56Med.nft
Time steps for ext file output	output.times-56-20a
I4c4 location; mean infiltration; 56 MTU/acre 30% Seepage onto Invert	
NUFT input (.in) file	I4c4-LDTH56-mi-inv.30.in
Restart file from preclosure run	I4c4-LDTH56-1Dds_mc-mi-a.res
Rock properties file	dkm_afc-1Dds-mc-mi-00
EBS properties file	dkm-afc-EBS_Rev21
Thermal conductivity "modification" file	modprop_dr-20
Heat generation file	LDTH-SDT-0.3Qheat-1e6y_vent-20
Solver control file	vtough.pkg
Run control file	run_control_param_LDTH-v09
Genmsh grid file	I4c4-LDTH56-5pt.xz
Flux output control file	fluxOutput100
Enthalpy history file for seepage flux	enthalpyWater56Med.nft
Time steps for ext file output	output.times-56-20a
I4c4 location; "lower" infiltration; 56 MTU/acre 3% Seepage onto Invert	
NUFT input (.in) file	I4c4-LDTH56-li-inv.03.in
Restart file from preclosure run	I4c4-LDTH56-1Dds_mc-li-a.res
Rock properties file	dkm_afc-1Dds-mc-li-00
EBS properties file	dkm-afc-EBS_Rev21
Thermal conductivity "modification" file	modprop_dr-20
Heat generation file	LDTH-SDT-0.3Qheat-1e6y_vent-20
Solver control file	vtough.pkg
Run control file	run_control_param_LDTH-v09
Genmsh grid file	I4c4-LDTH56-5pt.xz
Flux output control file	fluxOutput100
Enthalpy history file for seepage flux	enthalpyWater56Low.nft
Time steps for ext file output	output.times-56-20a

File Type	Filename
I4c4 location; "lower" infiltration; 56 MTU/acre 30% Seepage onto Invert	
NUFT input (.in) file	I4c4-LDTH56-li-inv.30.in
Restart file from preclosure run	I4c4-LDTH56-1Dds_mc-li-a.res
Rock properties file	dkm_afc-1Dds-mc-li-00
EBS properties file	dkm-afc-EBS_Rev21
Thermal conductivity "modification" file	modprop_dr-20
Heat generation file	LDTH-SDT-0.3Qheat-1e6y_vent-20
Solver control file	vtough.pkg
Run control file	run_control_param_LDTH-v09
Genmsh grid file	I4c4-LDTH56-5pt.xz
Flux output control file	fluxOutput100
Enthalpy history file for seepage flux	enthalpyWater56Low.nft
Time steps for ext file output	output.times-56-20a
I4c4 location; "upper" infiltration; 56 MTU/acre 3% Seepage onto Invert	
NUFT input (.in) file	I4c4-LDTH56-ui-inv.03.in
Restart file from preclosure run	I4c4-LDTH56-1Dds_mc-ui-a.res
Rock properties file	dkm_afc-1Dds-mc-ui-00
EBS properties file	dkm-afc-EBS_Rev21
Thermal conductivity "modification" file	modprop_dr-20
Heat generation file	LDTH-SDT-0.3Qheat-1e6y_vent-20
Solver control file	vtough.pkg
Run control file	run_control_param_LDTH-v09
Genmsh grid file	I4c4-LDTH56-5pt.xz
Flux output control file	fluxOutput100
Enthalpy history file for seepage flux	enthalpyWater56Upp.nft
Time steps for ext file output	output.times-56-20a
I4c4 location; "upper" infiltration; 56 MTU/acre 30% Seepage onto Invert	
NUFT input (.in) file	I4c4-LDTH56-ui-inv.30.in
Restart file from preclosure run	I4c4-LDTH56-1Dds_mc-ui-a.res
Rock properties file	dkm_afc-1Dds-mc-ui-00
EBS properties file	dkm-afc-EBS_Rev21
Thermal conductivity "modification" file	modprop_dr-20
Heat generation file	LDTH-SDT-0.3Qheat-1e6y_vent-20
Solver control file	vtough.pkg
Run control file	run_control_param_LDTH-v09
Genmsh grid file	I4c4-LDTH56-5pt.xz
Flux output control file	fluxOutput100
Enthalpy history file for seepage flux	enthalpyWater56Upp.nft
Time steps for ext file output	output.times-56-20a

File Type	Filename
I4c1 location; mean infiltration; 34 MTU/acre 3% Seepage onto Invert	
NUFT input (.ln) file	I4c1-LDTH34-mi-inv.03.ln
Restart file from preclosure run	I4c1-LDTH34-1Dds_mc-mi-a.res
Rock properties file	dkm_afc-1Dds-mc-mi-00
EBS properties file	dkm-afc-EBS_Rev21
Thermal conductivity "modification" file	modprop_dr-20
Heat generation file	LDTH-SDT-0.3Qheat-1e6y_vent-20
Solver control file	vtough.pkg
Run control file	run_control_param_LDTH-v09
Genmsh grid file	I4c1-LDTH34-5pt.xz
Flux output control file	fluxOutput100
Enthalpy history file for seepage flux	enthalpyWater34Med.nft
Time steps for ext file output	output.times-34-20a
I4c1 location; mean infiltration; 34 MTU/acre 30% Seepage onto Invert	
NUFT input (.ln) file	I4c1-LDTH34-mi-inv.30.ln
Restart file from preclosure run	I4c1-LDTH34-1Dds_mc-mi-a.res
Rock properties file	dkm_afc-1Dds-mc-mi-00
EBS properties file	dkm-afc-EBS_Rev21
Thermal conductivity "modification" file	modprop_dr-20
Heat generation file	LDTH-SDT-0.3Qheat-1e6y_vent-20
Solver control file	vtough.pkg
Run control file	run_control_param_LDTH-v09
Genmsh grid file	I4c1-LDTH34-5pt.xz
Flux output control file	fluxOutput100
Enthalpy history file for seepage flux	enthalpyWater34Med.nft
Time steps for ext file output	output.times-34-20a
I4c1 location; "lower" infiltration; 34 MTU/acre 3% Seepage onto Invert	
NUFT input (.ln) file	I4c1-LDTH34-li-inv.03.ln
Restart file from preclosure run	I4c1-LDTH34-1Dds_mc-li-a.res
Rock properties file	dkm_afc-1Dds-mc-li-00
EBS properties file	dkm-afc-EBS_Rev21
Thermal conductivity "modification" file	modprop_dr-20
Heat generation file	LDTH-SDT-0.3Qheat-1e6y_vent-20
Solver control file	vtough.pkg
Run control file	run_control_param_LDTH-v09
Genmsh grid file	I4c1-LDTH34-5pt.xz
Flux output control file	fluxOutput100
Enthalpy history file for seepage flux	enthalpyWater34Low.nft
Time steps for ext file output	output.times-34-20a

File Type	Filename
I4c1 location; "lower" infiltration; 34 MTU/acre 30% Seepage onto Invert	
NUFT Input (.In) file	I4c1-LDTH34-li-inv.30.in
Restart file from preclosure run	I4c1-LDTH34-1Dds_mc-li-a.res
Rock properties file	dkm_afc-1Dds-mc-li-00
EBS properties file	dkm-afc-EBS_Rev21
Thermal conductivity "modification" file	modprop_dr-20
Heat generation file	LDTH-SDT-0.3Qheat-1e6y_vent-20
Solver control file	vtough.pkg
Run control file	run_control_param_LDTH-v09
Genmsh grid file	I4c1-LDTH34-5pt.xz
Flux output control file	fluxOutput100
Enthalpy history file for seepage flux	enthalpyWater34Low.nft
Time steps for ext file output	output.times-34-20a
I4c1 location; "upper" infiltration; 34 MTU/acre 3% Seepage onto Invert	
NUFT Input (.In) file	I4c1-LDTH34-ui-inv.03.in
Restart file from preclosure run	I4c1-LDTH34-1Dds_mc-ui-a.res
Rock properties file	dkm_afc-1Dds-mc-ui-00
EBS properties file	dkm-afc-EBS_Rev21
Thermal conductivity "modification" file	modprop_dr-20
Heat generation file	LDTH-SDT-0.3Qheat-1e6y_vent-20
Solver control file	vtough.pkg
Run control file	run_control_param_LDTH-v09
Genmsh grid file	I4c1-LDTH34-5pt.xz
Flux output control file	fluxOutput100
Enthalpy history file for seepage flux	enthalpyWater34Upp.nft
Time steps for ext file output	output.times-34-20a
I4c1 location; "upper" infiltration; 34 MTU/acre 30% Seepage onto Invert	
NUFT Input (.In) file	I4c1-LDTH34-ui-inv.30.in
Restart file from preclosure run	I4c1-LDTH34-1Dds_mc-ui-a.res
Rock properties file	dkm_afc-1Dds-mc-ui-00
EBS properties file	dkm-afc-EBS_Rev21
Thermal conductivity "modification" file	modprop_dr-20
Heat generation file	LDTH-SDT-0.3Qheat-1e6y_vent-20
Solver control file	vtough.pkg
Run control file	run_control_param_LDTH-v09
Genmsh grid file	I4c1-LDTH34-5pt.xz
Flux output control file	fluxOutput100
Enthalpy history file for seepage flux	enthalpyWater34Upp.nft
Time steps for ext file output	output.times-34-20a

3.3.1 Description of TH Software Used

The software used for the thermohydrologic model is NUFT v3.0s (STN: 1088-3.0s-00) as discussed in Section 3.2.1.

3.3.2 Description of TH Routines Used

The routines used for the thermohydrologic model are listed in Table 3-2. Description of the routines is presented in Section 3.2.2.

3.4 DRIP SHIELD CONDENSATION MODEL

The computer software and model usage for the drip shield condensation model are the same as those discussed in Section 3.3, Thermohydrologic Model.

Microsoft Excel 97 spreadsheet files were used to calculate the condensation index using the data extracted from the Multiscale Thermohydrologic Model. The Excel files are named as "wdrdsc.xls" and "wdrdscu.xls" and are provided in the attached CD (Attachment XVI) under the "dscondensation" directory. A macro was also programmed in Microsoft Excel 97 to interpolate linearly the values of vapor pressure and temperature from a steam table. The steam table is obtained from Himmelblau (1996) for temperature (T) versus saturated vapor pressure (Vp) data at every 2 Fahrenheit-degree intervals (approximately 1.11 degrees Centigrade). Qualification of the macro is shown in Attachment XIII.

4. INPUTS

4.1 DATA AND PARAMETERS

4.1.1 Water Diversion Model

4.1.1.1 (Not Used)

4.1.1.2 Water and Water Vapor Properties

Thermophysical properties of water and water vapor are required for the film flow and vapor condensation calculations. Table 4-1 presents some of these property values at 60 °C while the properties as a function of temperature can be found in Table III-1 in Attachment III. These data are appropriately used.

Table 4-1. Selected Water and Water Vapor Properties at 60 °C ⁽¹⁾

Parameter	Symbol	Unit	Value
Liquid			
Density	ρ_w	kg/m ³	983.2
Absolute Viscosity	μ_w	Pa.s	4.7 x 10 ⁻⁴
Surface Tension	σ_w	N/m	0.06624
Vapor			
Density	ρ_v	kg/m ³	0.13
Saturated Pressure	P_{sat}	Pa	1.99 x 10 ⁴
Gas Constant	R	J/kg.°K	461.8

Note: ⁽¹⁾ Robinson R.N., (1987, p.4-28, and p.5-22)

4.1.2 Water Drainage Model

4.1.2.1 Hydrologic and Thermal Properties of the NBS

Tables 4-2 to 4-5 present the hydrologic and thermal properties for the hydro-stratigraphic units considered in this model. The data are from DTN: LB990861233129.001, generated by the UZ Model (CRWMS M&O 2000o). Fracture porosity, matrix porosity, tortuosity factor, fracture bulk permeability, matrix bulk permeability, maximum and residual saturation in fractures, maximum and residual saturation in matrix, van Genuchten parameters α and m (or λ) for fractures and matrix are used in the analysis. These data are appropriately used.

Table 4-2. Matrix Hydrologic Parameters for NBS (DTN: LB990861233129.001)

Unit	Permeability (m ²)	Porosity (Fraction)	van Genuchten α (Pa ⁻¹)	van Genuchten m	Residual Saturation (Fraction)	Saturated Saturation (Fraction)
Tcw11	3.86E-15	0.253	4.00E-05	0.47	0.07	1
Tcw12	2.74E-19	0.082	1.81E-05	0.241	0.19	1
Tcw13	9.23E-17	0.203	3.44E-06	0.398	0.31	1
Ptn21	9.90E-13	0.387	1.01E-05	0.176	0.23	1
Ptn22	2.65E-12	0.439	1.60E-04	0.326	0.16	1
Ptn23	1.23E-13	0.254	5.58E-06	0.397	0.08	1
Ptn24	7.86E-14	0.411	1.53E-04	0.225	0.14	1
Ptn25	7.00E-14	0.499	5.27E-05	0.323	0.06	1
Ptn26	2.21E-13	0.492	2.49E-04	0.285	0.05	1
Tsw31	6.32E-17	0.053	3.61E-05	0.303	0.22	1
Tsw32	5.83E-16	0.157	3.61E-05	0.333	0.07	1
Tsw33	3.08E-17	0.154	2.13E-05	0.298	0.12	1
Tsw34	4.07E-18	0.11	3.86E-06	0.291	0.19	1
Tsw35	3.04E-17	0.131	6.44E-06	0.236	0.12	1
Tsw36	5.71E-18	0.112	3.55E-06	0.38	0.18	1
Tsw37	4.49E-18	0.094	5.33E-06	0.425	0.25	1
Tsw38	4.53E-18	0.037	6.94E-06	0.324	0.44	1
Tsw39	5.46E-17	0.173	2.29E-05	0.38	0.29	1
Ch1z	1.96E-19	0.288	2.68E-07	0.316	0.33	1
Ch1v	9.90E-13	0.273	1.43E-05	0.35	0.03	1
Ch2v	9.27E-14	0.345	5.13E-05	0.299	0.07	1
Ch3v	9.27E-14	0.345	5.13E-05	0.299	0.07	1
Ch4v	9.27E-14	0.345	5.13E-05	0.299	0.07	1
Ch5v	9.27E-14	0.345	5.13E-05	0.299	0.07	1
Ch2z	6.07E-18	0.331	3.47E-06	0.244	0.28	1
Ch3z	6.07E-18	0.331	3.47E-06	0.244	0.28	1
Ch4z	6.07E-18	0.331	3.47E-06	0.244	0.28	1
Ch5z	6.07E-18	0.331	3.47E-06	0.244	0.28	1
ch6	4.23E-19	0.266	3.38E-07	0.51	0.37	1
pp4	4.28E-18	0.325	1.51E-07	0.676	0.28	1
pp3	2.56E-14	0.303	2.60E-05	0.363	0.1	1
pp2	1.57E-16	0.263	2.67E-06	0.369	0.18	1
pp1	6.40E-17	0.28	1.14E-06	0.409	0.3	1
bf3	2.34E-14	0.115	4.48E-06	0.481	0.11	1
bf2	2.51E-17	0.259	1.54E-07	0.569	0.18	1

Table 4-3. Fracture Hydrologic Parameters for NBS (DTN: LB990861233129.001)

Unit	Permeability (m ²)	Porosity (Fraction)	van Genuchten α (Pa ⁻¹)	van Genuchten m	Residual Saturation (Fraction)	Satiated Saturation (Fraction)
tcw11	2.41E-12	0.028	3.15E-03	0.627	0.01	1
tcw12	1.00E-10	0.02	2.13E-03	0.613	0.01	1
tcw13	5.42E-12	0.015	1.26E-03	0.607	0.01	1
ptn21	1.86E-12	0.011	1.68E-03	0.58	0.01	1
ptn22	2.00E-11	0.012	7.68E-04	0.58	0.01	1
ptn23	2.60E-13	0.0025	9.23E-04	0.61	0.01	1
ptn24	4.67E-13	0.012	3.37E-03	0.623	0.01	1
ptn25	7.03E-13	0.0062	6.33E-04	0.644	0.01	1
ptn26	4.44E-13	0.0036	2.79E-04	0.552	0.01	1
tsw31	3.21E-11	0.0055	2.49E-04	0.566	0.01	1
tsw32	1.26E-12	0.0095	1.27E-03	0.608	0.01	1
tsw33	5.50E-13	0.0066	1.46E-03	0.608	0.01	1
tsw34	2.76E-13	0.01	5.16E-04	0.608	0.01	1
tsw35	1.29E-12	0.011	7.39E-04	0.611	0.01	1
tsw36	9.91E-13	0.015	7.84E-04	0.61	0.01	1
tsw37	9.91E-13	0.015	7.84E-04	0.61	0.01	1
tsw38	5.92E-13	0.012	4.87E-04	0.612	0.01	1
tsw39	4.57E-13	0.0046	9.63E-04	0.634	0.01	1
ch1z	3.40E-13	0.0002	1.43E-03	0.631	0.01	1
ch1v	1.84E-12	0.0007	1.09E-03	0.624	0.01	1
ch2v	2.89E-13	0.0009	5.18E-04	0.628	0.01	1
ch3v	2.89E-13	0.0009	5.18E-04	0.628	0.01	1
ch4v	2.89E-13	0.0009	5.18E-04	0.628	0.01	1
ch5v	2.89E-13	0.0009	5.18E-04	0.628	0.01	1
ch2z	3.12E-14	0.0004	4.88E-04	0.598	0.01	1
ch3z	3.12E-14	0.0004	4.88E-04	0.598	0.01	1
ch4z	3.12E-14	0.0004	4.88E-04	0.598	0.01	1
ch5z	3.12E-14	0.0004	4.88E-04	0.598	0.01	1
ch6	1.67E-14	0.0002	7.49E-04	0.604	0.01	1
pp4	3.84E-14	0.0004	5.72E-04	0.627	0.01	1
pp3	7.60E-12	0.0011	8.73E-04	0.655	0.01	1
pp2	1.38E-13	0.0011	1.21E-03	0.606	0.01	1
pp1	1.12E-13	0.0004	5.33E-04	0.622	0.01	1
bf3	4.08E-13	0.0011	9.95E-04	0.624	0.01	1
bf2	1.30E-14	0.0004	5.42E-04	0.608	0.01	1

Table 4-4. Hydrologic Parameters for Fracture-Matrix Interaction for NBS (DTN: LB990861233129.001)

Unit	Active Fracture Parameter	Frequency (1/m)	Fracture to matrix connection area (m ² /m ³)
tcw11	0.30	0.92	1.56
tcw12	0.30	1.91	13.39
tcw13	0.30	2.79	3.77
ptn21	0.09	0.67	1.00
ptn22	0.09	0.46	1.41
ptn23	0.09	0.57	1.75
ptn24	0.09	0.46	0.34
ptn25	0.09	0.52	1.09
ptn26	0.09	0.97	3.56
tsw31	0.06	2.17	3.86
tsw32	0.41	1.12	3.21
tsw33	0.41	0.81	4.44
tsw34	0.41	4.32	13.54
tsw35	0.41	3.16	9.68
tsw36	0.41	4.02	12.31
tsw37	0.41	4.02	12.31
tsw38	0.41	4.36	13.34
tsw39	0.41	0.96	2.95
ch1z	0.10	0.04	0.11
ch1v	0.13	0.10	0.30
ch2v	0.13	0.14	0.43
ch3v	0.13	0.14	0.43
ch4v	0.13	0.14	0.43
ch5v	0.13	0.14	0.43
ch2z	0.10	0.14	0.43
ch3z	0.10	0.14	0.43
ch4z	0.10	0.14	0.43
ch5z	0.10	0.14	0.43
ch6	0.10	0.04	0.11
pp4	0.10	0.14	0.43
pp3	0.46	0.20	0.61
pp2	0.46	0.20	0.61
pp1	0.10	0.14	0.43
bf3	0.46	0.20	0.61
Bf2	0.10	0.14	0.43

Table 4-5. Thermal Parameters and Tortuosity Factor for NBS (DTN: LB990861233129.001)

Unit	Rock Grain Density (Kg/m ³)	Rock Grain Specific Heat (J/Kg K)	Dry Conductivity (W/m K)	Wet Conductivity (W/m K)	Tortuosity
tcw11	2550	823	1.60	2.00	0.7
tcw12	2510	851	1.24	1.81	0.7
tcw13	2470	857	0.54	0.98	0.7
ptn21	2380	1040	0.50	1.07	0.7
ptn22	2340	1080	0.35	0.50	0.7
ptn23	2400	849	0.44	0.97	0.7
ptn24	2370	1020	0.46	1.02	0.7
ptn25	2260	1330	0.35	0.82	0.7
ptn26	2370	1220	0.23	0.67	0.7
tsw31	2510	834	0.37	1.00	0.7
tsw32	2550	866	1.06	1.62	0.7
tsw33	2510	882	0.79	1.68	0.7
tsw34	2530	948	1.56	2.33	0.7
tsw35	2540	900	1.20	2.02	0.7
tsw36	2560	865	1.42	1.84	0.7
tsw37	2560	865	1.42	1.84	0.7
tsw38	2360	984	1.69	2.08	0.7
tsw39	2360	984	1.69	2.08	0.7
ch1z	2310	1060	0.70	1.31	0.7
ch1v	2310	1060	0.70	1.31	0.7
ch2v	2240	1200	0.58	1.17	0.7
ch3v	2240	1200	0.58	1.17	0.7
ch4v	2240	1200	0.58	1.17	0.7
ch5v	2240	1200	0.58	1.17	0.7
ch2z	2350	1150	0.61	1.20	0.7
ch3z	2350	1150	0.61	1.20	0.7
ch4z	2350	1150	0.61	1.20	0.7
ch5z	2350	1150	0.61	1.20	0.7
ch6	2440	1170	0.73	1.35	0.7
pp4	2410	577	0.62	1.21	0.7
pp3	2580	841	0.66	1.26	0.7
pp2	2580	841	0.66	1.26	0.7
pp1	2470	635	0.72	1.33	0.7
bf3	2570	763	1.41	1.83	0.7
bf2	2410	633	0.74	1.36	0.7

4.1.2.2 Fluid and Thermodynamic Properties of Water and Air

Thermophysical properties of water as a function of temperature are used in the NUFT models and some are shown in Attachment III, Table III-1 (Incropera and DeWitt (1996, pp. 839, 843, and 846). These data are appropriately used.

4.1.2.3 Universal Constants

The Ideal Gas Constant R (1.987 cal/(g.mol-K)) and Gravitational Constant g (9.807 m/s²) (Robinson, 1987, cover page) are accepted data incorporated into the NUFT code. These constants are appropriately used.

4.1.2.4 Hydrologic and Thermal properties of the EBS

As stated in the scope of work for this report (Section 1.3), the materials used and specifications for EBS components follow the LADS EDA II design concept (CRWMS M&O 2000r, p.2, Sections 2.2.2.2 and 2.3). The backfill consists of Overton sand (CRWMS M&O 2000g, Section 6.1.2.6.1) and the invert consists of crushed tuff (CRWMS M&O 2000w, Section 7.5). The crushed tuff is part of the TSW2 lithostratigraphic unit (CRWMS M&O 2000v, p.13). The hydrologic and thermal properties of the backfill are developed in Attachment X based on DTN: MO9912EBSPWR28.001 while the property values for the invert are developed in Attachments XIV and XV based on the following input data from DTNs: GS000483351030.003 (Table XIV-3), GS000683351030.006 (Section XIV.5), and GS980808312242.015 (Figures XIV-1 and XIV-2). These data sets are utilized in Attachments X, XIV and XV to calculate the hydrologic and thermal properties for the EBS. These data sets are appropriately used.

4.1.3 Thermohydrologic Model

4.1.3.1 Hydrostratigraphic Unit Properties

The hydrologic properties used in the TH portion of this report are fully consistent with the one-dimensional (1-D), drift-scale property sets from the UZ model (CRWMS M&O 2000o, Section 3.6). The property values for units in the 14c4 and 14c1 columns are exactly those given for these units by the following:

- DTN LB990861233129.002 (1-D, drift-scale, "upper" infiltration case)
- DTN LB990861233129.001 (1-D, drift-scale, mean infiltration case)
- DTN LB990861233129.003 (1-D, drift-scale, "lower" infiltration case)

These property sets include porosity, saturated permeability, and parameters for water potential vs. liquid-phase saturation and relative permeability vs. saturation relationships, based on the analytical expressions developed by van Genuchten (1980) and Mualem (1976). Each property set contains similar descriptions for the rock matrix and for the fracture network for each hydrostratigraphic unit. The fracture network is assumed to behave as a continuous porous medium in these calculations, and the continuum properties are assumed to be homogeneous within each hydrostratigraphic unit (Assumption 5.3.2).

The property sets listed previously also include values for parameters that describe

nonequilibrium fracture-matrix interaction using the AFC, which are input directly to NUFT V3.0s. These parameters include fracture spacings and the γ -parameter for each unit. The hydrostratigraphic unit properties are appropriately used.

4.1.3.2 (Not Used)

4.1.3.3 Model Gridding and Numerical Control Parameters

NUFT V3.0s input files (vtough.pkg; run_control_param_LDTH-v00; l4c*.in in attached CD in Attachment XVI) specify control parameters such as numerical-convergence tolerances, time-step control, and parameters for controlling implementation of the nonlinear relations among saturation, relative permeability, and potential. These numerical control parameters are appropriately used.

4.1.3.4 Thermal Properties for Natural Barrier Materials

The thermal properties (DTN: LB990861233129.001) used by NUFT V3.0s are dry thermal conductivity (zero liquid saturation), wet thermal conductivity (100 percent water saturation), specific heat, and grain density. The values used for these calculations are shown in Table 4-5 (Same as the Water Diversion Model). For partial saturation, the NUFT V3.0s code is instructed in the input file (l4c*.in) to linearly interpolate between dry and wet values, based on liquid saturation. Linear interpolation is appropriate because only two constraint data points (dry and wet) are available.

4.1.4 Drip Shield Condensation Model

The input data and parameters used for the drip shield condensation model are the same as those discussed in Section 4.1.3, thermohydrologic model.

4.1.5 Miscellaneous

Drip Shield for bounding calculation - The drip shield length is 5.485 meters for flow through the drip shield (CRWMS M&O 2000g, Attachment II).

4.2 CRITERIA

4.2.1 Drip Shield Material

The *Emplacement Drift System Description Document* (CRWMS M&O 2000r, Section 1.2.1.18) specifies that the drip shield will be titanium grade 7, at least 15 millimeters thick. This criterion is used throughout Section 6.

4.2.2 Emplacement Drift System

The Emplacement Drift System, as part of the Engineering Barrier System (CRWMS M&O 2000r, p.6), provides the interface between the various WP systems and the Ground Control System, and in conjunction with the WPs, limits the release and transport of radionuclides from the WP to the nature barrier. The Emplacement Drift System consists of the structural

support hardware (emplacement drift invert and WP emplacement pallet) and any performance-enhancing barriers (backfill, if used, drip shield, and invert ballast) installed or placed in the emplacement drifts (CRWMS M&O 2000r, Section 2.1).

From the above, it is inferred that a drip shield is part of the Emplacement Drift System and it is necessary to be included in modeling. This criterion is used throughout Section 6.

4.2.3 System Closure

The system shall be designed to be closed as early as 30 years after emplacement of the last WP (CRWMS M&O 2000r, Section 1.2.1.5). This criterion is used throughout Section 6.

4.2.4 Maximum Heat Load for Line Loading of Waste Packages

The system shall be designed for line loading of WPs within individual emplacement drifts, defined as a maximum heat load of 1.5 kW/m of emplacement drifts, averaged over the entire emplacement drift at the time of completion of loading of the emplacement drift (CRWMS M&O 2000r, Section 1.2.1.6). This criterion is used in Section 6.3.

4.2.5 Water Drainage

For 10,000 years, the system shall allow free-liquid-phase water, from the inflow of 2 m³ per m of emplacement drift, to drain out of emplacement drifts, via the emplacement drift floor (CRWMS M&O 2000r, Section 1.2.1.8). This criterion is used in Section 6.2.

4.2.6 Invert Ballast Material

The invert ballast material shall be granular (CRWMS M&O 2000r, Section 1.2.1.11). This criterion is used in Sections 6.2 and 6.3.

4.2.7 Drip Shield Life

The drip shield shall have an operating life of 10,000 years (CRWMS M&O 2000r, Section 1.2.1.12). This criterion is used in Section 6.1.

4.2.8 Water Diversion from Drip Shield

The drip shield shall divert water dripping into the emplacement drift around the WP and to the drift floor (CRWMS M&O 2000r, Section 1.2.1.13). This criterion is used in Section 6.1.

4.2.9 Emplacement Drift Wall Temperature

The system shall limit the emplacement drift wall temperature to less than 200 degrees C (CRWMS M&O 2000r, Section 1.2.3.1). This criterion is used in Section 6.3.

4.2.10 Heat Removal During Preclosure

The system shall accommodate removal of 70 percent of the heat generated by WPs by the Subsurface Ventilation System during the preclosure period (CRWMS M&O 2000r,

Section 1.2.4.5). This criterion is used in Section 6.3.

4.2.11 Waste Package Spacing

The system shall accommodate a minimum spacing of 10 cm between WPs within individual emplacement drifts (CRWMS M&O 2000r, Section 1.2.4.7). This criterion is used in Section 6.3.

4.2.12 Emplacement Drift Spacing

The system shall accommodate a nominal spacing of 81 m between individual emplacement drifts (CRWMS M&O 2000r, Section 1.2.4.8). This criterion is used in Section 6.3.

4.2.13 Emplacement Drift Diameter

The system shall accommodate a nominal emplacement drift excavated diameter of 5.5 m (CRWMS M&O 2000r, Section 1.2.4.9). This criterion is used in Sections 6.1, 6.2, and 6.3.

4.2.14 Closure and Heat Removal

At least 70 percent of the total heat generated by the WPs within the emplacement drifts during the first 50 years of the preclosure period shall be removed by ventilation. (CRWMS M&O 2000w, Section 5.1.3.1). Used in Section 6.3.

4.2.15 Invert Material

The invert is designed to provide support for the WP emplacement pallets during the preclosure period. It will be composed of a steel frame filled with crushed tuff ballast. (CRWMS M&O 2000w, Section 7.5). Used in Section 6.2.

4.3 CODES AND STANDARDS

The Water Distribution and Removal Model was prepared to comply with the DOE interim guidance (Dyer 1999) which directs the use of specified Subparts/Sections of the proposed NRC high-level waste rule, 10 CFR Part 63. Relevant requirements for performance assessment from Section 114 of that document are: "Any performance assessment used to demonstrate compliance with Sec. 113(b) shall; (a) include data related to the geology, hydrology, and geochemistry ... used to define parameters and conceptual models used in the assessment. (b) Account for uncertainties and variabilities in parameter values and provide the technical basis for parameter ranges, probability distributions, or bounding values used in the performance assessment. ... (g) Provide the technical basis for models used in the performance assessment such as comparisons made with outputs of detailed process-level models"

5. ASSUMPTIONS

5.1 WATER DIVERSION MODEL

5.1.1 Drip Site

The majority of the pendant drops are assumed to form at rough locations along the trace line of fractures. Drip site diameter is assumed to be equal to the aperture width of fractures. This assumption is based on engineering principles and such phenomenon is observed in caves, so verification is not required. These assumptions are used in Section 6.1.2.

5.1.2 Drip Falling Distance

Pendant drop falling distance (H) is defined as the air gap between the arched crowns of the drift roof and the upper side of the drip shield. $H = 2.304$ m is calculated based on the assumed EBS Geometry reported in *Tabulated In-Drift Geometric and Thermal Properties Used in Drift-Scale Models for TSPA-SR* (CRWMS M&O 2000u, Table 2). Dimensional variations in the configuration will have little effect on this model, this assumption does not require verification. This assumption is used in Section 6.1.3.

5.1.3 Drip Water Redistribution on Drip Shield

The pathways for seepage into the drifts are fractures, and as a result, seepage will vary spatially and temporally over the approximately 10,000 waste packages. Drops falling on the drip shield wet the solid surface by splashing, splashing is neglected in this analysis, and spreading. Kinetic energy of the falling drops causes the splashing and may lead to the ejection of secondary drops. Spreading from the primary and secondary drops produces a thin film of water on the drip shield. Therefore, the response of groups of waste packages is represented as averages for performance assessment. It is assumed that splashing and spreading cause the drip water to be uniformly redistributed on the drip shield and that any breach is located so that it will collect all fluid that drips onto the drip shield or waste package at the same axial location as the breach. This assumption conservatively ignores the fact that fluid dripping onto the lower portion of the drip shield or waste package will not flow through a breach high on the drip shield or waste package. Because of these conservatism's this assumption does not require verification. This assumption is used in Section 6.1.5.

5.1.4 Drip Shield Dimensions

The drip shield dimensional data are adopted from CRWMS M&O 2000u, Table 2, as best available information, and does not require verification since dimensional variations in the drip shield configuration will not affect this model.

Outside radius (R) = 1,300 mm

Chord = 2,505 mm

Internal structural reinforcement beam height (x) = 90 mm

Space between two water diversion rings = 245 mm

Space between outer water diversion ring and inner axial seismic stabilizer = 85 mm

Space between two axial seismic stabilizer = 250 mm

The following dimension is calculated:

Acute angle from the drip shield arched crown to the plate 1/plate 2 connection = 74.46 degrees (Figure 6.6).

The drip shield dimensional data are used in Sections 6.1.3 through 6.1.7.

5.1.5 Viscosity

Viscosity is a measure of the shear force between adjacent molecule layers when one layer is accelerating from the other. In water far away from a solid surface, the force that causes the shear is the intermolecular attraction. However, water in thin films is also attracted to the solid surface by hydrogen bonding and van der Waals forces. These additional forces cause greater viscosity of water in the thin film than in locations unaffected by the solid surface. Also, the Newtonian fluid characteristics of water are deviated in the thin film since the viscosity becomes nonlinear.

In the water diversion model analyses, it is assumed that water in the thin film still possesses the Newtonian fluid characteristics and the viscosity is not affected by the solid surface. This assumption is conservative as the smaller viscosity of water results in less shear force for the flow. This assumption is used in Sections 6.1.6 and 6.1.7 and does not require verification.

5.1.6 Maximum Percolation Rate at the Repository Horizon

The percolation rate at the repository horizon is assumed to be 25 mm/yr. This is based upon a review of the fluxes in DTN:MO9901YMP98017.001 (unqualified). Using this value and ignoring the capillary barrier effect adequately establishes an upper bound for the seepage rate into the drifts. This assumption is conservative and does not require verification. It is used Sections 6.1.2 and 6.1.5.

5.1.7 Parallel Plates

Capillary properties of the crevices are approximate by those of parallel plates. Irregular shape cracks possess large surface area and tend to exert greater surface force on water being held than parallel plates. This assumption is conservative and does not require verification. It is used in Sections 6.1.4 and 6.1.6.

5.1.8 Water Ponding on Drip Shield

Depressions or basins on the top of drip shields resulted from rock falls are assumed to occur in isolated places and do not represent a general phenomenon; therefore water ponding on drip shields is not considered in this analysis because isolated ponding will not impact model results. This assumption is used in Sections 6.1.5 and 6.1.6 and does not require verification.

5.1.9 Impact Time

Impact time (τ) between the moment that a drop touches the solid surface and before the drop splashes is 2.4 milli-seconds (Mutchler, 1967, p.92). This is assumed to reflect the same

time as a drop impacts the drip shield. This assumption is used in Section 6.1.3 and does not require verification.

5.1.10 Fracture Property of Rock in the Repository Horizon

Mongano et al. (1999, pp.83-84) indicates that most of the fractures are very close and more than 40% of the aperture size are between 0 and 1 mm in the Tptpll unit. This supports using an assumed aperture width (D_o) of 1 mm for the pendant drop calculation in Section 6.1.2. This input is appropriately used, and does not require verification.

5.1.11 Water Evaporation

For this model, it is assumed that any water contacting the drip shield or waste package does not evaporate. Water that contacts the drip shield would evaporate and this evaporation at the drip shield surface would reduce the potential flow rate, therefore, it is conservative to exclude evaporation for the purposes of calculation the flow rate through the drip shield at isothermal temperatures. This assumption is used through out as a bounding condition.

5.2 WATER DRAINAGE MODEL

The assumptions used in the Water Drainage Model are to support the backfill case. This model was developed for the backfill case and was not redone for the no-backfill case. The justification for that was that there was more seepage flow into the drift because of the backfill than without backfill, therefore the conclusion is that since the drainage was adequately addressed for backfill it did not need to be re-evaluated for the no-backfill case. These assumptions were developed for the backfill case and may vary from the values used for the no-backfill case used in other places in this report. These differences even though they may appear significant have little or no affect on the water drainage model results.

5.2.1 Drip Shield

For ease of modeling, the top of the drip shield is assumed to be stair-stepped in shape rather than curved. The technical basis of this assumption is that a flatter shape will result in a conservative estimate of the saturation level above the drip shield. This assumption is used in Section 6.2 and does not required verification.

5.2.2 Hydrologic Properties of Drip Shield

The drip shield, which is made of titanium, is assumed to be impermeable with properties the same as the waste package. The technical basis for this assumption is that the drip shield by design would limit water. This assumption is used in Section 6.2 and does not require verification because any leakage through interlocked sections of the drip shield will not be high enough to impact model results.

5.2.3 Backfill Material and Invert Placement

The Overton sand backfill is assumed to completely fill the outer annulus between the drip shield and the drift wall rather than leaving a relatively small air gap on top of the backfill. This

assumption is conservative because it allows any influx into the crown of the drift to be in direct contact with the backfill and, thus, would facilitate flow to the invert of the drift. These assumptions are used in Section 6.2 and do not require verification.

5.2.4 Tortuosity Factors

A factor of 0.0 is assigned to simulated waste packages and drip shields since they are assumed to be air and water tight and to be impermeable. A factor of 0.7 is assigned to the invert material since it is a granular material similar to the lithostratigraphic units at the repository horizon. This coefficient was estimated for a range of liquid saturation in soils by Fetter (1993, p.44) and was found to be 0.66 (~ 0.7) as an average value. This assumption is used in Section 6.2 and does not require verification.

5.2.5 Thermal-Hydrological-Chemical and Thermal-Hydrological-Mechanical Effects

The thermal-hydrological-chemical (THC) and thermal-hydrological-mechanical (THM) effects are accounted for by reducing the intrinsic permeability of the fractured welded tuff directly below the invert to the intrinsic permeability of the matrix for welded tuff. The technical basis for this assumption is that the THC effects would more likely affect the unsaturated flow properties of the existing fractures, and that THM effects would not likely induce additional fracturing. This assumption is used in Section 6.2.5.3 and does not require verification.

5.2.6 Location of Model

Inputs that vary with location are found by using an assumed location of the 14c4 block element, with coordinates Easting 170500.3 and Northing 233807.3 (Attachment V). This assumption is used in Attachment V and in all YMESH and NUFT input files. The technical basis for this assumption is that this point is near the center of the proposed repository (Section 1.3). Since edge effects are not considered in this model, the center of the repository is used as the representative location. This model is not sensitive to this input. This assumption is used in Section 6.2.

5.2.7 Steady State Two Dimensional Model at Isothermal Temperature

The NUFT analysis is performed using a steady-state two dimensional model at isothermal temperatures. The technical basis for this assumption is that temperatures in the EBS will be less and water flux rates will be higher than those predicted with repository heating. The heat given off by waste packages can be neglected for purposes of assessing water drainage. It is conservative to assume isothermal temperature conditions for the purposes of water drainage. This assumption is used in Section 6.2.

5.2.8 Thermal Conductivity of Stationary Components

The thermal conductivity of the welded tuff as measured in laboratory experiments (Brodsky et al. 1997, pp.27-34) is assumed to apply to the stationary components. The technical basis for this assumption is that measured values are in general agreement with values in the literature (Bear 1988, p.650). This assumption is used in Section 6.2.4 and does not require

verification.

5.2.9 Model for the Center of the Repository with Reflective Side Boundaries

The analysis assumes that the side boundaries are reflective with no flow of water, air or heat occurring across the side boundaries. The technical basis for this assumption is that flow in the vadose zone is dominantly in the vertical direction for the vertical system of fractures. This is a common practice for vadose zone flow simulations and does not require verification. This assumption is used in Section 6.2.3.

5.2.10 Modeling of the Rock Mass as a Dual Permeability Medium

The nonhomogeneous rock mass is modeled as two interacting materials representing the matrix, and a system of fractures. The interaction between the fractures and the matrix is explicitly calculated from the local temperature and pressure differences under transient flow conditions. The technical basis for this assumption is that rock mass is characterized by a matrix and system of fractures. Under low flux and high absolute moisture potential, flux occurs through matrix. Under high flux and low absolute moisture potential, flux occurs through the fractures. This is a recognized modeling technique and does not require verification. This assumption is used in Section 6.2.

5.2.11 Potential Field Theory for Closed Form Analytical Solution

The solution is based upon potential field theory (Phillips 1991, p.67) that assumes a small perturbation in one part of the field will effect the entire field, not just a local area. The basis for this assumption is that the flow is irrotational with vorticity equal to zero (Phillips 1991, p.67). This assumption is used in Attachment XII and does not require verification.

5.2.12 Water Flux Rate under Steady-State Conditions for a Deep Water Table

The water flux rate under a specified percolation rate for a deep water table occurs under steady-state conditions in which the flux rate equals the unsaturated hydraulic conductivity (Jury et al. 1991, p.127). The basis for this assumption is that over the long term, an equilibrium in hydraulic potential will develop along the boundary of the inclusion with the surrounding host rock. This is a recognized modeling technique and does not require verification. This assumption is used in Attachment XII.

5.2.13 Infiltration

It is assumed that infiltration data source estimated for the UZ site scale model (CRWMS M&O 2000o) adequately describes the glacial climate. These data are from DTN: MO9911MWDEBSWD.000 and support the computer files *.inf in Attachment VIII. The data contained in the DTN were developed from unqualified sources that do not meet current data quality requirements. These data are the only available source for glacial infiltration parameters and were developed using sound analytical methods. Glacial infiltration is used in this model as a bounding condition. These infiltration data are appropriately used in Section 6 and do not require confirmation.

5.2.14 Model Geometry for the NBS and EBS

The UZ site scale model (CRWMS M&O 2000o) is a three-dimensional model used to estimate the thickness of stratigraphic units. A lithostratigraphic column was developed for the 14c4 column with coordinates Easting 170500.3 and Northing 233807.3 in this analysis as discussed in Section 6.2.2. The assumed thickness at this column is based upon unqualified data from DTN: LB99EBS1233129.001. This is the best information available and any changes during data qualification are not expected to be of a magnitude as to impact model results. The data is used in Section 6.2 and does not required verification.

Also, additional layout details are required to supplement the global parameters listed in Section 4.2. These are summarized in Table 5-1 below and are assumed to construct the final in-drift configuration for the water drainage model used in Section 6.2. Any variation in dimensional data as the current design is advanced is not expected to be of magnitude as to impact model results. Verification is not necessary.

Table 5-1. Additional EBS Dimensional Details (CRWMS M&O 2000u, Table 2)

Model Input	Value
Waste package outer diameter	1.67 m
Location of waste package center above bottom of drift	1.945 m
Location of waste package center below the springline	0.805 m
Inside radius of drip shield	1.231 m
Top of invert as measured from bottom of drift	0.606 m

5.2.15 Temperature and Pressure Boundary conditions

The assumed data for the temperature and pressure boundary conditions at the ground surface and water table are based on DTN: LB99EBS1233129.003 from the UZ site scale model (CRWMS M&O 2000o). The derivation of temperature and pressure boundary conditions based on the source data is described in Section 6.2.3.

Although the data are from an unqualified source, changes resulting from data qualification are not expected to be of such a magnitude as to impact model results. The data used are the best available and were developed using sound analytical judgement. This assumption is used in Section 6.2 and does not require verification.

5.3 THERMOHYDROLOGIC MODEL

5.3.1 Effective Tortuosity Factor

See Section 5.2.4.

5.3.2 Homogeneous Fracture Continuum

In the conceptual basis for NUFT V3.0s, the fracture network is assumed to behave as a

continuous porous medium with homogeneous properties within each hydrostratigraphic unit. This assumption is used in development of the UZ model (CRWMS M&O 2000o), from which the unit properties used in this report were obtained, and therefore applies to this model. This assumption is consistent with the purpose of the TH calculations reported here, which is to calculate the average response to heating under a range of effective seepage inflow conditions.

This assumption is used in the calculations described in Section 6.3.1. No further justification of this assumption is required.

5.3.3 Component Properties

The properties of components air and water, distributed in the gas and liquid phases, are incorporated in a NUFT V3.0s input file (vtough.pkg, attached CD in Attachment XVI). The values used are approximations that are suitable either because different values would have a negligible effect on the NUFT V3.0s results, or because they are not used in TH simulations such as these which do not use the contaminant transport features of NUFT V3.0s. For those parameters that are used in TH simulations, the assumed values consist of the following:

- Equivalent molecular weight of air: 29.0 g/mol
- Molecular weight of water: 18.0 g/mol
- Binary diffusivity for water vapor into air in the gas phase:

$$D = \tau \phi S_g D_{va} \left(\frac{T + 273}{273} \right) \theta \quad (\text{Eq. 5.1})$$

where

$$D_{va} = 2.13 \times 10^{-5} \text{ m}^2/\text{sec}$$

$$\theta = 1.8 \text{ (dimensionless)}$$

$$T = \text{temperature in } ^\circ\text{C}$$

$$\tau = \text{effective tortuosity coefficient}$$

$$S_g = \text{gas saturation (calculated by NUFT)}$$

$$\phi = \text{porosity}$$

- Diffusivity of air in liquid water: 10^{-9} m²/sec
- Specific heat of air (C_p): 1009 J/kg-K

Vapor-pressure lowering is active for these calculations. This feature of the NUFT V3.0s code simulates the interaction between capillary water potential and the vapor pressure governing water mass transfer between the liquid and gas phases. The vapor pressure is lowered by an amount determined from the capillary pressure using the Kelvin Equation (Atkins 1990, Equation 13b, p. 148). The capillary radius for this calculation is computed from the capillary pressure (Atkins 1990, Equation 12, p. 148). This increases the boiling temperature for partially saturated capillary media, which is the point at which vapor pressure equals the total

pressure. The vapor pressure lowering due to the potential formation of salts within the EBS is neglected. This is conservative since the effects of vapor pressure lowering due to salt formation would lower moisture potential and reduce the potential for water to be retained within EBS components.

This assumption is used in the calculations described in Section 6.3.1. No further justification of this assumption is required.

5.3.4 Zero Dispersion Coefficients

For TH problems, the use of zero dispersion for the gas phase is equivalent to an assumption that dispersive behavior is small relative to diffusion or that velocities are small. For gas-phase mass flux rates, gas densities, and fracture porosities and apertures used in this report, the resulting Peclet Number is much less than unity, therefore dispersion can be neglected in TH simulations in accordance with established principles (Bear, 1988; p.608).

This assumption is used in the calculations described in Section 6.3.1. No further justification of this assumption is required.

5.3.5 Preclosure Ventilation Effects

For this report, the effects of preclosure ventilation on the TH state of the host rock is taken into account by running NUFT V3.0s for 50 yr (Sections 4.2.14 and 4.2.3) assuming that ventilation has effectively removed 70 percent of the heat generation from WPs (Sections 4.2.14 and 4.2.3). The drying effects of ventilation on the host rock and precipitation of solutes predominantly in the rock matrix are neglected in this model. The result is that the LDTH model overpredicts the water and relative humidity present in the drift environment for the first few tens or hundreds of years after closure. This tends to shorten the time until return of moisture to the environment, and is therefore conservative in conjunction with the assumed environmental conditions that promote corrosion (Assumption 5.3.6). This assumption is used in Section 6.3.4 and no further justification is required.

5.3.6 Thermal Loading and Aging of Waste Inventory

The heat-generation curves from CRWMS M&O 2000i are modified to account for the reduced lineal power density assumption for the no-backfill case (relative to the backfill case) and to account for the influence of ventilation. The assumption is based upon an initial bounded lineal thermal load of 1.45 kw/m averaged over all of the emplacement drifts in the repository for the current no-backfill case (CRWMS M&O 2000x, Section 6.2.3.2) and an initial thermal load of 1.5404 kw/m for the backfill case (CRWMS M&O 2000y, Attachment I-1). Therefore, the heat-generation decay curve for the LDTH submodels used in the backfill case in the thermohydrologic model is multiplied by a factor of $1.45/1.5404 (= 0.94131)$ to obtain the revised curves for the LDTH-model calculations for the no-backfill case (LDTH-SDT-0.3Qheat-1e6y_vent-20). This includes all of the LDTH-model calculations described in this report.

In addition, the line source strength (LDTH-SDT-0.3Qheat-1e6y_vent-20) was modified to account for the heat-removal effect of ventilation during the preclosure period. These calculations are based on the 70 percent heat removal ventilation (Sections 4.2.10 and

4.2.14). Accordingly, the heat-generation rates are therefore multiplied by a factor of 0.3 during the 50-yr preclosure period (Sections 4.2.3 and 4.2.14). Note that the drying influence of drift ventilation is neglected in these calculations.

This assumption is used in Section 6.3. It does not require verification because any deviations from the assumed heat generation curves are not expected to be significant enough to affect model results.

5.3.7 Thermal and Hydrologic Properties for EBS Materials

The EBS invert ballast material is crushed tuff (Section 4.2.15). This material (devitrified, welded) is assumed to behave hydrologically as an unfractured medium. When fractured rock is crushed, the fracture properties are lost so the crushed material behaves hydrologically as an unfractured porous medium. But because the NUFT program was used to simulate the entire unsaturated zone, including the undisturbed host rock, the DKM feature is applied. Since the invert crushed material does not possess fracture properties, only porous medium properties are used. This is represented in the DKM by splitting the total property value between the fracture and matrix continua. Half the porosity is assigned to the matrix continuum, and half is assigned to the fracture continuum. Density, specific heat, thermal conductivity, permeability, and other hydrologic properties are assigned the same way. The AFC is not used for EBS material properties. Any deviations from the assumed splits are not considered to be significant enough to affect model results. Verification is not required. This assumption is used in Section 6.3.

5.3.8 Geometry of the Drift and Drip Shield and Waste Package

For the models in this report, it is assumed that the waste package, drip shield, and pedestal supporting the waste package are combined into a single body with outside dimensions representing those of the drip shield. The rectilinear NUFT V3.0s grid is designed with spacing so that this composite body as well as the drift, invert, and drip shield are represented. The cross-sectional areas of each component (drift, invert, waste package/drip shield) in the grid are approximately the same as specified in Sections 4.2 and 5.2.14. Verification of this assumption is not required as changes in dimensional data are not expected to be significant enough to impact model results. The assumption is used throughout Section 6.

5.3.9 Properties of the Waste Package

The waste package is modeled as a uniform solid body, with thermal conductivity and heat capacity scaled to represent the response of the composite body. The waste package is assumed to have a thermal conductivity of 14.42 W/m-K, specific heat of 488.86 J/kg-K, and density of 8189.2 kg/m³ based on a review of available data (CRWMS M&O 2000u, p.11).

These values are based on area-averaging using prescribed geometry and materials for the waste package and drip shield. Treatment of the drip shield, waste package, and waste package supports as a composite body, is consistent with the objectives of this model, which include investigation of the bulk environment but not the fine-scale variability of conditions in the spaces enclosed by the drip shield. In addition, the temperature in the bulk environment during the thermal period will be determined by the processes that convey heat away from the drifts, but not by heat transfer within the spaces enclosed by the drip shields. The space between

the drip shield and waste package remains warmer, and therefore drier, than the bulk environment during cooldown, so aqueous processes will take place primarily outside the drip shield for these conditions. Finally, the storage of sensible heat by the waste package and drip shield will not be significant to the bulk environment, because temperature changes will occur very slowly. Accordingly, the results are insensitive to the value of specific heat, used to represent the composite body. This assumption is used in Section 6.3. Verification is not required because model results are not sensitive to potential small changes in waste package properties.

5.3.10 Thermal Conductivity, the Lower and Upper Invert Layer

The thermal conductivity, specific heat and density of crushed tuff are developed in Attachment XIV. The invert of the no-backfill case consists of two layers with respect to thermal conductivity K_{th} . The lower half of the invert (called the lower invert layer) has a K_{th} value for pure crushed tuff (Section 4.1.6). The document *Invert Effective Thermal Conductivity Calculation* (CRWMS M&O 2000n, pp. 15-24) presents a calculation thermal conductivity for a composite upper invert comprised of steel beams and crushed tuff of various thicknesses. Because of the orientation of the steel beams, there is directional anisotropy for the effective K_{th} of the upper invert layer. Because NUFT does not handle directional anisotropy in K_{th} , it was judged that a lateral value of K_{th} (1.520 W/m-K) is the most appropriate single value of K_{th} for the upper invert layer in the no-backfill calculations in the LDTH models. This assumption is used in Section 6.3. Verification is not required because model results are not sensitive to potential small variations in the conductivity.

5.3.11 Mass Density of the Waste-Package/Drip Shield Monolith

The drip shield and waste package are represented as a monolithic body in the LDTH model. The mass density of this monolith is based on the respective densities and cross-sectional areas of the waste package and drip shield (Table 4-1 and Figure 4-2 of CRWMS M&O 2000i). As stated in Section 5.3.10, the storage of sensible heat in the drip shield and waste package is negligible; consequently, it will not significantly affect heat flow in the EBS. This assumption is used in Section 6.3 and does not require verification.

5.3.12 Thermal Conductivity and Density for the Active Fracture Model

The thermal conductivity and density values of the fracture and matrix are apportioned by the following

fracture conductivity = total conductivity x (fracture porosity)
matrix conductivity = total conductivity x (1 - fracture porosity)
fracture density = total density x (fracture porosity)
matrix density = total density x (1 - fracture porosity)

There is no commonly accepted approach to apportioning fracture and matrix conductivity and density. However, it is important to note that the total value of conductivity and the total value of density. Therefore, the total conductive heat flow is the same as a single continuum with the same total value of thermal conductivity. Similarly, during the transient (heatup) period, we honor the correct mass density of the rock mass. This assumption has no impact on this

model. This method is used in all submodels (used throughout). This assumption does not require confirmation.

5.3.13 Hydrostratigraphic Unit Thickness, Contact Elevations, and Extents

Thirty one locations were selected to assure that the variability of host-rock units and local percolation flux were adequately represented in the Multiscale TH Model (CRWMS M&O 2000i). Integration with UZ model unit thicknesses, contact elevations, and lateral extents was accomplished using YMESH V1.53 (Table 3-2) to read mesh and grid files from the UZ model (CRWMS M&O 2000o).

It is assumed that data from an unqualified source (DTN: LB99EBS1233129.001) describe contact elevations for each of the 31 model locations. This information was manually incorporated into the NUFT V3.0s input files, and is best data available. Any change in this assumption during the data qualification process is not expected to be of a magnitude to impact model results. Therefore, confirmation of this assumption is not required. This assumption is used in Section 6.3.

5.3.14 Temperature and Total Pressure Boundary Conditions

For the 2-D models used in these calculations, the model domain extends from the ground surface to the water table. Temperature and total pressure conditions (Table 5-2) are assumed at each boundary based upon unqualified DTN: LB99EBS1233129.001. The values were obtained from the UZ model files "bcs_99.dat" and "tspa99_primary_mesh", which are read directly into the CHIM_SURF_TP V1.1 software routine. Inverse-squared distance weighting is used to interpolate the UZ model information at the required 14c1 and 14c4 locations.

These files represent the best available data because any change to the data during qualification is not expected to be of a magnitude as to impact model results. Confirmation is not necessary. The assumption is used in Section 6.3.

Table 5-2. Temperature and Total Pressure Boundary Conditions

Model Location	Ground Surface		Water Table	
	Temperature (°C)	Pressure (Pa)	Temperature (°C)	Pressure (Pa)
14c1	16.994	85,587	32.360	92,000
14c4	15.910	84,511	32.544	92,000

NOTE: Source: Software routine CHIM_SURF_TP V1.1 and CRWMS M&O (2000i)

The air mass-fraction at the ground surface is calculated from the temperature and total pressure such that the relative humidity is 100 percent. This prevents water from diffusing upward through the ground surface when NUFT V3.0s calculates initial, steady conditions prior to the application of heat. The air mass-fraction is calculated from

$$W = 0.622 \frac{P_v}{P_b - P_v} \quad (\text{Eq. 5.2})$$

where

W = specific humidity, weight of water per unit weight of dry air

P_v = partial pressure of water vapor

P_b = barometric pressure

0.622 = constant, mole wt H₂O to mole wt dry air

At the water table, the air mass-fraction is assigned a small value (comparable to the solubility of air-constituent gases in water). The air mass-fraction boundary condition values used in this report are shown in Table 5-3. The temperature and total pressure boundary conditions are appropriately applied.

Table 5-3. Air Mass-Fraction Boundary Conditions

Model Location	Ground Surface Air Mass-Fraction	Water Table Air Mass-Fraction
I4c1	0.98584	1.0×10^{-6}
I4c4	0.98660	1.0×10^{-6}

NOTE: Source: Equation 1, using barometric pressure
Vapor pressures are obtained for the ground surface temperatures indicated in Table 5-3, using a vapor pressure table (Weast and Astle 1981, p. D-168).

5.3.15 (Not Used)

5.3.16 Effective Thermal Conductivity of Cavities Inside Drifts

Thermal radiative heat transfer inside cavities within the emplacement drifts can be represented with the use of an effective thermal conductivity, which is given as a function of time. The only available source of effective thermal conductivity versus time relationships is *Effective Thermal Conductivity for Drift-Scale Models Used in TSPA-SR* (SN9907T0872799.002). It is assumed that these data from an unqualified input source adequately describe the effective thermal conductivity of cavities inside drifts with time. The assumption is justified because the data used were developed using sound analytical methods. Any changes to these data during qualification are not expected to be of such magnitude as to impact model results. Therefore, verification is not required. This assumption is used in Section 6.3.

5.3.17 Heat Generation Rate

The only available source of heat-generation decay curves for the LDTH models is information in the files 2-Dwperimeter.xls and heatTSPA-SR-99184.txt from unqualified DTN: SN9907T0872799.001. These curves apply directly to the backfill case. These curves are modified for the no-backfill case and to account for ventilation according to the assumptions in Section 5.3.6. The heat generation rate is appropriately used in Section 6.3. Any changes

during data qualification are not expected to be of such a magnitude as to impact model results. This assumption does not require verification.

5.3.18 Net Infiltration Boundary Conditions

Software routine CONVERTCOORDS V1.1 is used to convert unqualified infiltration grid files obtained from the U.S. Geological Survey (USGS) (LB99EBS1233129.004) from UTM to NSPC (metric), while reformatting the file from matrix to column format. Infiltration values at selected model locations are then interpolated using software routine COLUMNINFILTRATION V1.1. In the climate model represented by these files, the monsoonal values are assigned to begin at 600 yr after waste emplacement, and the glacial values are assigned to begin at 2000 yr (LB99EBS1233129.004).

The resulting assumed infiltration values for the model locations are shown in Table 5-4.

Table 5-4. Infiltration Values for Model Locations

Location	Infiltration Distribution	Present-Day (mm/yr)	Monsoonal (mm/yr)	Glacial (mm/yr)
I4c4	"lower"	0.00	10.13	1.99
	mean	10.13	28.88	42.00
	"upper"	24.29	47.61	82.01
I4c1	"lower"	0.18	4.79	3.31
	mean	4.79	12.09	18.88
	"upper"	10.98	19.40	34.45

NOTE: Source: Spreadsheet "infiltration.xls" (Attached CD in Attachment XVI)

These values are included in the NUFT V3.0s input file (*.in). The infiltration flux values for the 31 locations in the multiscale TH Model, produced in the manner described previously, are compiled in the spreadsheet "infiltration.xls" (Attached CD in Attachment XVI). For comparison purposes, the average flux values for all 31 locations are shown in Table 5-5. The infiltration boundary conditions are appropriately applied.

Table 5-5. Average Flux Values for Model Locations

Location	Infiltration Distribution	Present-Day (mm/yr)	Monsoonal (mm/yr)	Glacial (mm/yr)
Average (31 locations)	"lower"	0.56	5.98	2.99
	mean	5.98	16.07	24.86
	"upper"	14.56	26.17	46.73

NOTE: Source: Spreadsheet "infiltration.xls" (Attached CD in Attachment XVI)

This assumption is justified because it is based upon the best available data. Model conclusions are based upon a range of values and are not sensitive to variation, that may occur as the data is qualified. Verification is not required. The assumption is used in Section 6.3.

5.4 DRIP SHIELD CONDENSATION MODEL

Assumptions used in the drip shield condensation model are the same as those discussed in Section 5.3, thermohydrologic model.

6. ANALYSIS/MODEL

The purposes of the Water Distribution and Removal Model (CRWMS M&O 2000b) are to provide analyses that support the development of EBS PMR and FEP screening, which are important to waste isolation, repository design, and TSPA for the no-backfill case. Principle features of the model include the simulations and analyses of unsaturated flow and heat transfer in the geologic materials, temperature and relative humidity environment, and water diversion and water drainage within the emplacement drifts. This section presents a set of submodels which describes the movement of water within the emplacement drifts under ambient and thermally driven conditions. This section combines the results from:

- Water Diversion Model
- Water Drainage Model
- Thermohydrologic Model
- Drip Shield Condensation Model

This Section also presents the screening arguments for certain FEPs that are related to water distribution and removal in the EBS, and addresses the applicable acceptance criteria from the IRSRs.

The water diversion model analyzes the flow of water, resulted from seepage dripping, through breaches in the drip shield, and the thin film flow on vertical walls underneath the drip shield due to adsorptive condensation. It also investigates the possibility of capillary flow through the gaps between overlapping drip shield segments. The breaches include mainly fine cracks caused by stress corrosion and patches by general corrosion. The model uses the term "corroded crevices" to represent both the fine cracks and the patches. Results of the water diversion model can be used for evaluating the drip shield design.

The water drainage model simulates the unsaturated flow through fracture rocks using an implicit dual permeability model (DKM) to evaluate drift seepage, water movement in the drift, and permeability modification in the host rock, that could lead to complete saturation of the invert. This information is appropriate for evaluating the selection of invert materials, the invert configuration, and the needed drainage capacity to ensure free drainage throughout the evolution of the host rock. This model was based on the use of backfill, for the No-backfill case the justification is provided in Section 6.2.

In-drift thermal and hydrologic conditions are predicted in the thermohydrologic model. This model simulates the thermal-hydrologic conditions in the EBS, including: (1) drift crown temperature and relative humidity; (2) drip shield temperature and relative humidity; and (3) invert temperature, relative humidity, saturation, liquid flux, and evaporation rate. The spatial variability of liquid saturation, liquid flux, and evaporation rate throughout the invert is of interest for radionuclide transport modeling. The temperature and relative humidity at the invert, drip shield, and drift wall surfaces are of interest for predicting condensation under the drip shield and from the drift crown. The model analysis was performed for a range of hydrologic conditions that could be imposed on the drift environment.

The potential for condensation under the drip shield is evaluated in the drip shield

condensation model using the vapor pressure lowering in the invert as a model feature. The invert thermal-hydrologic conditions and drip shield temperatures from the thermohydrologic model are used to predict the onset of condensation.

The sources of uncertainty in the WD&R model include the variation in infiltration rates, spatial variability in drift seepage rates, waste types and waste placement locations, heat generation rates, thermal-hydrological-chemical (THC) and thermal-hydrological-mechanical (THM) effects on host rock fracture plugging, and uncertainties in corrosion properties for the drip shield. These uncertainty issues are addressed by the submodels presented in the following and are also summarized in Section 7.5.

6.1 WATER DIVERSION MODEL

The diversion of water within the emplacement drift is important to the long term postclosure performance of the EBS system. The distribution of seepage water in the emplacement drifts can be highly variable due in part to variations in the spatial distribution of percolation. The performance of the drip shield may divert the water flux around the waste packages to the invert. Diversion will occur along the drift wall, at the drip shield, and around the waste package surface, even after the drip shield and WP have been breached by corrosion. The water diversion model herein focuses on the drip shield performance based on the waste placement alternative without backfill. Water diversion on the waste package surfaces is discussed in CRWMS M&O (2000d).

Several scenarios that seepage water enters the underside of the drip shield, in the forms of liquid and vapor, through capillary flow and adsorptive condensation are investigated, including:

- capillary flow through drip shield connectors
- capillary flow through corroded crevices
- thin film flow due to adsorptive condensation on walls of the internal structural reinforcement beams

Conceptual models are developed in the following to describe these flow mechanisms and their related physical processes.

6.1.1 Model Processes

6.1.1.1 Capillary Flow through Drip Shield Connectors

Figure 6-1 shows the drip shield connection configuration that is designed to eliminate capillary flow through the gaps between overlapping segments (CRWMS M&O 2000g). Although water could be held in the capillaries between contacting surfaces of two drip shield segments, capillaries are broken by open spaces, e.g., between the two water diversion rings, between the outer water diversion ring and the inner axial seismic stabilizer, and between the two axial seismic stabilizers (Section 5.1.4). Also, structures and/or materials that could retain water on top of the drip shield and hence create driving force for the capillary flow do not exist. Therefore, capillary flow through drip shield connectors will be prevented by the current joint design.

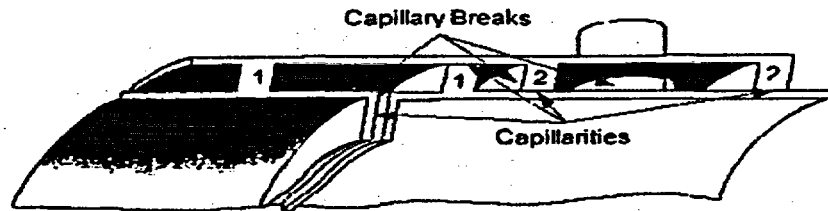


Figure 6-1. Drip Shield Connection Configuration
(1=Water Diversion Rings; 2=Axial Seismic Stabilizers)

6.1.1.2 Capillary Flow through Corroded Crevices

The NUFT simulations for the water drainage model in Section 6.2 indicate that the unsaturated flow in the repository host horizon is dominated by fracture flow as the matrix exhibits orders of magnitude lower hydraulic conductivity. As a result seepage water enters the emplacement drift primarily through fractures in the form of pendant drops. The formation and detachment of a drop is the result of dynamic equilibrium between surface tension and gravity. Figure 6-2 shows that a pendant drop is formed at the fracture intersection with the emplacement drift roof as the fracture flow continues to provide water to the drop. Due to the slow matrix flow and condensation of water vapor from the air, a thin film of water is developed on the drift roof that can also feed the pendant drop. At first, surface tension is in balance with the gravitational force. With slight incremental increases in the drop weight the hanging drop goes through a sequence of equilibrium shapes in response to the inflow. Finally, gravity overcomes the surface tension and the drop begins to fall (dripping).

Pendant drops tend to form at rough locations (drip sites) because the rough surfaces exert greater surface forces, and therefore provide more stable sites for water retention. Many drip sites could co-exist along the trace line of a fracture intersecting the drift roof. Drip site density is dependent on fracture spacing, trace length, and roughness on the drift roof. Drip sites could also exist outside the fracture trace line but the water supply is limited to the matrix flow and possibly condensation. Drip site density affects the frequency of drops at each drip site because the volumetric flow rates of seepage and dripping should be equal at steady state.

In early stages after ventilation stops, water dripping may not occur because any seepage water reaching the drift roof will evaporate owing to the high temperature and low humidity environment. As humidity increases the evaporation rate will decrease and dripping may start where there is sufficient seepage flux. If moisture loss to the host rock by vapor diffusion is insignificant, the air will eventually be saturated by water vapor. At this point, water dripping occurs at a rate that equals to the seepage rate.

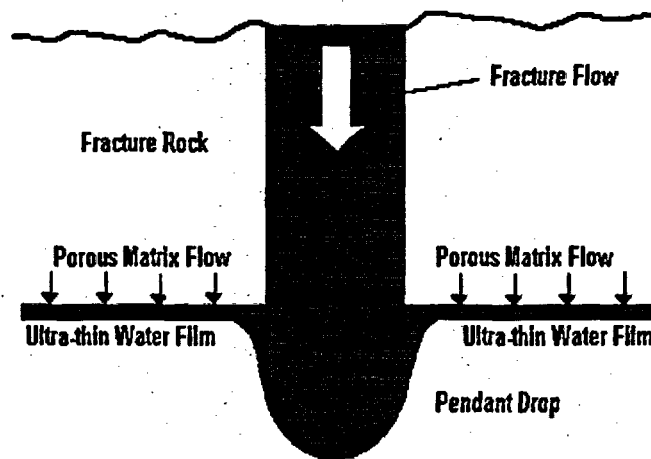


Figure 6-2. A Pendant Drop Formed at Fracture Intersection with Drift Roof

Water dripping on the drip shield wets the solid surface by splashing and spreading. Inertia of the falling drops causes the splashing that leads to the ejection of secondary drops. The spreading from the primary and secondary drops produces a thin film of water on the drip shield that very slightly thickens away from the crest (Figure 6-6 and Figure 6-8). It is assumed that splashing and spreading cause the dripping water to be uniformly distributed on the drip shield (Assumption 5.1.3).

Crevices of various sizes will be developed in the drip shields due to pitting and crevice corruptions, i.e., by general corrosion and by stress corrosion (CRWMS M&O, 2000e). Crevices in the drip shield can draw water from the thin film due to capillary suction and gravitational forces. Direction of the capillary force changes from downward to upward during the filling process. Figure 6-3 shows that the contact angle of water in the capillary increases from less than 90° to greater than 90° to accommodate the weight increase. The capillary force acts against gravity in holding the water in place when the contact angle is greater than 90° . Maximum contact angle is reached at 180° that corresponds to a maximum water holding capacity. Water contents in the crevices can vary from saturated, to partially-saturated, to not capable of holding water (see Table 6-1 for calculation results) as the aperture sizes increase.

Film flows over saturated crevices have little impact to the water held in the crevices due to the effect of capillary plug. However, film flows into the partially-saturated crevices can cause pendant drops to be formed and released on the underside of the drip shield in a discrete manner. In addition, drops falling directly on the crevices (saturated and unsaturated) result in kinetic energies to be converted to pressure pulses (impulsive force) that break the capillary and gravitational force equilibrium, causing some or all of the water to be squeezed out of the crevices. Film flow and falling drops will go through large cracks and patches and therefore are not analyzed.

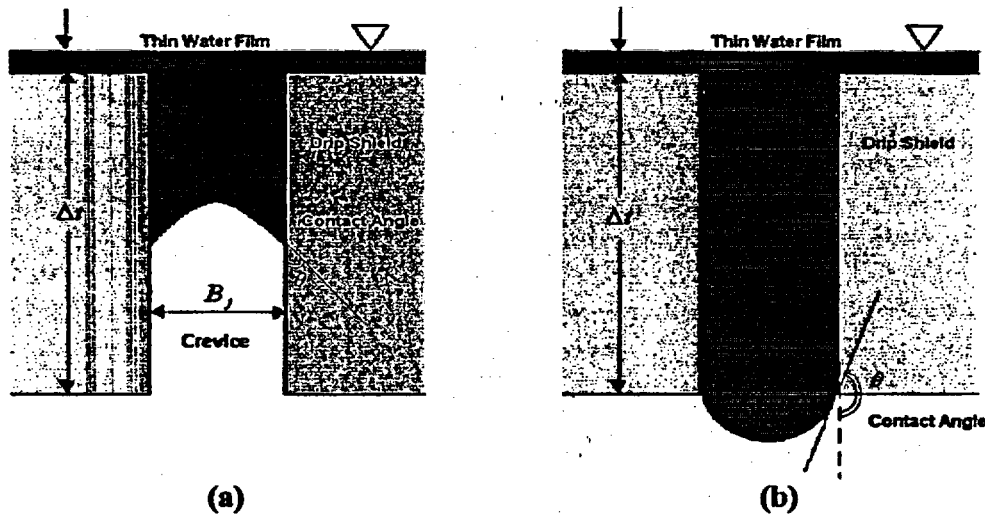


Figure 6-3. Contact Angle in a Crevice (a) Less Than 90° and (b) Greater Than 90°

6.1.1.3 Thin Film Flow by Adsorptive Condensation

Water vapor molecules will condense to solid surfaces by chemical and physical adsorption in addition to thermal condensation (discussions on the thermal condensation are provided in Section 6.4). In chemical adsorption the dipolar water molecules form covalent bonds with the positively charged metal surface, while in physical adsorption the water and metal molecules attract each other by the long-range van der Waals forces (Atkins, 1990, p.884). Physical adsorption is a weak interaction and the energy released is of the same order of magnitude as the enthalpy of thermal condensation. The enthalpy for chemical adsorption is much greater than the one for physical adsorption. A good discussion on adsorption of gases and vapors on solids can be found in Birdi, 1997 (pp.282-288). Further discussion in adsorptive condensation is provided in Section 6.7.

As a result, a film of water will be formed on the drip shield due to the adsorptive free energy associated with the interaction of the metal surface with the moisture in the air. The adsorptive potential for additional moisture deposition will decrease as the film thickness increases. At steady state, adsorption is in equilibrium with desorption and the film thickness becomes stable.

Water adsorbed on horizontal surfaces is immobile because hydraulic gradients for the flow do not exist. The thickness of films can vary from a mono-layer of water molecules to less than 100 Angstrom (\AA) depending on the relative humidity in the air (Philip, 1977, p.5074; Lee and Staehle, 1997, p.37). However, water adsorbed on vertical walls such as the surfaces of the internal structural reinforcement beams can flow under the influences of gravity (Figure 6-11). Films thicken along the downward flow paths to accommodate the increase of mass and drops can form at the bottoms of the vertical walls. The rate of film flow under such condition is controlled by the rate of adsorptive condensation.

6.1.2 Drop Size, Drip Site Density and Drip Rate

Tate's law (Middleman, 1995, p.94) gives a solution for predicting the maximum size of a pendant drop simply by equating the capillary force to the weight of the drop (Equation 6.1). It assumes that the capillary has a diameter (D_o) and the maximum drop volume (V_{max}) that could exist is when the contact angle $\theta = 180^\circ$ (Equation 6.2).

$$-\sigma_w \pi D_o \cos \theta = \rho_w g V \quad (\text{Eq. 6.1})$$

where:

σ_w = surface tension of water (N/m);
 ρ_w = density of water (kg/m³);
 θ = contact angle (degrees);
 D_o = aperture width (m); and
 V = volume (m³);

Negative sign indicates that surface tension and gravitational forces are in opposite directions, or

$$V_{max} = \frac{\sigma_w \pi D_o}{\rho_w g} \quad (\text{Eq. 6.2})$$

If the released drop were a sphere, then

$$D_d = \left(\frac{6V_{max}}{\pi} \right)^{1/3} \quad (\text{Eq. 6.3})$$

where:

D_d = diameter of pendant drop (m); and
 V_{max} = maximum drop volume (m³).

However, studies show that some residual liquid remains attached to the capillary when a pendant drop falls. Hence, the drop volume is lower than the one predicted by Equation (6.3). Harkins and Brown (Middleman, 1995, p.170) introduced a correction factor to the Tate's law based on experimental data. The correction factor is a function of the surface tension and drop diameter and is found to be between 0.5 and 0.8.

A larger drop will carry higher kinetic energy when it falls. To be conservative in estimating drop size, correction factor is not used in this analysis. Using $D_o = 0.001$ m (Section 4.1.1.1), the maximum drop volume V_{max} is determined to be 2.2×10^{-8} m³ (22 mm³) while the drop diameter D_d is 0.0035 m (3.5 mm).

The drip site density will depend on the roughness spacing, trace length, and spacing of the rock fractures on the drift roof. The drip rate is defined as the number of drops per drip site per time and is determined by

$$Q' = \frac{Q}{\eta V_{\max}} \quad (\text{Eq. 6.4})$$

where:

- η = drip site density (sites/m²),
- Q = maximum seepage rate to the drift (m/yr); and
- Q' = drip rate (drops/yr/drip site).

As mentioned previously, the distribution of seepage water in the emplacement drifts can be highly variable due in part to variations in the spatial distribution of infiltration. To account for the uncertainties, a wide range of seepage rate values is applied to Equation (6.4). The percolation rate at the repository horizon is assumed to be 25 mm/yr (Assumption 5.1.6, DTN: MO9901YMP98017.001). Figure 6-4 shows the drip rate as a function of drip site density at seepage rates of 10 mm/yr, 20 mm/yr, and 40 mm/yr.

Note that the range of estimated seepage flow rates are presented in the *Abstraction of Drift Seepage* (CRWMS M&O 2000a, Table 11). These estimated seepage rates indicate that the median seepage rates are much less than the values used in this analysis. The seepage rates used in this analysis are therefore conservative in estimating water diversion in and around the drip shield.

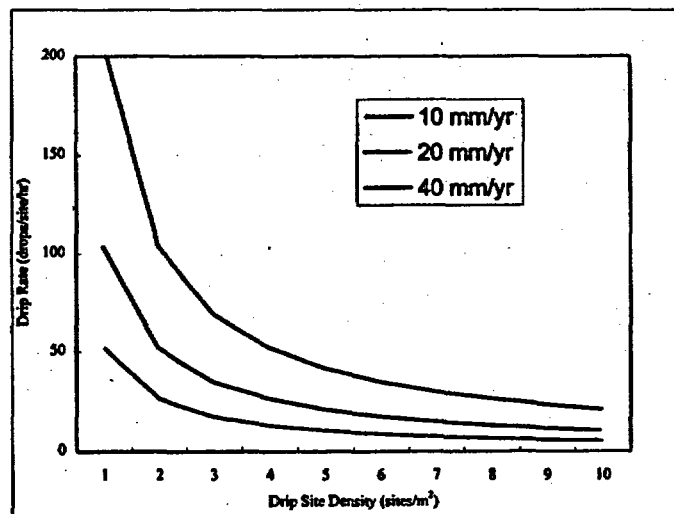


Figure 6-4. Drip Rate vs. Drip Site Density

6.1.3 Impulsive Force, Impact Time and Splashing

The maximum pressure (impulsive force) from a falling drop is achieved during the drop compression period (impact time) between the moment that the drop touches the drip shield and before the drop splashes. Neglecting air drag, the final velocity of a drop depends on the

falling distance from the drift roof to the drip shield surface

$$U = (2gH)^{1/2} \quad (\text{Eq. 6.5})$$

where:

U = final velocity (m/sec); and
H = falling distance (m).

The distance from the drift roof to the top of the drip shield is 2.304 m (Section 4.1.1.2), so the maximum final velocity of a falling drop is 6.72 m/sec.

The maximum pressure (P_{\max}) exerted on the drip shield surface equals to $\rho_w g H$, or

$$P_{\max} = 22,223 \text{ Pa} \quad (\text{Eq. 6.6})$$

High-speed photography has been used to study splashes from water drops on rigid surfaces with and without standing water (Mutchler, 1967; Rochester and Brunton, 1974). Generally, drop splashes are produced within milli-seconds (ms), depending on the depth of the standing water. The impact time (τ) of 2.4 ms (Assumption 5.1.7) is used in this analysis.

Splashing on the drip shield surface depends on drop size, final velocity, and surface roughness. CRWMS M&O (2000d, p.II-10) presents an equation for determining the threshold velocity for splashing

$$U_t = 3.3 \left(\frac{D_d}{2} \right)^{-0.59} \quad (\text{Eq. 6.7})$$

where:

U_t = threshold velocity for splashing (m/sec).

D_d is the drop diameter in mm. Using $D_d = 3.5$ mm as determined in Section 6.1.2, the threshold velocity for splashing is calculated to be 2.37 m/sec, smaller than the final velocity of 6.72 m/sec as calculated using Equation (6.5), therefore, splashing will generally occur.

6.1.4 Crevice Water Holding Capacity at Equilibrium

As shown in Figure 6-9a the capillary force is in static equilibrium with gravity in holding water in the crevices. It is assumed that the crevices can be represented by parallel plates (Assumption 5.1.5). The upward capillary force in the parallel plate is (Corey, 1977, p.18)

$$F_{up} = - \frac{2\sigma_w \cos\theta_l}{B_l} \quad (\text{Eq. 6.8})$$

while the downward gravitational force is

$$F_{\text{down}} = \rho_w g (\Delta t + h) \quad (\text{Eq. 6.9})$$

where:

- B_j = crevice width (m);
 Δt = drip shield thickness (m); and
 h = thin film thickness (m).

Equating Equations (6.8) and (6.9), we have

$$\cos \theta_j = - \frac{\rho_w g (\Delta t + h) B_j}{2\sigma_w} \quad (\text{Eq. 6.10})$$

Neglecting the thin film thickness ($h \cong 5.6 \times 10^{-6}$ m, see Figure 6.8), the contact angle can be calculated as a function of crevice width and thickness using Equation (6.10). Table 6-1 shows that $B_j = 0.916$ mm is the maximum crevice width that can hold the full column of water ($\Delta t = 15$ mm) when the maximum contact angle θ_j is reached at 180° . Less than 10 mm of water can be held when crevice width increases to greater than 2 mm. Capillarity breaks if air becomes interconnected from top to bottom when the water holding depth is thin, i.e., $B_j > 5$ mm.

Table 6-1. Contact Angle and Water Holding Capacity as a Function of Crevice Width

Crevice Width B_j (mm)	Water Holding Capacity H_j (mm)	Contact Angle θ_j (degree)
0.001	15	90.06
0.01	15	90.63
0.1	15	96.27
0.2	15	102.62
0.3	15	109.12
0.4	15	115.90
0.5	15	123.10
0.6	15	130.94
0.7	15	139.86
0.8	15	150.89
0.9	15	169.38
0.916	15	180
1.0	13.74	180
2.0	6.87	180
3.0	4.58	180
4.0	3.43	180
5.0	2.75	180

6.1.5 Crevice Flow By Interception of Film Flow

As shown in Table 6-1, crevices become unsaturated when aperture width increases to greater than 0.916 mm when capillary force can no longer support the weight of a 15 mm column of water. Under such circumstances, film flow on top of the drip shield will be intercepted by the unsaturated crevices and pendant drops will be developed on the underside of the drip shield (Figure 6-5). The dripping is discrete and the process is similar to the dripping from the fracture rock to the drip shield. For example, a drop is released when the maximum holding capacity is reached so the volume of water in the crevice is reduced by V_{max} . As the film flow continues to feed the crevice under the influence of capillary force and gravity, the volume of water in the crevice increases and so is the weight, which lead to the grow of a new pendant drop. If we ignore this transient process and focus on longer-term average, the dripping flow rate shall equal to the film flow being intercepted, depending on the orientation of the crevices.

Figure 6-6 illustrates the thin film profile on top of the drip shield due to splashing and spreading of water from the emplacement drift roof. The flux (q) from dripping is uniformly distributed on the drip shield not because of the primary drops, but the redistribution of secondary drops from splashing (Assumption 5.1.3). Section 6.1.3 concludes that splashing will generally occur on the drip shield because the final velocity of the drops is almost three times faster than the threshold velocity for splashing.



Figure 6-5. Film Flow as the Source of a Pendant Drop in an Unsaturated Crevice

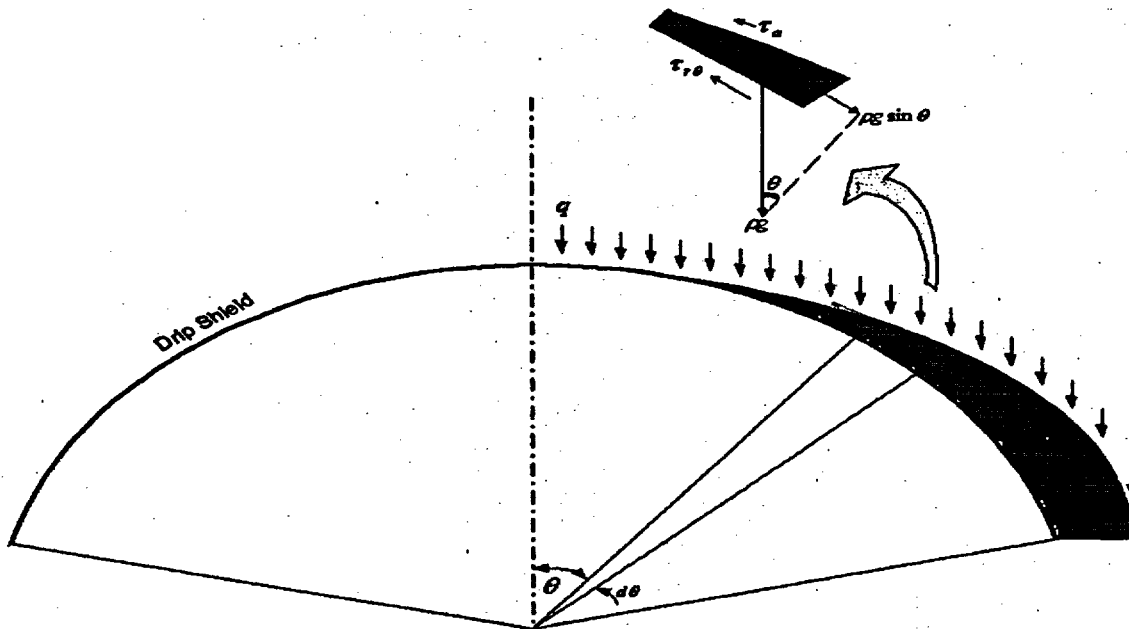


Figure 6-6. Control Volume for Force-Momentum Balance for Thin Film Flow down the Cylindrical Drip Shield Surface

The flow of thin film down the cylindrical drip shield surface can be derived through a force-momentum balance on the control volume

$$\rho_w g \sin \theta (R + r) d\theta (\delta - r) = \tau_{r\theta} (R + r) d\theta + \tau_a (R + \delta) d\theta \quad (\text{Eq. 6.11})$$

where:

- θ' = angle for the arc length from the drip shield crown (radians);
- R = drip shield outside radius (m);
- r = distance from drip shield surface to the bottom surface of control volume (m);
- $d\theta$ = finite angle for the control volume (radians);
- δ = film thickness at angle θ (m);
- $\tau_{r\theta}$ = shear at $(R + r)$ and angle θ (N/m^2); and
- τ_a = air drag on the film surface at $(R + \delta)$ and angle θ (N/m^2).

If τ_a is assumed to be negligible, Equation (6.11) reduces to

$$\tau_{r\theta} = \rho_w g \sin \theta (\delta - r) \quad (\text{Eq. 6.12})$$

$\tau_{r\theta}$ can also be written as

$$\tau_{r\theta} = \mu_w du_\theta/dr \quad (\text{Eq. 6.13})$$

where:

- u_θ = film flow velocity at r and angle θ (m/sec).

Combine Equations (6.12) and (6.13) and rearrange, we have

$$du_0 = \frac{\rho_w g \sin \theta}{\mu_w} (\delta - r) dr \quad (\text{Eq. 6.14})$$

Integrate Equation (6.14) once and apply boundary condition $u_0 = 0$ at $r = \delta$, we have

$$u_0 = \frac{\rho_w g \sin \theta}{\mu_w} \left(\delta r - \frac{1}{2} r^2 \right) \quad (\text{Eq. 6.15})$$

The volumetric flow rate of the thin film is obtained by integrating Equation (6.15)

$$Q(\theta) = \int_0^\delta u_0 dr = \frac{\rho_w g \sin \theta}{3\mu_w} \delta^3 \quad (\text{Eq. 6.16})$$

where:

$Q(\theta)$ = volumetric flow rate of film (m^3/sec).

$Q(\theta)$ can also be obtained by integrating the flux (q) from splashing

$$Q(\theta) = \int_0^\theta q R d\theta = q R \theta \quad (\text{Eq. 6.17})$$

Equate Equations (6.16) and (6.17) and rearrange, we have

$$\delta = \sqrt[3]{\frac{3\mu_w q R \theta}{\rho_w g \sin(\theta)}} \quad (\text{Eq. 6.18})$$

Assume an unsaturated crevice (aperture width greater than 0.916 mm) is perpendicular to the film flow, use $\mu_w = 4.7 \times 10^{-4}$ Pa.s and $\rho_w = 983.2$ kg/m^3 at 60 °C (Section 4.1.1.3), $R = 1.3$ m (Section 4.1.1.4), and $q = 25$ mm/yr (Assumption 5.1.4, this bounding drift seepage rate is used to determine the maximum film flow rate and thickness on the drip shield), the volumetric flow rate $Q(\theta)$ and film thickness (δ) are calculated in Attachment I and the results are summarized in Figures 6-7 and 6-8.

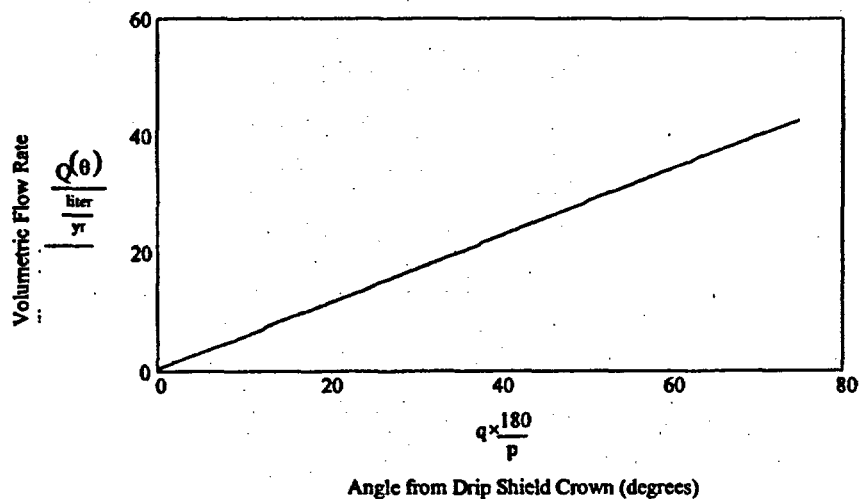


Figure 6-7. Volumetric Flow Rate vs. Crevice Location

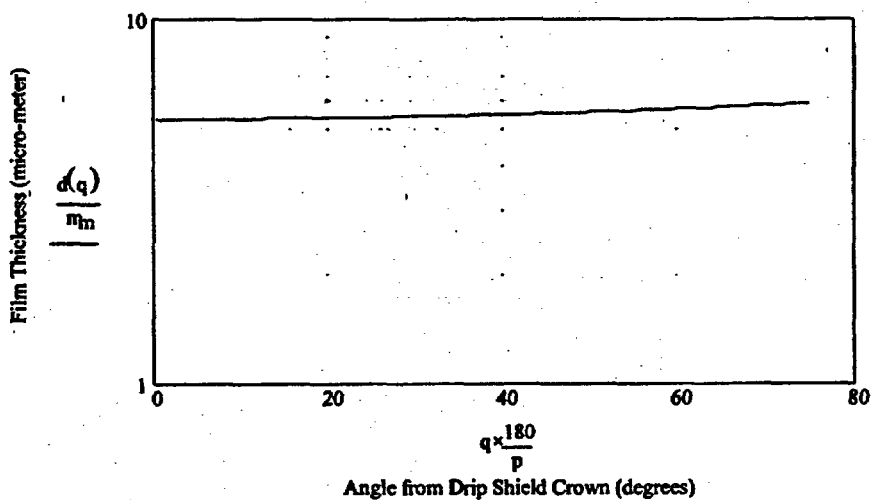


Figure 6-8. Film Thickness vs. Crevice Location

6.1.6 Crevice Flow by Impulsive Force

Figure 6-9 shows the balance of forces on the water body within the crevice prior to the impact of a falling drop and when the contact angle (θ) reaches 180° , respectively. These forces are presented for the water with a unit length as follows:

Gravitational force

$$\rho w' g \Delta t B_j$$

Capillary force in equilibrium with the gravity before a drop hits ($90^\circ \leq \theta_j \leq 180^\circ$)

$$-2 \cdot \sigma_w \cdot \cos(\theta_j)$$

Impulsive Force

$$P_{\max} \cdot B_j$$

Capillary force potential corresponding to contact angle increase from θ_j to 180°

$$-2 \cdot \sigma_w \cdot (1 + \cos(\theta_j))$$

Viscous force (Milne-Thomson, 1968, pp.650-651)

$$\frac{12 \cdot \mu_w \cdot U_o}{B_j}$$

where:

U_o = average velocity of the flow profile at time t (m/sec).

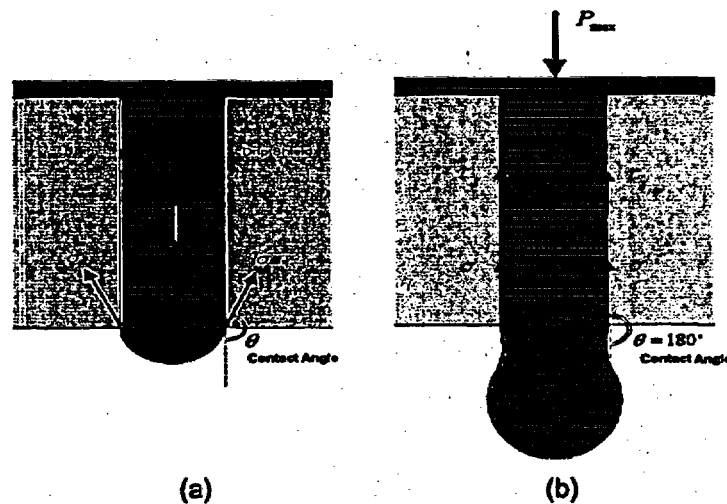


Figure 6-9. Force Balances (a) Prior to the Impact of a Falling Drop (b) When Contact Angle Reaches 180°

Write Newton's Second Law of Motion

$$\sum F = m \frac{du}{dt} \quad (\text{Eq. 6.19})$$

where:

F = force (N); and
 m = mass (kg).

Apply the forces shown in Figure 6-9b and use the mass $m = \rho_w \Delta t B_j$

$$P_{\max} B_j - 2\sigma_w(1 + \cos(\theta)) - \frac{12\mu_w U_o}{B_j} \Delta t = m \frac{du}{dt} \quad (\text{Eq. 6.20})$$

Rearrange Equation (6.20) and integrate

$$\int_0^{U_o} du = \int_0^t \left(\frac{P_{\max}}{\rho_w \Delta t} - \frac{2\sigma_w(1 + \cos(\theta))}{\rho_w \Delta t B_j} - \frac{12\mu_w U_o}{\rho_w B_j^2} \right) dt \quad (\text{Eq. 6.21})$$

$$U_o = \frac{\frac{P_{\max}}{\rho_w \Delta t} - \frac{2\sigma_w(1 + \cos(\theta))}{\rho_w \Delta t B_j}}{\frac{1}{t} + \frac{12\mu_w}{\rho_w B_j^2}} \quad (\text{Eq. 6.22})$$

Equation (6.22) is valid only if the impulsive force ($P_{\max} B_j$) is greater than or equal to the capillary force potential discussed previously in this Section. Negative velocities will be resulted if $P_{\max} B_j$ is less than the resistance force. In this case, the contact angle increases but not enough to reach 180° so water is not released from the crevice, or velocity is zero.

The average velocity of water over the drop impact time period is

$$U_o' = \frac{\int_0^{\tau} U_o dt}{\tau} \quad (\text{Eq. 6.23})$$

and the capillary flow through corroded crevices during the impact period is

$$Q_j'' = U_o' B_j w_c \tau \quad (\text{Eq. 6.24})$$

where:

- τ = impact time (sec);
- U_o' = average velocity over impact time (m/sec);
- w_c = crevice flow width (m); and
- Q_j'' = crevice flow induced by a drop (m^3/sec).

Set $w_c = D_d$ and use $\tau = 0.0024$ sec (2.4 ms), Q_j'' is calculated in Attachment II and the results are shown in Figure 6-10. Table II-2 in Attachment I shows that the crevice flows can vary from 0.0 mm^3/drop for $B_j \leq 0.01$ mm to the entire column of water in the capillary for $B_j \geq 4$ mm.

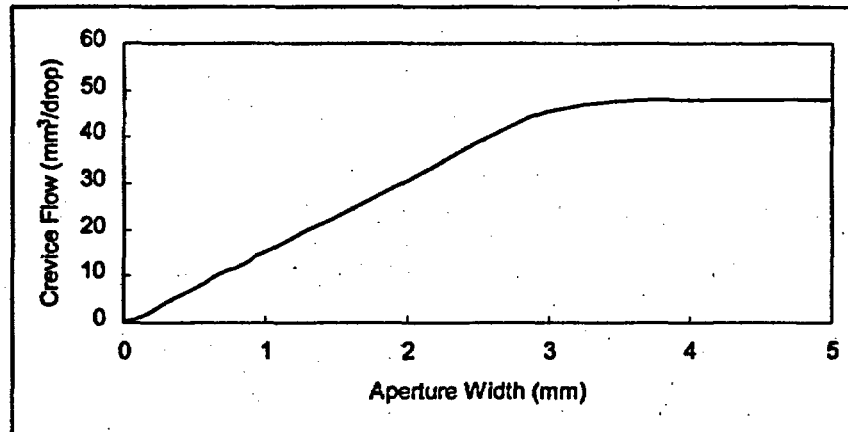


Figure 6-10. Crevice Flow Induced by a Drop

6.1.7 Thin Film Flow by Adsorptive Condensation

Philip (1977, p.5072) used the partial specific Gibbs free energy to correlate the adsorptive potential of a solid surface to the thickness of a water film

$$\Delta G_F = -\frac{\lambda RT}{\delta} \quad (\text{Eq. 6.25})$$

where:

- ΔG_F = Gibbs free energy (J/kg);
- λ = a constant (10^{-10} m);
- R = gas constant (461.8 J/kg-°K for water vapor);
- T = absolute temperature (°K); and
- δ = film thickness (m).

The film thickness can also be associated with the vapor pressures by applying ΔG_F to the Kelvin Equation (Philip, 1977, p.5070)

$$P_s = P_{sat} e^{\frac{\Delta G_F}{RT}} = P_{sat} e^{-\frac{\lambda}{\delta}} \quad (\text{Eq. 6.26})$$

where:

- P_s = water vapor pressure in the liquid and gas interface (Pa); and
- P_{sat} = saturated water vapor pressure at temperature T in the drift (Pa).

The water vapor pressure in the drift (P_∞) can be calculated using the relative humidity (RH) as

$$P_\infty = P_{sat} \cdot RH \quad (\text{Eq.6.27})$$

With the known pressure difference ($P_\infty - P_s$), the rate of adsorptive condensation can be determined. Figure 6-11 shows a thin film profile on the side wall of a parallel plate system, in which the thickness is controlled by the rates of adsorptive condensation and downward flow. Solving the momentum and mass transport equations will provide the solution for the mass flow rate in the film.

Write the Navier-Stokes equation in x-direction (Thibodeaux, 1979, p.99)

$$\frac{\partial U_x}{\partial \tau} + U_x \frac{\partial U_x}{\partial x} + U_y \frac{\partial U_x}{\partial y} + U_z \frac{\partial U_x}{\partial z} = \frac{1}{\rho_w} X - \frac{1}{\rho_w} \frac{\partial P}{\partial x} + \nu \left(\frac{\partial^2 U_x}{\partial x^2} + \frac{\partial^2 U_x}{\partial y^2} + \frac{\partial^2 U_x}{\partial z^2} \right) \quad (\text{Eq. 6.28})$$

where:

- x,y,z = dimensional values (m);
- U = velocity (m/sec);
- X = body force (N/m³);
- P = pressure (Pa);
- ν = kinematic viscosity (m²/sec); and
- τ = time (sec).

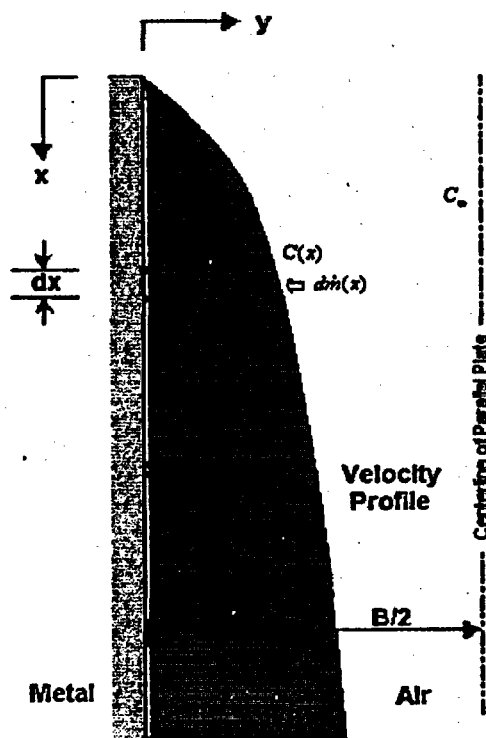


Figure 6-11. Thin Film Flow due to Adsorptive Condensation

Because the flow is one-dimensional and only occurs in the x-direction

$$U_y = U_z = 0$$

At steady state

$$\frac{\partial U_x}{\partial \tau} = 0$$

$$\frac{\partial U_x}{\partial x} = 0 \quad \frac{\partial^2 U_x}{\partial x^2} = 0$$

$$\frac{\partial U_z}{\partial z} = 0 \quad \frac{\partial^2 U_z}{\partial z^2} = 0$$

Therefore, Equation (6.28) is simplified as

$$\frac{\partial^2 U_x}{\partial y^2} = \frac{1}{\mu_w} \frac{\partial P}{\partial x} - \frac{1}{\mu_w} X \quad (\text{Eq. 6.29})$$

The body force X is equal to

$$X = \rho_w g \quad (\text{Eq. 6.30})$$

Use the boundary layer approximation (Incropera and DeWitt, 1981, p.486)

$$\frac{\partial P}{\partial x} \cong \rho_v g \quad (\text{Eq. 6.31})$$

Substitute Equations (6.30) and (6.31) to Equation (6.29)

$$\frac{\partial^2 U_x}{\partial y^2} = \frac{g}{\mu_w} (\rho_v - \rho_w) \quad (\text{Eq. 6.32})$$

Integrate Equation (6.32) twice using the following no-slip and no-flow boundary conditions, respectively

$$U_x|_{y=0} = 0$$

$$\frac{\partial U_x}{\partial y}|_{y=\delta(x)} = 0$$

the thin film velocity profile becomes

$$Ux(y) = \frac{g(\rho_w - \rho_v)\delta^2}{\mu_w} \left[\frac{y}{\delta} - \frac{1}{2} \left(\frac{y}{\delta} \right)^2 \right] \quad (\text{Eq. 6.33})$$

The mass flow rate at distance x in the thin film is

$$\dot{m}(x) = \int_0^{\delta(x)} \rho_w \cdot Ux(y) dy \quad (\text{Eq. 6.34})$$

where:

$\dot{m}(x)$ = mass flow rate at distance x (kg/sec).

or

$$\dot{m}(x) = \frac{\rho_w g (\rho_w - \rho_v) \delta^3}{3\mu_w} \quad (\text{Eq. 6.35})$$

The adsorptive condensation in Figure 6-11 can be expressed by the Fick's First Law of diffusion

$$\frac{d\dot{m}(x)}{dA} = -D_{AB} \frac{dC}{dy} \Big|_{y=\delta(x)} \quad (\text{Eq. 6.36})$$

where:

dA = finite area (m^2);

D_{AB} = binary diffusion coefficient (m^2/s) as given by (Ho, 1997, p.2665)

$$D_{AB} = D^0 \left(\frac{1 \times 10^5}{P} \right) \left(\frac{T}{273.15} \right)^{1.8} \quad (\text{Eq. 6.37})$$

and the negative sign states that diffusion occurs in the direction of decreasing concentration. The left side of Equation (6.36) can be obtained from Equation (6.35)

$$\frac{d\dot{m}(x)}{dx} = \frac{\rho_w g (\rho_w - \rho_v) \delta^2}{\mu_w} \frac{d\delta}{dx} \quad (\text{Eq. 6.38})$$

To obtain the right side of Equation (6.36), it is necessary to solve the Fick's Second Law of diffusion

$$\frac{\partial C}{\partial \tau} = D_{AB} \left(\frac{\partial^2 C}{\partial x^2} + \frac{\partial^2 C}{\partial y^2} + \frac{\partial^2 C}{\partial z^2} \right) \quad (\text{Eq. 6.39})$$

where:

C = water vapor concentration (kg/m^3);

Because of the steady state condition and one-dimensional diffusion in the y -direction

$$\frac{\partial C}{\partial \tau} = 0$$

$$\frac{\partial^2 C}{\partial x^2} = 0 \quad \frac{\partial^2 C}{\partial z^2} = 0$$

So Equation (6.39) is simplified to

$$\frac{\partial^2 C}{\partial y^2} = 0 \quad (\text{Eq. 6.40})$$

Integrate Equation (6.40) twice using the following boundary conditions

$$C(\delta) = C_s$$

$$C\left(\frac{B}{2}\right) = C_\infty$$

where:

C_s = water vapor concentration at film-air interface (kg/m^3); and

C_∞ = water vapor concentration in the drift (kg/m^3).

For capillary systems, the concentration of water vapor $C(y)$ between the film surface at δ and the centerline of a parallel plate at $B/2$ is

$$C(y) = \frac{C_s - C_\infty}{\delta - B/2} y - \frac{C_s - C_\infty}{\delta - B/2} \cdot \frac{B}{2} + C_\infty \quad (\text{Eq. 6.41})$$

For non-capillary surfaces, $B/2$ is the boundary layer thickness of air where water vapor diffusion occurs. Therefore, the right side of the Equation (6.36) is

$$-D_{AB} \frac{dC}{dy} \Big|_{y=\delta(x)} = \frac{D_{AB}(C_s - C_\infty)}{\delta - B/2} \quad (\text{Eq. 6.42})$$

Express $C_s - C_\infty$ in pressure terms using Equations (6.26) and (6.27)

$$-D_{AB} \frac{dC}{dy} \Big|_{y=\delta(x)} = \frac{D_{AB} P_{sat} (e^{\frac{\lambda}{\delta}} - RH)}{(\delta - B/2) RT} \quad (\text{Eq. 6.43})$$

Equate Equations (6.38) and (6.43) and rearrange, we have

$$\int_0^{\delta(x)} \frac{\delta^3 - \frac{B}{2} \delta^2}{e^{\frac{\lambda}{\delta}} - RH} d\delta = \frac{\mu_w D_{AB} P_{sat} x}{\rho_w g (\rho_w - \rho_v) RT} \quad (\text{Eq. 6.44})$$

Average velocity of the flow profile can be derived by integrating Equation (6.33) in respect to y and divided by δ

$$U_o = \frac{g(\rho_w - \rho_v) \delta^2}{3\mu_w} \quad (\text{Eq. 6.45})$$

where:

U_o = average velocity of the flow profile (m/sec).

Equation (6.44) presents an implicit solution for the adsorptive condensation film thickness as a function of flow distance, relative humidity and temperature. It is our particular interest to know the mass/volumetric flow rates at the bottom of the internal structural reinforcement beams on the underside of the drip shield ($x = 90$ mm, Section 4.1.1.4). Using the drip shield temperature and relative humidity histories for the 14c4 location with an approximate AML of 56 MTU/acre (CRWMS M&O 2000s, Section 2.3.1), the mean infiltration rate distribution, and 0% seepage as shown in Figure 6-34, the film thickness in Equation (6.44), average velocity in Equation (6.45), and mass flow rate in Equation (6.35) can be solved as a function of relative humidity. Mathcad 7 is used to solve the nonlinear, first-order integral equation as shown in Attachment III. Figures 6-12 through 6-15 illustrate the drip shield temperature, film thickness, mass flow rate, volumetric flow rate, and average film flow velocity as functions of relative humidity, respectively.

Results show that as temperature drops in time, relative humidity in the drift rises that creates a stronger driving force for the adsorptive condensation. As a result, the film thickness increases and that is associated with the increases in mass and volumetric flow rates and average film flow velocity.

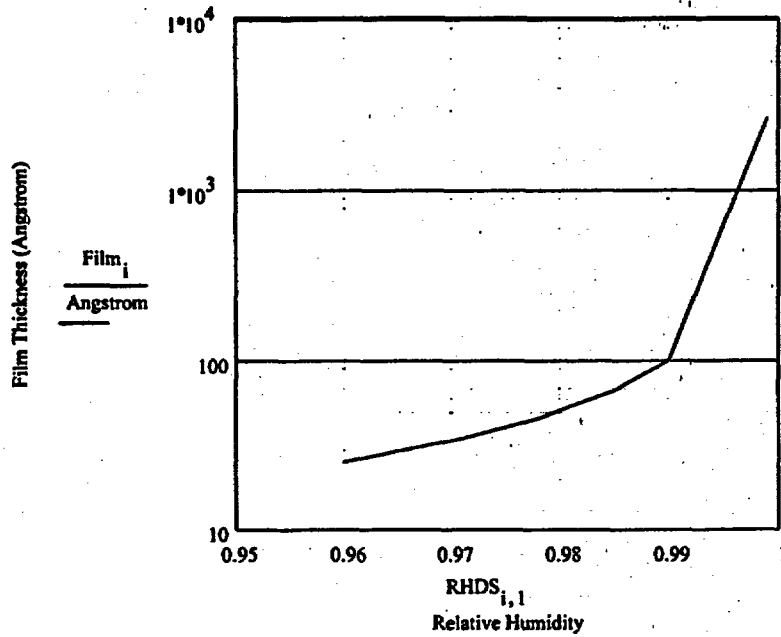


Figure 6-12. Film Thickness as a Function of Relative Humidity .

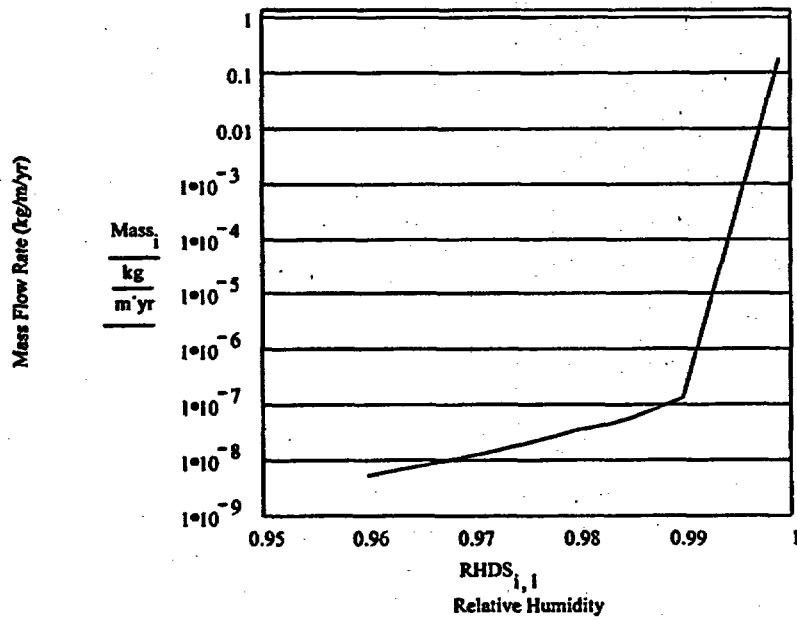


Figure 6-13. Mass Flow Rate as a Function of Relative Humidity

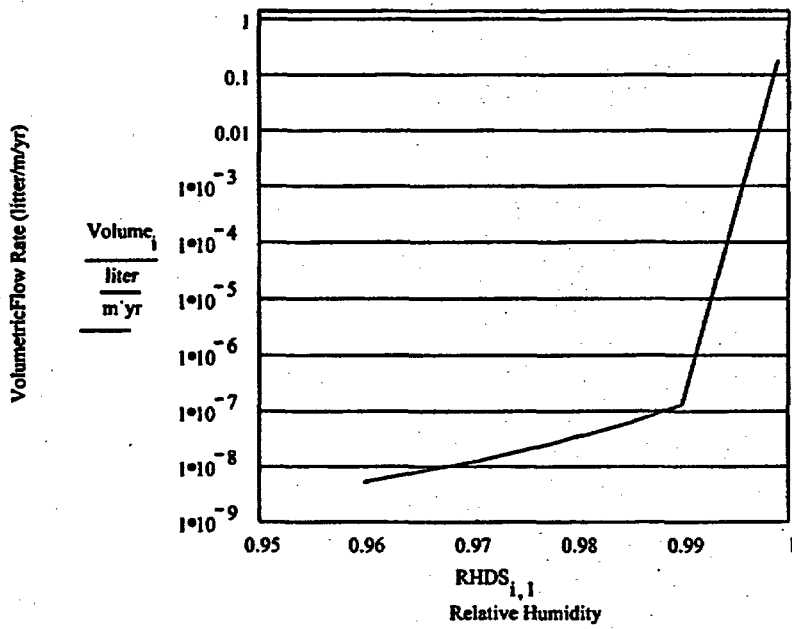


Figure 6-14. Volumetric Flow Rate as a Function of Relative Humidity

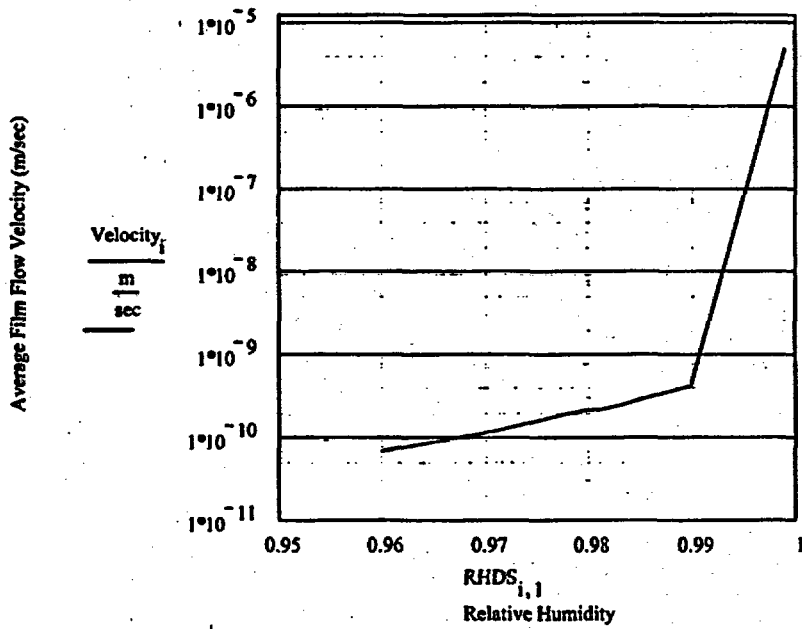


Figure 6-15. Average Velocity as a Function of Relative Humidity

6.1.8 Model Validation

The Water Diversion Model was prepared using standard analytic techniques and corroborative information. In accordance with AP-3.10Q, the model was validated by reviewing model calibration parameters for reasonableness and consistency. This included documentation and explanation of parameter inputs (Section 4.1.1), assumptions (Section 5.1), development (Sections 6.1.1 through 6.1.7), and calculations (Attachments I, II, and III). The information presented will allow independent repetition of the model results. The model is appropriate for its intended use.

6.2 WATER DRAINAGE MODEL

Water drainage from the emplacement drift is essential for the performance of the EBS. Hydrologic properties of the fractured rock beneath the invert determine how well the water will be drained naturally. The purpose of this water drainage model is to evaluate the capability of the drift to remove water resulted from a glacial infiltration under various conditions, including one case with engineered drainage features. The glacial infiltration rate is used as the upper bound for the water influx to the repository hydrologic system to provide the worst case scenario for water drainage analysis.

The analyses presented in the following sections are based on the simulations with backfill. However, the results for the ability of the EBS to drain water should not change based on the belief that without backfill, the drift opening will function as a capillary barrier for the flow in the host rock above so water is diverted around the drift, resulting in less water entering the invert. At steady state, the water flux at any cross section perpendicular to the flow equals the infiltration rate at the ground surface with or without backfill. Simulations presented in the following show that the backfill materials actually draw water into the drift laterally from the near-field host rock, resulting in greater volume of water at the invert that need to be drained.

6.2.1 Methodology

A two-dimensional, steady state NUFT model was used to simulate the simultaneous water flow and heat transfer in the fractured porous media. NUFT is based on the numerical technique called the integrated finite difference method or the finite volume method. This method allows for arbitrary polyhedral shapes. This method reduces to the standard finite difference method for a standard rectangular mesh. Because of the high degree of non-linearity in the van Genuchten constitutive relation for relative permeability for the fluid phase, NUFT uses various weighting approaches. The saturated permeability of a fluid phase between two adjacent cells is harmonically weighted, while the relative permeability is upstream weighted. This approach is used throughout the model domain.

The key options used for the NUFT simulations include the dual permeability model (DKM) and the active fracture concept (AFC). These modeling methods are NUFT options selected in the NUFT input files (see Attachment XI, files: *.in).

The DKM conceptualizes the fractured rock as having two interacting materials, one representing the matrix and one representing the fractures. The interaction between the fractures and the matrix is explicitly calculated from the local temperature and pressure differences, thus allowing transient behavior to be predicted. The DKM underestimates the fracture-matrix interaction for steep temperature and pressure gradients (Birkholzer and Tsang 1998, p.2). There are no steep temperature or pressure gradients simulated in this model. Therefore, the DKM is appropriate for the model developed in this document.

The active fracture concept accounts for the contact area between the fracture and the matrix, as well as the frequency of fractures. The AFC is that fracture flow only occurs through some of the fractures. This is more conservative than assuming the influx flows evenly through all

fractures. The flux through a fracture is greater when it has higher saturation and, therefore, focusing flow through a portion of the fractures (i.e., to active fractures) maximizes flux and results in fast pathways for flux through the mountain.

During repository excavation, the in-situ state of stress is relieved, and the potential exists for movement to occur due to elastic or elastoplastic deformation (Case and Kelsall, 1987, p.1). The stress redistribution and TBM excavation combine to form a modified permeability zone that depends upon the in-situ state of stress, rock deformational and strength properties. The drainage of the fractures might also be affected by rock fines resulting during TBM excavation. Further, during repository heating and cooling in the post-closure period, the potential exists for additional stress redistribution that would affect the retention and flow characteristics of the surrounding media. These combined effects result in alteration of the properties due to thermal and mechanical effects.

The effect of stress relief and dilatation on fractures would tend to result in an increase in the saturated hydraulic conductivity with an attendant reduction in retention characteristics. These combined effects may result in a lowering of unsaturated hydraulic conductivity. Rock fines resulting from TBM excavation will reduce the saturated hydraulic conductivity while increasing the retention characteristics of the fractures.

This model analysis takes into consideration the Thermal-Hydrological-Chemical (T-H-C) and the Thermal-Hydrological-Mechanical (T-H-M) effects and addresses the issues of fracture plugging. The heat transfer process was simulated under the natural temperature gradients and the heat output from the waste packages was not considered. Eliminating the temperature effects from the waste packages that lead to the increase of the water content in the vapor phase due to evaporation allows the model to simulate the flow with maximum water content in the liquid phase.

6.2.2 Model Domain and Grids

The repository block model (Attachment IV) is represented by a rectilinear array of 31 "chimney" locations, or columns of rock. Each location has a unique identifier, e.g. 14c4, which signifies the 4th row and the 4th column in the array. The locations of these columns are described in Attachment V. The 14c4 location is near the center of the repository layout, where the infiltration flux and rock properties are typical of much of the repository area. A lithostratigraphic column was developed for the 14c4 column with coordinates Easting 170500.3 and Northing 233807.3 (Attachment V) by the preprocessing software YMESH V1.53, which develops the lithostratigraphic cross section (Table 6-2) from the computer file LBL99-YMESH (Attachment XI) based upon the source data from the UZ (unsaturated zone) site scale model (Section 4.1.2.1). The repository is located at a depth of 343.131 m in the TSw35 unit that corresponds to the Tptpl unit.

The EBS model geometry is developed from the License Application Design Selection (LADS) EDA II design (CRWMS M&O 2000r, p.2, Section 2.2.2.2 and Section 2.3).

Because of symmetry, a two-dimensional model of NUFT is constructed to include only half of the waste package and the drift spacing (40.5 m) according to the EDA II design (Section

4.2.12) and the two vertical edges are treated as no-flow boundaries (Section 5.2.9). The model extends from the ground surface to the water table about 340 m below the repository invert level (CRWMS M&O 2000v). A simulation grid for the entire section is presented in Figure 6-16, with the spacing varying from 0.02 to 45.0 m. Figure 6-17 is a section of the emplacement drift with the drip shield and waste package in place. A corresponding model grid (derived from the main grid) that represents the drift with various EBS components is also shown in Figure 6-17.

Table 6-2. Hydrostatigraphy for I4c4

Model Unit	Thickness (m)
tcw11	33
tcw12	89
tcw13	5
ptn21	6
ptn22	3
ptn23	2
ptn24	7
ptn25	14
ptn26	16
tsw31	2
tsw32	42
tsw33	89
tsw34	30
tsw35	112
tsw36	27
tsw37	14
tsw38	23
tsw39	4
ch1VI	10
ch2VI	0
ch3VI	0
ch4VI	0
ch5VI	0
ch1Ze	0
ch2Ze	14
ch3Ze	14
ch4Ze	14
ch5Ze	14
ch6	20
pp4	8
pp3	34
pp2	15
pp1	61
bf3	17
bf2	0
Total	739

Source: Attachment XI file: I4c4.col.units

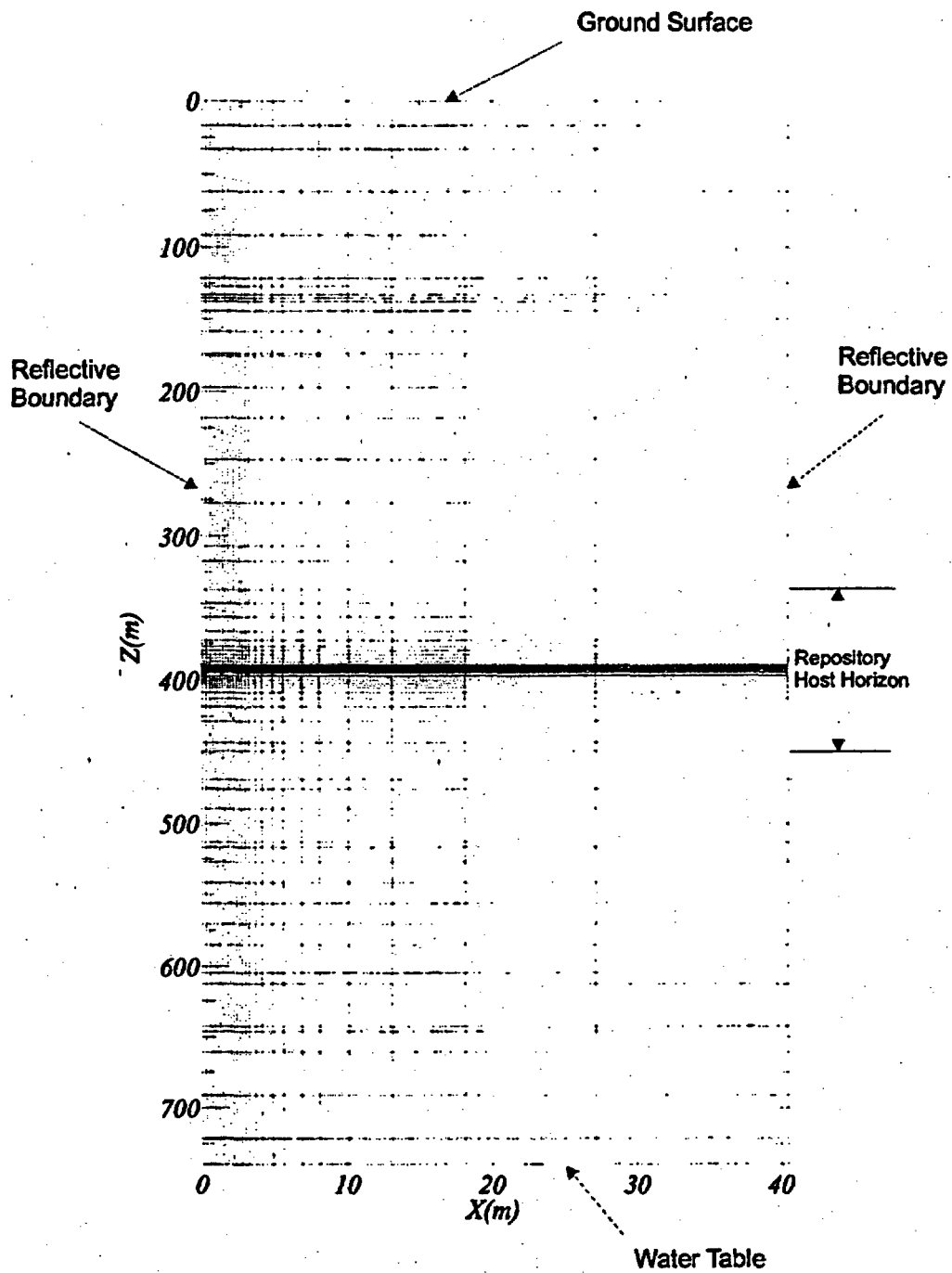


Figure 6-16. Model Domain and Boundary Conditions

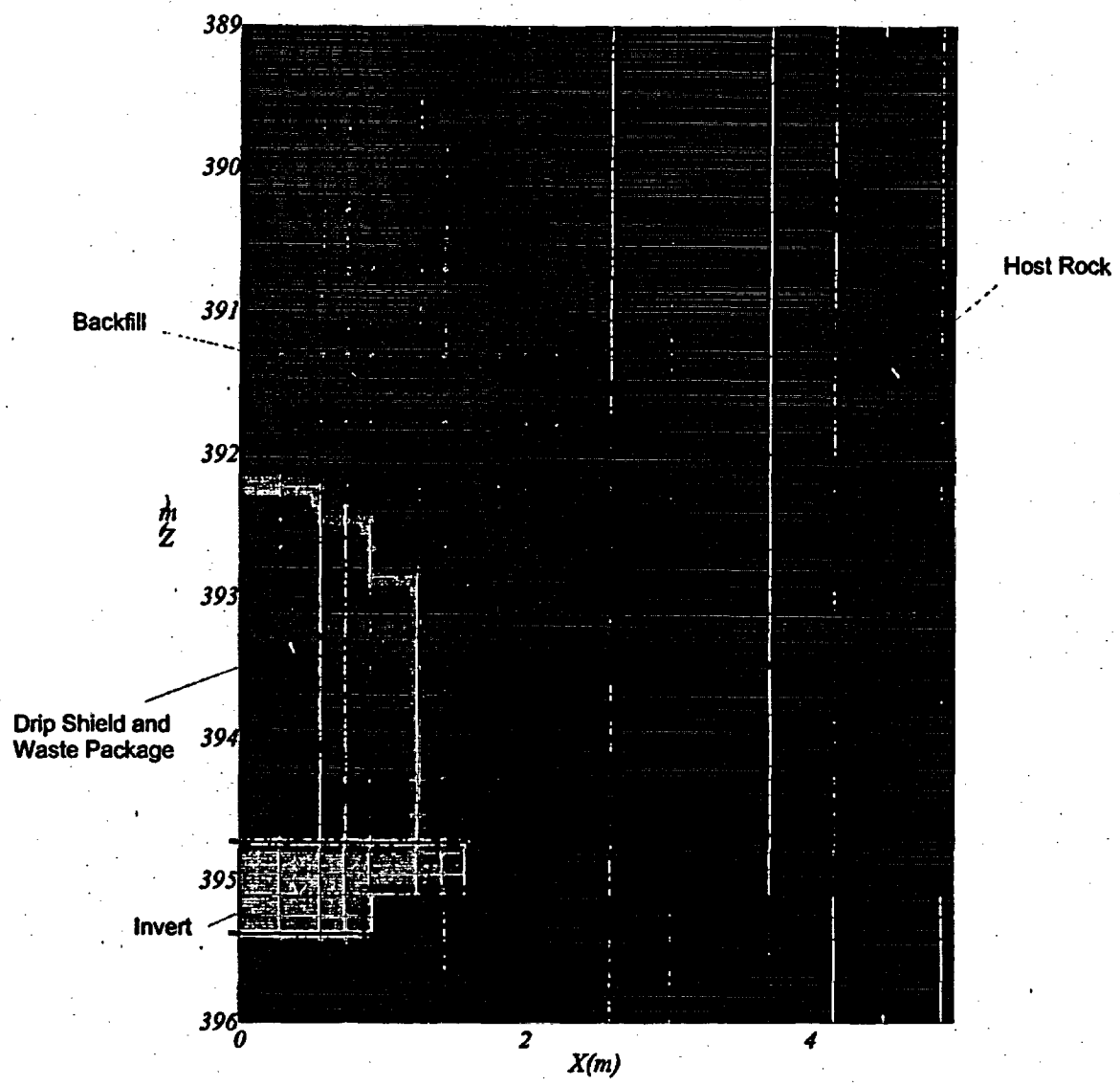


Figure 6-17. Engineered Barrier Segment Block Model

6.2.3 Boundary Conditions

The temperature and pressure boundary conditions for the 14c4 chimney were obtained from the output of Chim_Surf_TP V1.0 as detailed in Attachment VI. The source data for inputs to the Chim_Surf_TP V1.0 is from Section 4.1.2.1 (DTN: LB99EBS1233129.003). Table 6-3 presents the ground surface and water table conditions used in the model.

Table 6-3. Ground Surface and Water Table Conditions

Temperature at ground surface	15.91 °C
Pressure at ground surface	0.845e5 Pa
Temperature at water table	32.54 °C
Pressure at water table	0.92e5 Pa

Source: Attachment XI file: outpt and outpt_wt

The normalized mean glacial infiltration rate at 42 mm/yr (Table IX-1) was applied on the ground surface as a flux boundary condition.

6.2.4 Hydrologic and Thermal Properties

Sections 4.1.2.2 and 4.1.2.3 present hydrologic and thermal properties for the model units listed in Table 6-2. These data were developed from an inverse modeling technique. The thermal conductivity of the NBS is based upon the multiple linear regression analysis that in turn is based upon the measurement of thermal conductivity through a direct application of Fourier's Law. The thermal properties are assumed to apply to the stationary components for tuff, and water (Assumption 5.2.8). The wet thermal conductivity of the more porous non-welded PTn tuff are higher than the less porous welded TSw2 tuff.

6.2.5 Simulations and Case Studies

The NUFT model runs include the use of grids, hydrologic and thermal properties of the geologic materials, and boundary conditions discussed previously. The glacial infiltration rate used is 42 mm/yr as calculated for the chimney location 14c4 in Attachment IX, and provides a bound to the water in-flux.

A base case scenario (Case 1 in Table 6-4) was created to evaluate the water drainage without fracture plugging and the use of sand drains. Fracture plugging was simulated in Case 2 by reducing the intrinsic permeability of the fractured welded tuff directly below the invert to the intrinsic permeability of the matrix for welded tuff (Assumption 5.2.5). No drain is used in Case 2. To demonstrate how drains would enhance the drainage performance of the EBS system, Case 3 was developed with drains, that extended approximately 6 meters below the invert and were filled with crushed tuff, under the plugged conditions.

Table 6-4. Summary of Case Studies for the Water Drainage Model

Case Number	Plugging		Design	
	None	Plugged	No Sand Drains	Sand Drains
1	X		X	
2		X	X	
3		x		X

6.2.5.1 Base Case (Case 1)

The results of the NUFT analysis for the base case (Case 1) at isothermal temperature are presented in Figures 6-18 to 6-21 for the absolute value of the matrix capillary pressure (Pa), fracture and matrix saturation levels, and fracture mass flux rates ($\text{kg}/(\text{s}\cdot\text{m}^2)$), respectively.

Below the drip shield, the absolute value of the capillary pressure is increased from approximately 36,000 Pa (370 cm) to approximately 50,000 Pa (510 cm). As predicted by the contact and exclusion analysis for cylindrical cavities (Philip et al. 1989, p.21), a "dry shadow" forms below the drip shield in which the absolute value of the capillary pressure is increased and the saturation levels are reduced.

Figure 6-20 shows that the matrix saturation levels are high (exceeding approximately 0.90), while fracture saturation levels (Figure 6-19) are low (near the residual level) in the host rock. Saturation levels in the invert underneath the drip shield are generally less than 0.3, indicating no water ponding. Figure 6-21 illustrates that the fracture mass flux rates are increased adjacent and somewhat below the drip shield because of water diversion that creates a localized wet zone (i.e., saturation level is less than 0.6). Drainage capacity of the drift floor is sufficient for the removal of seepage water to the invert.

The fracture and matrix mass flux rates at three horizons above the repository, and at three locations within each horizon, are presented in Tables 6-5 and 6-6. It is found that the fracture mass flux rates are generally two orders of magnitude greater than those of the matrix, therefore, the unsaturated flow is dominated by fracture flow as the matrix exhibits lower hydraulic conductivity for the glacial climate percolation rate.

6.2.5.2 Fracture Plugging (Case 2)

The thermal-hydrologic-chemical (THC) and thermal-hydrologic-mechanical (THM) effects are accounted for by reducing the intrinsic permeability of the fractured welded tuff directly below the invert to the intrinsic permeability of the matrix for welded tuff. In Case 2, the fracture permeability was set equal to the matrix permeability in a 3-meter zone extending below the drift. Figures 6-22, 6-23, 6-24 and 6-25 show the absolute value of the matrix capillary pressure, fracture and matrix saturation levels, and fracture mass flux rates, respectively. These figures can be compared directly to the results from the base case.

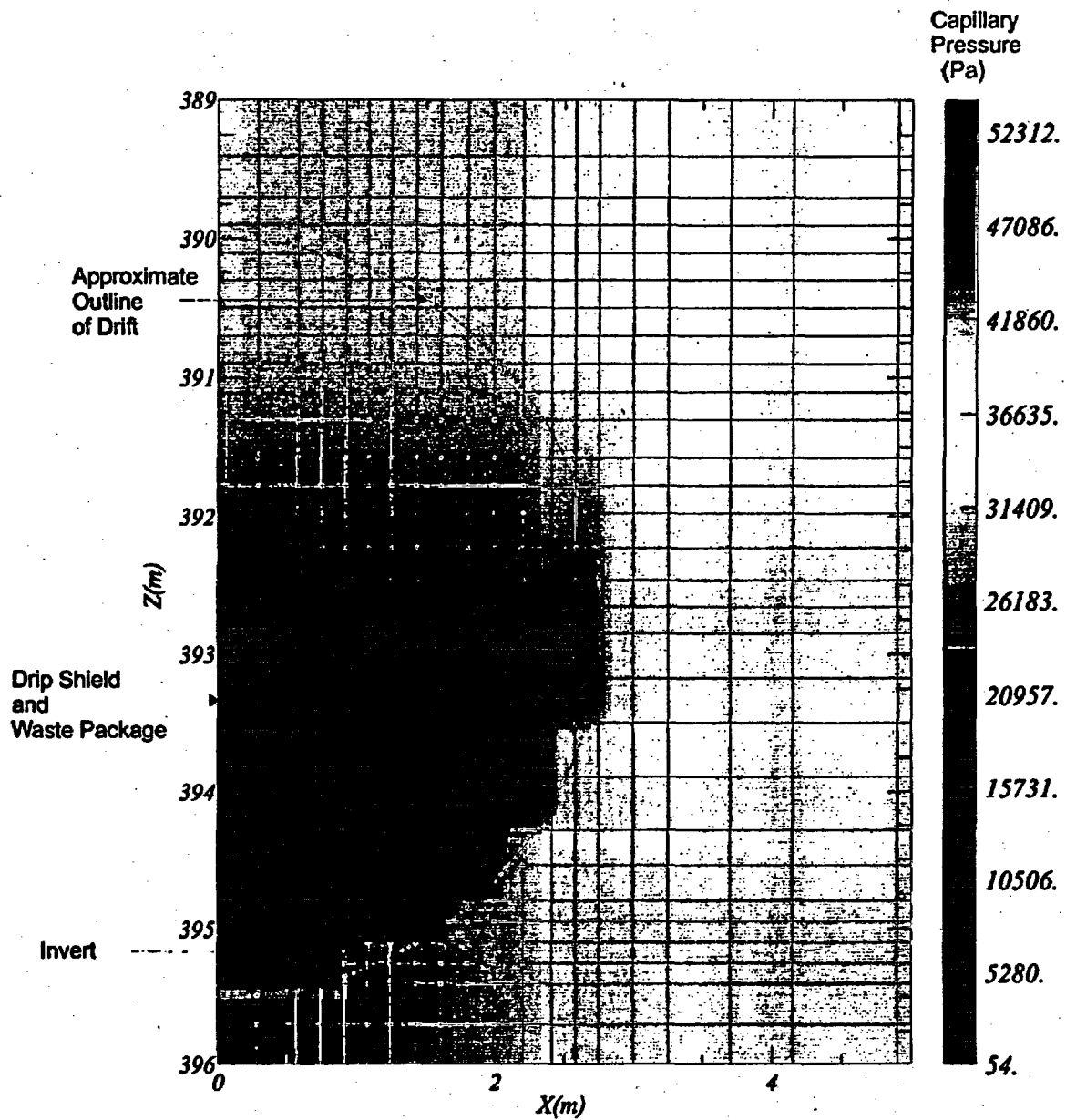


Figure 6-18. Absolute Matrix Capillary Pressure Near the Repository Horizon at Steady State (Case 1)

Figure 6-19. Fracture Saturation Levels Near the Repository Horizon at Steady State (Case1)

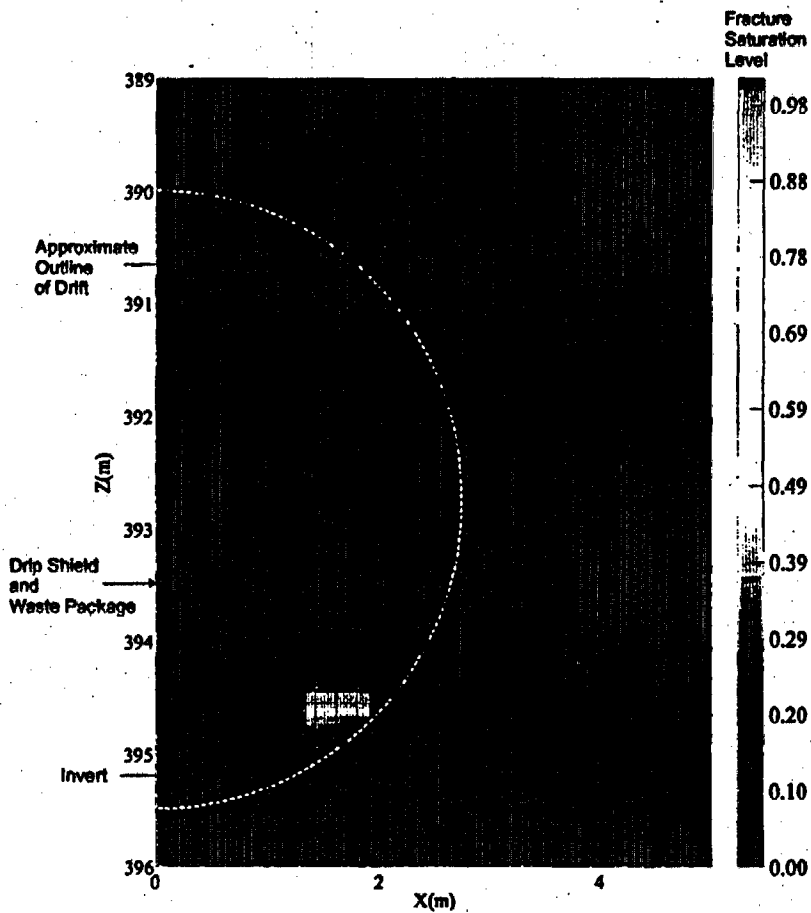
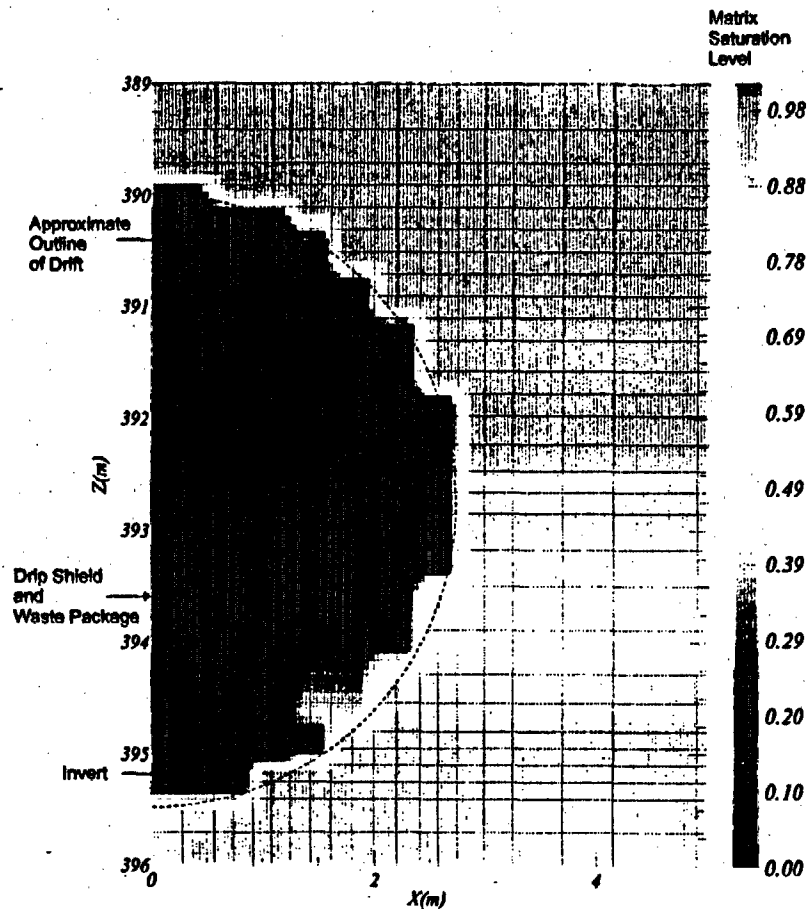


Figure 6-20. Matrix Saturation Levels Near the Repository Horizon at Steady State (Case1)



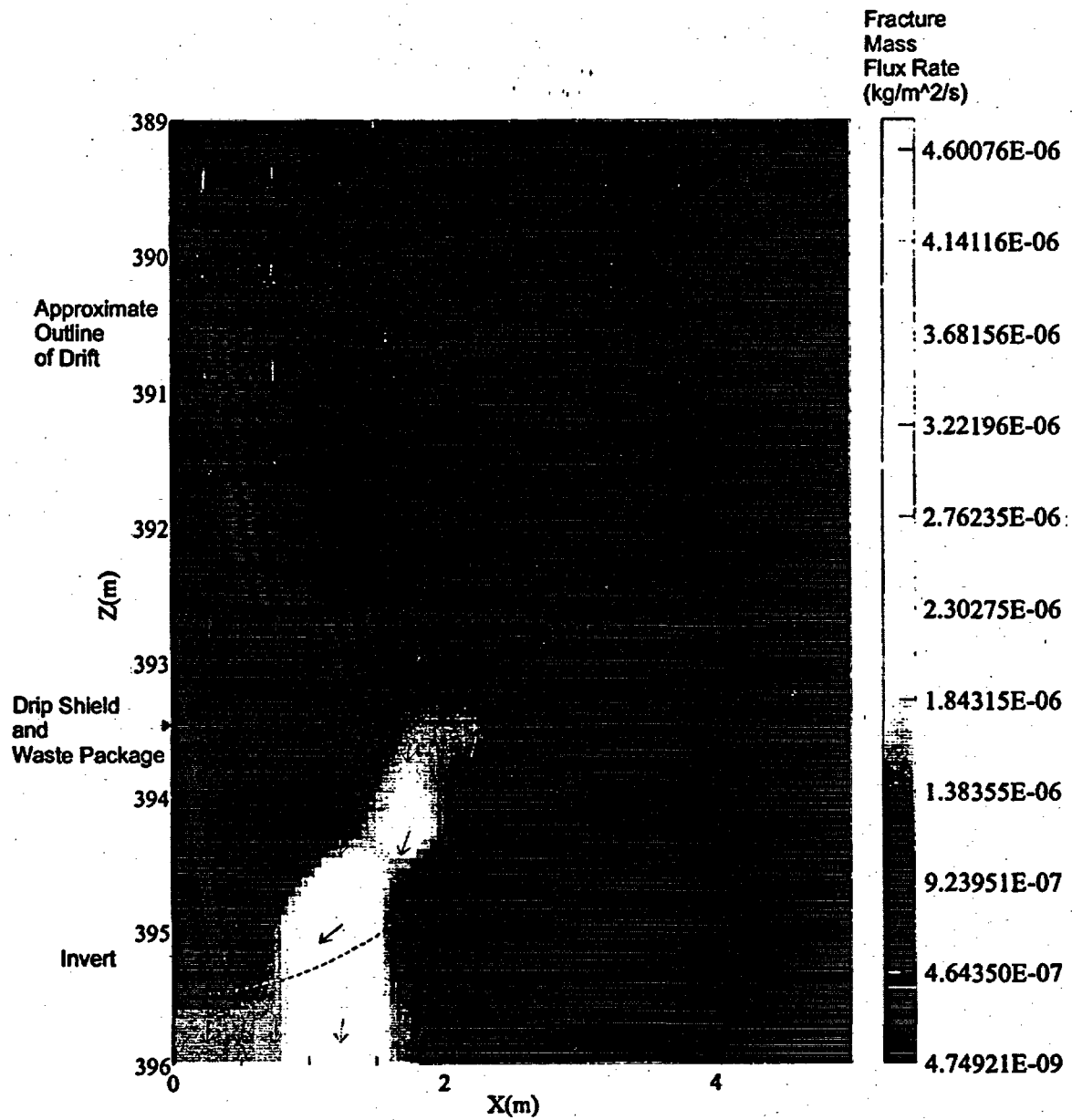


Figure 6-21. Fracture Mass Flux Rates (kg/m²-s) and Direction of Flow Near the Repository Horizon at Steady State (Case 1)

Table 6-5. Fracture Mass Flux Rate

Direction of Mass Flux	Depth (m)	Horizontal Distance from Center Line (m)		
		5.27	15.65	33.82
Fracture Mass Flux Rate (kg/m ² /sec) in the Horizontal Direction	100	9.70E-08	2.80E-10	9.10E-12
	200	2.30E-10	3.50E-10	1.20E-10
	350	1.80E-10	2.90E-10	9.90E-11
Fracture Mass Flux Rate (kg/m ² /sec) in the Vertical Direction	100	2.00E-06	6.30E-08	1.40E-08
	200	1.20E-06	1.20E-06	1.10E-06
	350	1.20E-06	1.20E-06	1.10E-06

Table 6-6. Matrix Mass Flux Rate

Direction of Mass Flux	Depth (m)	Horizontal Distance from Center Line (m)		
		5.27	15.65	33.82
Matrix Mass Flux Rate (kg/m ² /sec) in the Horizontal Direction	100	2.50E-12	1.20E-12	1.90E-13
	200	3.90E-10	8.20E-10	3.50E-10
	350	6.00E-11	1.20E-10	4.90E-11
Matrix Mass Flux Rate (kg/m ² /sec) in the Vertical Direction	100	1.00E-09	9.90E-10	9.90E-10
	200	3.50E-08	3.40E-08	3.30E-08
	350	3.50E-08	3.50E-08	3.40E-08

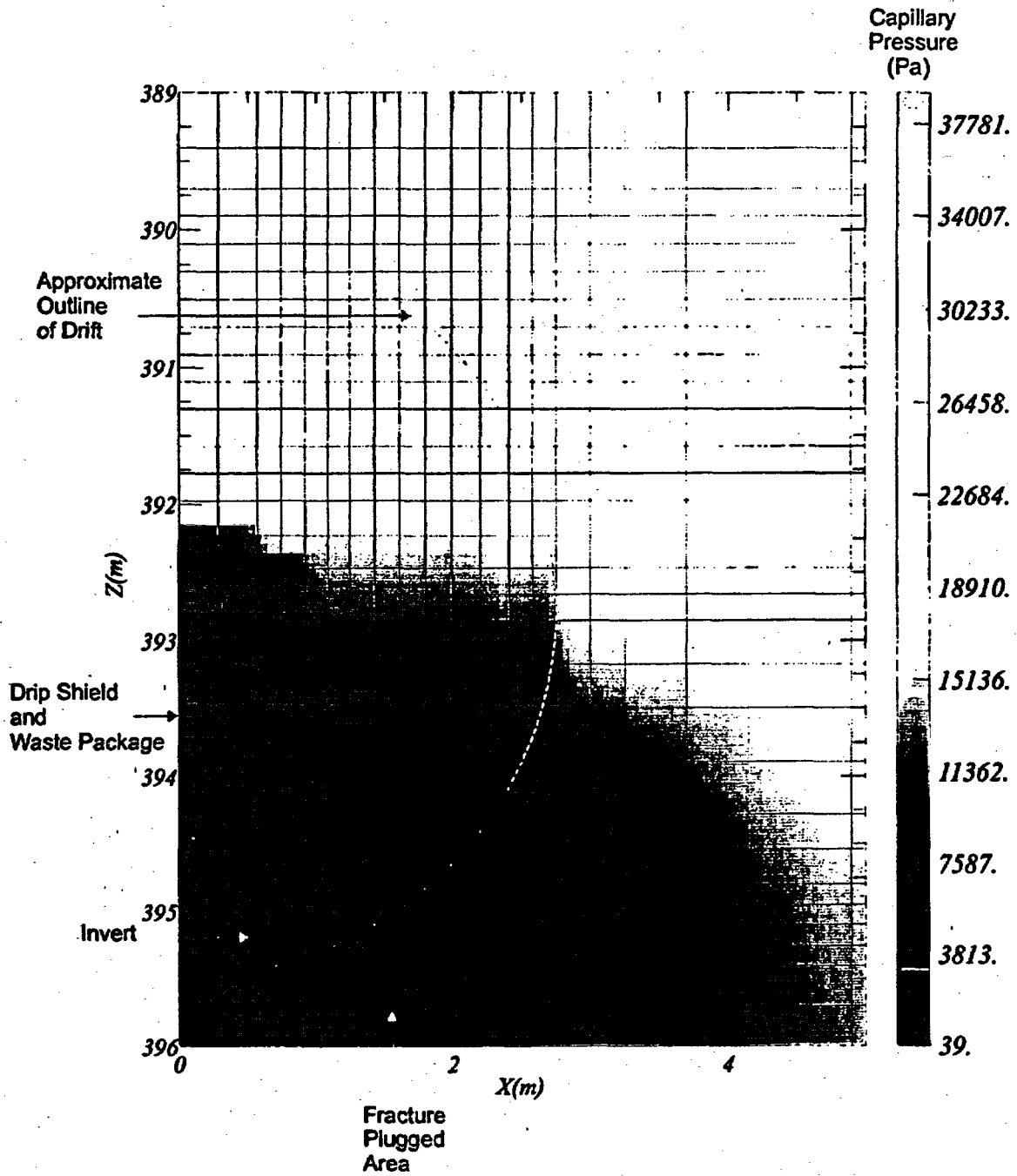


Figure 6-22. Absolute Matrix Capillary Pressure Near the Repository Horizon for Plugged Fractures at Steady State (Case 2)

Figure 6-23. Fracture Saturation Near the Repository Horizon for Plugged Fractures at Steady State (Case 2)

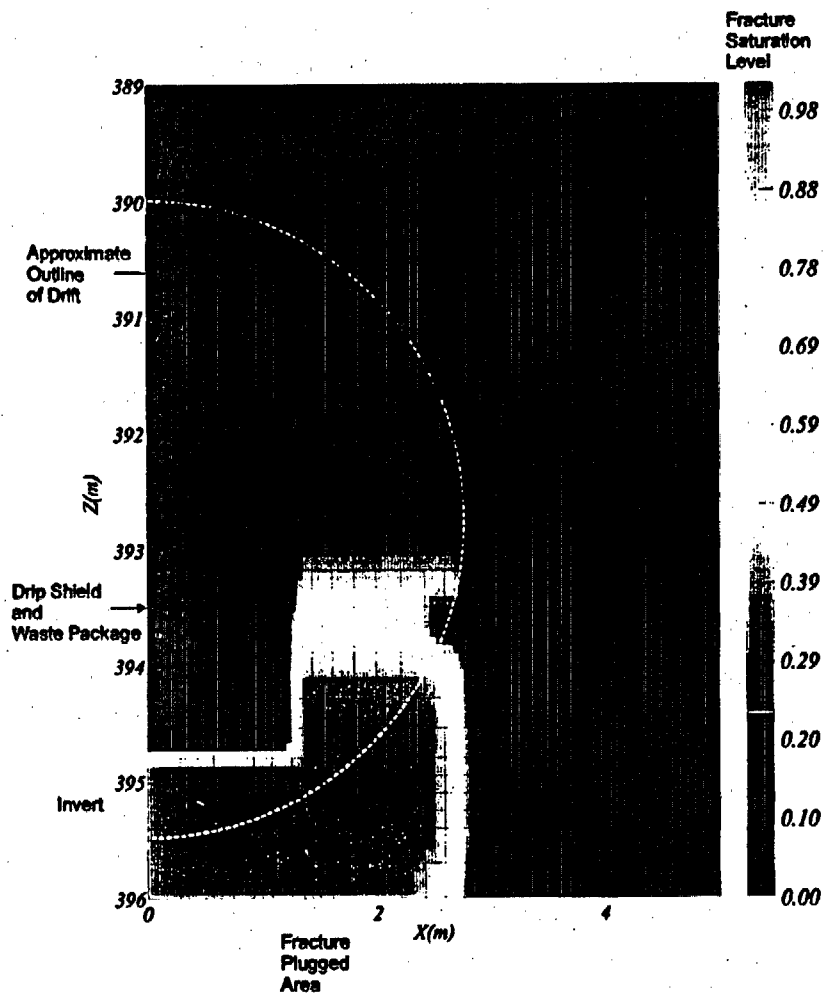
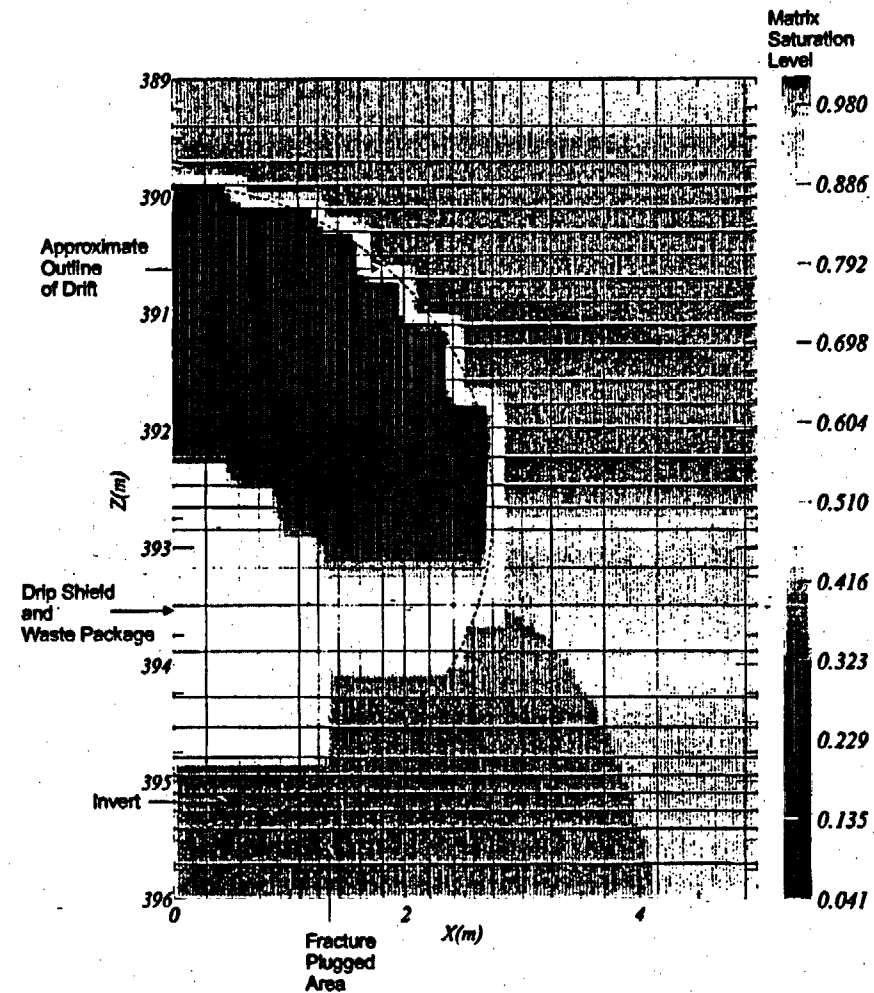


Figure 6-24. Matrix Saturation Levels Near the Repository Horizon for Plugged Fractures at Steady State (Case 2)



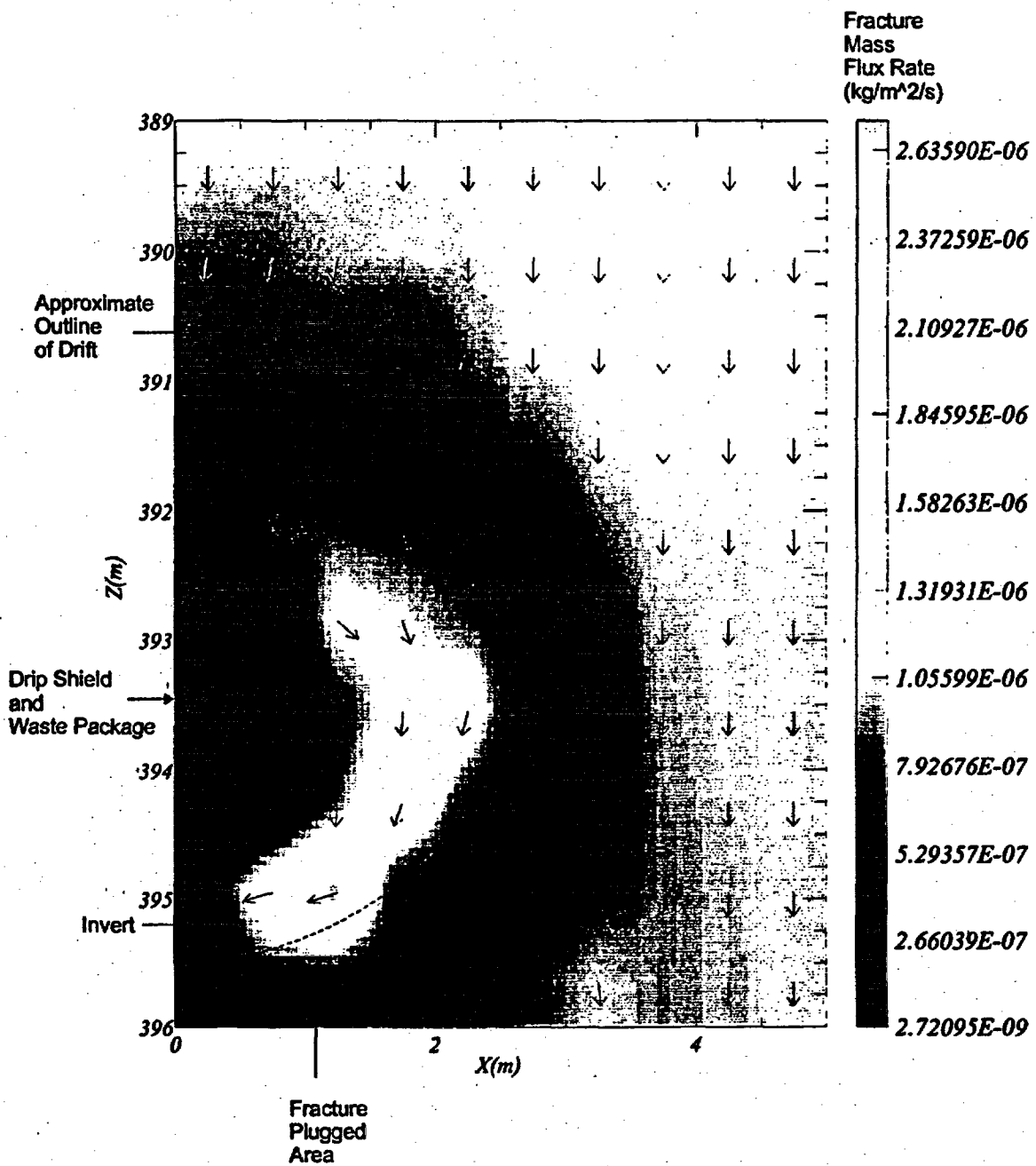


Figure 6-25. Fracture Mass Flux Rates ($\text{kg/m}^2\text{-s}$) and Direction of Near the Repository Horizon for Plugged Fractures at Steady State (Case 2)

Figures 6-23 and 6-24 show that the plugging of the floor rock increases the saturation levels in the invert and the surrounding floor rock. Saturation levels in the invert directly above the plugged floor rock are increased to near saturation with the absolute value of matrix capillary pressure near zero. Saturation levels through the rock matrix in the floor rock are increased from 0.88 to 0.98 or near saturation. Saturation levels in the invert increase from 0.15 to 0.98 or near saturation.

6.2.5.3 Drains (Case 3)

The results of the NUFT analysis for the plugged fractures with a drain (Case 3) are presented in Figures 6-26 to 6-29 for the absolute value of the matrix capillary pressure, fracture and matrix saturation levels, and fracture mass flux rates, respectively. These figures can be compared directly to the results from Case 2 for plugged fractures (Figures 6-22 to 6-25).

The results show that a drain strongly influences the flow regime in the invert and below the repository horizon. The distribution of the absolute value of capillary pressure (Figure 6-26) shows lower absolute values of capillary pressures than the surrounding tuff matrix, which is reduced near the base of the drain. The saturation levels within the drain are higher, and show nearly saturated conditions near the base of the drain.

The drain also drastically increases the mass flux rate into the floor as shown in Figure 6-29. The results show that mass flux rates locally are high relative to the fractured media and flow through the backfill. The high mass flux rate in the drain results in an increase in the absolute value of capillary pressure, and an attendant reduction of saturation level in the invert directly above the plugged fractures. The absolute value of the capillary pressure is of the order of 20,000 Pa (200 cm) for this case while for the case of plugged fractures without drains, the absolute value of the capillary pressure in the invert was near zero. A further discussion of the influence of the drains on invert mass flux rates is presented in Section 6.2.5.4.

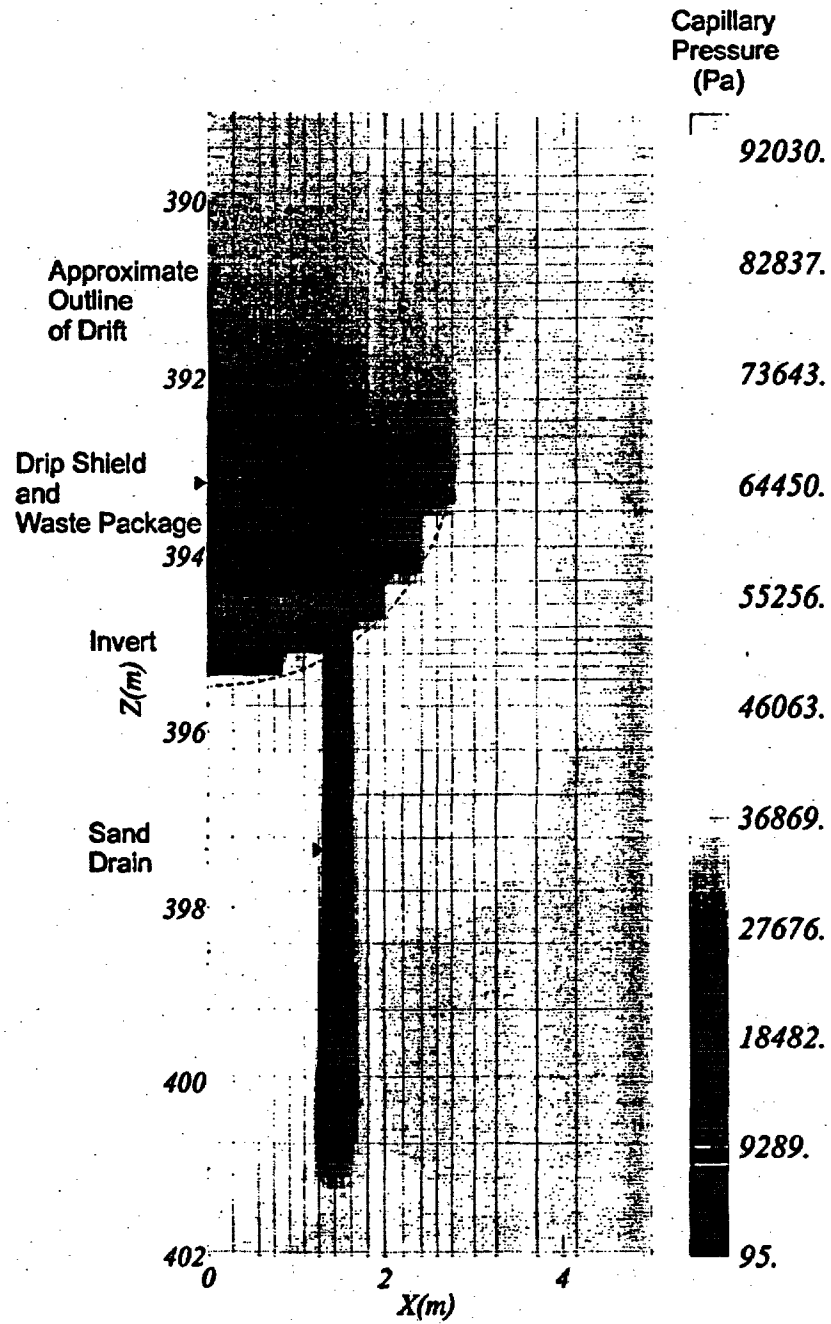


Figure 6-26. Absolute Matrix Capillary Near the Repository Horizon for Plugged Fractures with a Sand Drain (Case 3)

Figure 6-27. Fracture Saturation Near the Repository Horizon for Plugged Fractures with a Sand Drain (Case 3)

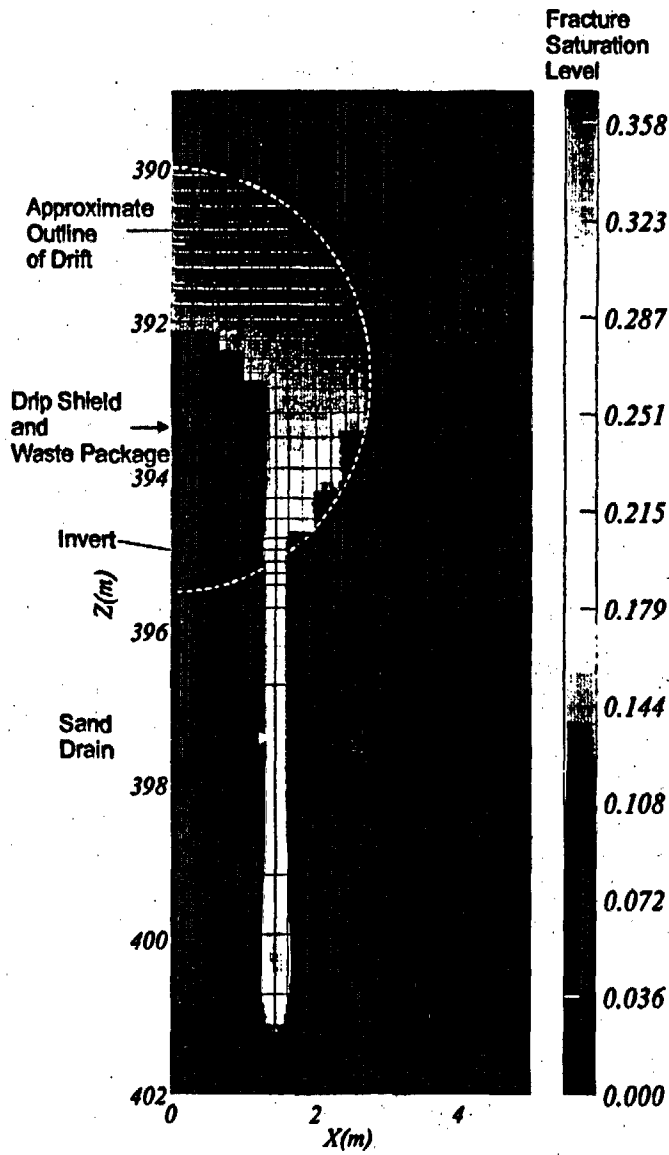
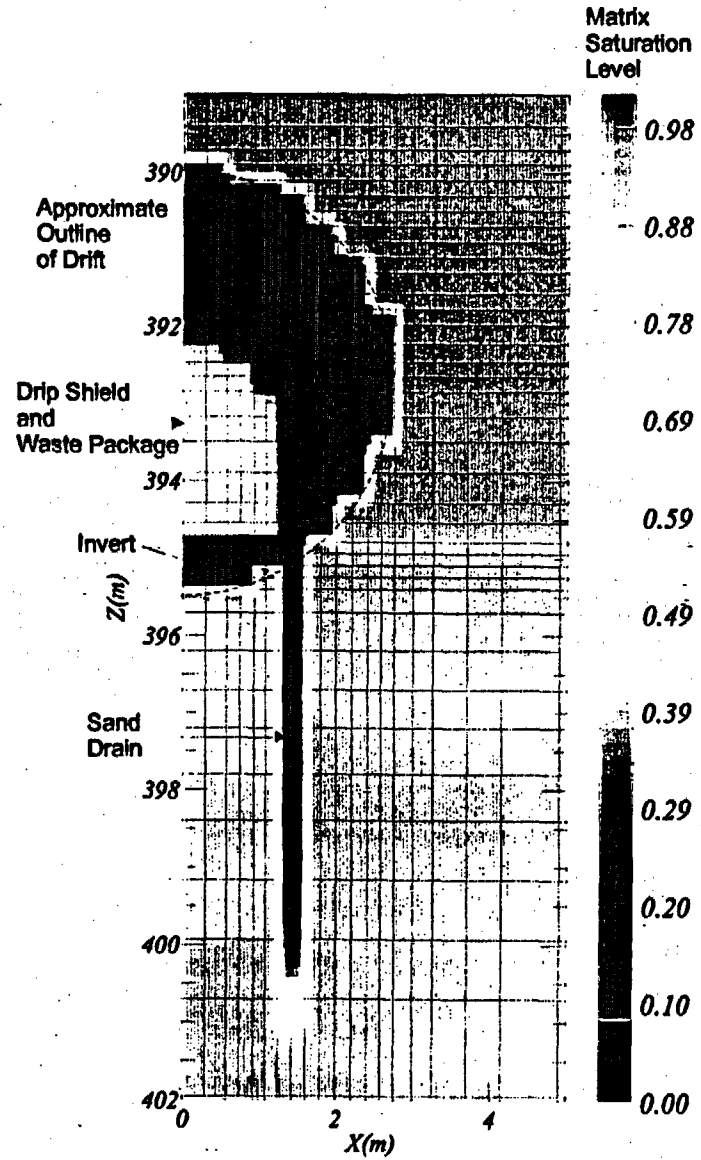


Figure 6-28. Matrix Saturation Near the Repository Horizon for Plugged Fractures with a Sand Drain (Case 3)



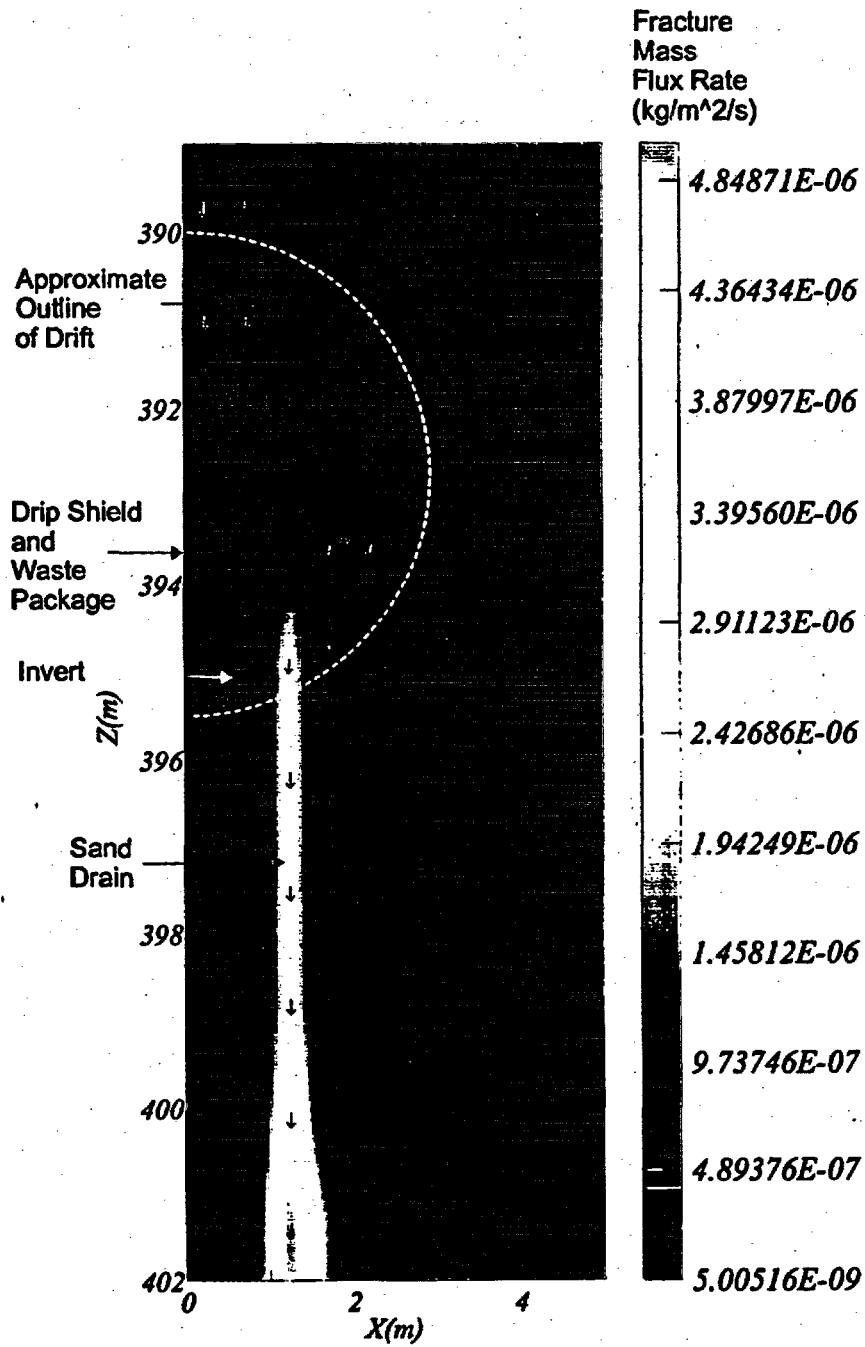


Figure 6-29. Fracture Mass Flux Rates (kg/m²-s) and Direction of Flow Near the Repository Horizon for Plugged Fractures with a Sand Drain (Case 3)

6.2.5.4 Flow Through Invert

Seepage water flow within the invert is summarized in Table 6-7 where the travel time is measured from the top to the base of the invert. A comparison between Case 1 and Case 3 shows that the placement of a sand drain for the plugged floor significantly reduces the water presence in the invert. The volumetric flow rate below the drip shield decreases from 0.16 m³/yr to 1.6x10⁻⁵ m³/yr while the travel time increases from 19.4 years to 13,150 years when a sand drain is used. Figures 6-30 and 6-31 present the fracture and matrix pore water velocities for Case 1. Within the invert away from the drift boundary, the velocity vectors in the fracture are close to those in the matrix while for grid blocks near the boundary, the flow is dominantly into the fractures. The pore water velocity in the adjacent column of grid blocks is increased by an approximate factor of 2.4.

Table 6-7. Summary of Invert Flow Characteristics

Flow Variables	Case Number	
	1	3
Flow below Drip Shield (m ³ /yr)	0.16	1.6E-5
Flow outside Drip Shield (m ³ /yr)	0.25	0.36
Travel Time (yr)	19.4	13,150
Average Pore Water Velocity (mm/yr)	31	4.6E-2
Average Saturation Level	0.13	0.12

For Case 3, Figures 6-32 and 6-33 of the fracture and matrix pore water velocities show that dominant drainage occurs vertically downward through the sand drain.

6.2.6 Impact of Backfill to Drainage

An examination of the flow direction vectors in Figures 6-21, 6-25, and 6-29 for Cases 1, 2 and 3, respectively, indicate that water in the host rock fractures are drawn into the backfill in the drift laterally. The explanation is that the capillary pressures in the backfill are more negative than the capillary pressures in the fracture which create the driving force for lateral flow. It is believed that without backfill, the drift opening will function as a capillary barrier for the flow in the host rock above so water is diverted around the drift, resulting in less water entering the invert.

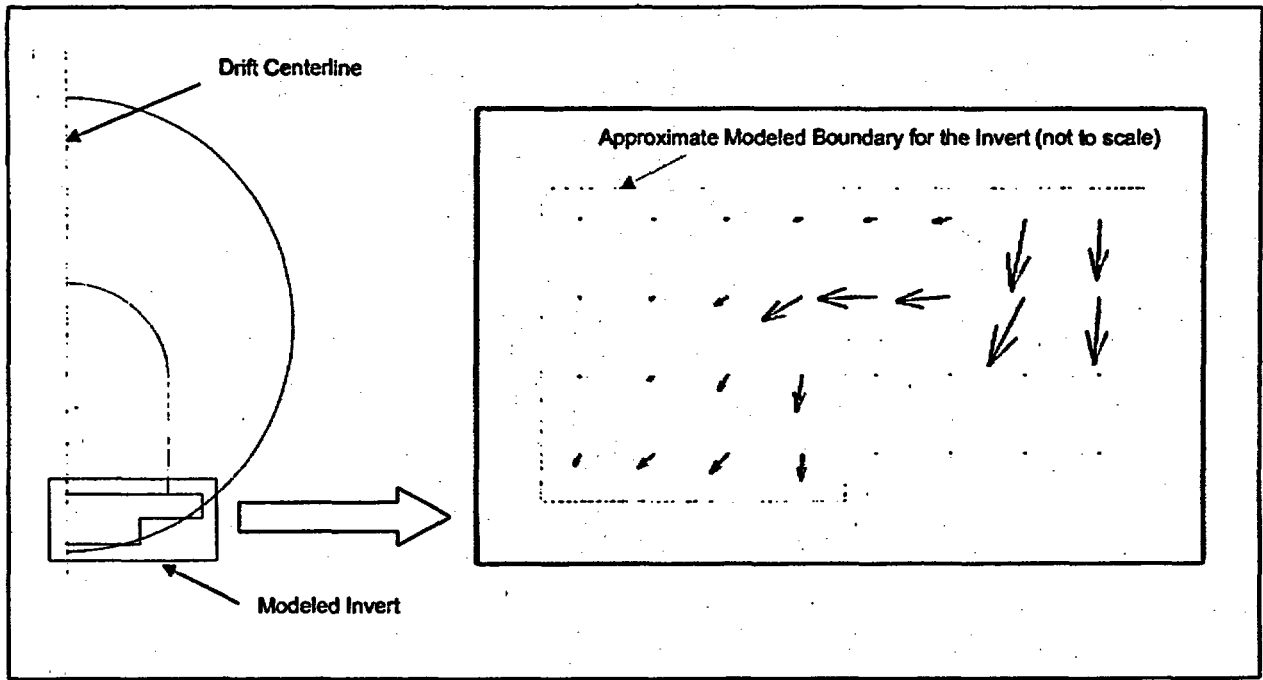


Figure 6-30. Fracture Pore Water Velocity Vectors in the Invert for Case 1

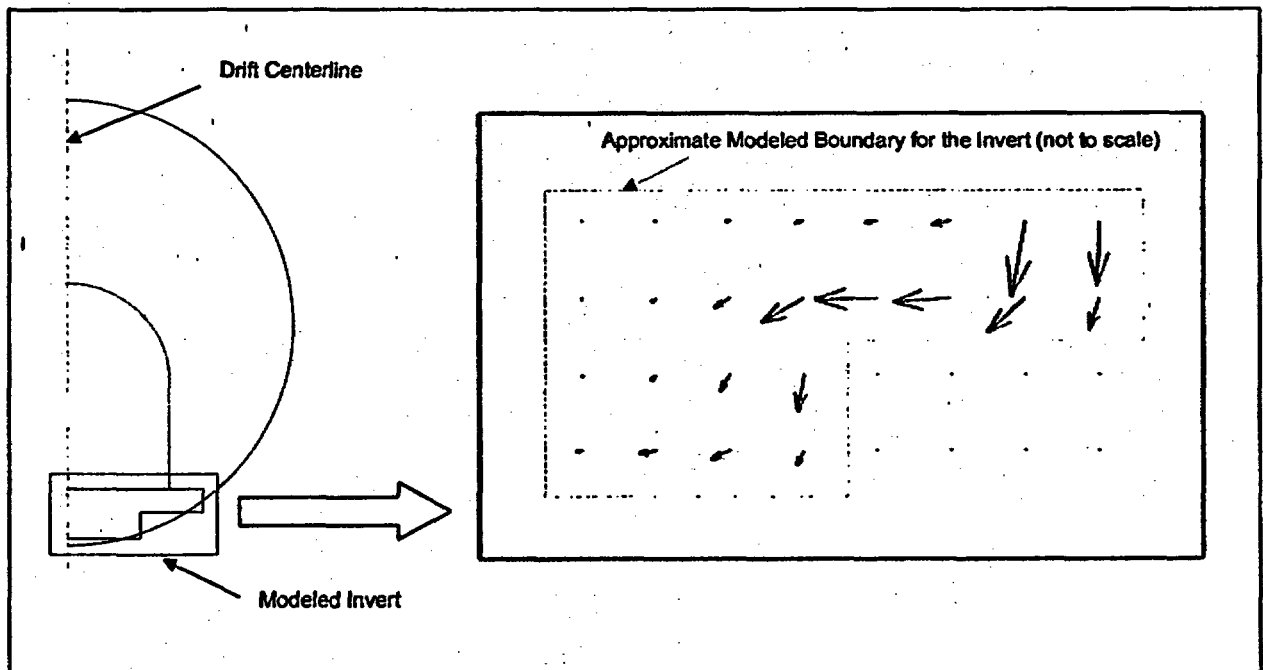


Figure 6-31. Matrix Pore Water Velocity Vectors in the Invert for Case 1

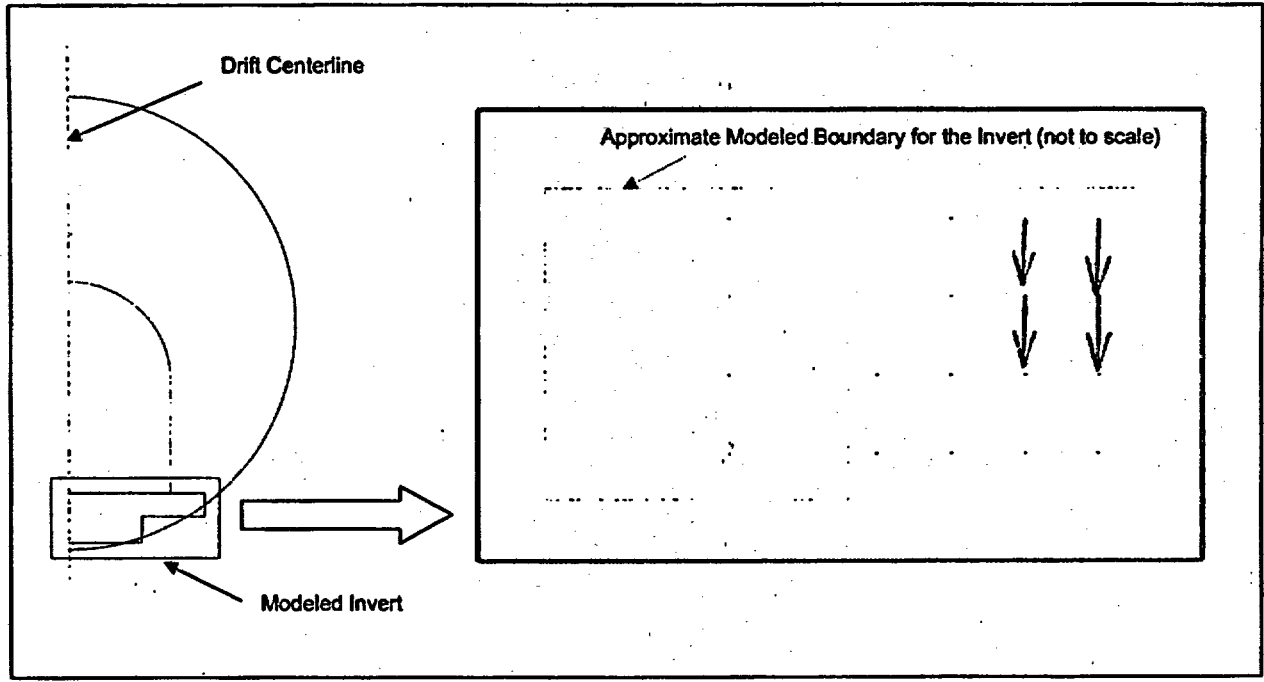


Figure 6-32. Fracture Pore Water Velocity Vectors in the Invert for Case 3

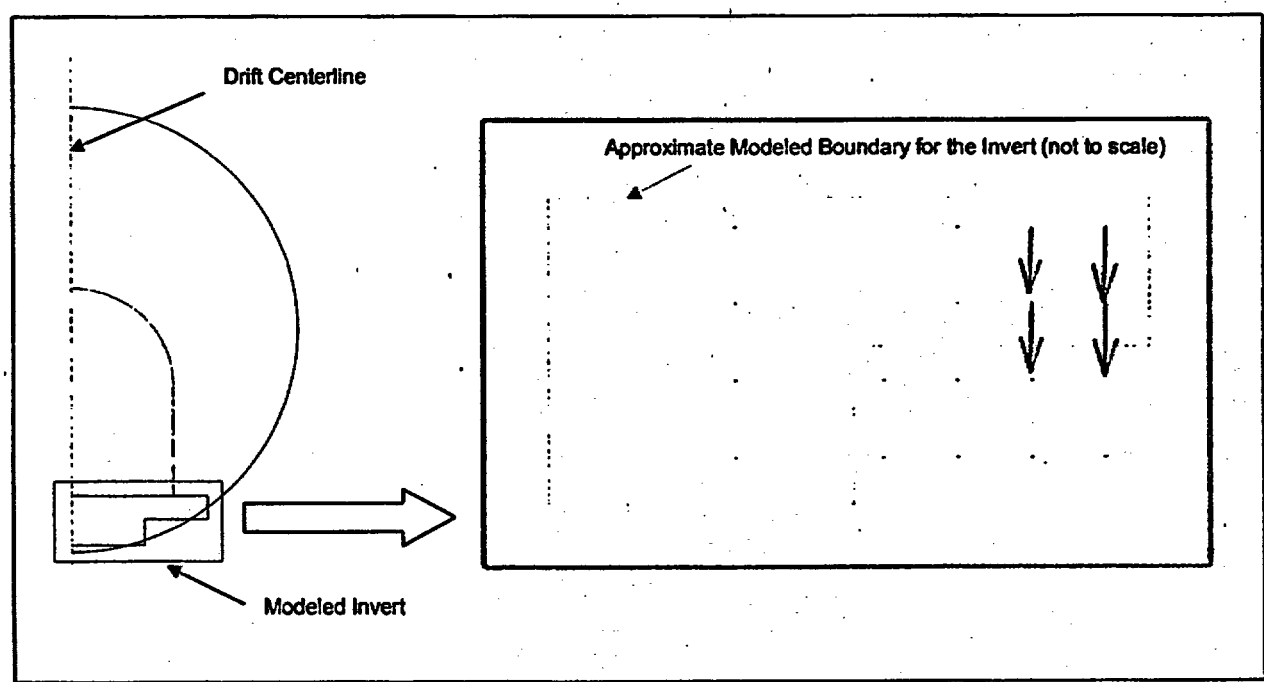


Figure 6-33. Matrix Pore Water Velocity Vectors in the Invert for Case 3

6.2.7 Model Validation

Validation requires review of the Water Drainage Model calibration parameters and corroborative information for reasonableness and consistency. In accordance with AP-3.10Q, this is documented internally in parameter inputs (Section 4.1.2), assumptions (Section 5.2) and development (Sections 6.2.1 and 6.2.2). The model uses a finite difference technique (i.e., the NUFT code) supplemented by other standard calculations. The model is based on appropriate inputs, including properties and boundary conditions. Grids, convergence, and other model settings are consistent with past practice.

In addition, a comparison of the base-case model output to a closed-form solution was made (Attachment XII). Data trends and magnitudes from both the closed-form solution and the model qualitatively agree. That is, the calculations show an increase in flux within the drift, and a decrease in flux outside the drift. These criteria are appropriate for demonstrating that the model results are reasonable and that the model is therefore validated and appropriate for its intended use.

When EBS pilot-scale testing results become available, this quantitative test data can be compared to predicted model results using NUFT to provide further validation of the model.

6.3 THERMOHYDROLOGIC MODEL

The purpose of the line-averaged-heat-source, drift-scale thermohydrologic (LDTH) model calculations is to support modeling of the in-drift physical and chemical environment. It is intended to provide estimates for the changes of temperature, relative humidity, liquid flux and saturation level, and rate of evaporation with time during the repository thermal evolution. Sensitivity analysis was performed to account for the uncertainties of waste placement locations, heat generation rates, and infiltration rate distributions. Thermal hydrologic conditions were investigated at the center and edge of the repository, for infiltration rates resulted from the present-day climate, Monsoon weather, and glacial melting, and for different heat generation rates in terms of areal spent-fuel mass loading. This model generates abstracted results for use as input to reaction cell models. The objectives to be met by the TH Model include the following:

- Identify the processes and model inputs that control TH performance measures.
- Use the active-fracture model for nonequilibrium fracture-matrix interaction, consistent with the unsaturated-zone site-scale hydrologic model to perform LDTH-model calculations for representative locations within the repository layout.
- Evaluate calculated results and select LDTH-model cases for further analysis of the EBS chemical environment.
- Develop values of TH performance measures extending to 1,000,000 years

All NUFT calculations and postprocessed results described in this subsection pertain to the half-drift symmetry model, unless specified to be full-drift results. Thus, the calculated zone-to-zone fluxes and zone evaporation rates should be doubled to represent full-drift results. For other variables including temperature, saturation, air mass-fraction, and gas-phase vertical mass flux, the half-drift and full-drift results are identical.

6.3.1 Background for the LDTH-Model Calculations Using NUFT

The LDTH predictive model that forms the basis of these calculations utilizes the NUFT V3.0s code (Nitao 1998). NUFT (Nonisothermal Unsaturated Flow and Transport) has been used to model a wide range of problems. NUFT was used for simulating waste-package environment conditions for *Total System Performance Assessment-Viability Assessment (TSPA-VA)* (CRWMS M&O 1998; Section 3.2) and has also been used for calculations in support of field-scale thermal testing (e.g., calculations reported in Buscheck et al. 1997). The implicit DKM version of NUFT that includes the Active Fracture Concept (AFC) is used in these calculations. General descriptions of physical principles used in NUFT V3.0s, with references for additional information, are provided in Hardin, E.L. 1998 (Sections 3.3.3, 3.3.4, and 3.3.5).

The DKM conceptualizes fractured rock as having two interacting continua, one representing the matrix and the other representing the fracture network. Fluxes of mass and heat between the fracture network and the matrix at each point in the model domain, are calculated from the local temperature and pressure differences. These differences can be nonzero; thus, nonequilibrium conditions can exist at that point. This feature of the DKM allows for more realistic treatment of

transient behavior when conditions such as saturation and temperature are changing with time.

The AFC is a scheme for dynamic modification of the contact area between the fracture network and the matrix (Liu et al. 1998). The underlying concept is that fracture flow occurs through some, not all, of the fractures at a given location and time. For transient conditions, this tends to produce stronger nonequilibrium response than does assuming that flux is uniformly distributed through all fractures. Flow through a fracture is greater when it has higher saturation, and focusing of flux through a limited population of active fractures tends to maximize the saturation, thereby enhancing fast pathways for flux through the mountain.

The hydrologic properties obtained from DTN LB990861233129.001 were developed for the unsaturated-zone site-scale model (herein called the unsaturated zone (UZ) model) using a procedure that assumes they will be applied in DKM employing AFC with the modified Brooks and Corey gas permeability function (Brooks and Corey 1966, Equation 33). That is how they are applied in this model.

A limited comparison of the LDTH model used in this report with other TH models, including the Multiscale Thermohydrologic Model (CRWMS M&O 2000i), the Drift-Scale Coupled Processes (DST and THC Seepage) Models (CRMWS M&O 2000k), and the Mountain-Scale Coupled Processes (TH) Models (CRWMS M&O 2000p) is provided as follows:

- Thermal and hydrologic properties for the rock units are the same for all the models. The same stratigraphic model is used, but the contact elevations depend on geographic location.
- The Multiscale Model and the Mountain-Scale Model represent the entire repository layout, either in 2-D cross section, or 3-D. The Drift-Scale THC Seepage Model, and the LDTH-model cases developed for this report, represent only one or two representative locations.
- The models use the same infiltration flux distribution, and the same variation of flux with climate states that switch at 600 yr and 2,000 yr after emplacement. Infiltration flux varies with location, so the Multiscale Model and Mountain-Scale Model have spatial functions representing flux. The Drift-Scale THC Seepage Model uses the value of the average flux over the entire repository layout, while the LDTH-model cases run for this report use the predicted flux at typical center and edge locations.
- The other boundary conditions include surface temperature, pressure, and humidity, which are all handled consistently among the different models. The lower, constant-temperature boundaries of the Multiscale Model and the Mountain-Scale Model are situated 1,000 meters below the water table, with fixed temperature values represented using estimates for the geothermal gradient. The other models use the water table as the lower, constant-temperature boundary.
- Gridding is similar for the Multiscale Model, the Drift-Scale THC Seepage Model, and the LDTH-model cases developed for this report; the elements that define the drift opening are on the order of a few tens of centimeters in size. Gridding for the Mountain-Scale Model is much more coarse, and the calculated results vary accordingly.

Line-averaged-heat-source, drift-scale, thermohydrologic (LDTH) model calculations are reported here for the 14c4 and 14c1 locations (Figure V-1 in Attachment V). These model calculations are performed using the same approach developed for the Multiscale Thermohydrologic Model (MSTHM) (CRWMS M&O 2000i) with minor modifications to represent different seepage scenarios. The Multiscale Model represents variation of TH conditions throughout the repository, anchored by LDTH-submodel calculations at 31 geographic locations uniformly distributed throughout the repository area. The LDTH-model calculations described in this report are limited to two of those 31 locations, the 14c4 and 14c1 locations. The rationale for selecting the 14c4 and 14c1 locations for investigation of the in-drift physical and chemical environment, is as follows:

- 14c4 is typical for locations internal to the repository layout. It is located near the geographic center, where temperatures and evaporation rates will be relatively high. Thermal loading for the 14c4 model is equivalent to the average for the repository layout (corresponds to areal spent-fuel mass loading of 56 MTU/acre required by CRWMS M&O 2000s, Section 2.3.1. The projected infiltration flux is near the average for the layout, as discussed subsequently.
- 14c1 is located at the repository edge, where the rate of cooling will be greatest because of conductive heat loss to unheated external regions. 34 MTU/acre thermal loading is used for the 14c1 model, which is appropriate for edge locations subject to cooling effects.

For each of these locations, TH conditions are simulated, using the "lower", mean, and "upper" infiltration distributions described in the Multiscale Model (CRWMS M&O 2000i), for different flux conditions. Note that the data used to describe the "lower", mean, and "upper" infiltration distributions were obtained from the same sources used for the Multiscale Model, and not directly from the Multiscale Model. Different hydrologic property sets are associated with the different infiltration conditions.

For calculated postclosure results, there also are separate output files for fracture and matrix data. Further discussion of the NUFT V3.0s inputs for these models is provided in the following subsections. The selection of locations 14c4 and 14c1 is appropriate.

The two locations in the potential repository layout, for which the LDTH-model calculations are performed for this report, are described in Section 4.1.1. The 14c1 location is along the eastern edge of the repository layout, and increased drift spacing is used to represent edge cooling effects in a 2-D model. Thus the drift spacing is increased by a factor of 56/34 or 167 percent of the nominal value ($1.67 \times 81 \text{ m} = 135 \text{ m}$). The model domain width is half the drift spacing because of symmetry.

6.3.2 Prescribing Drift Seepage in the LDTH Models

Over nearly the entire range of infiltration-flux conditions considered in the Multiscale Thermohydrologic Model calculations of the no-backfill case (CRWMS M&O 2000i), seepage into the drift is not predicted to occur. Nonzero drift-seepage fluxes are only predicted to occur in regions of the repository having the highest infiltration (and percolation) flux for the "upper" infiltration-flux case. An important reason for the very low occurrence of predicted drift seepage is the assumption of a uniform fracture continuum within any given hydrostratigraphic unit

(Section 5.3.2). This assumption is equivalent to assuming no drift-scale heterogeneity of fracture properties in the host rock. This assumption, together with the use of a 2-D LDTH model, reduces the tendency for drift seepage to be predicted to occur.

To overcome the tendency of the LDTH models to predict little or no seepage, the LDTH models described in this report are modified to allow for seepage to be "prescribed" (or imposed) within the drift. Two sets of LDTH seepage models are used. In the first set, drift seepage is prescribed to occur uniformly over the entire upper drip-shield surface. Thus, sources of liquid water are specified at each of the grid blocks overlying the drip shield, including the grid block overlying the column of grid blocks adjacent to the vertical side of the drip shield. In the second set of LDTH drift-seepage models, drift seepage is prescribed to occur directly onto the drift floor (i.e., upper invert surface) between the base of the drip shield and the intersection of the drift floor and lower drift wall. Thus, a source of liquid water is specified directly above the drift floor at the base of the drip shield. In effect, the second set of calculations assumes that seepage entirely bypassing the drip shield.

Three values of seepage percentage are considered: 0, 3, and 30%. For the purpose of this report, the seepage percentage is taken to be the percentage of the incident percolation flux in the host rock which directly overlies the invert that is prescribed to be entering the drift. Note that the invert is modeled as having a lateral width of 3.2214 m (see Figure 6-2 of CRWMS M&O 2000i). Therefore, the seepage percentage is based on the incident percolation flux over a lateral width of 3.2214 m (rather than the entire 5.5-m width of the drift). Note that because the LDTH models have lateral no-flow boundaries (which prevents any lateral diversion from occurring), the percolation flux in the host rock is equivalent to the infiltration flux that is specified at the top of the LDTH model. Referring to Table 4-6, the infiltration flux at the 14c4 location is 10.13, 28.88, and 42.00 mm/yr for the present-day, monsoonal, and glacial climate states, respectively. For the 30%-seepage case, the resulting seepage fluxes are 3.04, 8.66, and 12.6 mm/yr (calculated over a footprint which is 3.2214 m wide). These seepage flux values are uniformly specified in the grid blocks in the 3.2214-m-wide strip directly overlying the drip shield and invert. Consequently, all of the seepage flux drains down the side of the drip shield before reaching the invert.

The second set of LDTH drift-seepage models are equivalent to the first set except that the mass flux of water that was uniformly distributed over the 3.2214-m-wide strip overlying the drip shield and invert in the first set is now entirely focussed onto the two 0.3597-m-wide drift-floor strips to either side of the base of the drip shield. This results in the local seepage flux on the drift floor being $4.4779 (= 3.2214/2 \times 0.3597)$ times greater than the seepage flux that was uniformly distributed over the 3.2212-m-wide strip in the first set of models. Thus, for the mean-infiltration 30%-seepage case, the local seepage flux that is directly imposed onto the drift floor (and into the invert) is 13.61, 38.78, 56.42 mm/yr. Note that none of this seepage flux contacts the drip shield.

Another important consideration in the specification of drift seepage, is prescribing enthalpy values for the seepage flux that does not artificially add or subtract sensible heat from the drift. An assumption is made that the water seeping into the drift has equilibrated with the host-rock temperature at the crown of the drift, with a maximum allowable temperature of 96°C for the seepage flux. The maximum temperature is set to assure that the seepage flux enters the

drift as liquid water. This assumption is implemented by extracting the temperature history for the host rock at the crown of the drift for the case with 0% seepage (i.e., no prescribed seepage into the drift). The temperature history is used to linearly interpolate an enthalpy history from the steam tables (Keenan, et al., 1969). For the 0%-seepage case, there are six unique temperature histories considered in this report, resulting from two repository locations (14c4 and 14c1) and three infiltration-flux cases. Thus, it is necessary to generate six enthalpy histories.

6.3.3 LDTH-Model Results

The purpose of this section is to investigate the influence of infiltration flux, proximity to the edge of the repository, and seepage percentage on TH conditions in the EBS. The focus of this investigation is the influence of these factors on TH conditions on the drip shield and in the invert. Table 6-8 lists all of the plots of TH conditions that are given in Section 6.3.

Table 6-8. Summary of Figures and Associated Source Files (Attachment XVI)

Figure Number	TH Variable	Source File Name
Figure 6-34	Drip-shield temperature and relative humidity	14c4-LDTH56-mi-00.f.EBS.ext 14c4-LDTH56-mi-03.f.EBS.ext 14c4-LDTH56-mi-30.f.EBS.ext
Figure 6-35	Drip-shield temperature and relative humidity	14c4-LDTH56-li-00.f.EBS.ext 14c4-LDTH56-li-03.f.EBS.ext 14c4-LDTH56-li-30.f.EBS.ext
Figure 6-36	Drip-shield temperature and relative humidity	14c4-LDTH56-ui-00.f.EBS.ext 14c4-LDTH56-ui-03.f.EBS.ext 14c4-LDTH56-ui-30.f.EBS.ext
Figure 6-37	Drip-shield temperature and relative humidity	14c1-LDTH34-mi-00.f.EBS.ext 14c1-LDTH34-mi-03.f.EBS.ext 14c1-LDTH34-mi-30.f.EBS.ext
Figure 6-38	Drip-shield temperature and relative humidity	14c1-LDTH34-li-00.f.EBS.ext 14c1-LDTH34-li-03.f.EBS.ext 14c1-LDTH34-li-30.f.EBS.ext
Figure 6-39	Drip-shield temperature and relative humidity	14c1-LDTH34-ui-00.f.EBS.ext 14c1-LDTH34-ui-03.f.EBS.ext 14c1-LDTH34-ui-30.f.EBS.ext
Figure 6-40	Invert temperature and relative humidity	14c4-LDTH56-mi-00.f.EBS.ext 14c4-LDTH56-mi-03.f.EBS.ext 14c4-LDTH56-mi-30.f.EBS.ext
Figure 6-41	Invert temperature and relative humidity	14c4-LDTH56-li-00.f.EBS.ext 14c4-LDTH56-li-03.f.EBS.ext 14c4-LDTH56-li-30.f.EBS.ext
Figure 6-42	Invert temperature and relative humidity	14c4-LDTH56-ui-00.f.EBS.ext 14c4-LDTH56-ui-03.f.EBS.ext 14c4-LDTH56-ui-30.f.EBS.ext

Figure 6-43	Invert temperature and relative humidity	I4c1-LDTH34-mi-00.f.EBS.ext I4c1-LDTH34-mi-03.f.EBS.ext I4c1-LDTH34-mi-30.f.EBS.ext
Figure 6-44	Invert temperature and relative humidity	I4c1-LDTH34-li-00.f.EBS.ext I4c1-LDTH34-li-03.f.EBS.ext I4c1-LDTH34-li-30.f.EBS.ext
Figure 6-45	Invert temperature and relative humidity	I4c1-LDTH34-ui-00.f.EBS.ext I4c1-LDTH34-ui-03.f.EBS.ext I4c1-LDTH34-ui-30.f.EBS.ext
Figure 6-46	Drip-shield temperature vs. relative humidity	I4c4-LDTH56-mi-00.f.EBS.ext I4c4-LDTH56-mi-03.f.EBS.ext I4c4-LDTH56-mi-30.f.EBS.ext
Figure 6-47	Drip-shield temperature vs. relative humidity	I4c4-LDTH56-li-00.f.EBS.ext I4c4-LDTH56-li-03.f.EBS.ext I4c4-LDTH56-li-30.f.EBS.ext
Figure 6-48	Drip-shield temperature vs. relative humidity	I4c4-LDTH56-ui-00.f.EBS.ext I4c4-LDTH56-ui-03.f.EBS.ext I4c4-LDTH56-ui-30.f.EBS.ext
Figure 6-49	Drip-shield temperature vs. relative humidity	I4c4-LDTH56-mi-00.f.EBS.ext I4c4-LDTH56-li-00.f.EBS.ext I4c4-LDTH56-ui-00.f.EBS.ext
Figure 6-50	Drip-shield temperature vs. relative humidity	I4c4-LDTH56-mi-03.f.EBS.ext I4c4-LDTH56-li-03.f.EBS.ext I4c4-LDTH56-ui-03.f.EBS.ext
Figure 6-51	Drip-shield temperature vs. relative humidity	I4c4-LDTH56-mi-30.f.EBS.ext I4c4-LDTH56-li-30.f.EBS.ext I4c4-LDTH56-ui-30.f.EBS.ext
Figure 6-52	Drip-shield temperature vs. relative humidity	TSPA_SR00nbf_mean_infiltration.ext
Figure 6-53	Invert liquid saturation	I4c4-LDTH56-mi-00.f.EBS.ext I4c4-LDTH56-mi-03.f.EBS.ext I4c4-LDTH56-mi-30.f.EBS.ext
Figure 6-54	Invert liquid saturation	I4c1-LDTH34-mi-00.f.EBS.ext I4c1-LDTH34-mi-03.f.EBS.ext I4c1-LDTH34-mi-30.f.EBS.ext
Figure 6-55	Liquid-phase flux at bottom of invert	I4c1-LDTH34-mi-00.f.EBS.ext I4c1-LDTH34-mi-03.f.EBS.ext I4c1-LDTH34-mi-30.f.EBS.ext

6.3.3.1 Temperature and Relative Humidity on the Drip Shield

Figures 6-34 through 6-36 show the influence of drift seepage percentage and the magnitude of infiltration (and percolation) flux on temperature and relative humidity on the drip shield at the I4c4 location in the Multiscale Thermohydrologic Model of the repository (see Figure 5-2 in CRWMS M&O 2000i). This location is relatively close to the geographic center of the

repository and experiences slightly higher than average infiltration (and percolation) flux conditions. Drift seepage flux is seen to have very little influence on drip-shield temperature. However, the magnitude of infiltration (and percolation) flux is seen to significantly influence peak temperature, as well as the duration of boiling. Peak temperature and duration of boiling both increase with decreasing infiltration flux.

Drift seepage is seen to have a minimal influence on relative humidity *RH* on the drip shield during the boiling period (Figs. 6-34b, 6-35b, and 6-36b). However, during the post-boiling period, drift seepage strongly influences *RH* on the drip shield for the mean and "upper" infiltration-flux cases, while drift seepage only weakly influences *RH* on the drip shield for the "lower" infiltration-flux case. In general, the duration of reduced *RH* on the drip shield decreases with increasing drift seepage percentage.

Figures 6-37 through 6-39 show the influence of seepage percentage and the magnitude of infiltration (and percolation) flux on temperature and relative humidity on the drip shield at the 14c1 location in the Multiscale Thermohydrologic Model of the repository (see Figure 5-2 in CRWMS M&O 2000i). This location is relatively close to the eastern edge of the repository and experiences slightly lower than average infiltration (and percolation) flux conditions. Seepage flux is seen to have very little influence on drip-shield temperature. However, the magnitude of infiltration (and percolation) flux is seen to significantly influence peak temperature, as well as the duration of boiling. Peak temperature and duration of boiling both increase with decreasing infiltration flux. A comparison of Figures 6-34a, 6-35a, and 6-36a with Figures 6-37a, 6-38a, and 6-39a show that the duration of boiling conditions decreases with proximity to the edge of the repository.

Drift seepage is seen to have a minimal influence on relative humidity *RH* on the drip shield during the boiling period (Figs. 6-37b, 6-38b, and 6-39b). However, during the post-boiling period, drift seepage strongly influences *RH* on the drip shield for all three infiltration-flux cases. In general, the duration of reduced *RH* on the drip shield decreases with increasing drift seepage percentage. A comparison of Figures 6-34b, 6-35b, and 6-36b, 6-37b, 6-38b, and 6-39b show that the duration of reduced *RH* on the drip shield decreases with increasing infiltration flux and also decreases with proximity to the edge of the repository.

6.3.3.2 Temperature and Relative Humidity in Invert

Figures 6-40 through 6-42 show the influence of drift seepage percentage and the magnitude of infiltration (and percolation) flux on temperature and relative humidity in the invert at the 14c4 location. Seepage flux is seen to have very little influence on invert temperature. However, the magnitude of infiltration (and percolation) flux is seen to significantly influence peak temperature, as well as the duration of boiling. Peak temperature and duration of boiling both increase with decreasing infiltration flux.

Drift seepage is seen to have a minimal influence on relative humidity *RH* in the invert during the boiling period (Figs. 6-40b, 6-41b, and 6-42b). However, during the post-boiling period, drift seepage strongly influences *RH* in the invert for the mean and "upper" infiltration-flux cases, while drift seepage only weakly influences *RH* in the invert for the "lower" infiltration-flux case

In general, the duration of reduced RH in the invert decreases with increasing drift seepage percentage.

Figures 6-43 through 6-45 show the influence of seepage percentage and the magnitude of infiltration (and percolation) flux on temperature and relative humidity in the invert at the 14c1 location. Seepage flux is seen to have very little influence on invert temperature. However, the magnitude of infiltration (and percolation) flux is seen to significantly influence peak temperature, as well as the duration of boiling. Peak temperature and duration of boiling both increase with decreasing infiltration flux.

Drift seepage is seen to have a minimal influence on relative humidity RH in the invert during the boiling period (Figs. 6-37b, 6-38b, and 6-39b). However, during the post-boiling period, drift seepage strongly influences RH in the invert for all three infiltration-flux cases, with the duration of reduced RH in the invert decreasing with increasing drift seepage percentage. A comparison of Figures 6-40b, 6-41b, and 6-42b, 6-43b, 6-44b, and 6-45b show that the duration of reduced RH in the invert decreases with increasing infiltration flux and also decreases with proximity to the edge of the repository.

6.3.3.3 Temperature versus Relative Humidity Trajectories on the Drip Shield

Figures 6-46 through 6-50 show the influence of drift seepage percentage and the magnitude of infiltration (and percolation) flux on drip-shield temperature versus relative humidity trajectories at the 14c4 and 14c1 locations. At the 14c4 location, drift seepage percentage has very little influence on the shape of the trajectories until RH exceeds 95% (see Figures 6-46a, 6-47a, and 6-48a). At the 14c1 location, drift seepage percentage has very little influence on the shape of the trajectories until RH exceeds 90% (see Figures 6-46b, 6-47b, and 6-48b).

A comparison of Figures 6-49, 6-50, and 6-51 show that as a function of relative humidity, temperature decreases with decreasing infiltration flux. In other words, for lower infiltration fluxes result in a lower temperature at a given relative humidity value. For the 14c4 location, this trend holds until RH exceeds 95%. For the 14c1 location, this trend holds until RH exceeds 90%.

Figure 6-52 gives the temperature versus relative humidity relationship for three geographic locations and two WP types in the Multiscale Thermohydrologic Model (CRWMS M&O 2000i). These combinations of geographic locations and WP types were chosen to envelope the entire range of temperature versus relative humidity trajectories encountered in the repository area. The temperature versus relative humidity trajectories predicted by the LDTH models in this report (Figures 6-42 through 6-47) fall close to the upper two curves in Figure 6-52.

6.3.3.4 Liquid Saturation and Liquid-Phase Flux in the Invert

Figures 6-53 and 6-54 show the influence of drift seepage percentage on liquid saturation in the invert for the 14c4 and 14c1 locations. At the top of the invert, the duration of zero liquid saturation decreases with increasing drift seepage percentage (Figures 6-53a and 6-54a). The terminal (i.e., long-term steady-state) value of liquid saturation increases with increasing drift seepage percentage. At the bottom of the invert, the duration of zero saturation increases weakly with seepage percentage, while the terminal value of liquid saturation increases strongly with drift seepage percentage (Figures 6-53b and 6-54b). A comparison of Figure 6-53 and 6-54

also shows that the duration of zero liquid saturation decreases with proximity to the edge of the repository.

Figure 6-55 shows the influence of drift seepage percentage on the liquid-phase flux in the invert for the 14c4 and 14c1 locations. The period of zero liquid-phase flux corresponds to the duration of the boiling period. Consequently, the 14c4 location has a longer duration of zero liquid-phase flux than the 14c1 location. After the end of the boiling period, there is a period of negative liquid-phase flux, corresponding to a period when water is being imbibed into the invert. Eventually the influence of gravity-driven seepage flux overwhelms imbibition, resulting in a final long-term, steady-state period of positive liquid-phase flux. For the 14c4 location, the long-term, steady-state liquid-phase flux is 0.58, 2.37, and 17.8 mm/yr for the 0%, 3%, and 30% seepage cases, respectively. For the 14c1 location, the long-term, steady-state liquid-phase flux is 0.60, 1.82, and 16.5 mm/yr for the 0%, 3%, and 30% seepage cases, respectively.

6.3.3.5 Evaporation in the Invert

Figure 6-56 shows the average evaporation rate in the invert for the 14c4 location with the mean infiltration distribution. The peak evaporation rates for the 0%, 3%, and 30% seepage cases reach about 200 kg/m²/yr at roughly the same time. However, the evaporation rate for the 30% seepage case drops to zero much earlier than the other cases because the invert temperature recedes at a faster rate and the duration of boiling is shortened as discussed previously. In general, this pattern applies to the "lower" and "upper" infiltration distributions and to the 14c1 location.

6.3.3.6 Temperature and Relative Humidity in Drift Crown

Figure 6-57 compares the drift crown temperature and relative humidity for the "lower", mean, and "upper" infiltration rate distributions. Generally, the temperature and relative humidity histories follow the same patterns for different infiltration rates. Temperature is higher and relative humidity is lower at the drift crown for the lower infiltration rates.

6.3.4 Thermohydrologic Model Validation

The hydrologic properties used for these models are taken directly from the Unsaturated Zone (UZ) Flow and Transport Model (CRWMS M&O 2000o). Thermal properties are based on laboratory-measured data (DTN: LB990861233129.001). It is noted that values for "wet" thermal conductivity are currently under review. Thermal output of the emplaced waste is based on best-available information for the characteristics of spent fuel and defense high-level waste (DTN: SN9907T0872799.001).

The temperature and pressure boundary conditions used for these models are based on averages for the ground surface and water table, constrained by measured data. Values for average infiltration flux are also taken directly from the UZ Model, for representative center and edge locations. Alternative infiltration flux boundary conditions are selected from the "lower", mean, and "upper" infiltration distributions developed for the UZ Model, to represent the range of uncertainty. These alternative values are used comparatively in several cases discussed in this section.

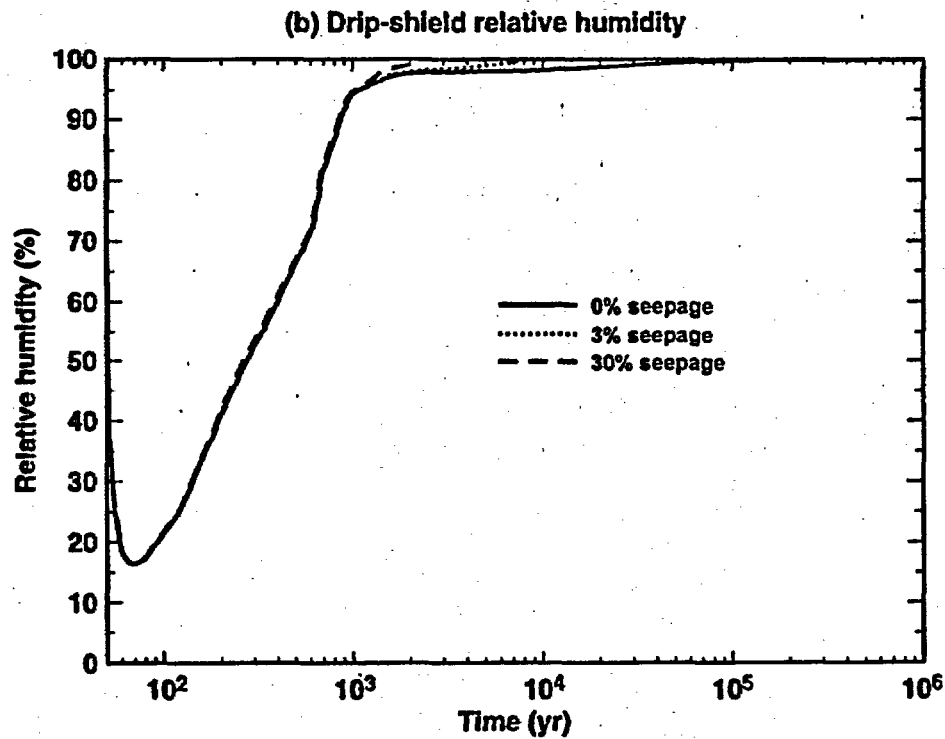
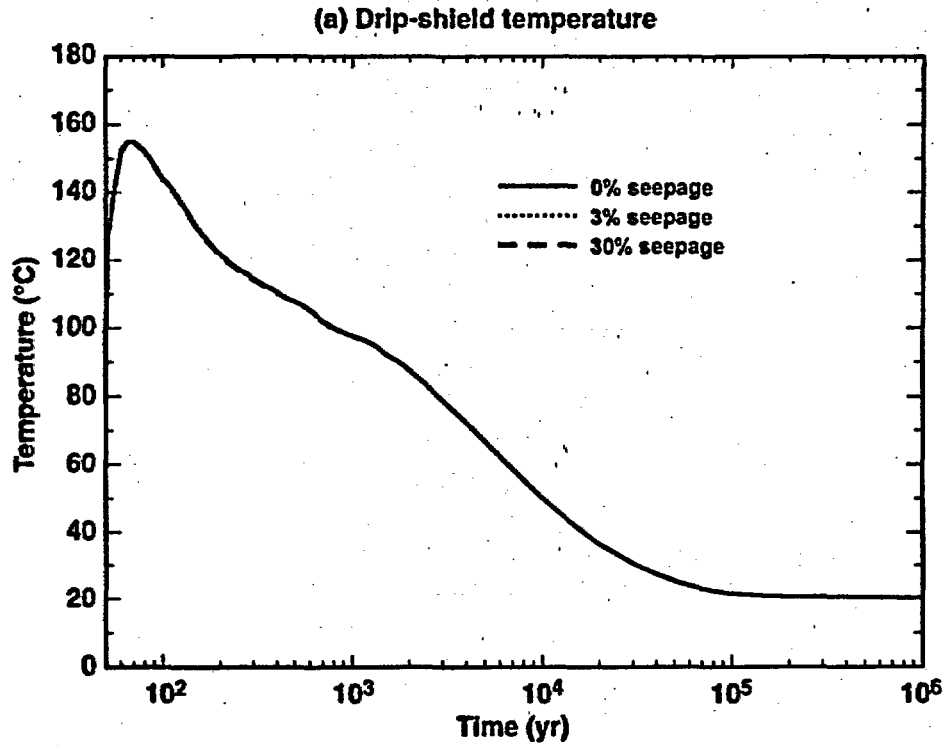
The LDTH models were conducted using an industry standard finite-difference method that includes mass balance and energy balance. The model validation includes various validation techniques described below:

1. **Comparison of NUFT TH model results against the Large Block Test.** *The Thermal Tests Thermal-Hydrological Analysis/Model Report* (CRWMS M&O 2000l, Section 6.2.4.) documents the comparison of NUFT TH model calculations against measurements made in the Large Block Test. A brief summary of this comparison is given in Section 6.13.1 of the Multiscale Thermohydrologic Model AMR (CRWMS M&O 2000i).
2. **Comparison of NUFT TH model results against the Drift Scale Test.** *The Thermal Tests Thermal-Hydrological Analysis/Model Report* (CRWMS M&O 2000l, Section 6.2.3) documents the comparison of NUFT TH model calculations against measurements made in the Drift Scale Test. A brief summary of this comparison is given in Section 6.13.2 of the Multiscale Thermohydrologic Model AMR (CRWMS M&O 2000i).
3. **Inspection of model inputs and outputs.** A detailed visual inspection of the model input files was conducted to verify that the models faithfully represented the intended conceptual model and accurately included all source-input data. A detailed and comprehensive analysis was conducted (Section 6.3.3) that carefully compared the relationship between the model inputs and the model outputs. This comparison uncovered no unexpected or difficult to explain model results; the relationships between the model outputs and the model inputs (for the range of inputs considered in this AMR) are consistent with the physical processes that are accounted for in the LDTH model.

6.3.5 Alternative Models and Approaches

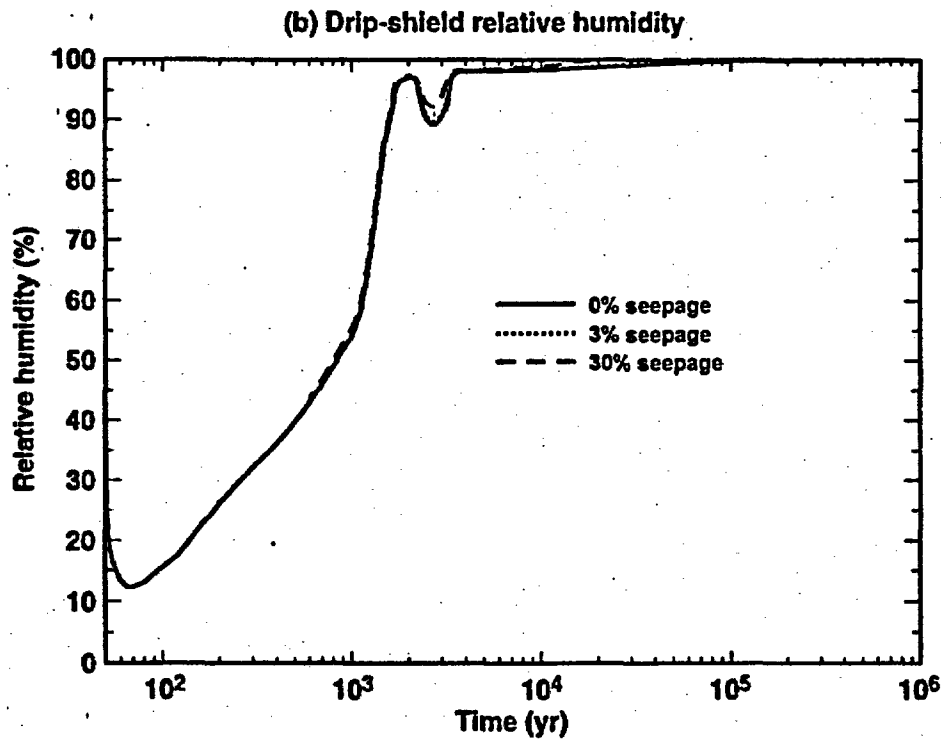
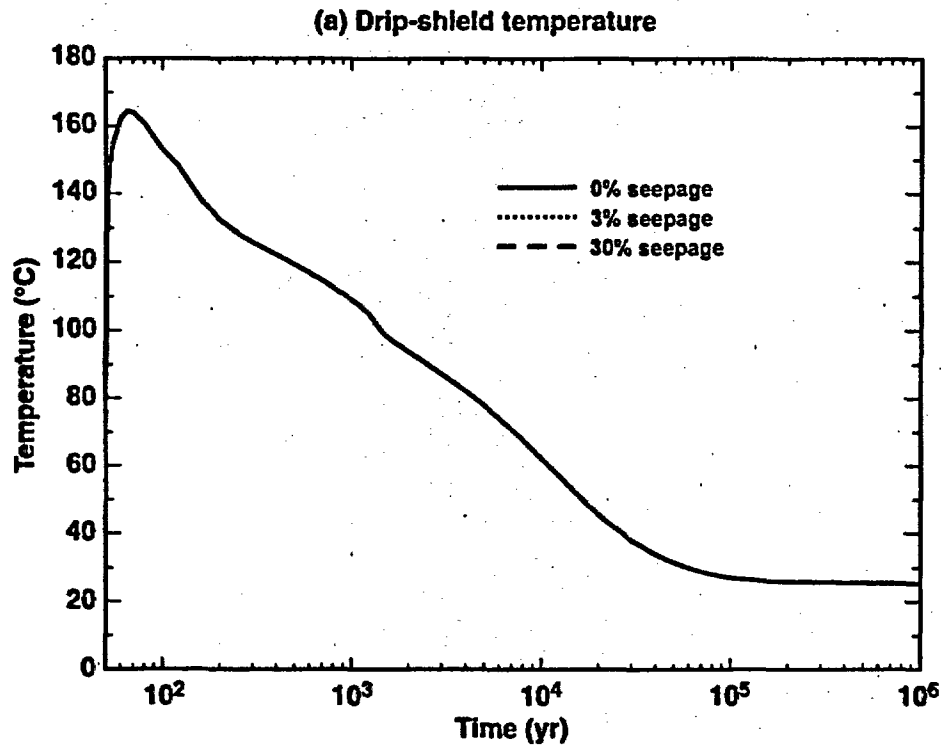
The models presented in this report represent an evolution from previous TH and TH seepage models (see Chapter 3 of Hardin 1998). Noteworthy changes relate to the representation of fracture-matrix interaction, with a dynamic coupling approach, called the Active Fracture Concept, now being used.

A useful alternative model is the 3-D discrete-heat-source, drift-scale thermohydrologic (DDTH) model with spatially heterogeneous fracture properties. The DDTH model could without prescribing seepage in the drift to investigate whether extreme examples of highly focussed percolation flux result in drift seepage during the boiling period. The DDTH model could also be run with prescribed seepage conditions in the drift as was done in the LDTH drift-seepage models described in this report. Whereas the LDTH drift-seepage models effectively assume a "line-averaged" seep, the DDTH drift-seepage model could be used to investigate the influence of "discrete" (or "point") seeps that are sparsely distributed along the axis of the drift.



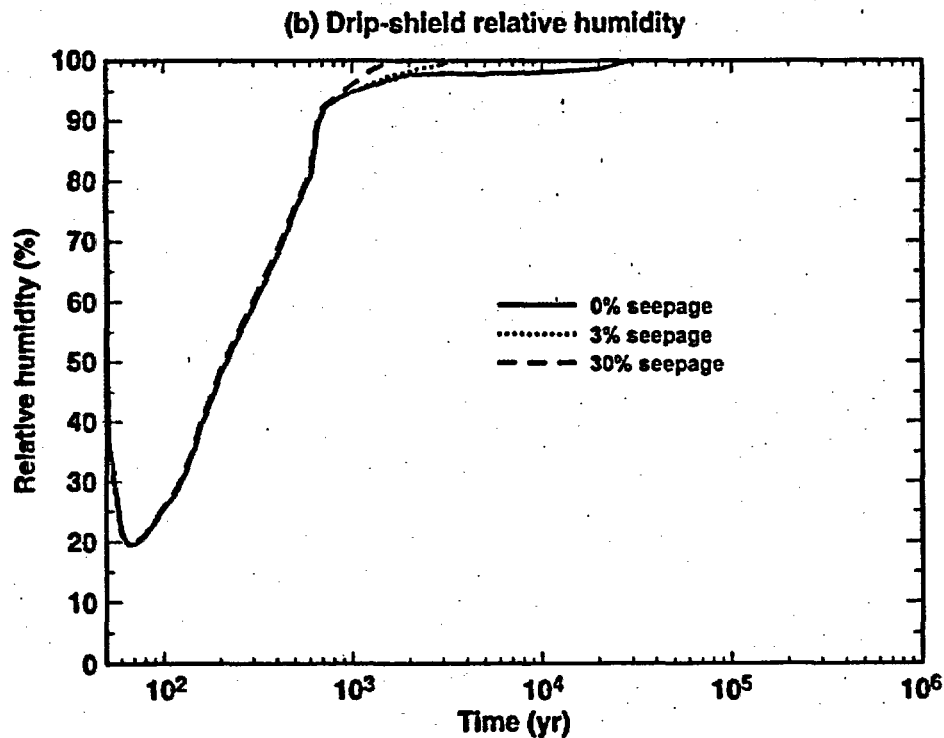
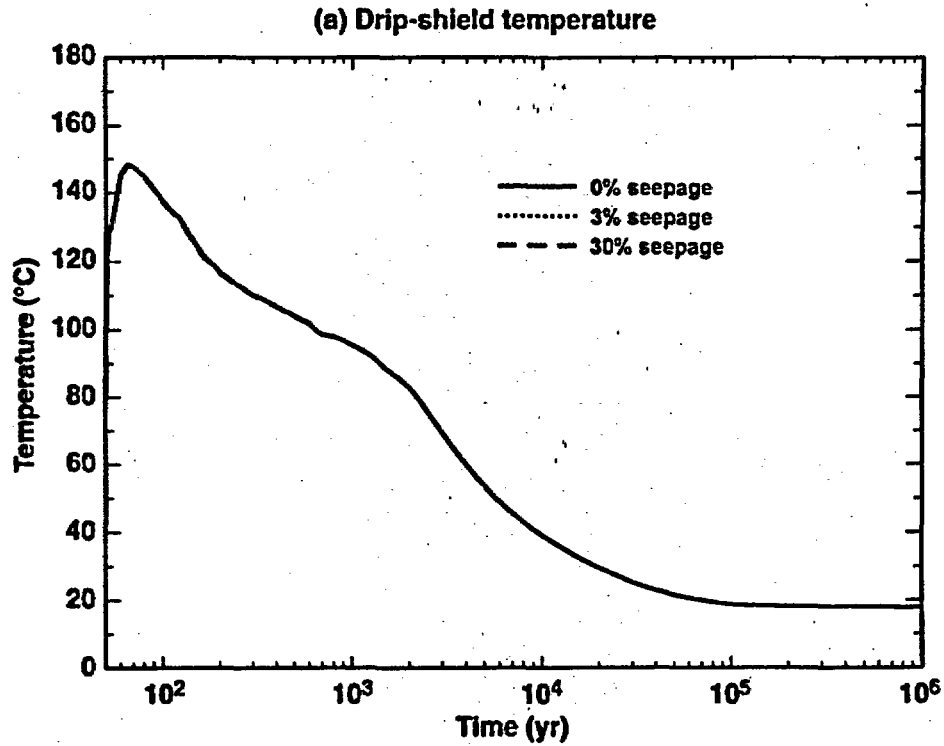
1&rhds_all-14c4-56-mi

Figure 6-34. Temperature (a) and Relative Humidity (b) Histories on the Drip Shield for the 14c4 Location, an AML of 56 MTU/acres, and the Mean Infiltration-Flux Distribution Are Plotted for the 0%, 3%, and 30% Seepage Cases



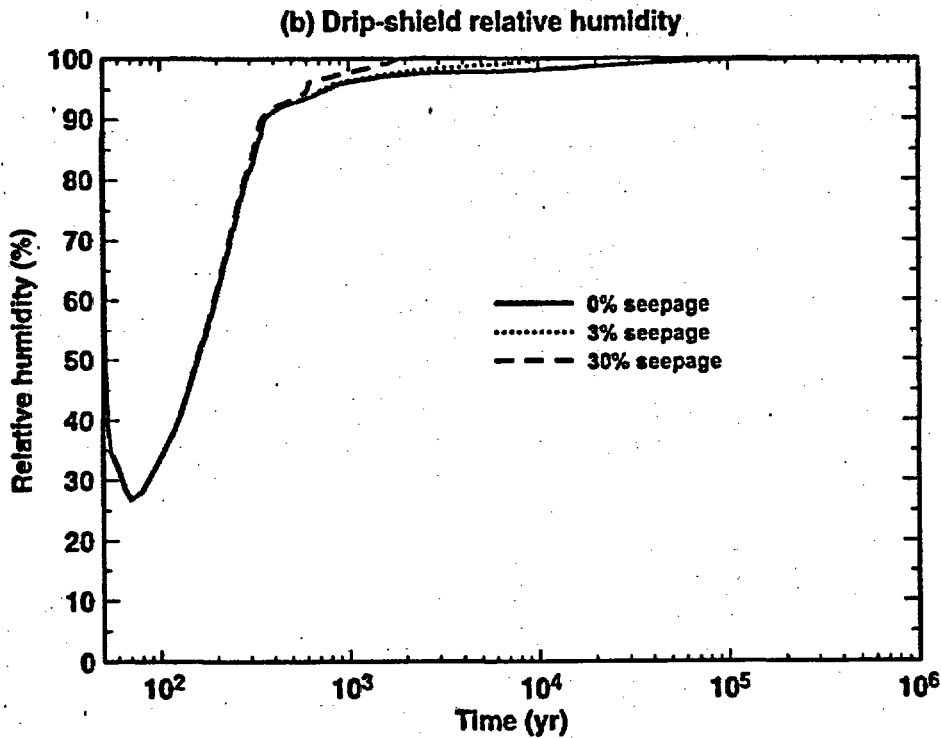
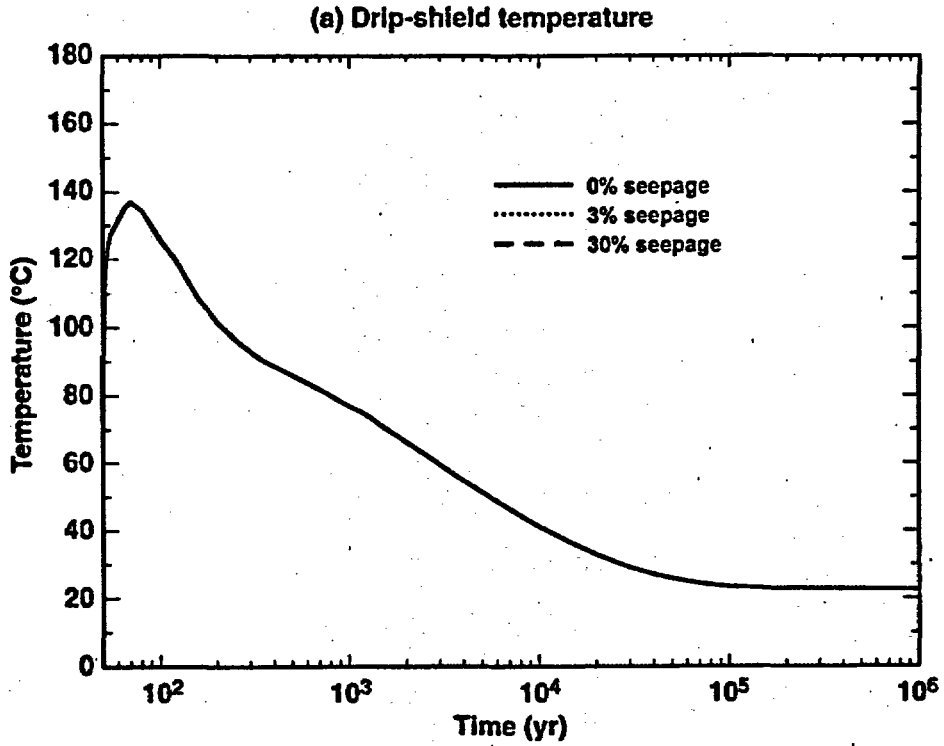
t&fnds_all-14c4-56-li

Figure 6-35. Temperature (a) and relative humidity (b) histories on the drip shield for the 14c4 location, an AML of 56 MTU/acres, and the "lower" infiltration-flux distribution are plotted for the 0%, 3%, and 30% seepage cases



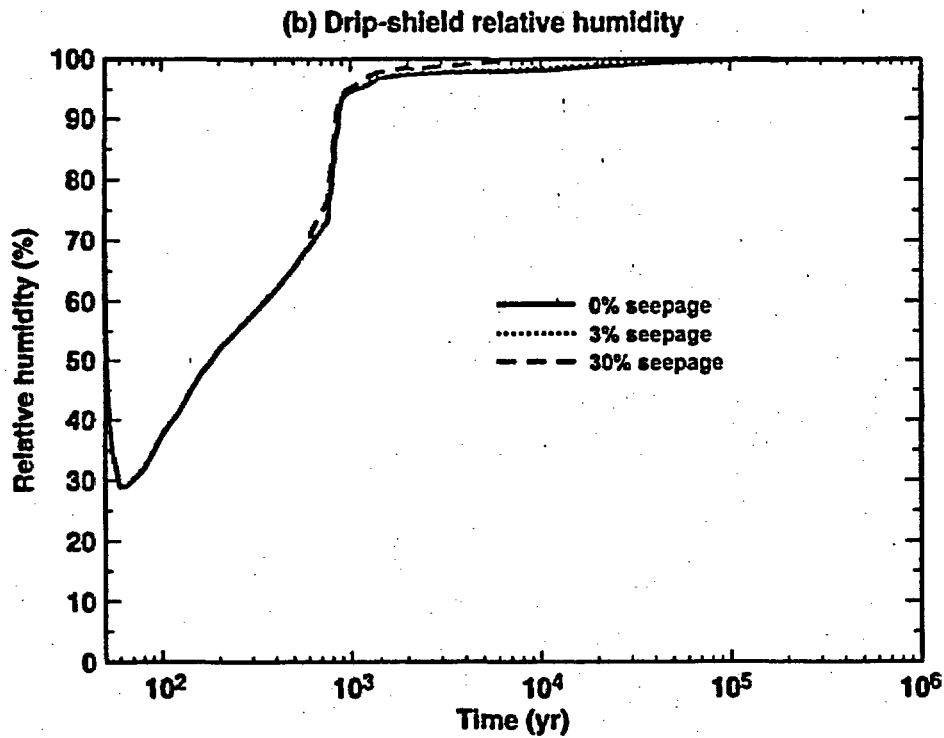
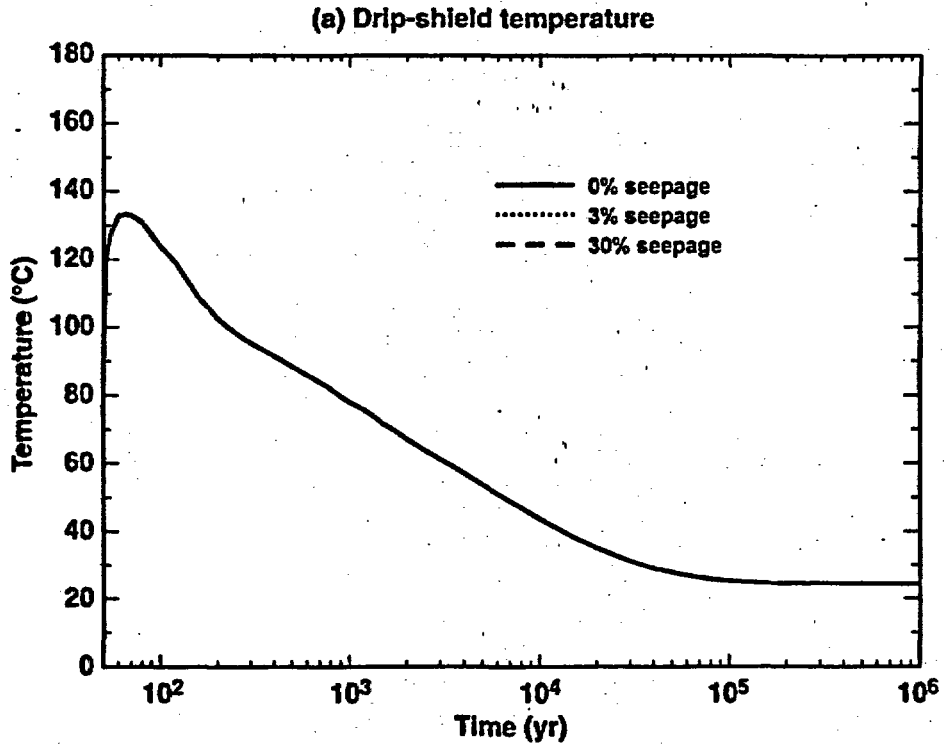
t&rhds_all-14c4-56-ui

Figure 6-36. Temperature (a) and relative humidity (b) histories on the drip shield for the 14c4 location, an AML of 56 MTU/acres, and the "upper" infiltration-flux distribution are plotted for the 0%, 3%, and 30% seepage cases



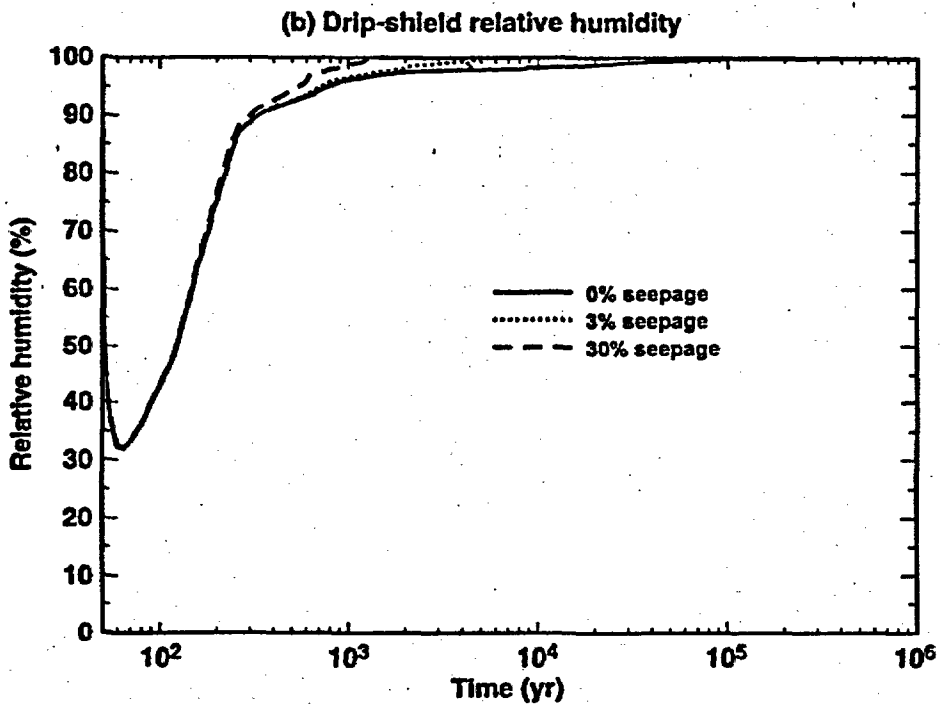
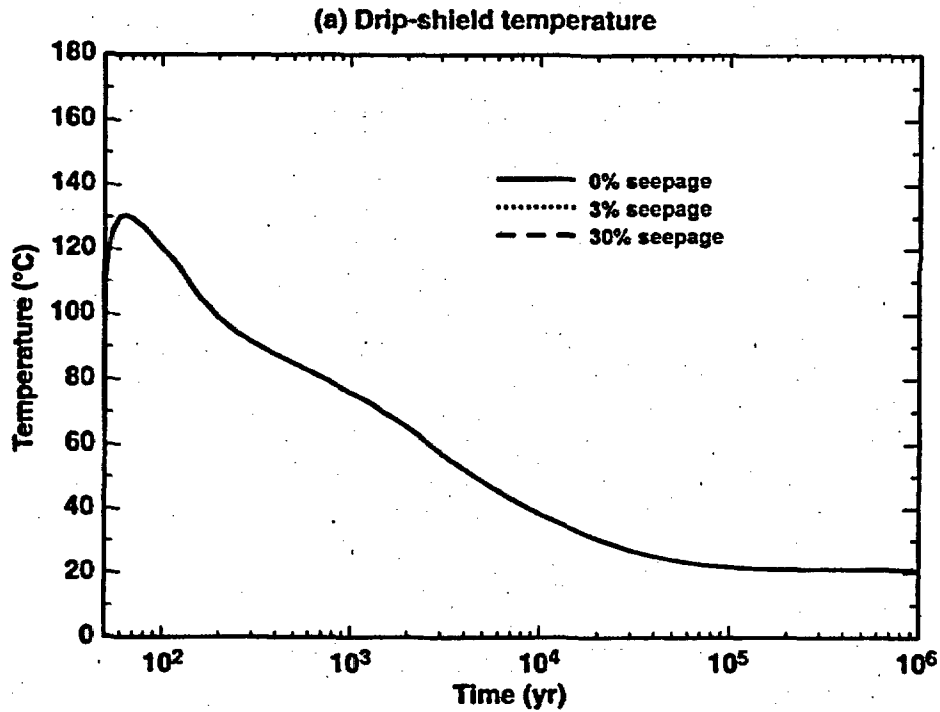
t&rhds_all-14c1-34-mi

Figure 6-37. Temperature (a) and relative humidity (b) histories on the drip shield for the 14c1 location, an AML of 34 MTU/acres, and the mean infiltration-flux distribution are plotted for the 0%, 3%, and 30% seepage cases



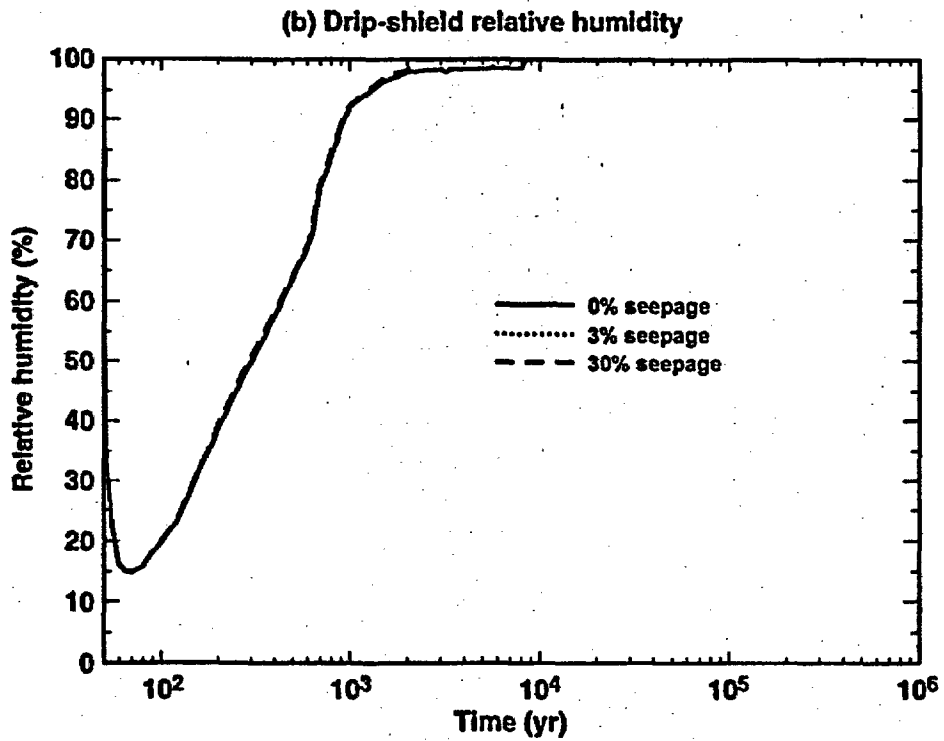
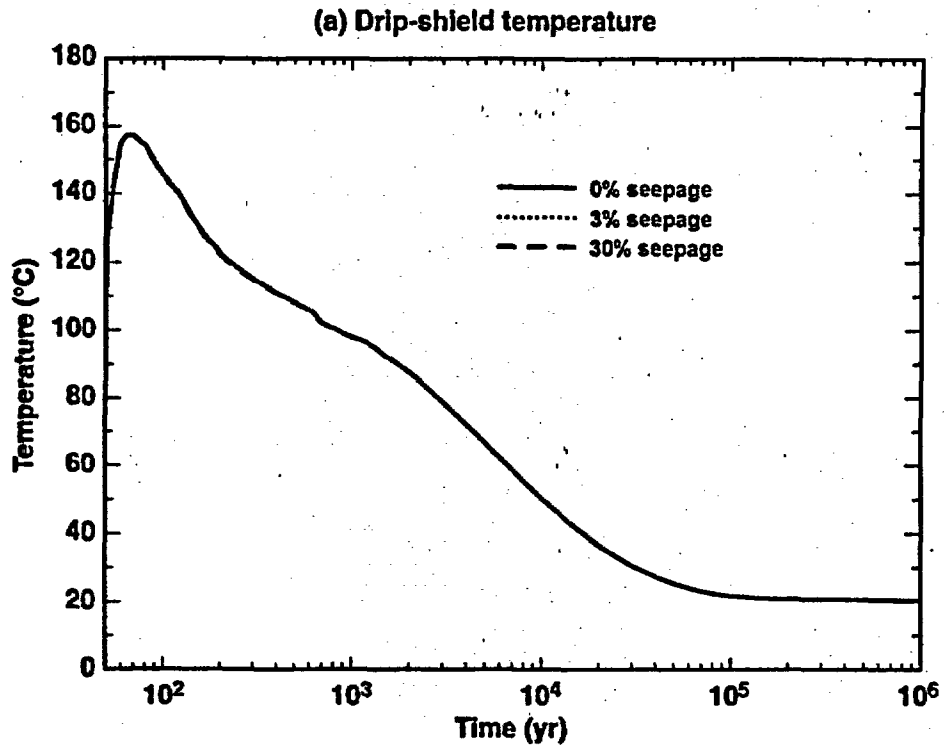
l&rhds_all-14c1-34-li

Figure 6-38. Temperature (a) and relative humidity (b) histories on the drip shield for the 14c1 location, an AML of 34 MTU/acres, and the "lower" infiltration-flux distribution are plotted for the 0%, 3%, and 30% seepage cases



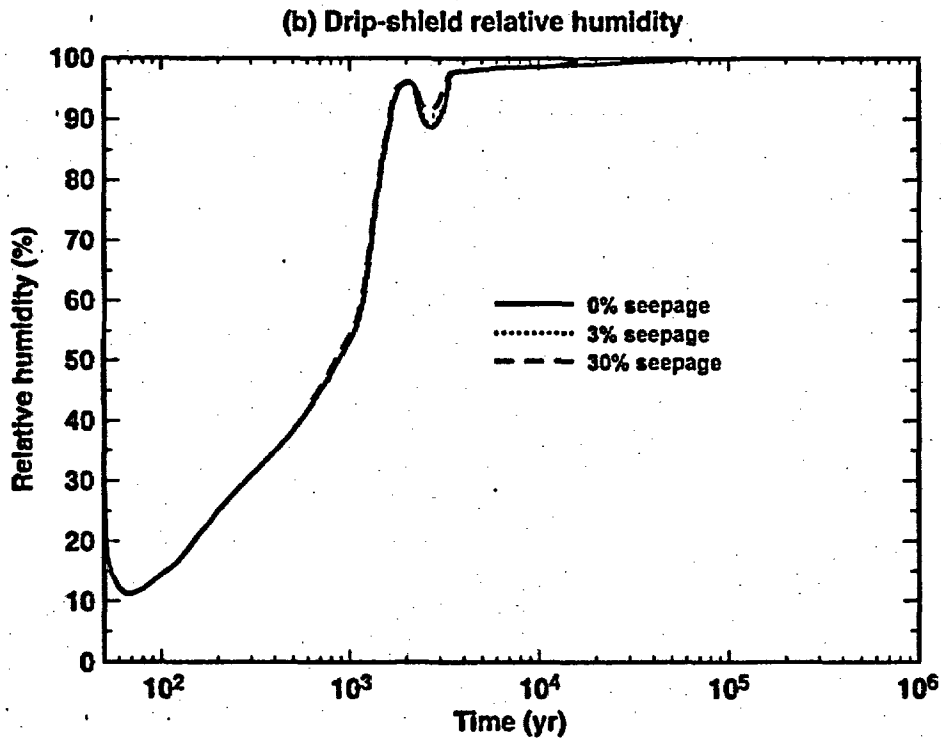
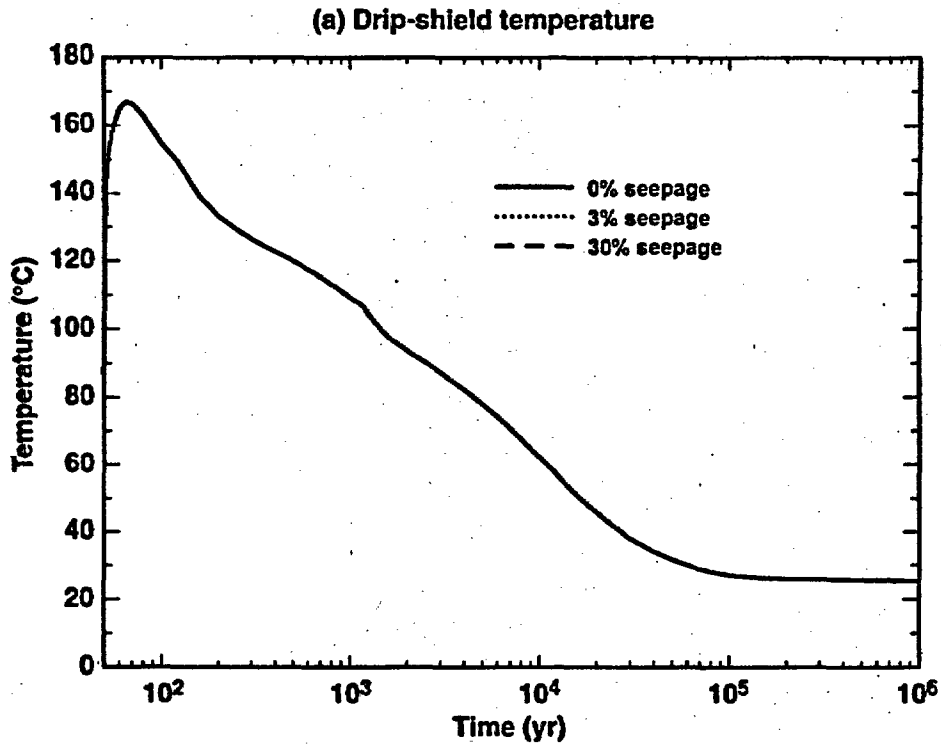
l&rhds_all-14c1-34-ui

Figure 6-39. Temperature (a) and relative humidity (b) histories on the drip shield for the l4c1 location, an AML of 34 MTU/acres, and the "upper" infiltration-flux distribution are plotted for the 0%, 3%, and 30% seepage cases



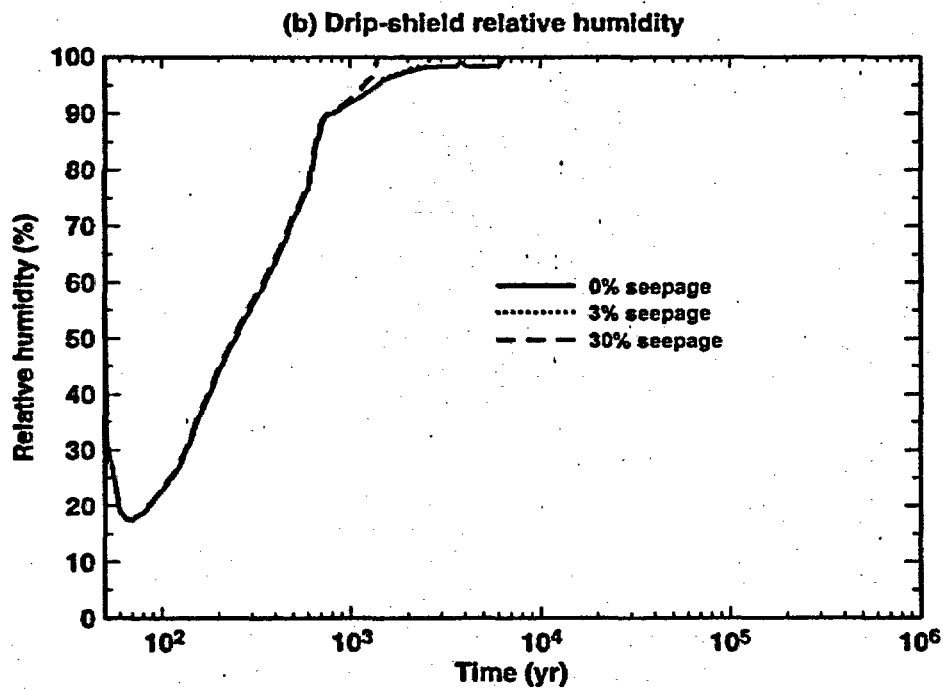
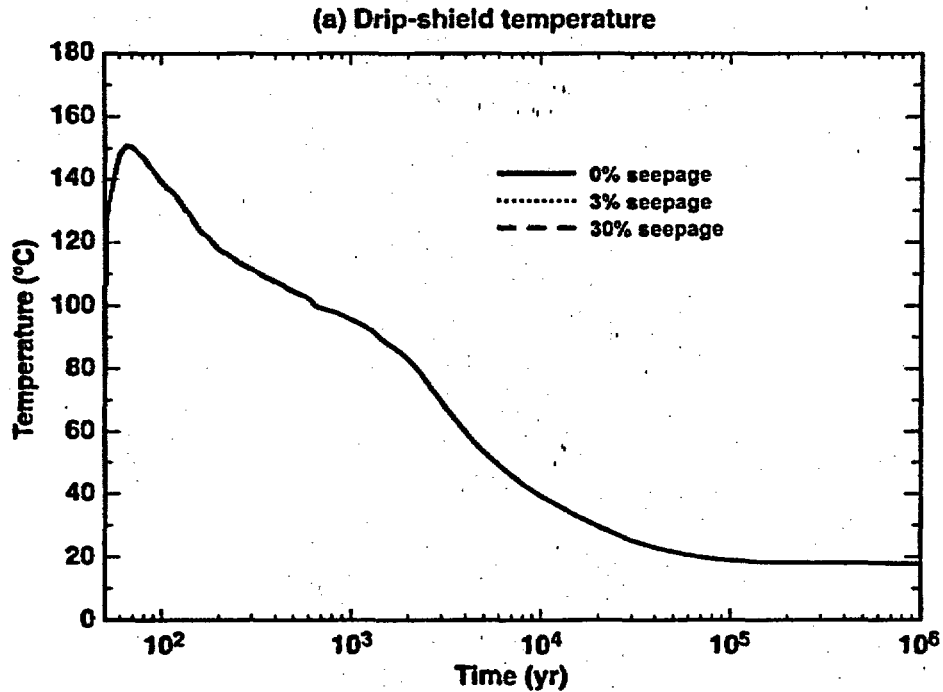
t&rhin_all-14c4-56-mi

Figure 6-40. Temperature (a) and relative humidity (b) histories in the upper invert below the WP for the 14c4 location, an AML of 56 MTU/acres, and the mean infiltration-flux distribution are plotted for the 0%, 3%, and 30% seepage cases



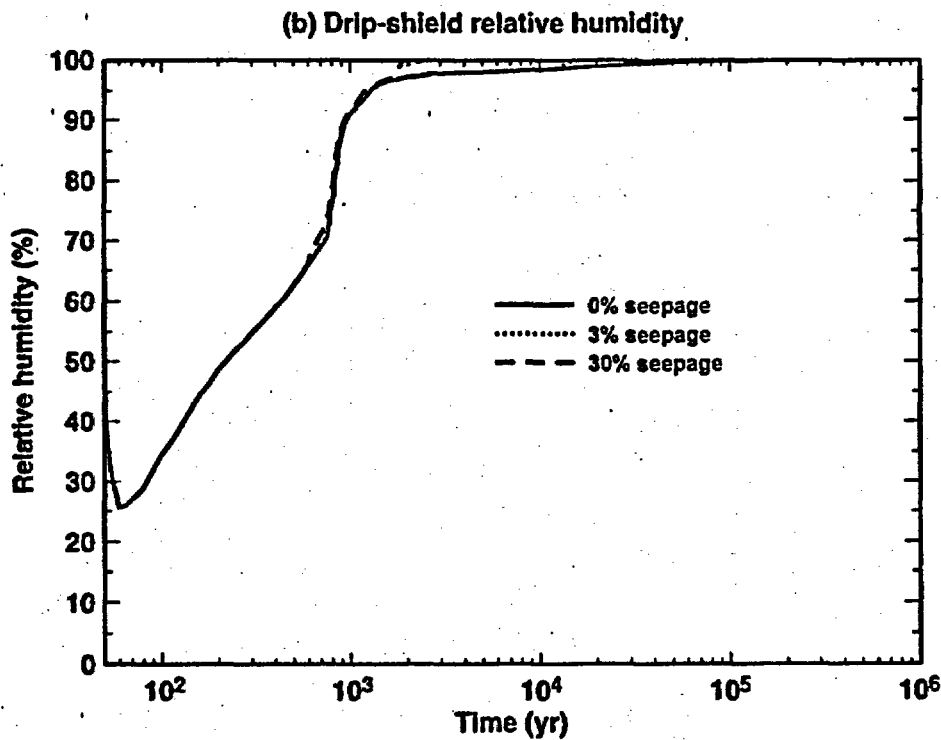
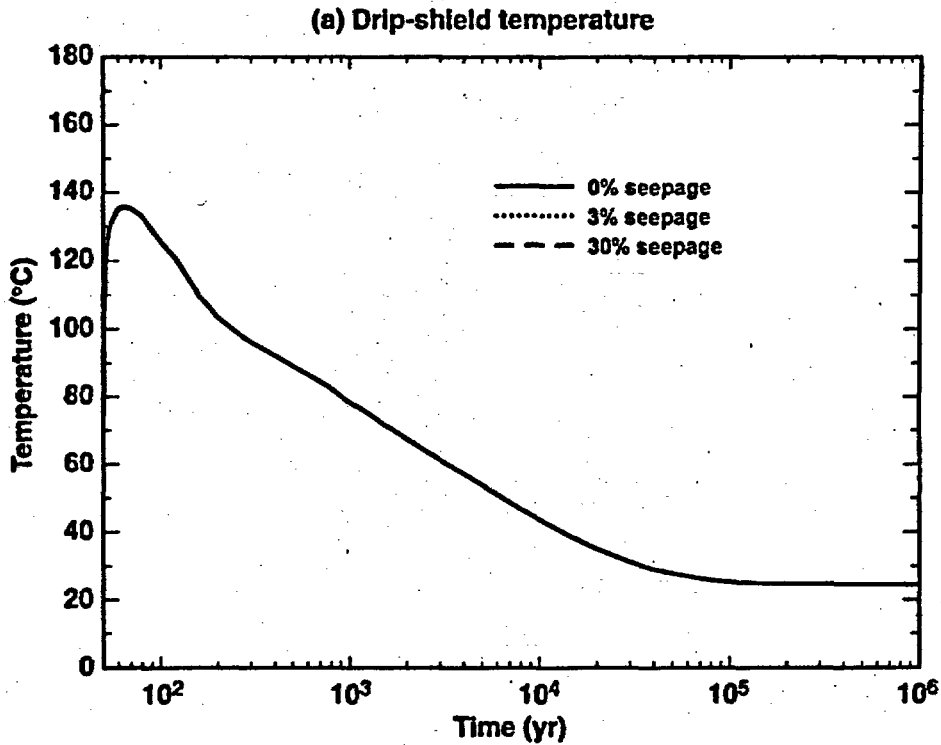
t&rhin_atl-14c4-56-li

Figure 6-41. Temperature (a) and relative humidity (b) histories in the upper invert below the WP for the 14c4 location, an AML of 56 MTU/acres, and the "lower" infiltration-flux distribution are plotted for the 0%, 3%, and 30% seepage cases



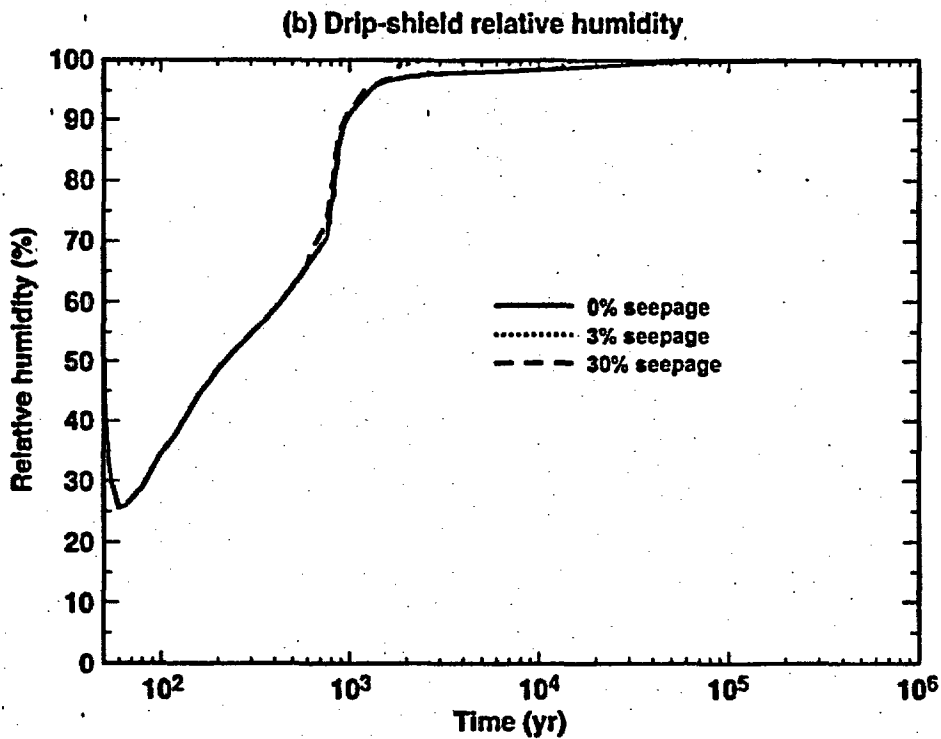
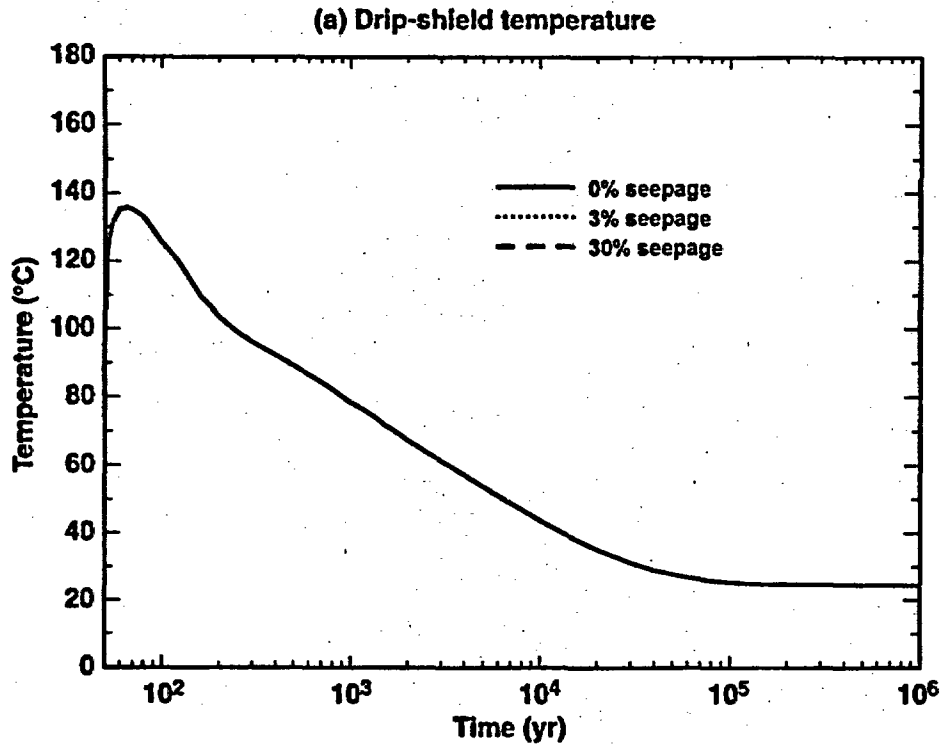
t&rhin_all-14c4-56-ul

Figure 6-42. Temperature (a) and relative humidity (b) histories in the upper invert below the WP for the 14c4 location, an AML of 56 MTU/acres, and the "upper" infiltration-flux distribution are plotted for the 0%, 3%, and 30% seepage cases



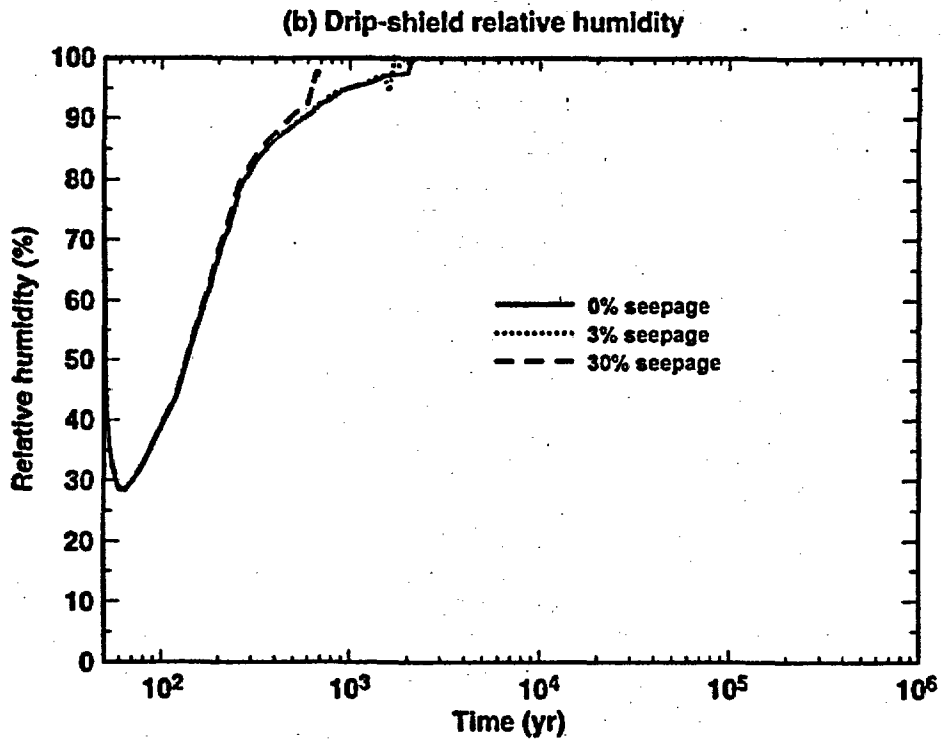
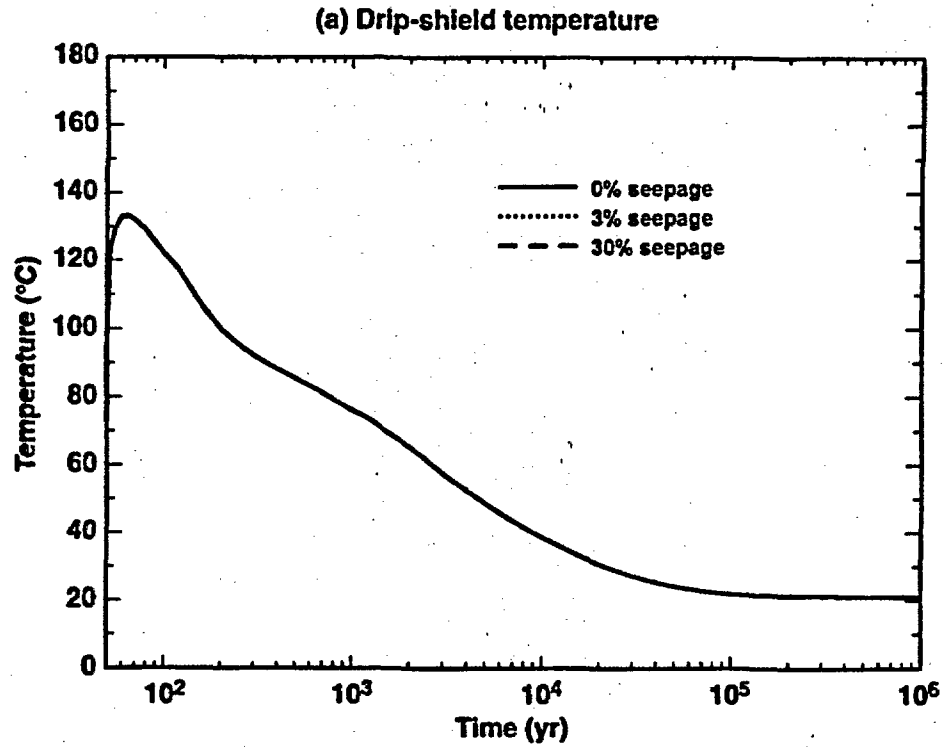
l&min_all-14c1-34-mi

Figure 6-43. Temperature (a) and relative humidity (b) histories in the upper invert below the WP for the 14c1 location, an AML of 34 MTU/acres, and the mean infiltration-flux distribution are plotted for the 0%, 3%, and 30% seepage cases



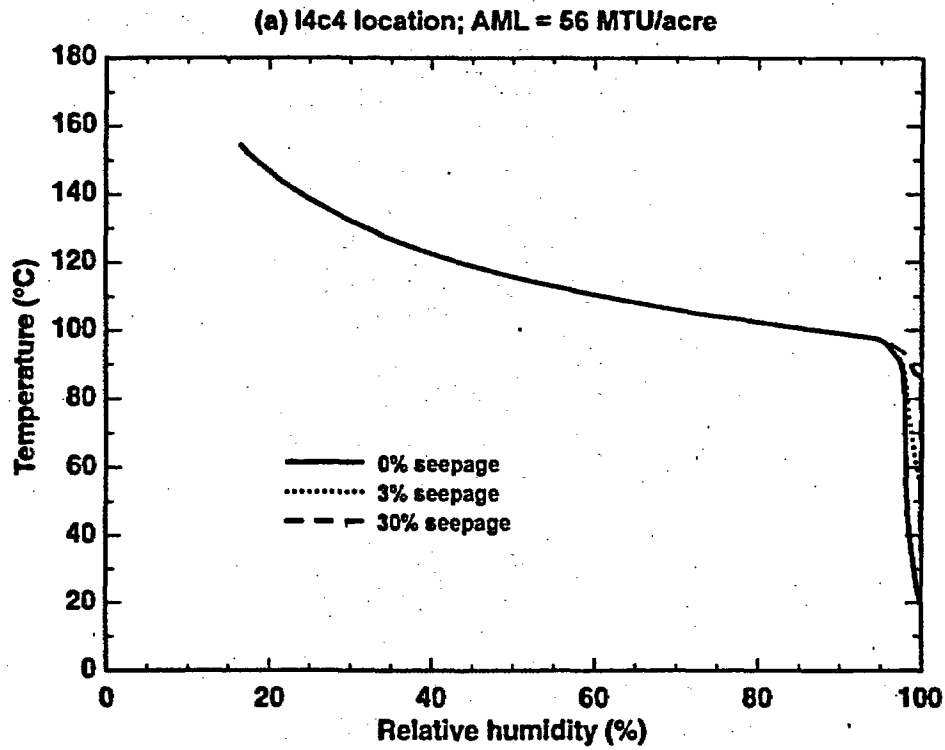
t&rhin_all-14c1-34-li

Figure 6-44. Temperature (a) and relative humidity (b) histories in the upper invert below the WP for the 14c1 location, an AML of 34 MTU/acres, and the "lower" infiltration-flux distribution are plotted for the 0%, 3%, and 30% seepage cases

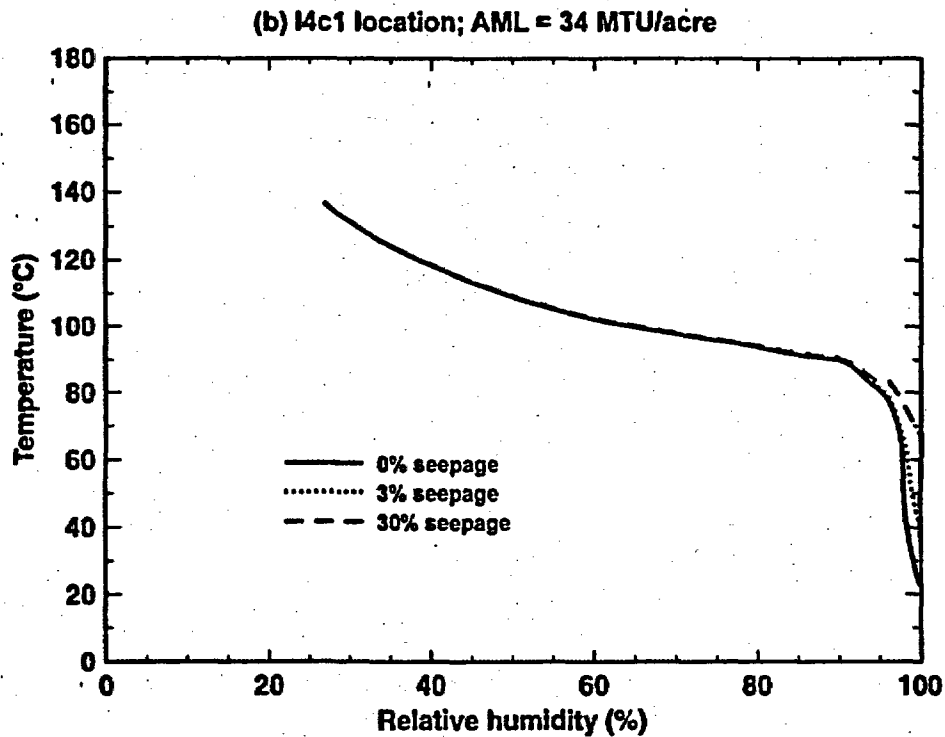


t&rhin_all-14c1-34-ui

Figure 6-45. Temperature (a) and relative humidity (b) histories in the upper invert below the WP for the 14c1 location, an AML of 34 MTU/acres, and the "upper" infiltration-flux distribution are plotted for the 0%, 3%, and 30% seepage cases

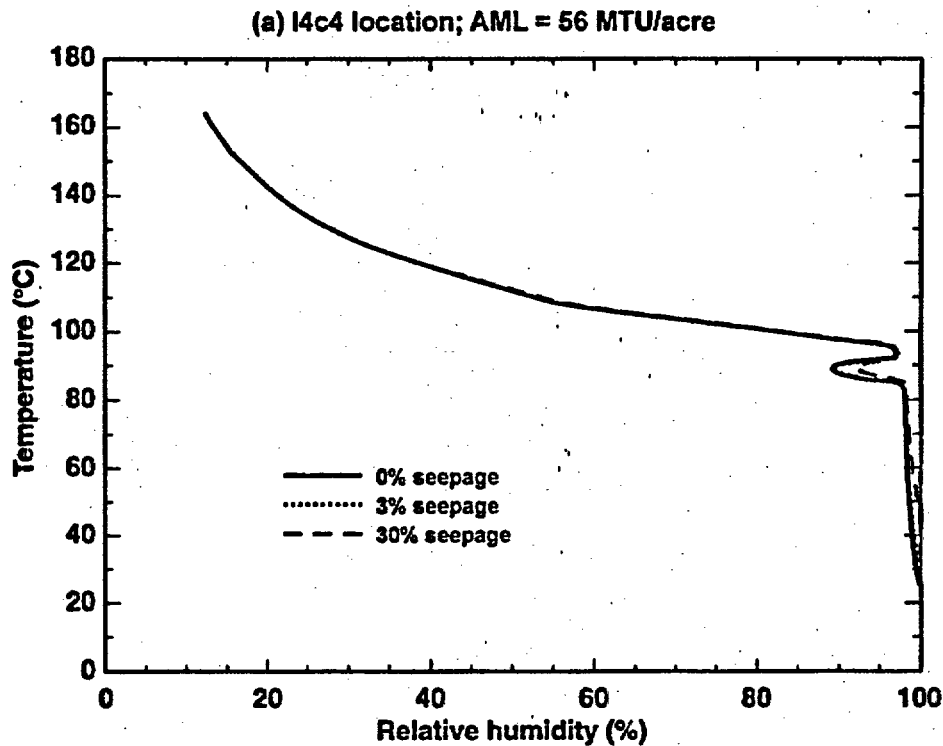


trh_all-14c4-LDTH56-mi

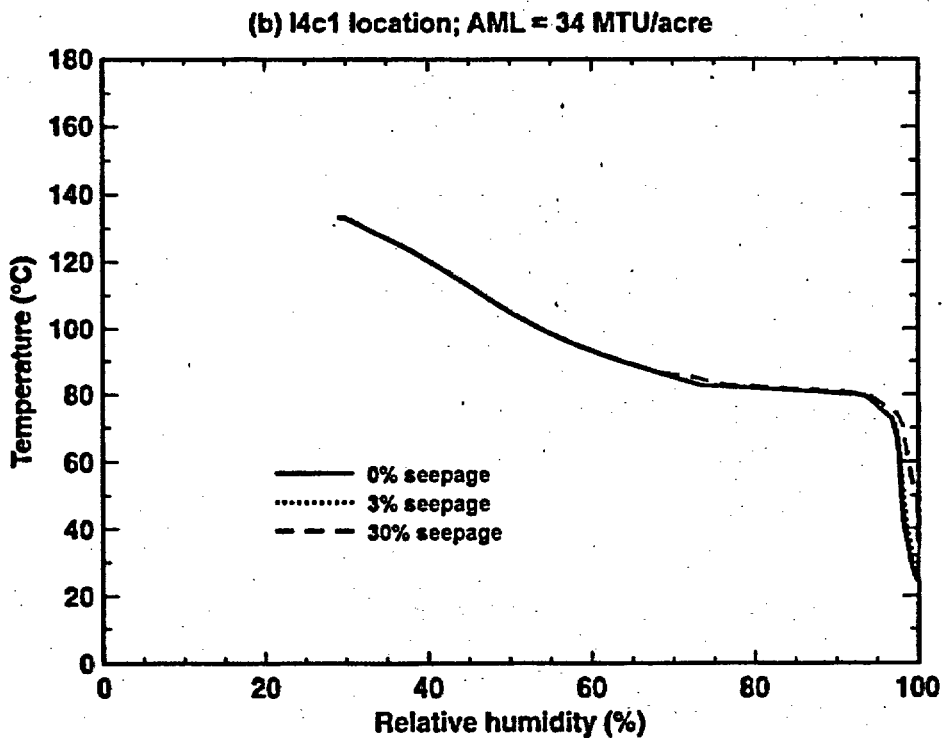


trh_all-14c1-LDTH34-mi

Figure 6-46. (a) Drip-shield temperature versus drip-shield relative humidity for the I4c4 location, an AML of 56 MTU/acres, and the mean infiltration-flux distribution is plotted for the 0%, 3%, and 30% seepage cases. (b) The same is plotted for the I4c1 location and an AML of 34 MTU/acre

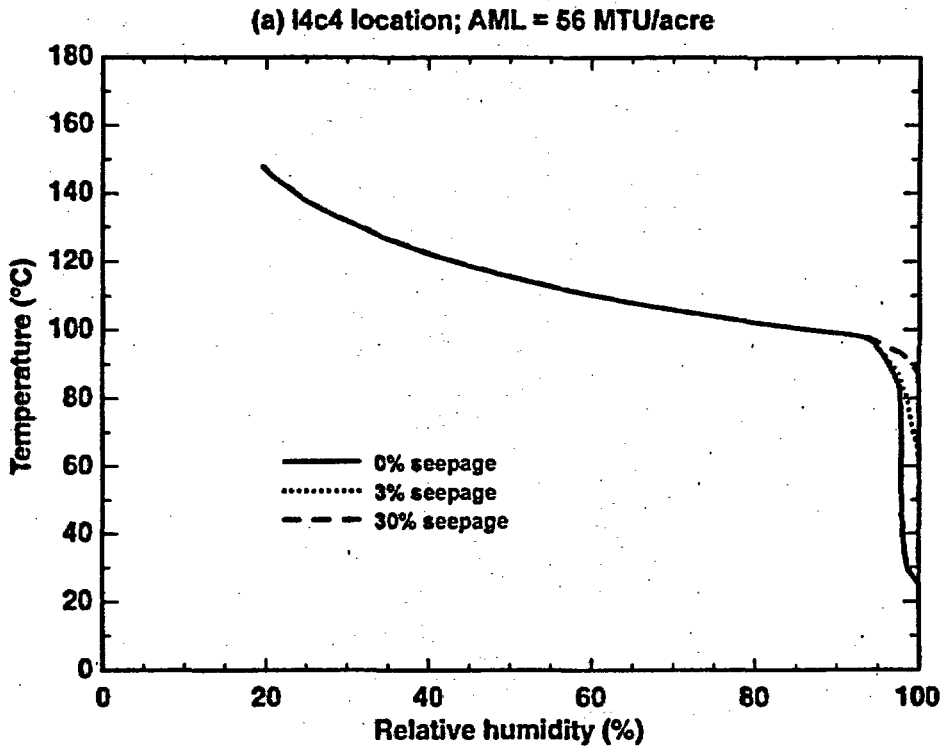


trh_all-14c4-LDTH56-II

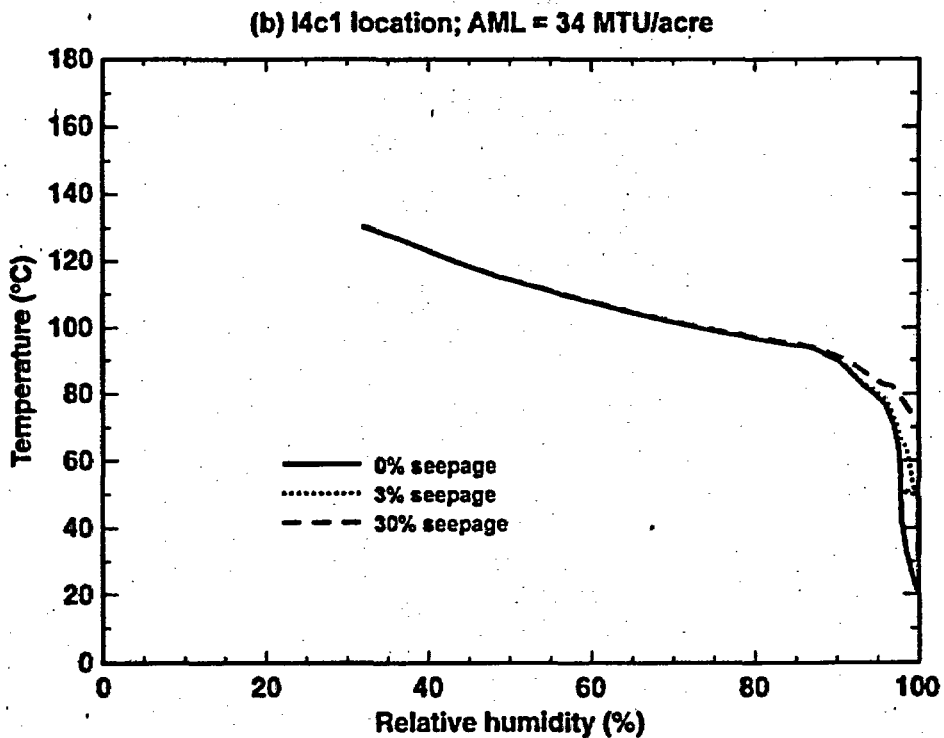


trh_all-14c1-LDTH34-II

Figure 6-47. (a) Drip-shield temperature versus drip-shield relative humidity for the I4c4 location, an AML of 56 MTU/acres, and the "lower" infiltration-flux distribution is plotted for the 0%, 3%, and 30% seepage cases. (b) The same is plotted for the I4c1 location and an AML of 34 MTU/acre



trh_all-14c4-LDTH56-ui



trh_all-14c1-LDTH34-ui

Figure 6-48. (a) Drip-shield temperature versus drip-shield relative humidity for the I4c4 location, an AML of 56 MTU/acres, and the "upper" infiltration-flux distribution is plotted for the 0%, 3%, and 30% seepage cases. (b) The same is plotted for the I4c1 location and an AML of 34 MTU/acre

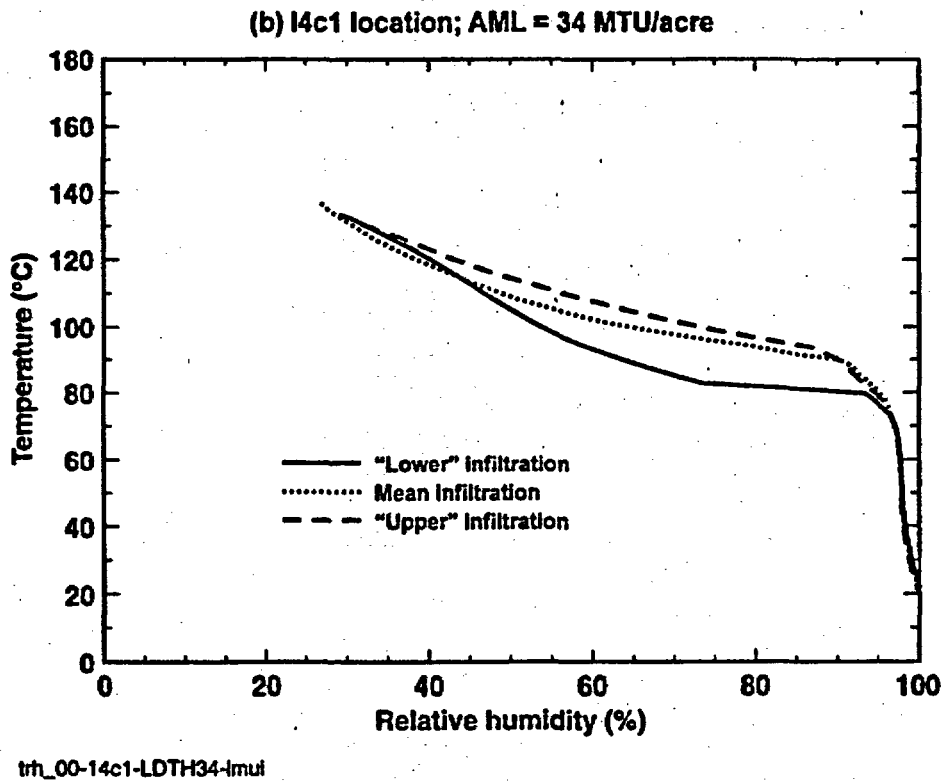
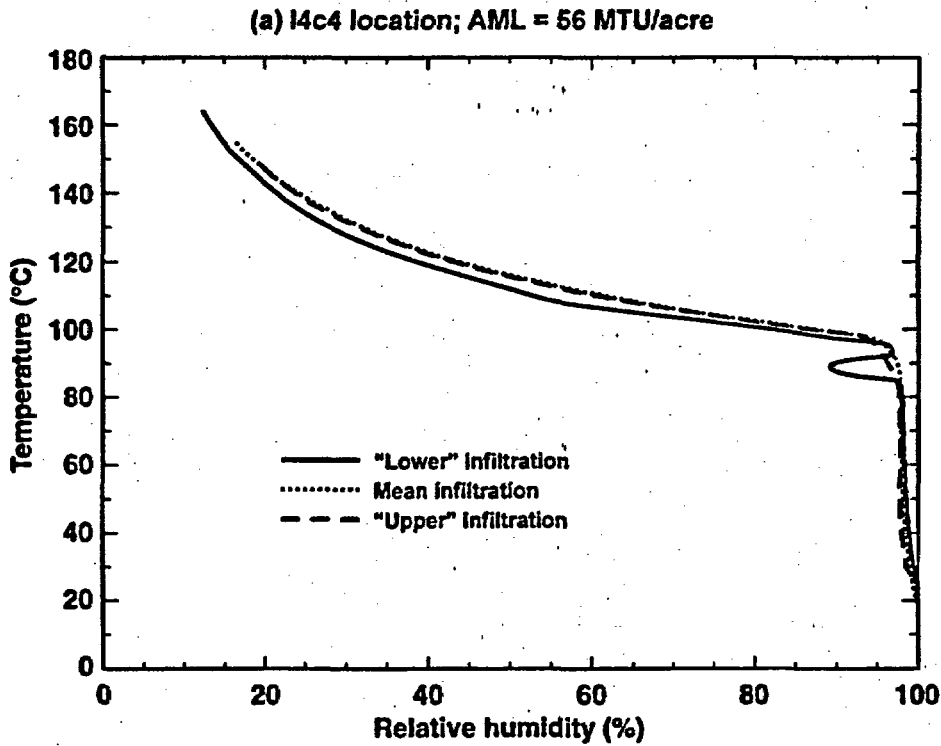


Figure 6-49. (a) Drip-shield temperature versus drip-shield relative humidity for the I4c4 location, an AML of 56 MTU/acres, and the 0% seepage case is plotted for "lower", mean, and "upper" infiltration-flux distributions. (b) The same is plotted for the I4c1 location and an AML of 34 MTU/acre

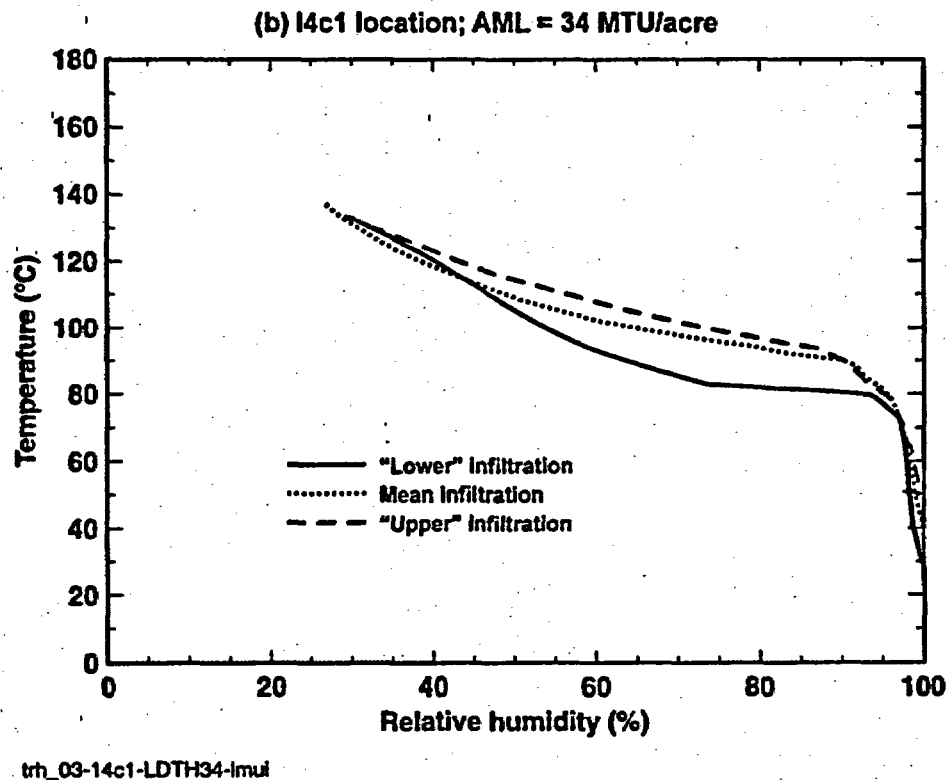
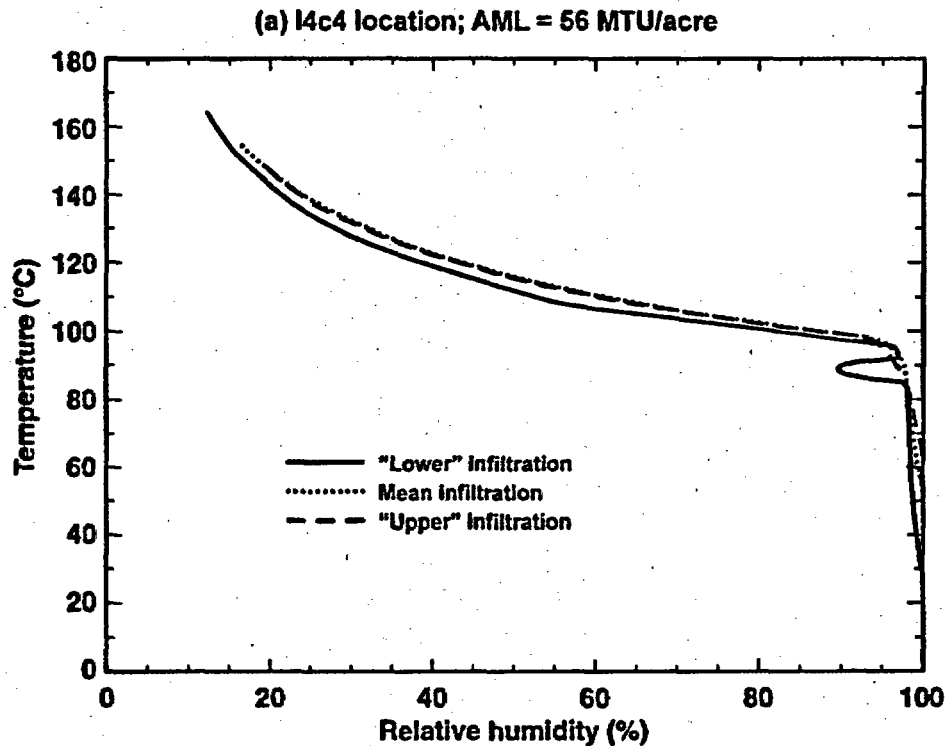
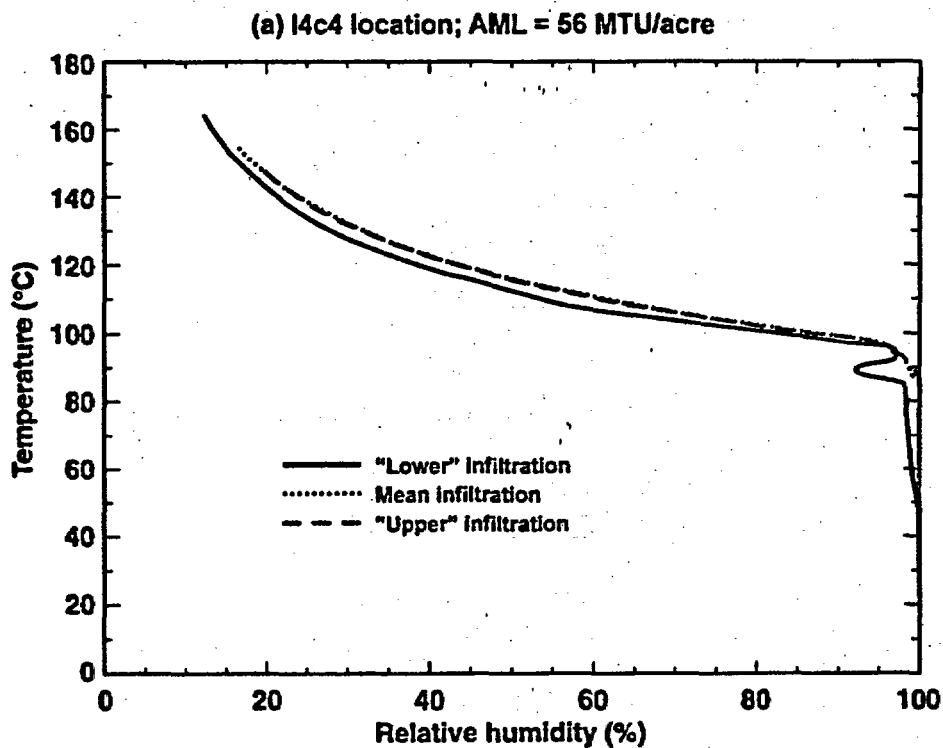
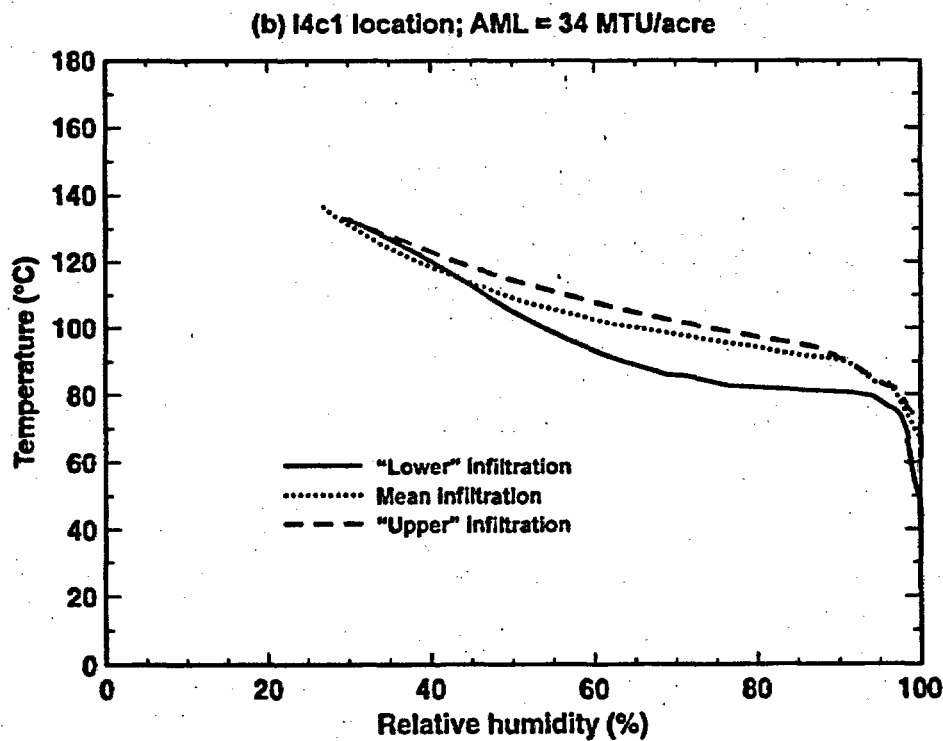


Figure 6-50. (a) Drip-shield temperature versus drip-shield relative humidity for the I4c4 location, an AML of 56 MTU/acres, and the 3% seepage case is plotted for "lower", mean, and "upper" infiltration-flux distributions. (b) The same is plotted for the I4c1 location and an AML of 34 MTU/acre

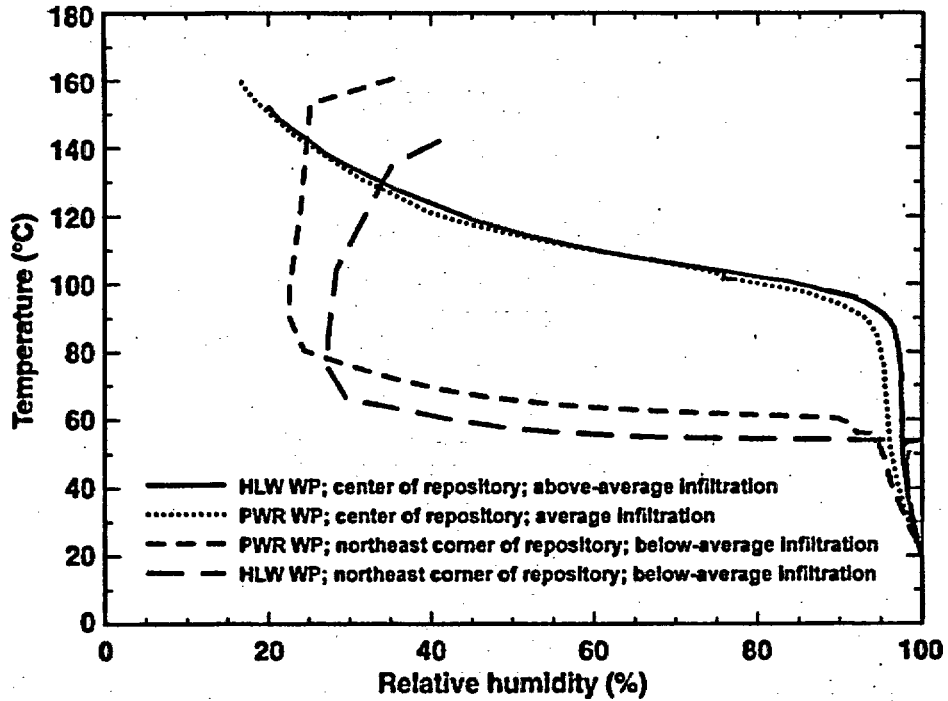


trh_30-14c4-LDTH56-lmui



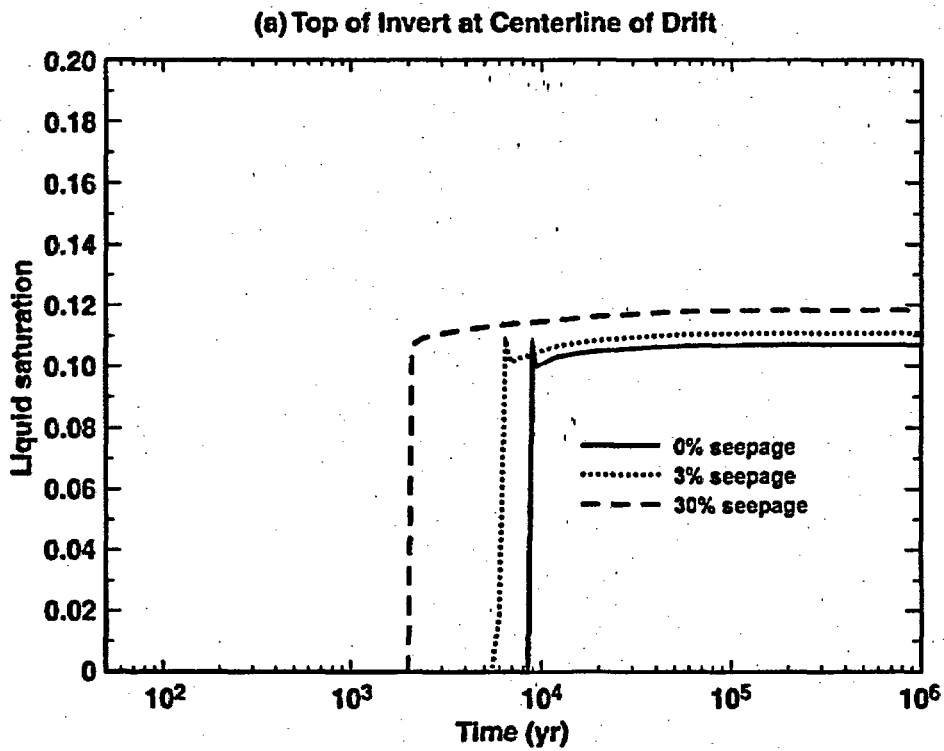
trh_30-14c1-LDTH34-lmui

Figure 6-51. (a) Drip-shield temperature versus drip-shield relative humidity for the I4c4 location, an AML of 56 MTU/acres, and the 30% seepage case is plotted for "lower", mean, and "upper" infiltration-flux distributions. (b) The same is plotted for the I4c1 location and an AML of 34 MTU/acre

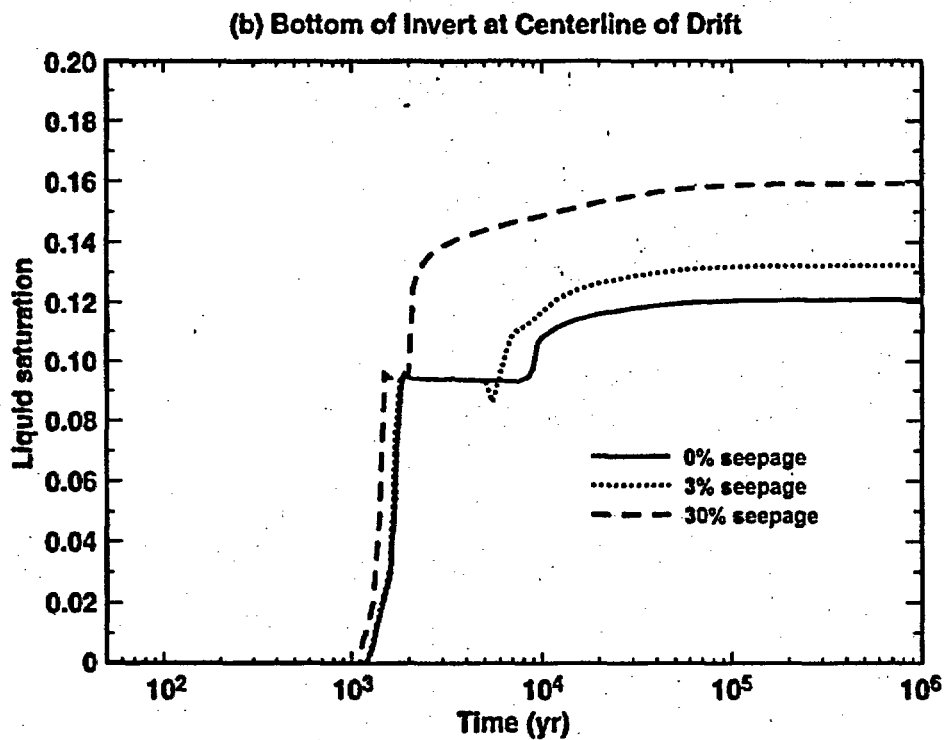


trh_all-msthac

Figure 6-52. Drip-shield temperature versus drip-shield relative humidity is plotted for three geographic locations and two WP types, resulting in four combinations of locations and WP types. These plots are obtained from the Multiscale Thermohydrologic Model calculations (CRWMS M&O 2000i) for the mean-infiltration-flux no-backfill case (DTN LLL000509112312.003; file: TSPA_SR00nbf_mean_Infiltration.ext)

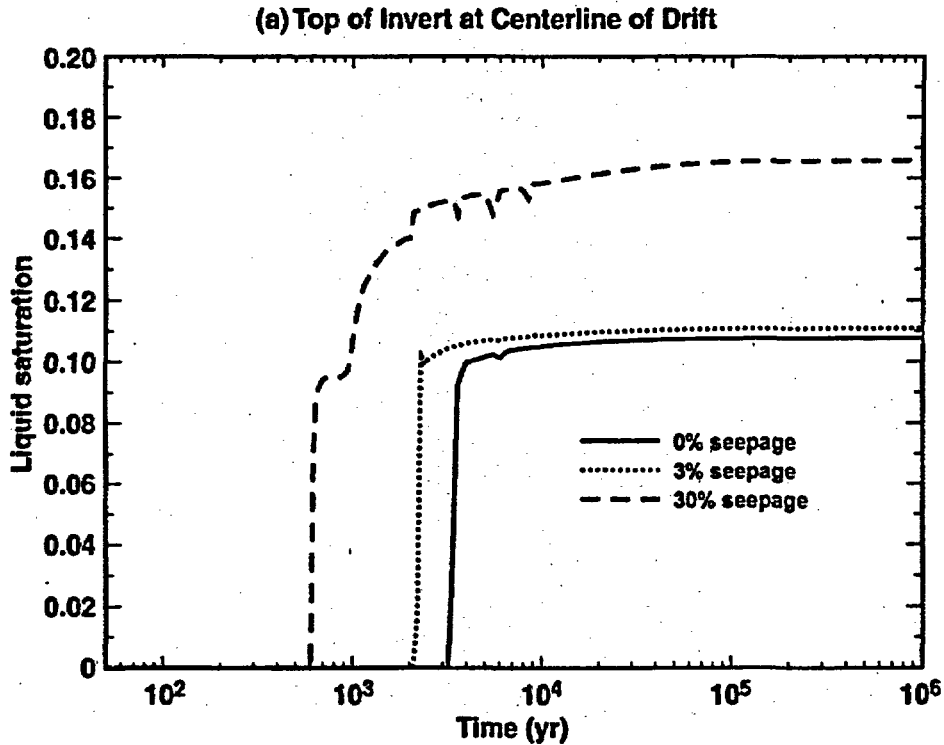


sl_topinv-all-14c4-56-mi

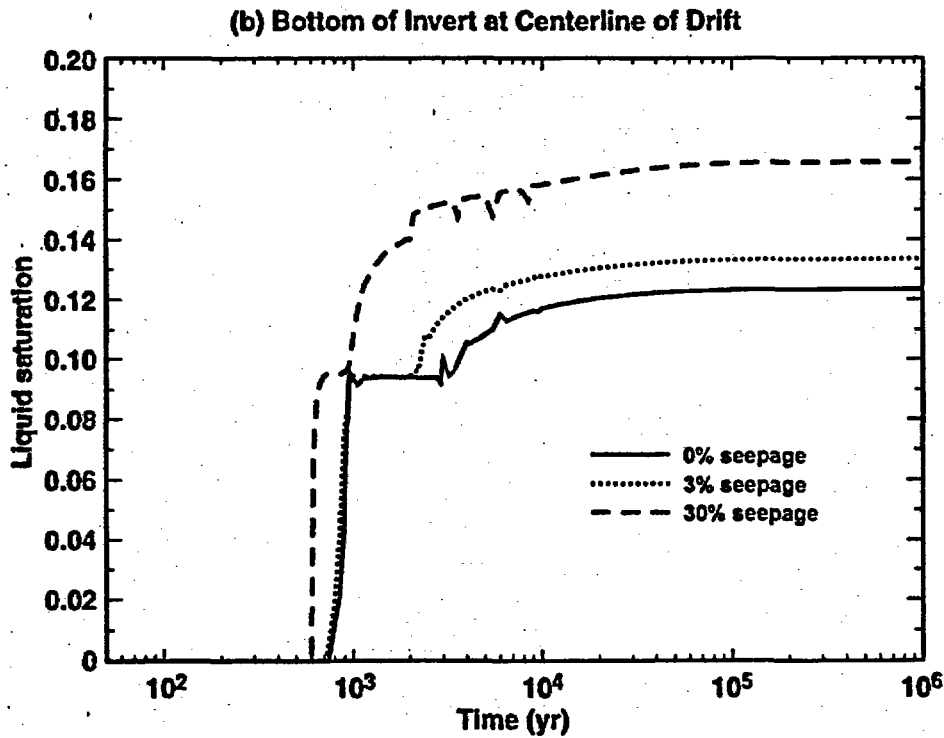


sl_botinv-all-14c4-56-mi

Figure 6-53. Liquid saturation at (a) the top of the invert and (b) the bottom of the invert at the centerline of the drift for the 14c4 location, an AML of 56 MTU/acres, and the mean infiltration-flux distribution is plotted for the 0%, 3%, and 30% seepage cases

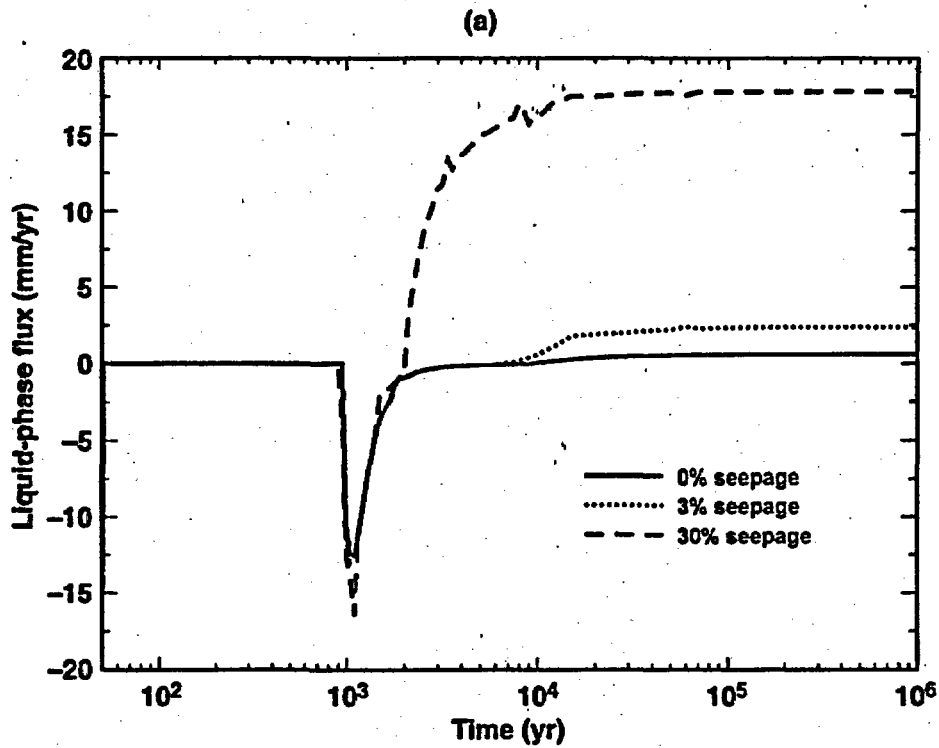


sl_topinv-all-14c1-34-mi

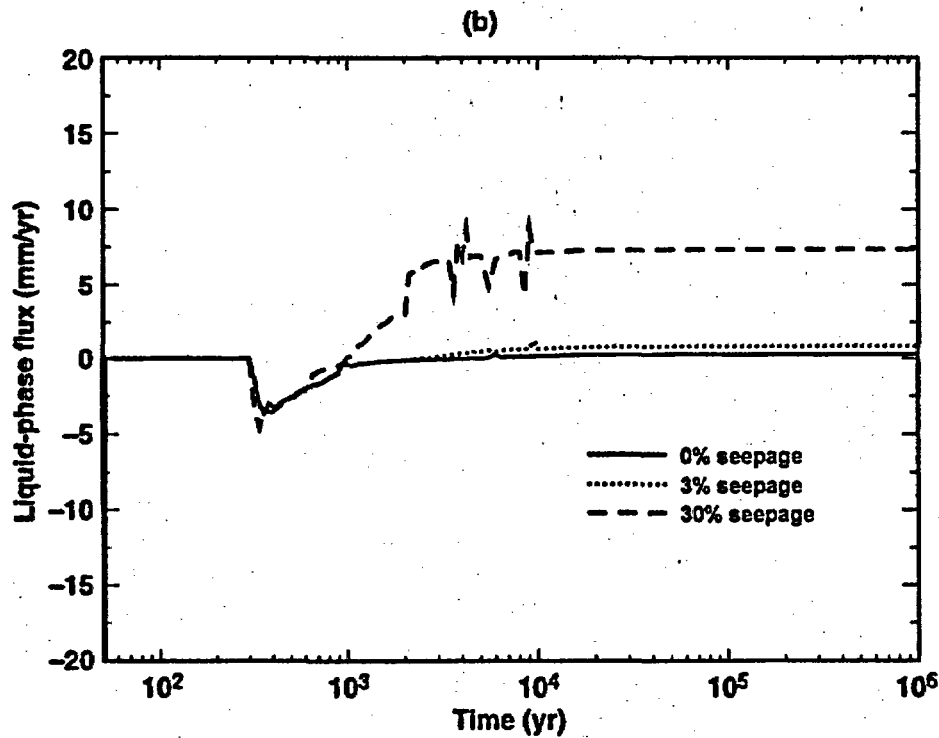


sl_botinv-all-14c1-34-mi

Figure 6-54. Liquid saturation at (a) the top of the invert and (b) the bottom of the invert at the centerline of the drift for the 14c1 location, an AML of 34 MTU/acres, and the mean infiltration-flux distribution is plotted for the 0%, 3%, and 30% seepage cases



qliq-inv-hstrk-I4c1-56-mi



qliq-inv-hstrk-I4c1-34-mi

Figure 6-55. (a) Liquid-phase flux at the bottom of the invert at the centerline of the drift for the I4c4 location, an AML of 56 MTU/acre, and the mean infiltration-flux distribution is plotted for the 0%, 3%, and 30% seepage cases. (b) The same is plotted for the I4c1 location and an AML of 34 MTU/acre

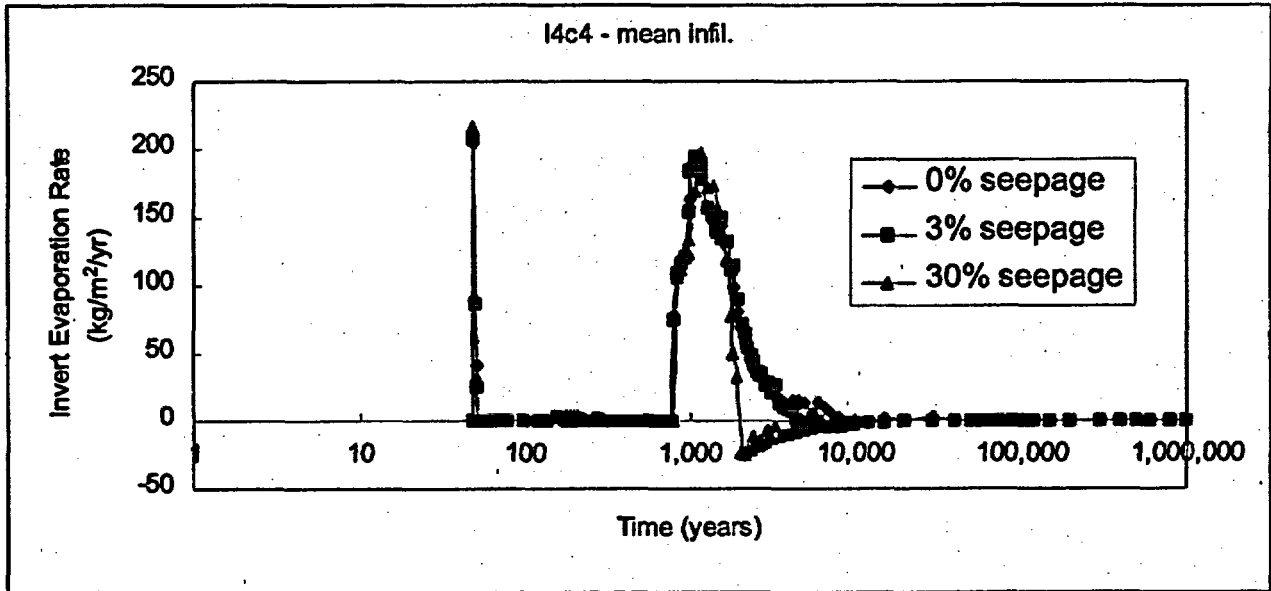


Figure 6-56. Evaporation Rate at the Invert for I4c4 Location with Mean Infiltration Distribution

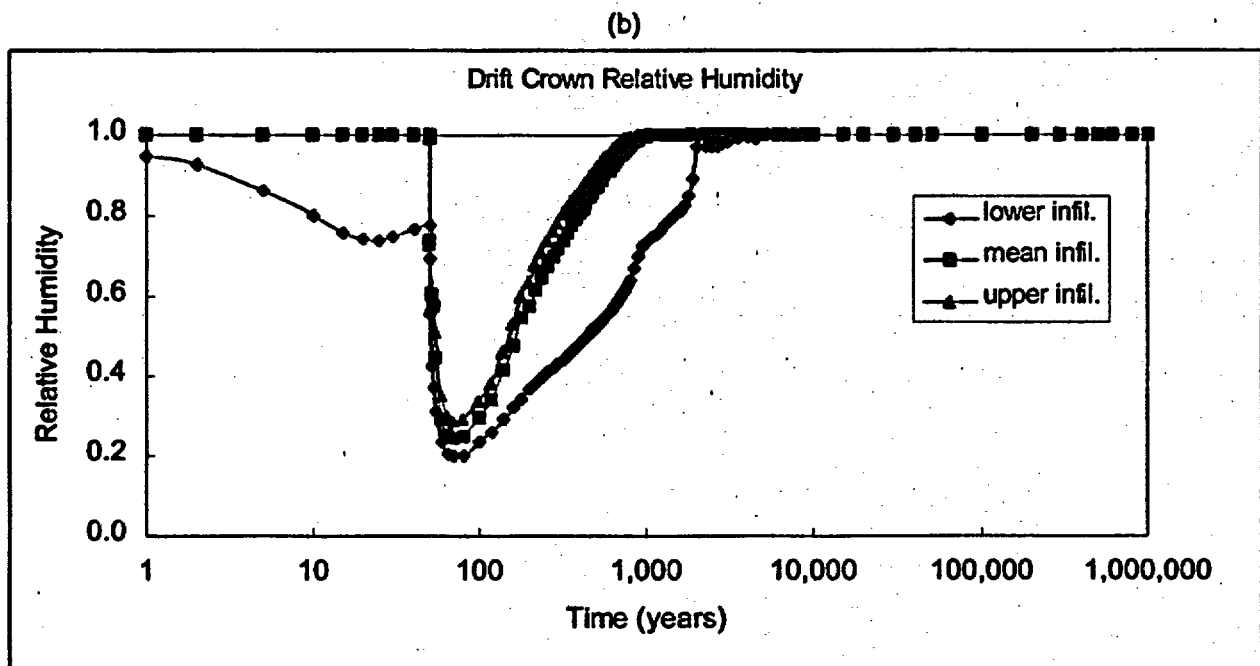
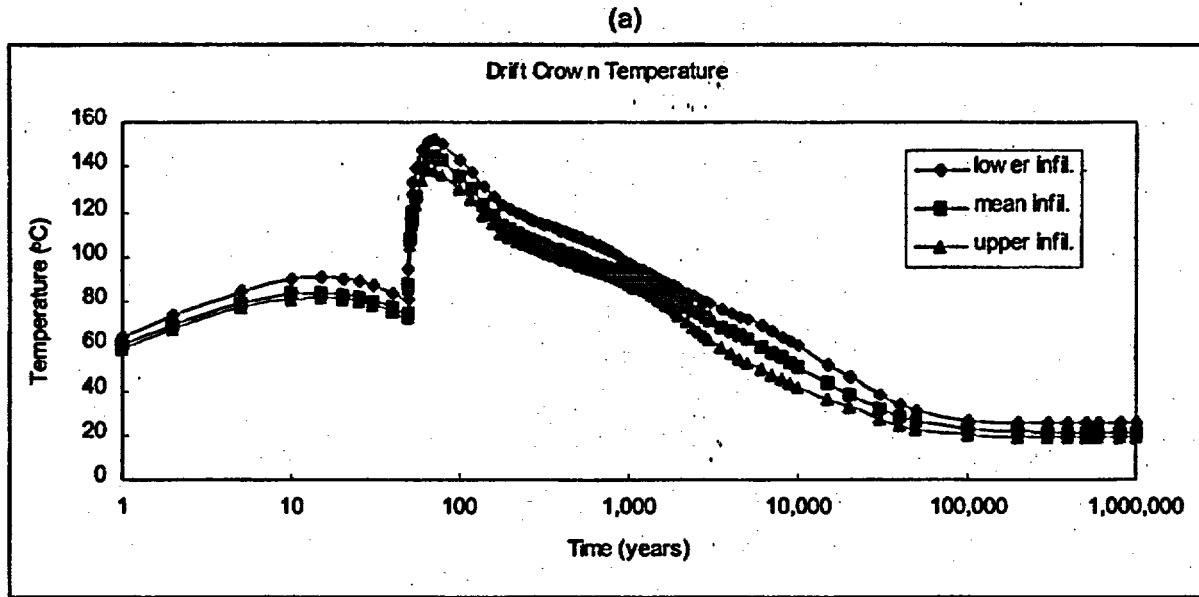


Figure 6-57. Comparisons of Drift Crown (a) Temperature (b) Relative Humidity for the Various Infiltration Rate Distributions

6.4 DRIP SHIELD CONDENSATION MODEL

During the heating period of the repository when its temperature has become above-boiling, a dry-out zone occurs in the drift and its close proximity. Upon the onset of cooling which starts in about a thousand years and beyond, liquid and gas from the surrounding rock will drift back to the repository. It is during this cooling period when condensation underneath the drip shield may be possible.

For condensation to form underneath the drip shield, several conditions must exist simultaneously. Firstly, either gas or liquid water has to enter the air space below the drip shield through the invert material. Secondly, the temperature of the invert material has to be warmer than that of the drip shield and thirdly, the partial vapor pressure in the invert material has to be high enough that its dew-point temperature will be the same or above the drip shield temperature.

To assess the condensation potential underneath the drip shield, a condensation index has been designated to represent the ratio (R) of partial vapor pressure in the invert material (Vp_{in}) to the saturated vapor pressure at the drip shield temperature (Sat. Vp_{ds}), namely:

$$R = Vp_{in} / \text{Sat. } Vp_{ds} \quad (\text{Eq. 6-46})$$

$$Vp_{in} = RH_{in} \times \text{Sat. } Vp_{in} \quad (\text{Eq. 6-47})$$

where:

RH_{in} = relative humidity at the invert.

Then condensation is possible if R is equal to or greater than 1.0.

Nine locations are selected throughout the repository area to represent the variation of conditions that would exist for the assessment of condensation potential below the drip shield. These locations are shown in Figure 6-58. The conversion from model grid indices x and y to Nevada State Coordinates is contained in the file "repos_to_Nvcentral" in attached CD (Attachment XVI) under "dscondensation" directory. The time-history data of average RH_{in} , Sat Vp_{in} , and Sat. Vp_{ds} for the nine locations are extracted from the results of the Multiscale Thermohydrologic Model (CRWMS M&O 2000i) as shown in files "wdrdsc.xls" and "wdrdscu.xls" in the attached CD, and the corresponding R ratios are calculated as a function of time in these Excel files. The R versus time plots are presented in Figure 6-60 which shows condensation for the mean-infiltration case is not expected until after 40,000 years.

As for the upper-infiltration case (no seepage imposed), only three locations are calculated (based on no significant differences between the 9 locations) in Figure 6-59 which shows the results are not sensitive to infiltration fluxes. These results are consistent with those from an earlier report (CRWMS M&O 2000i), which modeled the backfill case and predicted there would not be any condensation underneath the drip shield for the first 10,000 years.

Output from the MSTHM shows the RH, temperature within the invert material and on the underside of the drip shield vary approximately by 1% or less at any given time during the cooling period. This suggests that the use of average RH and temperature in predicting condensation is adequate.

Condensate formed on the underside of the drip shield would start its downward flow from the top of the drip shield and along the vertical surface of the shield. This film of condensate would thicken as it continues its course downward and accordingly, would provide a resistance to heat transfer between the vapor and the drip shield (Incropera and Dewitt, 1996). As the total rate of condensation is proportional to the overall heat transfer rate, this thickened film of condensate would tend to prohibit further condensation (Bejan, 1995). The MSTHM does not consider film condensation and thus, the results are conservative.

Additionally, the assumption of the drip shield as an impervious barrier in assessing condensation underneath the drip shield is also conservative due to the following:

- Outward transport of moisture through a leaking drip shield would decrease the possibility of condensation under the drip shield because input to the drip shield is finite, and any outward transport would decrease the humidity there.
- Inward transport of moisture would decrease the possibility of condensation under the drip shield because the air outside the drip shield is closer to moisture equilibrium with the drift wall, which is the coolest part of the in-drift system, so that the mole fraction of water must be smaller than that under the drip shield.

6.4.1 Model Validation

Validation requires review of the Drip Shield Condensation Model calibration parameters and corroborative information for reasonableness and consistency. The input parameters (Section 4.1.4) and assumptions (Section 5.4) and software are the same as used in the Thermohydrologic model. An additional calculation to assess condensation potential is fully documented in Section 6.4. Model results are also compared in Section 6.4 with output from the Multiscale Thermohydrologic Model (CRWMS M&O 2000i) and found to be consistent. Therefore, in accordance with AP-3.10Q, the Condensation model is appropriate for its intended use.

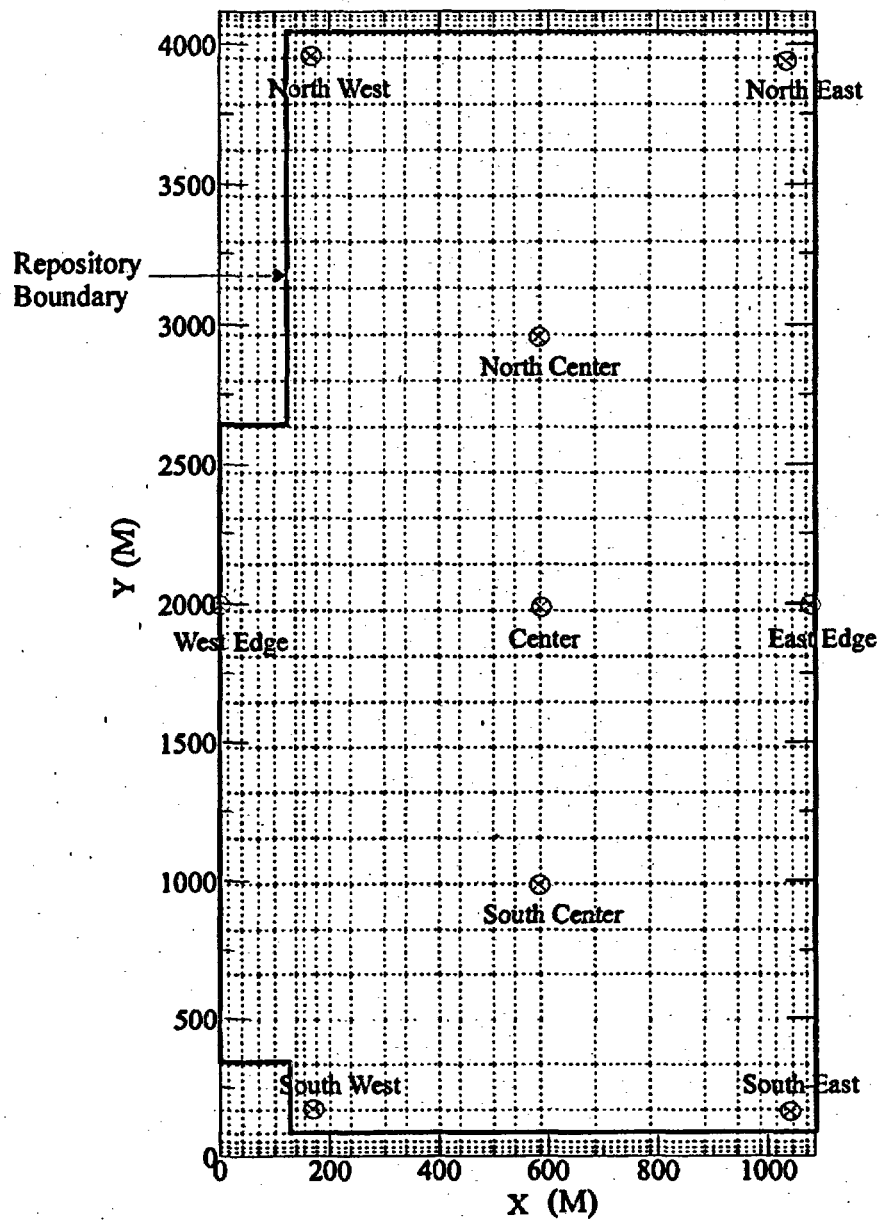


Figure 6-58. Repository Area Used In the MSTHM

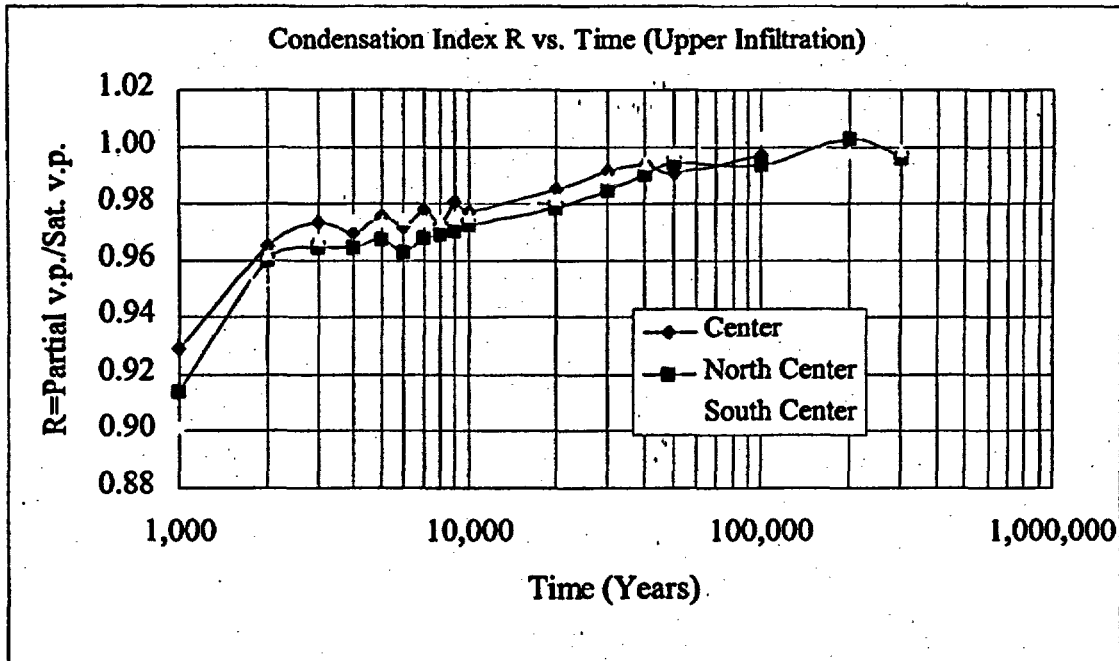


Figure 6-59. Condensation Index vs. Time for Upper Infiltration (No Seepage Imposed)

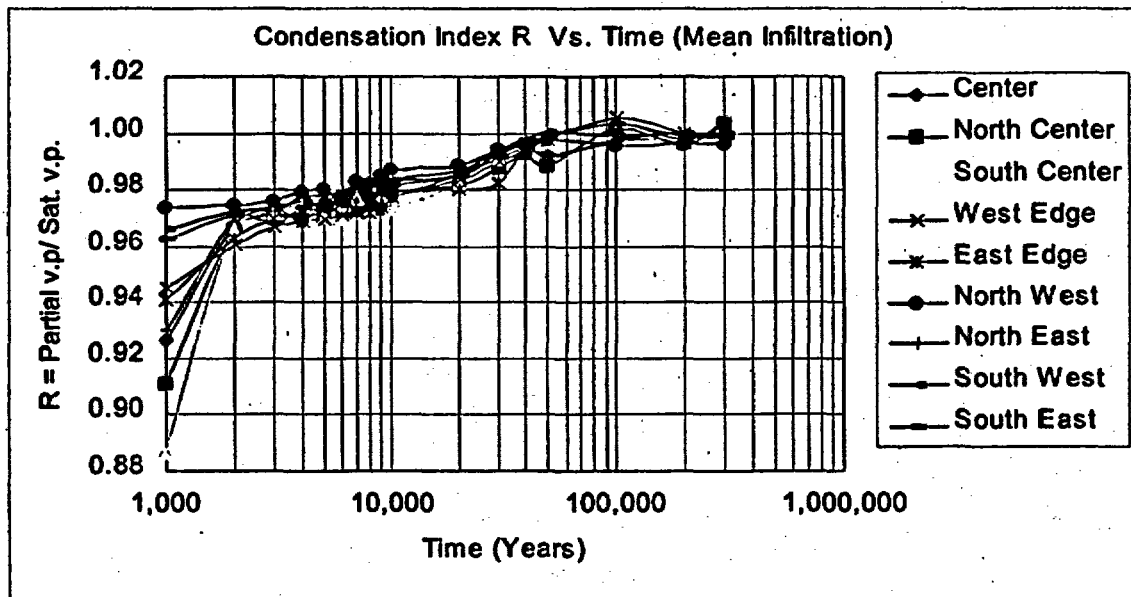


Figure 6-60. Condensation Index R vs. Time for Mean Infiltration (No Seepage Imposed)

6.5 INCLUSION AND EXCLUSION OF FEPS

Under the provisions of the DOE interim guidance (Dyer 1999), DOE must provide a reasonable assurance that the regulatory-specified performance objectives for the Yucca Mountain project can be achieved for a 10,000-year post-closure period. The assurance must be demonstrated in the form of a performance assessment that: (1) identifies the features, events, and processes (FEPS) that might affect the performance of the geologic repository; (2) examines the effects of such FEPS on the performance of the geologic repository; and (3) estimates the expected annual dose to a specified nearby population group. The performance assessment must also provide the technical basis for inclusion or exclusion of specified FEPS.

An FEP must be considered in the TSPA, unless it can be demonstrated that one of both of the following two criteria are met:

- Exclude on the basis of "Low Probability", if a FEP has less than one chance in 10,000 of occurrence over 10,000 years.
- Exclude on the basis of "Low Consequence", if omission of the FEP does not significantly change the expected annual dose.

This section summarizes the rationale for determining which FEPS should be "included" in, or "excluded" from the TSPA. The input for the analysis are the EBS FEP subset extracted from CRWMS M&O (2000h) that are applicable to the water distribution and removal aspects of the repository design. The screening arguments are for the "included" and the "excluded" are provided in Table 6-9.

6.6 IRSR ACCEPTANCE CRITERIA

The key technical acceptance criteria from the Issue Resolution Status Reports (IRSRs) developed by the U.S. Nuclear Regulatory Commission (NRC 1999a; 1999b; 1999c; and 1999d) are addressed in Table 6-10.

Table 6-9. Inclusion and Exclusion of Features, Events, and Processes Related to the WD&R Model

YMP FEP #	FEP Name	Database Rev 00 EBS FEP Description [Other PMRs]	Considerations for Inclusion in TSPA (Reference to section in this report)	Considerations for Exclusion from TSPA (Reference to section in this report)
1.1.02.00.00	Excavation/ construction	<p>This FEP is concerned with the effects associated with excavation/construction of the underground regions of the repository on the long-term behavior of the engineered and natural barriers. Excavation-related effects include changes to rock properties due to boring and blasting and chemical changes to the rock and incoming groundwater due to potential explosives residue. Excavation and other construction activities could also directly cause groundwater chemistry changes within the tunnel due to the impact of such contaminants as diesel exhaust, explosives residues, or other organic contaminants (Secondary FEP 1.1.02.00.03). Finally, oxidizing water introduced into the repository during excavation/construction could impact repository conditions/performance (Secondary FEP 1.1.02.00.04).</p> <p>[NFE, UZ]</p>		<p>Chemical effects of excavation are negligible; contamination will be limited through the use of tunnel boring (instead of drill-and-blast) and electrically powered equipment, which will limit microbial effects caused by excavation, as well as abiotic chemical contamination (CRWMS M&O 2000f, Sections 6.3 & 6.4).</p> <p>Sufficient drainage capacity in the drift floor will remain even after fines migration associated with excavation, based on observed drainage behavior in exploratory tunnels (this report, Section 6.2).</p> <p>Rockfall models are based on observation of rock characteristics in the as-built (post-excavation) condition, so that excavation effects, if any, are included. Other effects of excavation on rockmass response are minor (CRWMS M&O 2000c, Section 6).</p>

Table 6-9. Inclusion and Exclusion of Features, Events, and Processes Related to the WD&R Model (Continued)

YMP FEP #	FEP Name	Database Rev.00 EBS FEP Description (Other PMRs)	Considerations for Inclusion in TSPA (Reference to section in this report)	Considerations for Exclusion from TSPA (Reference to section in this report)
1.1.02.01.00	Site flooding (during construction and operation)	Flooding of the site during construction and operation could introduce water into the underground tunnels, which could affect the long-term performance of the repository. (Note that this is a specific example of an accident or unplanned event discussed under FEP 1.1.12.01.00.) [UZ]		Regulatory exclusion (this report, Section 6.2)
1.1.02.02.00	Effects of pre-closure ventilation	The duration of preclosure ventilation acts together with waste package spacing (as per design) to control the extent of the boiling front within the NFE. [NFE]	Heat removal by ventilation is included in TH models for TSPA (this report, Section 6.3).	
1.1.03.01.00	Error in waste or backfill emplace- ment	Deviations from the design and/or errors in waste and backfill emplacement could affect long-term performance of the repository. A specific example of such an error that has been raised involves erroneously emplacing the waste packages in the saturated zone of the repository (Secondary FEP 1.1.03.01.04). This would clearly impact the repository performance both by impacting container corrosion and failure as well as by impacting radionuclide transport. [WP]		Regulatory exclusion. See CRWMS M&O 2000h (Section 5.1.2, Assumptions, Repository Closure) for discussion.

Table 6-9. Inclusion and Exclusion of Features, Events, and Processes Related to the WD&R Model (Continued)

YMP FEP #	FEP Name	Database Rev 00 EBS FEP Description [Other PMRs]	Considerations for Inclusion in TSPA (Reference to section in this report)	Considerations for Exclusion from TSPA (Reference to section in this report)
1.1.07.00.00	Repository design	This category contains FEPs related to the design of the repository, and the ways in which the design contributes to long-term performance. Changes to or deviations from the specified design may affect the long-term performance of the disposal system. [SYS]		Regulatory exclusion (CRWMS M&O 2000h, Section 6).
1.1.08.00.00	Quality control	This category contains FEPs related to quality assurance and control procedures and tests during the design, construction, and operation of the repository, as well as the manufacture of the waste forms, containers, and engineered features. Lack of quality control could result in material defects, faulty waste package fabrication, and faulty or non-design-standard construction, all of which may lead to reduced effectiveness of the engineered barriers. [SYS]		Regulatory exclusion (CRWMS M&O 2000h, Section 6).
1.1.12.01.00	Accidents and unplanned events during operation	The long-term performance of the disposal system might be seriously affected by unplanned or improper activities that take place during construction, operation, and closure of the repository. [SYS]		Regulatory exclusion (CRWMS M&O 2000h, Section 6).
2.1.04.01.00	Preferential pathways in the backfill	Preferential pathways for flow and diffusion may exist within the backfill and may affect long-term performance of the waste packages. Backfill may not preclude hydrological, chemical, and thermal interactions between waste packages within a drift.		Backfill is not included in the current design (CRWMS M&O 2000h).

Table 6-9. Inclusion and Exclusion of Features, Events, and Processes Related to the WD&R Model (Continued)

YMP FEP #	FEP Name	Database Rev 00 EBS FEP Description (Other PMRs)	Considerations for Inclusion in TSPA (Reference to section in this report)	Considerations for Exclusion from TSPA (Reference to section in this report)
2.1.04.04.00	Mechanical effects of backfill	Backfill may alter the mechanical evolution of the drift environment by providing resistance to rock creep and rock fall, by changing the thermal properties of the drift, or by other means. Impacts of the evolution of the properties of the backfill itself should be considered. Note that this FEP also encompasses FEP ebs # 5 from table 3 [EBS FEP AMR Rev00, see FEP 2.1.06.05.00].		Backfill is not included in the current design (CRWMS M&O 2000h).
2.1.04.05.00	Backfill evolution	Properties of the backfill may change through time, due to processes such as silica cementation, alteration of minerals, thermal effects, and physical compaction. These changes could then affect the movement of water and radionuclides in the backfill. Note that this FEP also encompasses FEP ebs # 5 from table 3 [EBS FEP AMR Rev00, see FEP 2.1.06.05.00].		Backfill is not included in the current design (CRWMS M&O 2000h).
2.1.04.08.00	Diffusion in backfill	Diffusion processes in backfill may affect waste package performance and radionuclide transport.		Backfill is not included in the current design (CRWMS M&O 2000h).
2.1.04.09.00	Radio-nuclide transport through backfill	Radionuclide transport in the drift environment may be affected by the presence of backfill. Transport of both dissolved and colloidal species, advective and diffusive effects and sorption processes should be considered.		Backfill is not included in the current design (CRWMS M&O 2000h).

Table 6-9. Inclusion and Exclusion of Features, Events, and Processes Related to the WD&R Model (Continued)

YMP FEP #	FEP Name	Database Rev 00 EBS FEP Description [Other PMRs]	Considerations for Inclusion in TSPA (Reference to section in this report)	Considerations for Exclusion from TSPA (Reference to section in this report)
2.1.06.04.00	Flow through the liner	Groundwater flow may occur through the liner.		A concrete liner is not included in the current design (CRWMS M&O 2000h).
2.1.06.06.00	Effects and degradation of drip shield	<p>The drip shield will affect the amount of water reaching the waste package. Behavior of the drip shield in response to rockfall, ground motion, and physical, chemical degradation processes should be considered. Effects of the drip shield on the disposal region environment (for example, changes in relative humidity and temperature below the shield) should be considered for both intact and degraded conditions. Degradation processes specific to the chosen material should be identified and considered. For example, oxygen embrittlement should be considered for titanium drip shields.</p> <p>Note that this FEP also encompasses FEPs ebs # 2, 9, 10, 11, 15, 17, 19, 20, 24, 30, 31, and 32 from table 3 [EBS FEP AMR Rev00, see FEPs 2.1.06.05.00, 2.1.06.07.00, 2.1.07.01.00, 2.1.07.02.00].</p> <p>[WP].</p>	Water diversion performance of the degraded drip shield is considered (this report, Section 6.1). The environment under the drip shield is evaluated for intact conditions (this report, Section 6.4). Seepage leaking through degraded drip shields is considered (this report, Section 6.1; also see the CRWMS M&O 2000t). See the WP PMR, and associated abstraction AMRs, for discussion of corrosion modes and rates, and assumptions made regarding microbial degradation modes, for TSPA.	Drip shield corrosion will occur slowly, and degradation potentially significant to environmental conditions will not occur until after cooldown. Thus the temperature and relative humidity on the waste package would not differ much from elsewhere in the drift, or from the intact drip shield calculation results (this report, Section 6.3).

Table 6-9. Inclusion and Exclusion of Features, Events, and Processes Related to the WD&R Model (Continued)

YMP FEP #	FEP Name	Database Rev 00: EBS FEP Description [Other PMRs]	Considerations for Inclusion in TSPA (Reference to section in this report)	Considerations for Exclusion from TSPA (Reference to section in this report)
2.1.07.02.00	Mechanical degradation or collapse of drift	<p>Partial or complete collapse of the drifts, as opposed to discrete rockfall, could occur as a result of seismic activity, thermal effects, stresses related to excavation, or possibly other mechanisms. Drift collapse could affect stability of the engineered barriers and waste packages. Drift collapse may be localized as stopping at faults or other geologic features. Rockfall of small blocks may produce rubble throughout part or all of the tunnel.</p> <p>Note that this FEP also encompasses FEPs: ebs # 9, 11, and 37 from EBS FEP AMR Rev00, Table 3; also see FEPs 2.1.06.05.00, 2.1.06.06.00, 2.1.06.07.00, and 2.1.07.01.00.</p> <p>[DE]</p>		<p>Rockfall models are based on site characterization data, and extend to conditions that can represent drift collapse. Probabilistic descriptions of rock size and rockfall frequency are provided for use in engineering design analyses (CRWMS M&O 2000c). Standoff criteria will be used to limit or prevent waste emplacement in the immediate vicinity of faults. The effects of rubble would be similar to analyzed cases involving larger blocks.</p>
2.1.07.03.00	Movement of containers	<p>Waste packages may move as a result of seismic activity, degradation of the invert or pedestal, rockfall, fault displacement, or other processes (also see FEP 2.1.06.05.00).</p> <p>Note that this FEP also encompasses FEP: ebs # 3 from EBS FEP AMR Rev00, Table 3; also see FEP 2.1.07.03.00.</p>	<p>Included by assumptions made for radionuclide transport from the waste package to the top of the invert (CRWMS M&O 2000h).</p>	<p>Rockfall models are based on site characterization data, and extend to conditions that can represent drift collapse. Probabilistic descriptions of rock size and rockfall frequency are provided for use in engineering design analyses (CRWMS M&O 2000c).</p>
2.1.07.04.00	Hydrostatic pressure on container	<p>Waste packages emplaced in the saturated zone will be subjected to hydrostatic pressure in addition to stresses associated with the evolution of the waste and barrier system.</p> <p>This FEP is not relevant for the YMP design, which calls for emplacement in the</p>		<p>Free drainage conditions will prevail in the potential repository (this report, Section 6.2).</p>

Table 6-9. Inclusion and Exclusion of Features, Events, and Processes Related to the WD&R Model (Continued)

YMP FEP #	FEP Name	Database Rev. 00 EBS FEP Description [Other PMRs]	Considerations for Inclusion in TSPA (Reference to section in this report)	Considerations for Exclusion from TSPA (Reference to section in this report)
2.1.08.01.00	Increased unsaturated water flux at the repository	An increase in the unsaturated water flux at the repository affects thermal, hydrological, chemical, and mechanical behavior of the system. Extremely rapid influx could reduce temperatures below the boiling point during part or all of the thermal period. Increases in flux could result from climate change, but the cause of the increase is not an essential part of the FEP. [NFE, UZ]	Increased flux representing the uncertainty as to future climate change, is considered in thermal-hydrologic models (this report, Section 6.3).	Increased flux is considered in models of drainage (this report, Section 6.2). Free drainage is expected to prevail in the potential repository.
2.1.08.02.00	Enhanced influx (Phillip's drip)	An opening in unsaturated rock alters the hydraulic potential, affecting local saturation around the opening and redirecting flow. Some of the flow is directed to the opening where it is available to seep into the opening. [NFE, UZ]	See the UZ PMR for discussion of drift seepage models. The possible presence of seepage is included in models for the chemical environment (CRWMS M&O 2000h), and water diversion performance of the drip shield and waste package (this report, Section 6.1).	
2.1.08.04.00	Condensation forms on backs of drifts	Emplacement of waste in drifts creates a large thermal gradient across the drifts. Moisture condenses on the roof and flows downward through the backfill.	The effects of condensation on the chemical environment at the surface of the drip shield, is included in current models (CRWMS M&O 2000f, Section 6.7).	By analogy to the effects of seepage during the thermal period, such condensation would be inconsequential to the performance of the intact drip shield and/or drip shield (this report, Section 6.3).
2.1.08.05.00	Flow through invert	The invert, consisting mostly of porous, crushed tuff, separates the waste package from the bottom of the tunnel (boundary to the UZ). Water may flow through the invert, either in its intact or degraded state, either in fractures or matrix porosity.	Unsaturated flow in the invert is included in thermal-hydrologic models, and the effects of seepage on this flow are evaluated (this report, Section 6.3).	

Table 6-9. Inclusion and Exclusion of Features, Events, and Processes Related to the WD&R Model (Continued)

YMP FEP #	FEP Name	Database Rev 00 EBS FEP Description (Other PMRs)	Considerations for Inclusion in TSPA (Reference to section in this report)	Considerations for Exclusion from TSPA (Reference to section in this report)
2.1.08.06.00	Wicking in waste and EBS	Capillary rise, or wicking, is a potential mechanism for water to move through the waste and engineered barrier system.	Unsaturated capillary flow is included in thermal-hydrologic models for TSPA (this report, Section 6.2), and in models for drainage (Section 6.2). Capillary processes are also included in models for water diversion performance of the drip shield and waste package (Section 6.3).	
2.1.08.07.00	Pathways for unsaturated flow and transport in the waste and EBS	Unsaturated flow and radionuclide transport may occur along preferential pathways in the waste and EBS. Physical and chemical properties of the EBS and waste form, in both intact and degraded states, should be considered in evaluating pathways. [WFMisc]	EBS radionuclide transport models for TSPA are developed using a lumped-parameter approach that accommodates preferential pathways in the invert (CRWMS M&O 2000h). Breaches in the drip shield and waste package are also treated as preferential pathways, in an average sense that holds for many waste packages (this report, Section 6.1).	

Table 6-9. Inclusion and Exclusion of Features, Events, and Processes Related to the WD&R Model (Continued)

YMP FEP #	FEP Name	Database Rev 00 EBS FEP Description [Other PMRs]	Considerations for Inclusion in TSPA (Reference to section in this report)	Considerations for Exclusion from TSPA (Reference to section in this report)
2.1.08.08.00	Induced hydrological changes in the waste and EBS	<p>Thermal, chemical, and mechanical processes related to the construction of the repository and the emplacement of waste may induce changes in the hydrological behavior of the system.</p> <p>Note that this FEP also encompasses FEPs: ebs # 13 and 14 from EBS FEP AMR Rev00, Table 3; also see FEPs 2.1.08.08.00.</p> <p>[WFMisc]</p>		Coupled processes can only decrease the transmissivity of breaches in the drip shield or waste package, and are not considered in these models developed for TSPA (this report, Section 6.1). See the WP PMR for discussion of material degradation modes for the drip shield and waste package. The effects of minerals and salts that may be deposited by evaporation in the invert are limited (CRWMS M&O 2000f, Section 6.3). See the NFE PMR for discussion of potential THC effects in the host rock adjacent to the drift openings.
2.1.08.09.00	Saturated groundwater flow in waste and EBS	Saturated flow and radionuclide transport may occur along preferential pathways in the waste and EBS. Physical and chemical properties of the EBS and waste form, in both intact and degraded states, should be considered in evaluating pathways.		The EBS outside the waste package will remain unsaturated because free drainage conditions will be maintained (this report, Section 6.2).
2.1.08.11.00	Resaturation of repository	<p>Water content in the repository will increase following the peak thermal period.</p> <p>[NFE]</p>	Return of moisture to the EBS environment is included in thermal-hydrologic models (this report, Section 6.3).	

Table 6-9. Inclusion and Exclusion of Features, Events, and Processes Related to the WD&R Model (Continued)

YMP FEP #	FEP Name	Database Rev.00 EBS FEP Description [Other PMRs]	Considerations for Inclusion in TSPA (Reference to section in this report)	Considerations for Exclusion from TSPA (Reference to section in this report)
2.1.08.12.00	Drainage with Transport - Sealing and Plugging	Normal functioning of drainage in the drifts is not established, so how drainage will change if fractures are plugged is unclear. Suggestions include ponding until fractures in the wall are reached by the water level or until there is sufficient head to clear the fractures.		Analysis indicates that drainage capacity will be sufficient to handle extreme seepage into the drifts (this report, Section 6.2).
2.1.08.13.00	Drains	Water accumulation in the drift would wet the invert materials, possibly pond, and provide a continuing source of water vapor beneath the drip shield and backfill for interaction with waste packages and their supports. Engineered drains are a consideration for mitigating such water accumulation and ponding.		Engineered drains are not included in the current design (this report, Section 6.2).
2.1.09.12.00	Rind (altered zone) formation in waste, EBS, and adjacent rock	Thermo-chemical processes involving precipitation, condensation, and redissolution alter the properties of the waste, EBS, and the adjacent rock. These alterations may form a rind, or altered zone, in the rock, with hydrological, thermal, and mineralogical properties different from the current conditions. [NFE, WFMisc]		The potential for changes in properties of the crushed tuff invert, caused by local evaporation, is limited (CRWMS M&O 2000f, Section 6.3).

Table 6-9. Inclusion and Exclusion of Features, Events, and Processes Related to the WD&R Model (Continued)

YMP FEP #	FEP Name	Database Rev 00 EBS FEP Description (Other PMRs)	Considerations for Inclusion in TSPA (Reference to section in this report)	Considerations for Exclusion from TSPA (Reference to section in this report)
2.1.11.01.00	Heat output/ temperature in waste and EBS	<p>Temperature in the waste and EBS will vary through time. Heat from radioactive decay will be the primary cause of temperature change, but other factors to be considered in determining the temperature history include the in-situ geothermal gradient, thermal properties of the rock, EBS, and waste materials, hydrological effects, and the possibility of exothermic reactions (see FEP 2.1.11.03.00). Considerations of the heat generated by radioactive decay should take different properties of different waste types, including DSNF, into account.</p> <p>[NFE, WFMisc]</p>	Heat and mass transfer processes are included in thermal-hydrologic models for TSPA (this report, Section 6.3).	

Table 6-9. Inclusion and Exclusion of Features, Events, and Processes Related to the WD&R Model (Continued)

YMP FEP #	FEP Name	Database Rev 00 EBS FEP Description (Other PMRs)	Considerations for Inclusion in TSPA (Reference to section in this report)	Considerations for Exclusion from TSPA (Reference to section in this report)
2.1.11.04.00	Tempera- ture effects/ coupled processes in waste and EBS	This FEP broadly encompasses all coupled- process effects of temperature changes within the waste and EBS. Technical discussions relevant to this FEP are provided individually for each relevant process. See FEP 2.1.11.01.00 for a discussion of the temperature history of repository. See FEP 2.1.11.03.00 for a discussion of possible exothermic reactions. See FEP 2.1.11.05.00 for a discussion of the effects of differential thermal expansion of repository components. See FEP 2.1.11.07.00 for a discussion of thermally-induced stresses in the waste and EBS. See FEP 2.1.11.08.00 for a discussion of thermal effects on chemical and microbial processes. See FEP 2.1.11.09.00 for a discussion of thermal effects on fluid flow in the waste and EBS. See 2.1.11.10.00 for a discussion of the Soret effect. [WFMisc]	Effects of temperature changes on the EBS are addressed in the models that support TSPA (this report, Section 6.3; CRWMS M&O 2000f, Sections 6.2, 6.3, 6.4, and 6.7).	
2.1.11.05.00	Differing thermal expansion of repository components	Thermally-induced stresses could alter the performance of the waste or EBS. For example, thermal stresses could create pathways for preferential fluid flow in the backfill or through the drip shield. [WP, WFMisc]		The EBS components are designed to accommodate thermal strains. Design analyses indicate that the drip shield will maintain modeled water diversion performance through changes in temperature (this report, Section 6.3).

Table 6-9. Inclusion and Exclusion of Features, Events, and Processes Related to the WD&R Model (Continued)

YMP FEP #	FEP Name	Database Rev.00 EBS FEP Description (Other PMRs)	Considerations for Inclusion in TSPA (Reference to section in this report)	Considerations for Exclusion from TSPA (Reference to section in this report)
2.1.11.07.00	Thermally-induced stress changes in waste and EBS	Thermally-induced stress changes in the waste and EBS may affect performance of the repository. Relevant processes include rockfall, drift stability, changes in physical properties of the disturbed rock zone around the repository, and changes in the physical properties of the surrounding rock. [WFMisc]		Probabilistic descriptions of rock size and rockfall frequency, for conditions representing elevated stress and temperature, are provided for use in engineering design analyses (CRWMS M&O 2000c). No credit is taken for ground support (which could be impacted by thermal stress especially in the post-closure period) in rockfall models.
2.1.11.09.00	Thermal effects on liquid or two-phase fluid flow in the waste and EBS	Temperature differentials may result in convective flow in the waste and EBS. [WFMisc]	Two-phase flow is included in thermal-hydrologic models (this report, Section 6.3), such that the indirect effects of such flow on other processes are also included (CRWMS M&O 2000f, Sections 6.2 and 6.7)	
2.2.07.06.00	Episodic/pulse release from repository	Episodic release of radionuclides from the repository and radionuclide transport in the UZ may occur both because of episodic flow into the repository, and because of other factors including intermittent failures of waste packages. Note that this FEP also encompasses FEP ebs # 16 from table 3 [see EBS FEP AMR Rev00, table did not transfer, see FEP 2.2.07.06.00]. [UZ]	Water diversion and drainage response of the EBS has been evaluated over a range of infiltration/seepage conditions (this report, Section 6.1). Increased infiltration/seepage associated with climate change is included in models for TSPA (this report, Section 6.3). The radionuclide release and transport models developed for TSPA represent the average response of many waste packages (CRWMS M&O 2000h, Section 6).	

Table 6-10. Key Technical Issue Acceptance Criteria Addressed by the WD&R Model

Subissue	Crit. #	Description (Comments)
Container Life and Source Term KTI		
CLST (Applicable to all 6 subissues) (NRC 1999a)	1	<p>The collection and documentation of data, as well as development and documentation of analyses, methods, models, and codes, were accomplished under approved quality assurance and control procedures and standards.</p> <p>(Activities associated with development of this report were determined to be subject to the quality assurance program as described in the Quality Assurance Requirements and Description [DOE 2000] document.)</p>
	2	<p>Expert elicitations, when used, were conducted and documented in accordance with the guidance provided in NUREG-1563 or other acceptable approaches.</p> <p>(No expert elicitation was conducted for this report.)</p>
	3	<p>Sufficient data (field, laboratory, and natural analog) are available to adequately define relevant parameters for the models used to evaluate performance aspects of the subissues.</p> <p>(This report together with the other, referenced reports describe field, laboratory, and natural analog data that are applied to geological, thermal, mechanical, hydrological, chemical, and biological characterization of potential repository performance.)</p>
	4	<p>Sensitivity and uncertainty analyses (including consideration of alternative conceptual models) are used to determine whether additional data would be needed to better define ranges of input parameters.</p> <p>(This report describes a set of sensitivity analyses designed to address uncertainties. Where additional data could be used to reduce uncertainty in key areas, these needs are identified as assumptions with to-be-verified status.)</p>
	5	<p>Parameter values, assumed ranges, test data, probability distributions, and bounding assumptions used in the models are technically defensible and can reasonably account for known uncertainties.</p> <p>(The selection of input data, and the basis for each assumption, are justified in this report.)</p>
	6	<p>Mathematical model limitations and uncertainties in modeling were defined and documented.</p> <p>(Model limitations and uncertainties are identified in this report, where they may have important implications for use of model results.)</p>
	7	<p>Primary and alternative modeling approaches consistent with available data and current scientific understanding were investigated and their results and limitations considered in evaluating the subissue.</p> <p>(Alternative modeling approaches, scoping calculations, and other methods consistent with current understanding are used in evaluating the subissue.)</p>
	8	<p>Model outputs were validated through comparisons with outputs of detailed process models, empirical observations, or both.</p> <p>(Model validation is documented in this report, following the guidance in AP-3.10Q.)</p>
	9	<p>The structure and organization of process and abstracted models were found to adequately incorporate important design features, physical phenomena, and coupled processes.</p> <p>(The process models developed in this report are considered to adequately represent important design features and processes.)</p>

Subissue	Crit. #	Description (Comments)
CLST 6 Effects of Alternate Features on Waste Package Life and Radionuclide Release (NRC 1999a)	4	<p>DOE has identified and considered the effects of drip shields (with backfill) on WP lifetime, including extension of the humid-air corrosion regime, environmental effects, breakdown of drip shields and resulting mechanical impacts on WP, the potential for crevice corrosion at the junction between the WP and the drip shield, and the potential for condensate formation and dripping on the underside of the shield.</p> <p>(The thermal-hydrologic environment under the drip shields is a major focus of this report. The drip shield is modeled as an functioning barrier throughout the 10,000-yr performance period because this is a requirement on the design.)</p>
Evolution of the Near-Field Environment KTI		
ENFE 1 Effects of T-H-C on Seepage & Flow (NRC 1999b)	3 Data & Model Justification	<p>Sufficient data were collected on the characteristics of the natural system and engineered materials, such as the type, quantity, and reactivity of material, to establish initial and boundary conditions for conceptual models and simulations of THC coupled processes that affect seepage and flow.</p> <p>(Properties of engineered materials, and the potential effects from fines migration on drainage, are considered in this report. The effect of invert properties on the environment under the drip shield, and the potential for radionuclide transport, are also considered.)</p>
	3 Integration	<p>Not all THC couplings may be determined to be important to performance, and DOE may adopt assumptions to simplify PA analyses. If potentially important couplings are neglected, DOE should provide a technical basis for doing so. The technical basis can include activities such as independent modeling, laboratory or field data, or sensitivity studies.</p> <p>(This report focuses on sensitivity analyses which provide a technical basis for treatment of certain coupled processes, including coupled chemical processes that could affect flow.)</p>
	1 Model Uncert.	<p>Appropriate models, tests, and analyses were used that are sensitive to the THC couplings under consideration for both natural and engineering systems.</p> <p>(This report considers important changes in EBS performance that could result from in-drift THC processes, particularly plugging of fractures and the resulting loss of invert drainage capacity. It also considers the sensitivity of in-drift conditions to seepage during the thermal period. In other cases, such as the analysis of flow through cracks and breaches, no credit is taken for coupled processes that could mitigate the quantity of water contacting the waste package.)</p>
	3 Model Uncert.	<p>Alternative modeling approaches consistent with available data and current scientific understanding were investigated, and their results and limitations were appropriately considered.</p> <p>(Alternative models consistent with current understanding, and model limitations and uncertainties, are considered in this report.)</p>
	4 Model Uncert.	<p>DOE provided a reasonable description of the mathematical models included in its analyses of coupled THC effects on seepage and flow. The description included a discussion of alternative modeling approaches not considered in its final analysis and the limitations and uncertainties of the chosen model.</p> <p>(Alternative models consistent with current understanding, and model limitations and uncertainties, are considered in this report. Models are described using a mathematical basis where practicable.)</p>
	1 Model Verification	<p>The mathematical models for coupled THC effects on seepage and flow were consistent with conceptual models based on inferences about the near-field environment, field data and natural alteration observed at the site, and expected engineered materials.</p> <p>(Mathematical and conceptual models presented in this report are consistent.)</p>

Subissue	Crit. #	Description (Comments)
	2 Model Verifica- tion	DOE appropriately adopted accepted and well-documented procedures to construct and test the numerical models used to simulate coupled THC effects on seepage and flow. (The models described in this report were constructed, tested, and documented using accepted and well-documented procedures.)
ENFE 4 Effects of Coupled Thermal-Hydrologic-Chemical Processes on Radionuclide Transport Through Engineered and Natural Barriers (NRC 1999b)	3 Data & Model Justifica- tion	Sufficient data were collected on the characteristics of the natural system and engineered materials, such as the type, quantity, and reactivity of material, in establishing initial and boundary conditions for conceptual models and simulations of THC coupled processes that affect transport of radionuclides in the near field. (Properties of engineered materials are considered in this report, including those that can control the mode and rate for radionuclide transport in the invert.)
	2 Data Uncert. & Verifi- cation	Uncertainty in data due to both temporal and spatial variations in conditions affecting coupled THC effects on radionuclide transport in the near field were considered. (Uncertainty and variability in the temporal and spatial distributions of percolation flux, heat generation, and other variables are considered in this report. Location within the repository layout is also considered.)
	4 Data Uncert. & Verifi- cation	The initial conditions, boundary conditions, and computational domain used in sensitivity analyses involving coupled THC effects on radionuclide transport in the near field were consistent with available data. (The thermal-hydrologic conditions affecting radionuclide transport in the EBS are analysed in a manner that is consistent with available data, and with other predictive models.)
	2 Integra- tion	Models reasonably accounted for known temporal and spatial variations in conditions affecting coupled THC effects on transport of radionuclides in the near field. (The thermal-hydrologic conditions affecting radionuclide transport in the EBS are analyzed using boundary conditions that account for possible future climate conditions, and variation of hydrologic conditions and rock properties throughout the repository layout.)
	3 Model Uncert.	DOE provided a reasonable description of the mathematical models included in its analyses of coupled THC effects on radionuclide transport in the near field. The description included a discussion of alternative modeling approaches not considered in its final analysis and the limitations and uncertainties of the chosen model. (The thermal-hydrologic conditions affecting radionuclide transport in the EBS are predicted using a well-documented model. Alternative modeling approaches, particularly the evolution of thermal-hydrologic modeling in conjunction with field thermal testing, are considered in this report.)
	Thermal Effects on Flow KTI	
TEF 1 Is the DOE Thermohydrologic Testing Program, Including Performance Confirmation Testing, Sufficient To Evaluate The Potential For Thermal Reflux To Occur In The Near Field? (NRC 1999c, NRC 1999d)	1.1 Tech. Accept.	Thermohydrologic tests are designed and conducted with the explicit objective of testing conceptual and numerical models so that critical thermohydrologic processes can be observed and measured. (The thermal-hydrologic models used to described environmental conditions in the EBS for this report, are validated by comparison to field thermal test data. The models presented in this report also address the sensitivity of environmental conditions to processes that have been inferred from, although not necessarily observed directly, in field tests.)
	1.2 Tech. Accept.	Thermohydrologic tests are designed and conducted with explicit consideration of TH, thermal-chemical, and hydrologic-chemical couplings. (The thermal-hydrologic models used to describe environmental conditions in the EBS for this report, are validated by comparison to results from field tests that are designed with explicit consideration for coupled processes.)

Subissue	Crit. #	Description (Comments)
	1.3 Tech. Accept.	<p>Thermohydrologic tests are designed and conducted at different scales to discern scale effects on observed phenomena.</p> <p>(The thermal-hydrologic models used to described environmental conditions in the EBS for this report, are validated by comparison to results from field tests that have been performed at different scales up to and including the drift-scale test.)</p>
	1.4 Tech. Accept.	<p>Thermohydrologic tests are designed and conducted for temperature ranges expected for repository operating conditions.</p> <p>(The thermal-hydrologic model results discussed in this report were validated by comparison to results from field tests designed to produce temperature conditions representing those which are expected in the potential repository.)</p>
	1.5 Tech. Accept.	<p>Thermohydrologic tests are designed and conducted to determine if water refluxes back to the heaters during the heating or cool-down phases of the tests.</p> <p>(The thermal-hydrologic models used to described environmental conditions in the EBS for this report, are validated by comparison to results from field tests that have been designed to investigate the processes that could cause water to reflux back to the drifts.)</p>
	1.6 Tech. Accept.	<p>Thermohydrologic tests are designed and conducted to evaluate the possibility for occurrence of cyclic wetting/drying on WP surfaces.</p> <p>(Sensitivity studies documented in this report show the limiting effects of episodic hydrologic conditions represented by seepage, on temperature, humidity, and evaporation in the EBS.)</p>
	1.7 Tech. Accept.	<p>Thermohydrologic tests are designed and conducted to account for all mass and energy losses/gains in the thermal test system.</p> <p>(The thermal-hydrologic models used to described environmental conditions in the EBS for this report, are validated by comparison to results from field tests that have been designed to control mass and energy fluxes.)</p>
	1.8 Tech. Accept.	<p>Thermohydrologic tests are designed and conducted such that the thermal test environment is sufficiently characterized so that uncertainty in property values does not result in unacceptable uncertainty in thermal test results interpretation.</p> <p>(The thermal-hydrologic models used to describe environmental conditions in the EBS for this report, are validated by comparison to results from field tests that have been supported by measurement of properties for natural and engineered materials.)</p>
	1.9 Tech. Accept.	<p>Thermohydrologic tests are designed and conducted such that the accuracy in the measurement of the test environment saturation is sufficient to discern the relative ability of different conceptual models to represent TH processes in heated partially saturated fractured porous media.</p> <p>(The thermal-hydrologic models used to describe environmental conditions in the EBS for this report, are validated by comparison to results from field tests that have been supported by measurement of saturation and humidity.)</p>
<p>TEF 2 Is the DOE Thermohydrologic Modeling Approach Sufficient to Predict the Nature and Bounds of Thermal Effects on Flow in the Near Field? (NRC 1999c, NRC 1999d)</p>	1.1 Tech. Accept.	<p>Sufficient data are available to adequately define relevant parameters, parameter values, and conceptual models. Specifically, DOE should demonstrate that uncertainties and variabilities in parameter values are accounted for using defensible methods. The technical bases for parameter ranges, probability distributions or bounding values used are provided. Parameter values (single values, ranges, probability distributions, or bounding values) are derived from site-specific data or an analysis is included to show the assumed parameter values lead to a conservative effect on performance.</p> <p>(The parameters and property values used in this report were developed using technically defensible, documented analyses and models. Alternative sets of properties represent uncertainty. Conceptual models have evolved from field thermal testing. Conservatism is clearly identified in the model development.)</p>

Subissue	Crit. #	Description (Comments)
	1.2 Tech. Accept.	<p>Sufficient data are available to adequately define relevant parameters, parameter values, and conceptual models. Specifically, DOE should demonstrate that analyses are consistent with site characteristics in establishing initial conditions, boundary conditions, and computational domains for conceptual models evaluated.</p> <p>(The model inputs and constraints documented in this report are consistent with site characteristics.)</p>
	2.1 Tech. Accept.	<p>Models are based on well-accepted principles of heat and mass transfer applicable to unsaturated geologic media.</p> <p>(Models used in this report for heat-mass transfer are based on accepted principles.)</p>
	2.2 Tech. Accept.	<p>Models include, at a minimum, the processes of evaporation and condensation and the effects of discrete geologic features.</p> <p>(The effects seepage caused by fracture flow, and drainage from the drifts through fractures, are considered in this report.)</p>
	5 Tech. Accept.	<p>Equivalent continuum models are acceptable for the rock matrix and small discrete features, if it can be demonstrated that water in small discrete features is in continuous hydraulic equilibrium with matrix water. Significant discrete features, such as fault zones, should be represented separately unless it can be shown that inclusion in the equivalent continuum model (ECM) produces a conservative effect on calculated overall performance.</p> <p>(This report relies on dual-permeability, non-equilibrium thermal-hydrologic models because they have been shown to better represent observations from field tests.)</p>
TEF 3 Does The DOE Total System Performance Assessment Adequately Account For Thermal Effects On Flow? (NRC 1999c, NRC 1999d)	3.1 Tech. Accept.	<p>Performance-affecting heat and mass transfer mechanisms, including processes observed in available thermohydrologic tests and experiments, have been identified and incorporated into the TSPA. Specifically, it is necessary to either demonstrate that liquid water will not reflux into the underground facility or incorporate refluxing water into the TSPA and bound the potential adverse effects of: (i) corrosion of the WP; (ii) accelerated transport of radionuclides; and (iii) alteration of hydraulic and transport pathways that result from refluxing water.</p> <p>(This report focuses on sensitivity testing for the thermal-hydrologic models used for TSPA-SR. The effects of thermal refluxing, represented as seepage during the thermal period, on the in-drift environment are evaluated.)</p>
	3.2 Tech. Accept.	<p>Significant Geologic Repository Operations Area (GROA) underground facility design features, such as the addition of backfill or drip shields, that can result in changes in TSP have been identified and incorporated into the TSPA.</p> <p>(The EBS process models are consistent with the current conceptual design. Small differences between the geometry of in-drift features such as the invert and drip shield, are not expected to produce important differences in performance.)</p>
	3.5 Tech. Accept.	<p>Alternative models and modeling approaches, consistent with available data and current scientific understanding, are investigated; limitations are defined, and results appropriately considered.</p> <p>(This report-together with companion EBS reports- evaluates sensitivity of the thermal-hydrologic models used for TSPA-SR, to alternative approaches and model limitations.)</p>
	3.6 Tech. Accept.	<p>Results from different mathematical models have been compared to judge robustness of results.</p> <p>(Comparisons between different formulations for thermal-hydrologic models are available and support the models presented in this report.)</p>
	7 Tech. Accept.	<p>Sensitivity and importance analyses were conducted to assess the need for additional data or information with respect to TEF.</p> <p>(This report-together with companion EBS reports- evaluates sensitivity of the thermal-hydrologic models used for TSPA-SR, to alternative approaches and model limitations.)</p>

7. CONCLUSIONS

7.1 WATER DIVERSION MODEL

Four potential flow mechanisms that move the seepage water to the underside of the drip shield, in the forms of liquid and vapor, through capillary flows and adsorptive condensation are investigated. These potential flow mechanisms include:

- capillary flow through drip shield connectors;
- unsaturated crevice flow due to the interception of films on top of the drip shield;
- saturated and unsaturated crevice flow due to the impulsive force of dripping; and
- film flow and dripping due to adsorptive condensation on the internal structural reinforcement beams.

Analyses show that the current drip shield connection configuration effectively prevents water from flowing through the apertures between two overlapping drip shield segments. The open spaces between the water diversion rings and the axial seismic stabilizers form capillary breaks that discontinue the hydraulic connections between the upper side and the lower side of the drip shields.

It is concluded that seepage water enters the emplacement drift primarily through fractures in the form of pendant drops. Water dripping on the drip shield form a thin film on the solid surface by splashing and spreading. Crevices of various sizes will be developed in the drip shield by pitting and crevice corrosions. The apertures in the drip shield draw water from the thin film due to capillary suction and gravitational forces. Water content in the crevices can vary from saturated, to partially-saturated, to not capable of holding water as the aperture sizes increase. For the 20-mm thick drip shield, it is calculated that the crevices will be saturated when the aperture widths are 0.687 mm or smaller. Capillary water depth in the crevices decreases to 2.75 mm when aperture width increases to 5 mm. Crevices with aperture width greater than 5 mm are unlikely to hold any water as the capillaries break easily when air becomes interconnected from top to bottom.

Saturated crevices act like plugs for the film flow because the capillary force can support the additional weight of the thin film. Water will not be released from the underside of the saturated crevices due to film flow, but only if the water drip directly on the saturated crevices.

Water falling on the drip shield surface results in the conversion of kinetic energy to pressure energy such as the impulsive force. Depending on the aperture widths of the crevices, water held in the apertures by capillary force will be unremoved, or partly or completely pushed out of the crevices due to the impulsive forces. The crevice flows can vary from 0.0 mm³/drop for $B_j \leq 0.01$ mm to the entire column of water in the capillary for $B_j \geq 5$ mm.

Unlike the saturated crevices, unsaturated crevices will release water from the underside of the drip shield because of the film flows and dripping. When unsaturated, film flow on top of the drip shield will be intercepted by the crevices and pendant drops will be developed on the underside of the drip shield. The film flow rate equals to the crevice flow rate which depends on the crevice locations and orientation in the drip shield. The farther apart the crevice is

from the drip shield crown, the more water it will intercept. For the seepage rate of 25 mm/yr, the film thickness is determined to vary from 5 to 6 micro-meters as shown in Figure 6-8 and the volumetric flow rate as a function of crevice location can be found in Figure 6-7 in Section 6.1.5.

Water vapor molecules will condense to the drip shield surface by chemical and physical adsorption that create ultra-thin water films. Water adsorbed on horizontal surfaces is immobile because hydraulic gradients for the flow do not exist. However, water adsorbed on vertical walls of the internal structural reinforcement beams beneath the drip shield will flow under the influence of gravity. The film thickens along the downward flow path to accommodate the increase of mass. Pendant drops will be formed at the bottom of the vertical walls that fall to the waste packages. The film flow and dripping are controlled by the rate of adsorptive condensation.

Because adsorption is a function of temperature and relative humidity, the film thickness, mass and volumetric flow rates, and maximum velocity are calculated using the temperature and relative humidity histories predicted by the thermohydrologic model. With the temperature drops from 94.2 °C to 21.5 °C from year 1,500 to year 1,000,000 after closure, relative humidity rises from 96.0% to 99.9%. In response, the film thickness at the bottom of the internal structural reinforcement beams increases from 0.0025 μm to 0.260 μm, the mass and volumetric flow rates increase from 4.9×10^{-9} kg/m/yr to 1.3×10^{-1} kg/m/yr and from 5.0×10^{-9} liter/m/yr to 1.3×10^{-1} liter/m/yr, respectively. Average film flow velocity increases from less than 6.5×10^{-11} m/sec to about 3.9×10^{-6} m/sec.

7.2 WATER DRAINAGE MODEL

Water drainage of the drift floor are simulated with a glacial infiltration rate (normalized mean) for various drainage conditions. The glacial infiltration rate was used to bound the water influx to the repository geologic system. The heat output from the waste packages was not considered in order to minimize evaporation and to simulate the flow with maximum water content in the liquid phase. The THC and THM effects were accounted for by assuming fracture plugging. Fracture plugging is assumed to extend 3-meters below the drift floor. The drainage conditions evaluated include:

- Unplugged drift floor without sand drain (Case 1);
- Plugged drift floor without sand drain (Case 2); and
- Plugged drift floor with sand drain (Case 3).

For unplugged drift floor, drainage capacity of the fractures is sufficient for the removal of seepage water, and the invert is prevented from becoming saturated. Saturation levels in the invert are generally low, especially under the drip shield due to water diversion. A drip shield lobe which is defined as the zone of increased flux rate is evident. The fluxes in the zone adjacent to the drip shield are increased by a factor of three to four with respect to farfield flow.

The most significant effect due to plugging of the floor rock is to increase saturation levels in the invert and the surrounding floor rock. Saturation levels in the matrix of the floor rock are

increased from 0.88 to 0.98 or near saturation. Saturation levels in the invert increase from 0.15 to 0.98 or near saturation.

The placement of a sand drain for plugged floor results in a significant reduction of flux rates in the invert, and the extension of the dry shadow below the rock. Results show an increase in the absolute value of capillary pressure, and an attendant reduction of saturation level in the invert directly above the plugged fractures. The sand drain also provides a high degree of capillary driven flow in the same vicinity of the drip shield lobe.

With backfill in the emplacement drift, water is drawn laterally into the drift from the fractures in the host rock due to the more negative pressure in the backfill materials. It is our belief that without backfill, the drift opening will function as a capillary barrier for the flow in the host rock so water is diverted around the drift, resulting in less water entering the invert.

7.3 THERMOHYDROLOGIC MODEL

The line-averaged-heat-source, drift-scale thermohydrologic (LDTH) model used in the Multiscale Thermohydrologic Model was utilized in this study to investigate the influence of drift seepage on thermohydrologic (TH) conditions in the EBS, with an emphasis on TH conditions on the drip shield and in the invert. The LDTH model was modified so that drift seepage could be prescribed to occur on the drip shield. Various levels of drift seepage percentage (0%, 3%, and 30%) were considered for two different geographic locations in the repository, including one close to the repository center and another close to the eastern edge of the repository. Three infiltration-flux cases were also considered, including "lower", mean, and "upper" infiltration-flux cases.

Seepage onto the drip shield has a negligible effect on temperature on the drip shield and in the invert. Seepage onto the drip shield has a negligible effect on relative humidity on the drip shield and in the invert during the boiling period. The only significant change is to substantially increase the evaporation rate on the drip shield and in the invert. During the post-boiling period, drift seepage significantly shortens the duration of reduced *RH* conditions, particularly for the mean and "upper" infiltration-flux cases, with a smaller influence for the "lower" infiltration case.

The magnitude of peak temperatures and the duration of boiling conditions are found to increase with decreasing infiltration flux and with decreasing proximity to the edge of the repository. The duration of reduced *RH* conditions is also found to increase with decreasing infiltration flux and with decreasing proximity to the edge of the repository.

Temperature versus relative humidity trajectories are relatively unaffected by drift seepage until relative humidity exceeds 90 to 95%. Temperature as a function of relative humidity decreases with decreasing infiltration flux.

The liquid saturation in the invert is zero during the boiling period. Consequently, the duration of zero saturation in the invert increases with decreasing proximity to the repository edge and with decreasing infiltration flux. The period of zero liquid saturation in the invert also decreases with increasing drift seepage percentage. The magnitude of the final steady-state liquid saturation

increases with increasing seepage percentage.

The liquid-phase flux in the invert is zero during the boiling period. After the boiling period, there is a period during which water imbibes upward into the invert; thereafter, the influence of gravity-driven seepage overwhelms imbibition and the seepage flux drains out of the bottom of the invert.

7.4 DRIP SHIELD CONDENSATION MODEL

The onset of condensation is controlled more by the amount of seepage imposed on the drift than by infiltration at the ground surface. Condensation would start earlier as seepage increases. Condensation would also be triggered to form earlier in areas closer to the edge of the repository due to an earlier start on the cooling process, as compared to areas close to the center. Condensation is also controlled by the amount and direction of gas and liquid fluxes through the invert other than the temperature distribution within the EBS.

7.5 UNCERTAINTY ASSESSMENT

As discussed in Section 6, the sources of uncertainty in the WD&R model mainly include the variation in infiltration rates, spatial variability in drift seepage rates, waste types and waste placement locations, heat generation rates, thermal-hydrologic-chemical (THC) and thermal-hydrologic-mechanical (THM) effects on host rock fracture plugging, and uncertainties in corrosion properties for the drip shield. These uncertainty issues are addressed in the submodels in Section 6 and are summarized below. Uncertainty issues relating to the use of unqualified data corroborating assumptions are described in Section 7.6.

For the water diversion model, the major uncertainties are the spatial variation of in-drift seepage rates and the drip shield corrosion. Uncertainty in in-drift seepage rates was eliminated in the drip shield water diversion analysis by the use of the maximum seepage rate that could occur at the repository horizon (Section 5.1.6). The uncertainty in drip shield corrosion was accounted for by calculating the crevice flow with a wide range of crack apertures, i.e., from fine cracks that result in a capillary plug, to large openings that can pass any amount of water.

Uncertainties for the water drainage model include the variation in infiltration rates, the degree of host rock fracture plugging on the drift floor due to the THC and THM effects, and the effects of backfill vs. no-backfill. The drainage capacity of the drift floor was evaluated with the bounding infiltration rate based on glacial melting conditions and with the drift floor fractures varying from no plugging to completely plugged.

Sensitivity analyses were performed in the thermohydrologic model to account for the uncertainties, such as the variation in infiltration rates, spatial variability in drift seepage rates, waste types and waste placement locations, and heat generation rates. Uncertainties associated with the drip shield condensation model are the same as those in the thermohydrologic model and were addressed in the sensitivity analyses.

7.6 DISCUSSION OF DTNS AND TBVS

The thermohydrologic information and data within the emplacement drift with emphasis on conditions on the drip shield and invert are provided as a function of time in Figures 6-34 through 6-57. Appropriate developed data was submitted to the TDMS, this output data was assigned the following DTN: LL000903512342.003. The Water Drainage model part of the Water Distribution and Removal Model was not repeated for the no-backfill case (Section 1.2).

This document may be affected by technical product input information that requires confirmation. Any changes to the document that may occur as a result of completing the confirmation activities will be reflected in subsequent revisions. The status of the input information quality may be confirmed by review of the Document Input Reference System database.

There are two To Be Verified (TBV) data requirements in this report. This unqualified data consists of measured thermal and physical properties of crushed tuff invert material and is found in input DTNs:GS000483351030.003 and GS000683351030.006. Any changes in this input data during qualification will require reproducing the model.

Other unqualified data was used in the model as the basis for assumptions 5.2.13, 5.2.14, 5.2.15, 5.3.6, 5.3.9, 5.3.13, 5.3.14, 5.3.15, 5.3.16, 5.3.17, and 5.3.18. These were addressed through bounding calculations or sensitivity analyses. Any changes during data qualification are not considered to be of a magnitude as to significantly affect model results.

8. REFERENCES

8.1 DOCUMENTS CITED

Atkins, P.W. 1990. *Physical Chemistry*. 4th Edition. New York, New York: W.H. Freeman and Company, TIC: 245483.

Bear, J. 1988. *Dynamics of Fluids in Porous Media*. New York, New York: Dover Publications. TIC: 217568.

Bejan, A. 1995. *Convection Heat Transfer*. 2nd Edition. New York, New York. John Wiley & Sons. TIC: 241140.

Beyer, W. H., ed. 1987. *CRC Standard Mathematical Tables*. 28th Edition. 674. Boca Raton, Florida: CRC Press. TIC: 240507.

Birdi, K.S., ed. 1997. *Handbook of Surface and Colloid Chemistry*. Boca Raton, Florida: CRC Press. TIC: 249044.

Birkholzer, J.T. and Tsang, Y.W. 1998. *Numerical Analysis of Thermal-Hydrological Conditions in the Single Heater Test at Yucca Mountain*. Technical Paper TPM# 826. Berkeley, California: Lawrence Berkeley National Laboratory. ACC: MOL.19980715.0257.

Brodsky, N.S.; Riggins M.; Connolly, J.; and Ricci P. 1997. *Thermal Expansion, Thermal Conductivity, and Heat Capacity Measurements for Boreholes UE25 NRG-4, UE25 NRG-5, USW NRG-6, and USW NRG-7/7A*. SAND95-1955. Albuquerque, New Mexico: Sandia National Laboratories. ACC: MOL.19980311.0316.

Brooks, R.H. and Corey, A.T. 1966. "Properties of Porous Media Affecting Fluid Flow." *Journal of the American Society of Civil Engineers, Irrigation and Drainage Division*, 92, (IR2), 61-89. New York, New York: American Society of Civil Engineers. TIC: 216867.

Buscheck, T.A.; Shaffer, R.J.; and Nitao, J.J. 1997. *Pretest Thermal-Hydrological Analysis of the Drift-Scale Thermal Test at Yucca Mountain*. Livermore, California: Lawrence Livermore National Laboratory. ACC: MOL.19980507.0359.

Case, J.B. and Kelsall, P.C. 1987. *Modification of Rock Mass Permeability in the Zone Surrounding a Shaft in Fractured, Welded Tuff*. SAND86-7001. Albuquerque, New Mexico: Sandia National Laboratories. ACC: HQS.19880517.2264.

Chapman, A. J. 1974. *Heat Transfer*. New York, New York: Macmillan Company, Inc. TIC: 245061.

Corey, Arthur T. 1977. *Mechanics of Heterogeneous Fluids in Porous Media*. Fort Collins, Colorado: Water Resources Publications. TIC: 249047.

Crane, R. A. Vachon, R. I., and Khader, M. S. 1977. "Thermal Conductivity of Granular Materials – A Review." *Proceedings of the Seventh Symposium on Thermophysical Properties*. pp. 109-123. New York, New York: American Society of Mechanical Engineers. TIC 246057.

CRWMS M&O (Civilian Radioactive Waste Management System Management and Operating Contractor) 1996. *Engineered Barrier System Performance Requirements for Systems Study Report*. BB0000000-01717-5705-00001 REV01. Las Vegas, Nevada: CRWMS M&O. ACC: MOL.19970407.0169.

CRWMS M&O 1998. "Thermal Hydrology." *Chapter 3 of Total System Performance Assessment-Viability Assessment (TSPA-VA) Analyses Technical Basis Document*. B00000000-01717-4301-00003 REV 01. Las Vegas, Nevada: CRWMS M&O. ACC: MOL.19981008.0003.

CRWMS M&O 1999a. Not Used.

CRWMS M&O 1999b. *Classification of the MGR Ex-Container System*. ANL-XCS-SE-000001 REV 00. Las Vegas, Nevada: CRWMS M&O. ACC: MOL.19990928.0221.

CRWMS M&O 1999c. Enhanced Design Alternative II Report. B00000000-01717-5705-00131 Rev 00. Las Vegas, Nevada: CRWMS M&O. ACC: MOL.19990712.0194.

CRWMS M&O 2000a. *Abstraction of Drift Seepage*, ANL-NBS-MD-000005. REV 00. Las Vegas, Nevada: CRWMS M&O. ACC: MOL.20000322.0671.

CRWMS M&O 2000b. *Technical Work Plan: Subsurface Process Modeling FY 01 Work Activities*. TWP-MGR-MD-000013, REV 00. Las Vegas, Nevada: CRWMS M&O. ACC: MOL.20001117.0052

CRWMS M&O 2000c. *Drift Degradation Analysis*, ANL-EBS-MD-000027 REV 01. Las Vegas, Nevada: CRWMS M&O. ACC: MOL. Submit to RPC URN-0616.

CRWMS M&O 2000d. *Flow of Water and Pooling in a Waste Package*, ANL-EBS-MD-000055 REV 00. Las Vegas, Nevada: CRWMS M&O. ACC: MOL. Pending. URN-0663.

CRWMS M&O 2000e. *Engineered Barrier System Degradation, Flow, and Transport Process Model Report*. TDR-EBS-MD-000006 REV 00 ICN 01. Las Vegas, Nevada: CRWMS M&O. ACC: MOL.20000724.0479.

CRWMS M&O 2000f. *Engineered Barrier System Physical and Chemical Environment Model*. ANL-EBS-MD-000033 REV 01. Las Vegas, Nevada: CRWMS M&O. Submit to RPC URN-0618.

CRWMS M&O 2000g. *Design Analysis for the Ex-Container Components.*
ANL-XCS-ME-000001 REV 00. Las Vegas, Nevada: CRWMS M&O.
ACC: MOL.20000525.0374.

CRWMS M&O 2000h. *Engineering Barrier System/Features, Events, and Processes (FEPs)/
Degradation Modes Abstraction*, ANL-WIS-PA-000002 REV 01. Las Vegas, Nevada: CRWMS
M&O. ACC: MOL. Pending. URN-0655.

CRWMS M&O 2000i. *Multiscale Thermohydrologic Model.* ANL-EBS-MD-000049 REV 00
ICN 1. Las Vegas, Nevada: CRWMS M&O. Submit to RPC URN-0574.

CRWMS M&O 2000j. (Not used).

CRWMS M&O 2000k. *Drift-Scale Coupled Processes (DST and THC Seepage) Models.*
MDL-NBS-HS-000001 Rev 00. Las Vegas, Nevada: CRWMS M&O.
ACC: MOL.19990721.0523.

CRWMS M&O 2000l. *Thermal Tests, Thermal-Hydrological Analyses/Model Report.*
ANL-NBS-TH-000001 Rev 00. Las Vegas, Nevada: CRWMS M&O.
ACC: MOL.20000505.0231.

CRWMS M&O 2000m. (Not used).

CRWMS M&O 2000n. *Invert Effective Thermal Conductivity Calculation.*
CAL-WIS-TH-000004 REV 00. Las Vegas, Nevada: CRWMS M&O.
ACC: MOL.20000317.0593.

CRWMS M&O 2000o. *Unsaturated Zone Flow and Transport Model Process Model Report.*
TDR-NBS-HS-000002 REV 00 ICN 2. Las Vegas, Nevada: CRWMS M&O.
ACC: MOL.20000831.0280.

CRWMS M&O 2000p. *Mountain-Scale Coupled Processes (TH) Models.* MDL-NBS-HS-
000007 REV 00. Las Vegas, Nevada: CRWMS M&O. ACC: MOL.19990721.0528.

CRWMS M&O 2000q. *Determination of Granular Materials Thermal and Physical Properties.*
Input Transmittal 00396.T. Las Vegas, Nevada: CRWMS M&O.
ACC: MOL.20001113.0309.

CRWMS M&O 2000r. *Emplacement Drift System Description Document.*
SDD-EDS-SE-000001 REV 01. Las Vegas, Nevada: CRWMS M&O.
ACC: MOL.20000803.0348.

CRWMS M&O 2000s. *Subsurface Facility System Description Document.*
SDD-SFS-SE-000001 REV 01. Las Vegas, Nevada: CRWMS M&O.
ACC: MOL.20000807.0078.

CRWMS M&O 2000t. *EBS Radionuclide Transport Abstraction*. ANL-WIS-PA-000001 REV 00 ICN 01. Las Vegas, Nevada: CRWMS M&O. ACC: MOL.20000821.0358.

CRWMS M&O 2000u. *Tabulated In-Drift Geometric and Thermal Properties Used in Drift-Scale Models for TPSA-SR*. CAL-EBS-HS-000002 Rev 00. Las Vegas, Nevada: CRWMS M&O. ACC: MOL.20000718.0219.

CRWMS M&O 2000v. *Determination of Available Repository Siting Volume for the Site Recommendation*. TDR-NBS-GS-000003 Rev 00. Las Vegas, Nevada; CRWMS M&O. ACC: MOL.20000705.0054.

CRWMS M&O 2000w. *Monitored Geologic Repository Project Description Document*. TDR-MGR-SE-000004 Rev 02. Las Vegas, Nevada: CRWMS M&O. ACC: MOL.20001031.0062.

CRWMS M&O 2000x. *Site Recommendation Subsurface Layout*. ANL-SFS-MG-000001 Rev 00. Las Vegas, Nevada: CRWMS M&O. ACC: MOL.20000908.0276.

CRWMS M&O 2000y. *Ventilation Model*. ANL-EBS-MD-000030 Rev 00. Las Vegas, Nevada: CRWMS M&O. ACC: MOL.20000107.0330.

DOE (U.S. Department of Energy) 2000. *Quality Assurance Requirements and Description*. DOE/RW-0333P, Rev. 10. Washington, D.C.: Department of Energy, Office of Civilian Radioactive Waste Management. ACC: MOL.20000427.0422.

DeMarsily, G. 1986. *Quantitative Hydrology: Groundwater Hydrology Engineers*. San Diego, California: Academic Press. TIC: 208450.

Dyer, J.R. 1999. "Revised Interim Guidance Pending Issuance of New U.S. Nuclear Regulatory Commission (NRC) Regulations (Revision 01, July 22, 1999), for Yucca Mountain, Nevada." Letter from J.R. Dyer (DOE/YMSCO) to D.R. Wilkins (CRWMS M&O), September 3, 1999, OL&RC:SB-1714, with enclosure, "Interim Guidance Pending Issuance of New NRC Regulations for Yucca Mountain (Revision 01)." ACC: MOL.19990910.0079.

Fetter, C.W. 1993. *Contaminant Hydrogeology*. Upper Saddle River, New Jersey: Prentice-Hall. TIC: 240691.

Freeze, R.A. and Cherry, J.A. 1979. *Groundwater*. Englewood Cliffs, New Jersey: Prentice-Hall. TIC: 217571.

Hardin, E.L. 1998. *Near-Field/Altered-Zone Models Report*. UCRL-ID-129179. Livermore, California: Lawrence Livermore National Laboratory. ACC: MOL.19980630.0560.

Hartman, H.L., ed. 1992. *SME Mining Engineering Handbook*. 2nd Edition, Volume 2. Littleton, Colorado: Society for Mining, Metallurgy and Exploration. TIC: 206894.

- Himmelblau, D. M. 1996. *Basic Principles and Calculations in Chemical Engineering*. 6th Edition. Upper Saddle River, New Jersey: Prentice Hall. TIC: 249043.
- Ho, C.K. 1997. "Evaporation of Pendant Water Droplets in Fractures". *Water Resources Research*. 33, (12), 2665-2671. Washington, D.C.: American Geophysical Union. TIC: 246969.
- Holman, J.P. 1997. *Heat Transfer*. 8th Edition. New York, New York: McGraw-Hill Publishing. TIC: 239954.
- Incropera, F.P. and DeWitt, D.P. 1981. *Fundamentals of Heat Transfer*. New York, New York. John Wiley & Sons. TIC: 243842.
- Incropera, F.P. and DeWitt, D.P. 1996. *Introduction to Heat Transfer*. 3rd Edition. New York, New York. John Wiley & Sons. TIC: 241057.
- Isaaks, E.H. and Srivastava, R.M. 1989. *Applied Geostatistics*. New York, New York: Oxford University Press. TIC: 200301.
- Jury, W.A.; Gardner, W.R.; and Gardner, W.H. 1991. *Soil Physics*. 5th Edition. New York, New York: John Wiley & Sons. TIC: 241000.
- Keenan, J.H.; Keyes, F.G.; Hill, P.G.; and Moore, J.G. 1969. *Steam Tables, Thermodynamic Properties of Water Including Vapor, Liquid, and Solid Phases*. New York, New York: John Wiley & Sons. TIC: 246766.
- Kitanidis, P.K. 1997. *Introduction to Geostatistics: Applications in Hydrogeology*. New York, New York: Cambridge University Press. TIC: 236758.
- Lee, S., and Staehle R.W. 1997. "Adsorption of Water on Copper, Nickel, and Iron." *Corrosion*, 53, (1), 33-42. Houston, Texas: National Association of Corrosion Engineers. TIC: 244501.
- Lide, D.R. and Frederikse, H.P.R., eds. 1997. *CRC Handbook of Chemistry and Physics*. 78th Edition. Boca Raton, Florida: CRC Press. TIC: 243741.
- Liu, H.H.; Doughty, C.; and Bodvarsson, G.S. 1998. "An Active Fracture Model for Unsaturated Flow and Transport in Fractured Rocks." *Water Resources Research*, 34, (10), 2633-2646. Washington, D.C.: American Geophysical Union. TIC: 243012.
- Middleman, S. 1995. *Modeling Axisymmetric Flows – Dynamics of Films, Jets, and Drops*. Academic Press. San Diego, California: TIC: 246835.
- Milne-Thomson, L.M. 1968. *Theoretical Hydrodynamics*. 5th Edition. New York, New York: Dover Publications. TIC: 245838.

Mongano, G.S., Singleton, W.L., Moyer, T.C., Beason, S.C., Eatman, G.L.W., Albin, A.L., and Lung, R.C. 1999. *Geology of the ECRB Cross Drift - Exploration Studies Facility*. Yucca Mountain Project, Nevada. [Milestone SPG42GM3], Denver, Colorado: US Geological Survey. ACC: MOL.20000324.0614.

Mualem, Y. 1976. "A New Model for Predicting the Hydraulic Conductivity of Unsaturated Porous Media." *Water Resource Research*, 12, (3), 513-522. Washington, D.C.: American Geophysical Union. TIC: 217339.

Mutchler, C.K. 1967. "Parameters for Describing Raindrop Splash." *Journal of Soil Water Conservation*, 2, (x), 91-94. Ankeny, Iowa: Soil Conservation Society of America. On Order Library Tracking Number - 249049.

Nitao, J.J. 1998. *Reference Manual for the NUFT Flow and Transport Code, Version 2.0*. UCRL-MA-130651. Livermore, California: Lawrence Livermore National Laboratory. TIC: 238072.

NRC (U.S. Nuclear Regulatory Commission) 1999a. *Issue Resolution Status Report Key Technical Issue: Container Lift and Source Term*. Rev. 2. Washington, D.C.: U.S. Nuclear Regulatory Commission. TIC: 245538.

NRC 1999b. *Issue Resolution Status Report Key Technical Issue: Evolution of the Near-Field Environment*. Rev. 2. Washington, D.C.: U.S. Nuclear Regulatory Commission. ACC: MOL.19990810.0640.

NRC 1999c. *Issue Resolution Status Report Key Technical Issue: Repository Design and Thermal-Mechanical Effects*. Rev. 2. Washington, D.C.: U.S. Nuclear Regulatory Commission. ACC: MOL.20000306.0670.

NRC 1999d. *Issue Resolution Status Report Key Technical Issue: Thermal Effects on Flow*. Rev. 2. Washington, D.C.: U.S. Nuclear Regulatory Commission. ACC: MOL.19991021.0156.

Philip, J.R. 1977. "Unitary Approach to Capillary Condensation and Adsorption." *Journal of Chemistry and Physics*, 66, (11), 5069-5075. New York, New York: American Institute of Physics. TIC: 249050.

Philip, J.R.; Knight, J.H.; and Waechter, R. T. 1989. "Unsaturated Seepage and Subterranean Holes: Conspectus, and Exclusion Problem for Circular Cylindrical Cavities." *Water Resources Research*, 25, (1), pp. 16-28. Washington D.C.: American Geophysical Union. TIC: 239117.

Phillips, O. M. 1991. *Flow and Reactions in Permeable Rocks*. New York, New York: Cambridge University Press. TIC: 236237.

Robinson, R.N. 1987. *Chemical Engineering Reference Manual*. 4th Edition. Belmont, California: Professional Publications, Inc. On Order Library Tracking Number - 248647.

Rochester, M.C. and J.H. Brunton. 1974. "Surface Pressure Distribution during Drop Impingement." *The Fourth International Conference on Raindrop Erosion and Related Phenomena, Meersburg, Germany, I*, 371-393. City, State: Publisher. On Order Library Tracking Number - 249051.

Ryder, E.E.; Finley, R.E; George, J.T.; Ho, C.K.; Longenbaugh, R.S.; and Connolly, J.R. 1996. *Bench-Scale Experimental Determination of the Thermal Diffusivity of Crushed Tuff*. SANO94-2320. Albuquerque, New Mexico: Sandia National Laboratories. ACC: MOL.19961111.0011.

Saxena, N. S., Chohan, M.A.; and Guustafsson, S.E. 1986. "Effective Thermal Conductivity of Loose Granular Materials," *Journal of Applied Physics*. Volume 19 pp. 1625-1630. New York, New York : The Physics Institute. On Order Library Tracking Number - 249120.

Sokolnikoff, I.S. and Redheffer, R.M. 1966. *Mathematics of Physics and Modern Engineering*. 2nd Edition. New York, New York: McGraw-Hill. TIC: 238682.

Thibodeaux, L.J. 1979. *Chemodynamics - Environmental Movement of Chemicals in Air, Water, and Soil*. New York, New York: John Wiley & Sons. TIC: 249046.

van Genuchten, M.T. 1980. "A Closed-Form Equation for Predicting the Hydraulic Conductivity of Unsaturated Soils." *Soil Science Society of America Journal*, 44, (5), 892-898. Madison, Wisconsin: Soil Science Society of America. TIC: 217327.

van Genuchten, M.T.; Leij, F.J.; and Yates, S.R. 1991. *The RETC Code for Quantifying the Hydraulic Functions of Unsaturated Soils*. EPA Report 600/2-91/065. Riverside, California: U.S. Salinity Laboratory, U.S. Department of Agriculture. TIC: 236938.

Weast, R.C. and Astle, M.J., eds. 1981. *CRC Handbook of Chemistry and Physics: A Ready Reference Book of Chemical and Physical Data*. 62nd Edition. Boca Raton, Florida: CRC Press. TIC: 240722.

Winterkorn, H.F. and Fang, H-Y, eds.. 1975. *Foundation Engineering Handbook*. pages 37, 72, 78, 79, 117, 156, 256, 257, 266, and 267. New York, New York: Van Nostrand Reinhold Company. TIC: 241820.

Willhite, G. P.; Kunii, D.; and Smith, J. M. 1962. "Heat Transfer in Beds of Fine Particles." *American Institute of Chemical Engineers Journal*. Volume 8, No. 3, p. 340. New York, New York: American Institute of Chemical Engineers. On Order Library Tracking Number - 249121.

YMP (Yucca Mountain Site Characterization Project) 2000. *Q-List*. YMP/90-55Q, Rev. 6. Las Vegas, Nevada: Yucca Mountain Site Characterization Office. ACC: MOL.20000510.0177.

8.2 CODES, STANDARDS, REGULATIONS, AND PROCEDURES

AP-2.21Q, Rev. 0. Quality Determinations and Planning for Scientific, Engineering, and Regulatory Compliance Activities. Washington, D.C.: U.S. Department of Energy, Office of Civilian Radioactive Waste Management. ACC: MOL.20000802.0003.

AP-3.10Q, Rev. 2, ICN 3. *Analyses and Models*. Washington, D.C.: U.S. Department of Energy, Office of Civilian Radioactive Waste Management. ACC: MOL.20000918.0282.

AP-3.15Q, Rev. 2, ICN 0. *Managing Technical Product Inputs*. Washington, D.C.: U.S. Department of Energy, Office of Civilian Radioactive Waste Management. ACC: MOL.20001109.0051.

AP-SI.1Q, Rev. 2, ICN 4, ECN 1. *Software Management*. Washington, D.C.: U.S. Department of Energy, Office of Civilian Radioactive Waste Management. ACC: MOL.20001019.0023.

AP-SIII.3Q, Rev. 0, ICN 3. *Submittal and Incorporation of Data to the Technical Data Management System*. Washington, D.C.: U.S. Department of Energy, Office of Civilian Radioactive Waste Management. ACC: MOL.20000418.0808.

AP-SV.1Q, Rev. 0 ICN 2. *Control of the Electronic Management of Information*. Washington, D.C.: U.S. Department of Energy, Office of Civilian Radioactive Waste Management. ACC: MOL.20000831.0065.

ASTM C1252-98. 1998. "Standard Test Methods for Uncompacted Void Content of Fine Aggregate (as Influenced by Particle Shape, Surface Texture, and Grading)." West Conshohocken, Pennsylvania: American Society for Testing and Materials. TIC: 247431.

CRWMS M&O 1999. *Software Code: RETC V1.1*. V1.1. 10099-1.1-00. URN-0360.

Lawrence Livermore National Laboratory 1999a. *Software Code: NUFT V3.0s*. V3.0s. 10088-3.0s-00.

Lawrence Livermore National Laboratory 1999b. *Software Routine: CONVERTCOORDS V1.1*. V1.1. 10209-1.1-00.

Lawrence Livermore National Laboratory 1999c. *Software Routine: XTOOL V10.1*. V10.1. 10208-10.1-00.

Lawrence Livermore National Laboratory 1999d. *Software Routine: YMESH V1.53*. V1.53. 10172-1.53-00.

Lawrence Livermore National Laboratory 2000a. *Software Routine: chim_surf_TP V1.0*. V1.0. ANL-EBS-MD-000032.

Lawrence Livermore National Laboratory 2000b. *Software Routine: columnInfiltration V1.1*. V1.1. ANL-EBS-MD-000032.

Lawrence Livermore National Laboratory 2000c. *Software Routine: cover V1.1. V1.1.*
ANL-EBS-MD-000032.

Lawrence Livermore National Laboratory 2000d. *Software Routine: rme6 V1.1. V1.1.*
ANL-EBS-MD-000032.

QAP-2-3, Revision 10. *Classification of Permanent Items.* Las Vegas, Nevada: CRWMS M&O.
ACC: MOL.19990316.0006.

8.3 SOURCE DATA BY DATA TRACKING NUMBER

GS000483351030.003. Thermal Properties Measured 12/01/99 to 12/02/99 Using the ThermoLink Soil Multimeter and Thermal Properties Sensor on Selected Potential Candidate Backfill Materials Used in the Engineered Barrier System. Submittal Date 04/21/2000.

GS000683351030.006 Uncompacted Bulk Density for Analyses Analysis Performed 02/02/00 to 05/23/00 on Potential Backfill Materials (White Wyoming#2, White Wyoming #3, Apex Crushed Limestone, Overton Sand, Colorado Silica, Sand Ramp Sand, Fine Crushed Tuff, 4-10 Crushed Tuff, 4-10 Silica, 8-20 Sand, 12-20 Sand, 50-200 Dolostone) Used in the Engineered Barrier System. Submittal date: 08/21/1998.

GS980808312242.015. Water Retention and Unsaturated Hydraulic Conductivity Measurements for Various Size Fractions of Crushed, Sieved, Welded Tuff Samples Measured Using a Centrifuge. Submittal date: 08/21/1998.

LB990861233129.001. Drift Scale Calibrated 1-D Property Set, FY99. Submittal date: 08/06/1999.

LB990861233129.002. Drift Scale Calibrated 1-D Property Set, FY99. Submittal date: 08/06/1999.

LB990861233129.003. Drift Scale Calibrated 1-D Property Set, FY99. Submittal date: 08/06/1999.

LB99EBS1233129.001. Natural Environment Data for Engineered Barrier System (EBS) Basecase. Submittal date: 11/29/1999.

LB99EBS1233129.003. Natural Environment Data for Engineered Barrier System (EBS) Basecase. Submittal date: 11/29/1999.

LB99EBS1233129.004. Natural Environment Data for Engineered Barrier System (EBS) Basecase. Submittal date: 11/29/1999.

MO9912EBSPWR28.001. Particle Size Data, Water Potential Data, and hydraulic Conductivity Data for Overton Sand Used in the Water Diversion Model AMR (ANL-EBS-MS-000028 Rev 00). Submitted date: 12/02/99.

MO9901YMP98017.001. Fracture Flux at Repository for QB.OUT. Submittal date: 01/05/1999.

MO9911MWDEBSWD.000. EBS Water Drainage Model. Submittal date: 11/29/1999.

SN9907T0872799.001. Heat Decay Data and Repository Footprint for Thermal-Hydrologic and Conduction-Only Models for TSPA-SR (Total System Performance Assessment-Site Recommendation). Submittal date: 07/27/1999.

SN9907T0872799.002. Effective Thermal Conductivity for Drift Scale Models Used in TSPA-SR (Total System Performance Assessment-Site Recommendation). Submittal date: 03/26/1998.

9. ATTACHMENTS

- Attachment I. Crevice Flow by Interception of Film Flow
- Attachment II. Crevice Flow by Impulsive Force
- Attachment III. Thin Film Flow by Adsorptive Condensation
- Attachment IV. Verification of software Routine COVER V1.1
- Attachment V. Calculation of the Coordinates of the Chimney Locations
- Attachment VI. Verification of Software Routines CHIM_SURF_TP V1.0
- Attachment VII. Verification of Software Routine COLUMNINFILTRATION V1.1
- Attachment VIII. Verification of Software Routine RME6 V1.1
- Attachment IX. Calculation of the Normalized Infiltration Rates
- Attachment X. Hydrologic and Thermal Properties of the Overton Sand
- Attachment XI. Computer Files for Water Drainage Model
- Attachment XII. Comparison of NUFT Flux Rates with a Closed Form Solution for Flow near a Cylindrical Inclusion
- Attachment XIII. Verification of Excel 97 Macro expand
- Attachment XIV. Hydrologic and Thermal Properties of the Invert
- Attachment XV. RETC Analysis for the Crushed Tuff Invert
- Attachment XVI. Attached Compact Disk (CD)

ATTACHMENT I
Crevice Flow by Interception of Film Flow

ATTACHMENT I. CREVICE FLOW BY INTERCEPTION OF FILM FLOW

Section 6.1.5 describes this calculation and its inputs. Electronic file of this attachment is saved as "crevice_flow_f.mcd" in attached CD in Attachment XVI.

$$\rho_w := 983.2 \frac{\text{kg}}{\text{m}^3} \quad \mu_w := 4.665 \cdot 10^{-4} \text{ Pa}\cdot\text{s} \quad q := 25 \frac{\text{mm}}{\text{yr}}$$

$$w_c := 1.0 \cdot \text{m} \quad R := 1.3 \cdot \text{m}$$

$$g = 9.80665 \text{ ms}^{-2} \quad \mu\text{m} := 10^{-6} \cdot \text{m}$$

$$\theta := 0, 0.5 \cdot \frac{\pi}{180} .. 75 \cdot \frac{\pi}{180}$$

$$Q(\theta) := q \cdot R \cdot \theta \cdot 1 \cdot \text{m} \quad (\text{Equation 6.17})$$

$$\delta(\theta) := \sqrt[3]{\frac{3 \cdot \mu_w \cdot q \cdot R \cdot \theta}{\rho_w \cdot g \cdot \sin(\theta)}} \quad (\text{Equation 6.18})$$

Results

Spot check Mathcad calculations at $\theta = 10^\circ \pi/180$

$$\delta_1 \left(10 \cdot \frac{\pi}{180} \right) = 5.32 \mu\text{m}$$

$$Q \left(10 \cdot \frac{\pi}{180} \right) = 5.67 \frac{\text{liter}}{\text{yr}}$$

Results using a calculator at $\theta = 10^\circ \pi/180$

$$\delta(\theta) = 5.32 \mu\text{m, and}$$

$$Q(\theta) = 5.67 \text{ liter/yr}$$

(Check)

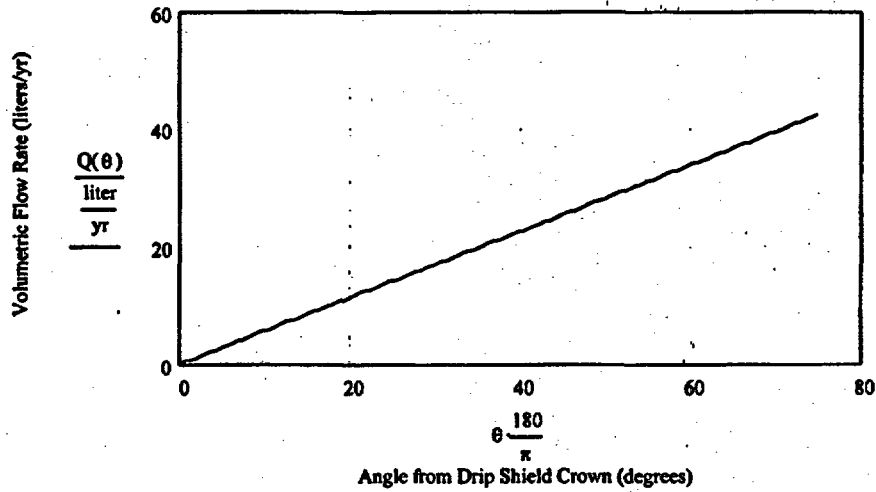


Figure I-1 Volumetric Flow Rate vs. Crevice Location

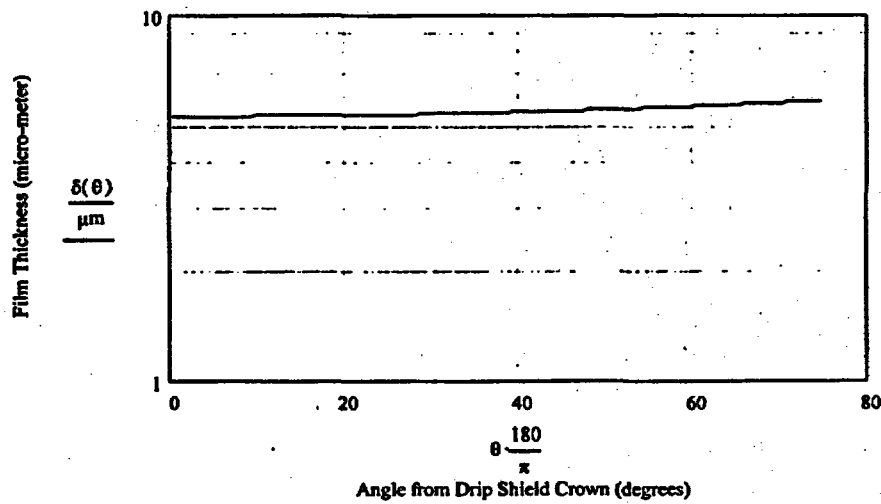


Figure I-2 Film Thickness vs. Crevice Location

ATTACHMENT II.
Crevice Flow by Impulsive Force

ATTACHMENT II. CREVICE FLOW BY IMPULSIVE FORCE

Section 6.1.6 describes the calculation and inputs presented below, electronic file of this attachment is saved as "crevid_flow_p.mcd" in attached CD:

$$\begin{aligned} \sigma_w &:= 0.06624 \frac{\text{N}}{\text{m}} & \rho_w &:= 983.2 \frac{\text{kg}}{\text{m}^3} & \mu_w &:= 4.665 \cdot 10^{-4} \cdot \text{Pa} \cdot \text{s} \\ P_{\text{max}} &:= 22223 \cdot \text{Pa} & \tau &:= 2.4 \cdot 10^{-3} \cdot \text{s} & \Delta t &:= 15 \cdot \text{mm} \\ j &:= 1, 2, \dots, 17 & w_c &:= 3.5 \cdot \text{mm} \end{aligned}$$

Table II-1 Input Parameters for Calculation (from Table 6-1)

$B_j :=$	$H_j :=$	$\theta_j :=$
0.001-mm	15-mm	90.06
0.01-mm	15-mm	90.63
0.1-mm	15-mm	96.27
0.2-mm	15-mm	102.62
0.3-mm	15-mm	109.12
0.4-mm	15-mm	115.90
0.5-mm	15-mm	123.10
0.6-mm	15-mm	130.94
0.7-mm	15-mm	139.86
0.8-mm	15-mm	150.89
0.9-mm	15-mm	169.38
0.916-mm	15-mm	180
1-mm	13.74mm	180
2-mm	6.87-mm	180
3-mm	4.58-mm	180
4-mm	3.43-mm	180
5-mm	2.75-mm	180

Solving Equations

$$U_{0j} := \int_0^{\tau} \frac{P_{\text{max}} - \frac{2 \cdot \sigma_w \cdot (1 + \cos(\theta_j))}{\rho_w \cdot \Delta t \cdot B_j}}{\frac{1}{t} + \frac{12 \cdot \mu_w}{\rho_w \cdot (B_j)^2}} dt$$

(Equations 6.22 & 6.23)

$U_{0j} := \text{if}(U_{0j} > 0, U_{0j}, 0)$ Negative velocity implies that the impulsive force is insufficient to overcome the resistance forces, hence no water flows in the crevices (See discussions in Section 6.1.6). This conditional statement is to set negative velocity to zero.

$Q_j := U_{0j} \cdot B_j \cdot w_c \cdot \tau$ (Equation 6.24)

$V_j := B_j \cdot w_c \cdot H_j$ V_j is the volume of water being held in the capillarity, or the maximum flow that could be induced by a drop.

$Q_j := \text{if}(Q_j > V_j, V_j, Q_j)$ Set $Q_j = V_j$ if the crevice flow induced by a drop is greater than the volume of water being held in the capillarity.

Results

Table II-2 Capillary Flow Induced by a Drop

$\frac{B_j}{\text{mm}} =$	$\frac{Q_j}{\text{mm}^3} =$	$\frac{V_j}{\text{mm}^3} =$	$\frac{U_{0j}}{\frac{\text{m}}{\text{s}}} =$
0.001	0	0	0
0.01	0	1	0.02
0.1	0.8	5	0.95
0.2	2.4	11	1.46
0.3	4.1	16	1.63
0.4	5.7	21	1.71
0.5	7.3	26	1.74
0.6	8.7	31	1.73
0.7	10.4	37	1.76
0.8	11.8	42	1.76
0.9	13.3	47	1.76
0.916	13.7	48	1.78
1	15	48	1.79
2	30.3	48	1.8
3	45.5	48	1.8
4	48	48	1.81

The capillary flow Q_j is used for graphic presentation in Figure 6-10.

Check the above calculations using the integrated equation

Set parameters

$$a_j := \frac{P_{\max}}{\rho_w \cdot \Delta t} - \frac{2 \cdot \sigma_w \cdot (1 + \cos(\theta_j))}{\rho_w \cdot \Delta t \cdot B_j}$$

$$b_j := \frac{12 \cdot \mu_w}{\rho_w \cdot (B_j)^2}$$

The integrated equation for U_{oj} can be expressed as

$$U_{oj} := \frac{a_j}{\tau \cdot (b_j)^2} \cdot (b_j \cdot \tau - \ln(1 + b_j \cdot \tau))$$

$U_{oj} =$

5.22·10 ⁻⁴
0.02
0.95
1.46
1.63
1.71
1.74
1.73
1.76
1.76
1.76
1.78
1.79
1.8
1.8
1.81

ms⁻¹

Set negative velocity equal to zero, the velocities calculated using the integrated equation are the same as those calculated in Table II-2.

(Check)

ATTACHMENT III.
Thin Film Flow by Adsorptive Condensation

ATTACHMENT III. THIN FILM FLOW BY ADSORPTIVE CONDENSATION

Section 6.1.7 discusses the theory development and equation derivation presented in the following and the electronic file of this attachment is saved as "adsorptive_film.mcd" in attached CD.

Input thermophysical properties of water to define interpolation functions. Data in matrix A include: (0) temperature; (1) saturated vapor pressure; (2) specific volume of liquid water; (3) specific volume of water vapor; and (4) viscosity of liquid water.

A := READPRN ("properties.prn")

Table III-1 Thermophysical Properties of Water

A =

	0	1	2	3	4
0	273.15	$6.11 \cdot 10^{-3}$	1	206.3	$1.75 \cdot 10^3$
1	275	$6.97 \cdot 10^{-3}$	1	181.7	$1.652 \cdot 10^3$
2	280	$9.9 \cdot 10^{-3}$	1	130.4	$1.422 \cdot 10^3$
3	285	0.014	1	99.4	$1.225 \cdot 10^3$
4	290	0.019	1.001	69.7	$1.08 \cdot 10^3$
5	295	0.026	1.002	51.94	959
6	300	0.035	1.003	39.13	855
7	305	0.047	1.005	29.74	769
8	310	0.062	1.007	22.93	695
9	315	0.081	1.009	17.82	631
10	320	0.105	1.011	13.98	577
11	325	0.135	1.013	11.06	528
12	330	0.172	1.016	8.82	489
13	335	0.217	1.018	7.09	453
14	340	0.271	1.021	5.74	420
15	345	0.337	1.024	4.683	389
16	350	0.416	1.027	3.846	365
17	355	0.51	1.03	3.18	343
18	360	0.621	1.034	2.645	324
19	365	0.751	1.038	2.212	306
20	373.15	1.013	1.044	1.673	284

Note: Data adopted from Incropera and DeWitt 1996, page 846

- 1) Locate the electronic source file(s) in the O:\DocControl\Ecopies\[folder by DC tracking].
- 2) Locate and move the zip file into the FTP server by DC tracking number, native(s).
- 3) Verify electronic source file (native file).

Items to check:

- a) Headers/Footers
 - b) page numbers
 - c) first line/last line of each page
 - d) hand written notes, get approval before proceeding
 - e) electronic file for attachments (TWP's may have scanned attachments)
- 4) Resolve discrepancies.
 - a) Check the entire document and flag before discrepancy notification.
 - b) Prepare discrepancy using Lotus-Notes, no phone calls.
 - c) Give a copy of Lotus-Note and the document to QC'r prior to sending to document owner.
 - d) Use the following format:

To: [Document Owner]
Cc: Linda Mantor
Subject line: [Document ID],[DC tracking number]

During the AP-6.1Q Controlled Document Acceptance process (Section 5.3) the following discrepancy was identified:

(List discrepancies in this area. If more than one, please number them)

Please note that this document is being placed on hold. If the discrepancy is not resolved by cob (three days away), the document will be returned to you.

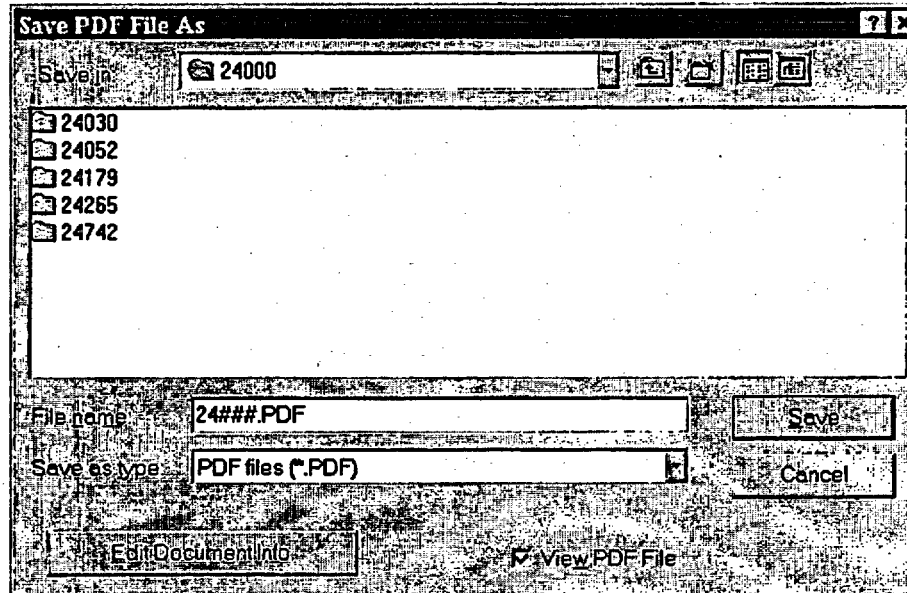
If you have any questions about this issue, please contact myself at (your number) or Linda Mantor at (702) 295-7162.

- e) Follow up on all discrepancies at the beginning of your shift. Please follow up with a Lotus-Note and a phone call, cc supervisor on all follow-up Lotus-Notes.
 - f) If you receive no response send a final Lotus-Notes informing the Document Owner that their document will be returned to them, cc supervisor.
- 5) When discrepancies are resolved, replace electronic source file (native file) in the FTP Server, as necessary.
 - 6) Pdf using the Document Control Tracking number as the file name. Create one pdf file for the entire document, unless the document is divided into sections, volumes, books, or have their own tables of contents. Operator may have to create separate pdf files and merge them into one.

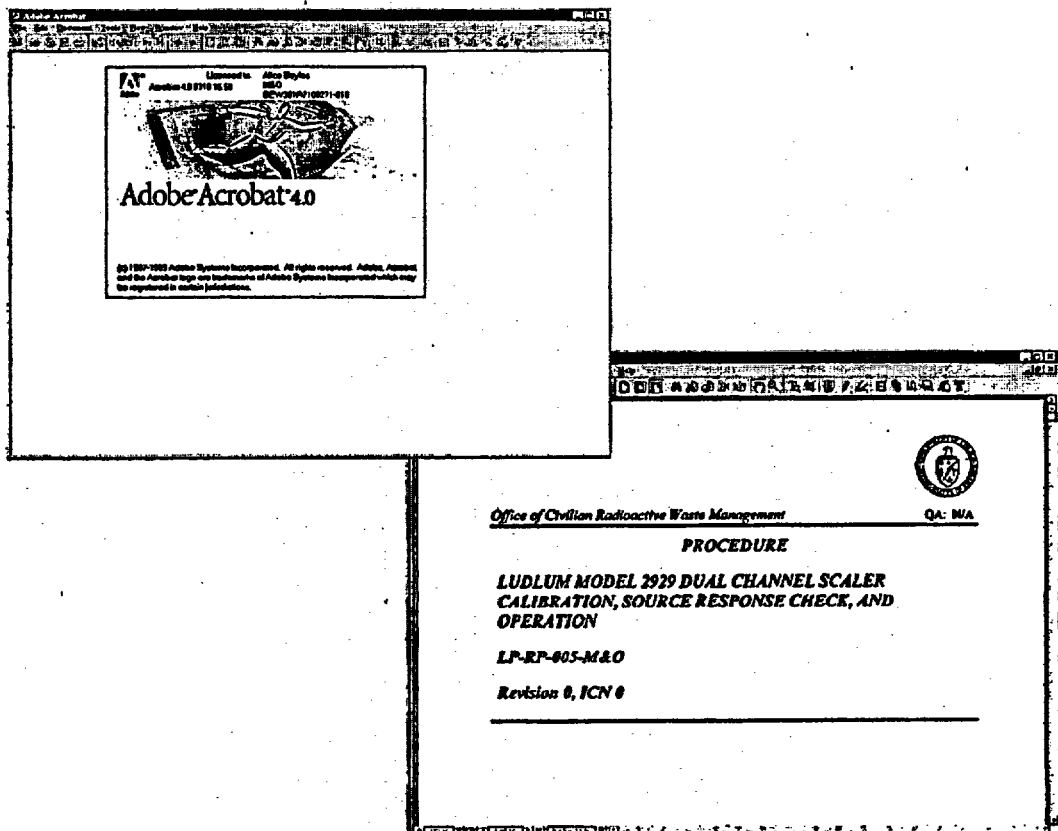
Note: Pdf creation may be slightly different on each computer. Every effort is being made to unilaterally make pdf creation standard on each computer. Please be patient during this process.

Method 1:

- 1) With the electronic file opened Select File>Print from the text menu. Once the print dialog appears, select from the pull-down menu on the Printer Name and select *Adobe PDFWriter*. Click OK. The "Save PDF File As" dialog box will appear. Ensure you are in the correct location for the document.

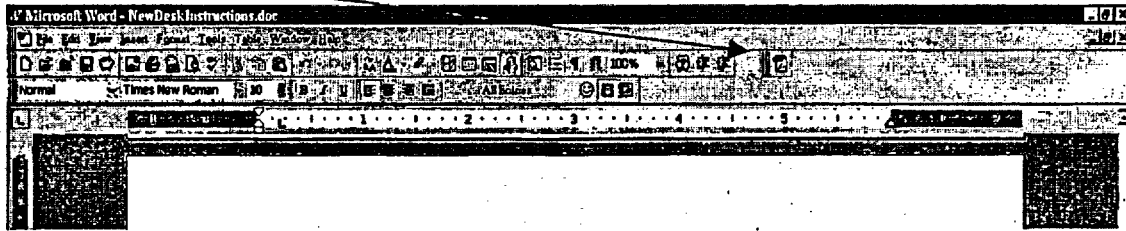


- 2) Save the file in the O:\DocControl\Ecopies[tracking number subset, for example 24000]. Use the DC tracking number as the new pdf file name. Click Save. Adobe Acrobat will launch.

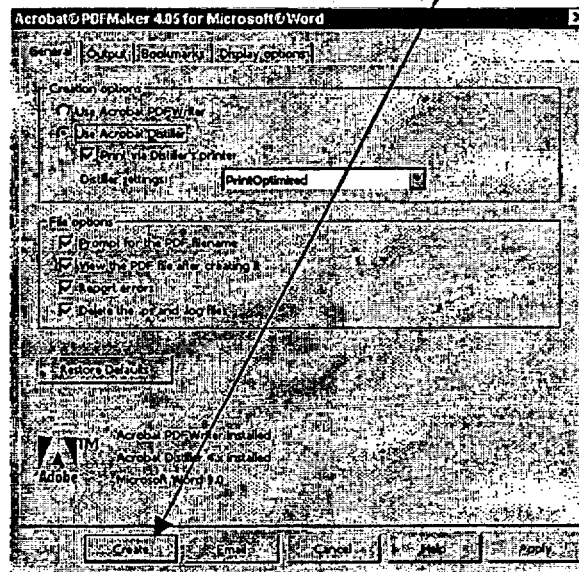


Method 2

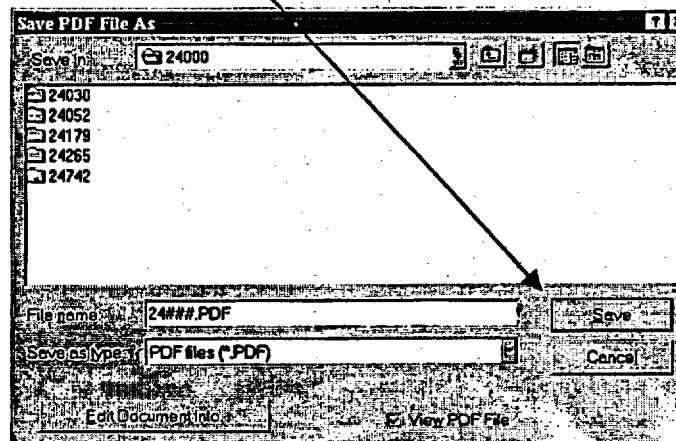
- 1) If available from any Microsoft software, (MSWord, MSExcel, etc.,) select the Adobe Acrobat PDF Maker Icon:



- 2) Acrobat PDF Maker dialog box will appear. Click create.

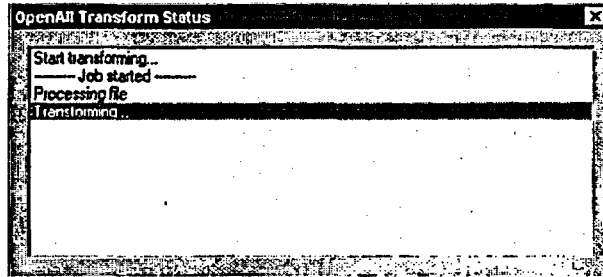


- 3) Several Dialog boxes will appear. If you need to stop the PDF process at any time click "Cancel". The final dialog box will prompt you for a file name. Insure you are in the correct menu location for the procedure/document you are saving. Click "Save."



Method 3 – (Will be used upon the approval of AP-6.1Q, Revision 6 and the installation of new Adobe Acrobat 4.05 software.)

- 1) From Windows Explorer locate the electronic files and insure all electronic files, which create the document, are present in the O:\Document Control\Ecopies\[DC Tracking number subsection]\by DC Tracking number.
- 2) Open Adobe Acrobat. Create the pdf by click>hold>drag>drop from Windows Explorer to Adobe Acrobat. The "Open All Transform Status" dialog box will appear. Allow the program to run uninterrupted. This may take a few seconds to a few minutes depending on size and intricacy of the document.

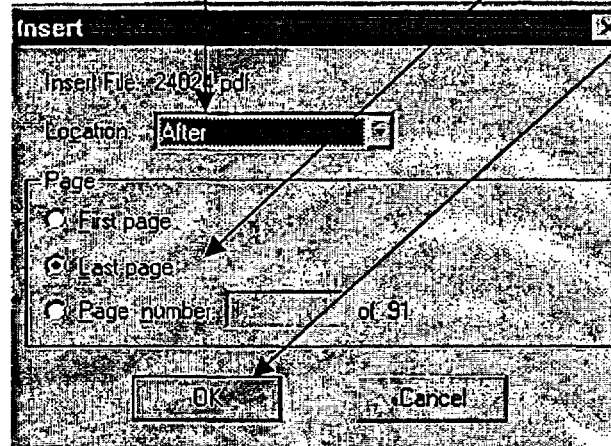


- 3) Repeat step 2 for all remaining electronic file in the "O" drive.
- 4) If the document require merging several pdfs, go to the Merge Pdfs section.

7) Merge pdfs:

For all Methods used merging the pdf's created which make up the document may need to be done. Follow these steps.

- 1.) From Adobe Acrobat, open the first pdf that creates the document. From the text menu select "Document" . From the drop down menu select "Insert Pages". The "Select File to Insert" dialog box will appear. Select the next file to insert. Click "Open". The "Insert" dialog box will appear. Ensure the file location is set to "AFTER" and the page is set to "Last page". Click OK.



- 2.) Continue merging until all pdfs are inserted. Save.

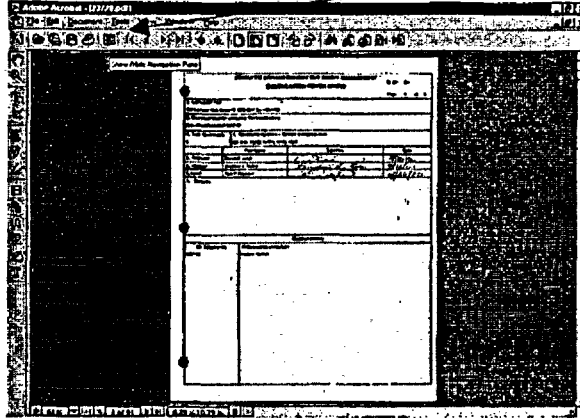
Note: Do not merge files for Pdfs, which are extremely large, beyond a 100mb files size, and are intended to be divided into sections, volumes, books, or have their own tables of contents and are directed not to merge.

- 3.) For all documents except procedures and technical work plans "Bookmarking" is mandatory.

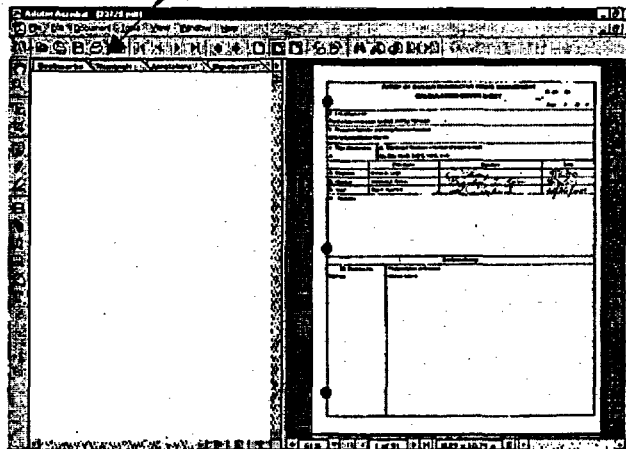
7) Create Bookmarks for the PDF file as follows:

NOTE: A bookmark is a Table of Contents that allows hypertext links to connect one instantly to a section of the PDF file without scrolling to locate desired information within the document.

- a) Open the navigation window in Adobe Acrobat, by clicking the Show/Hide Navigation Pane icon on the button bar menu.



- b) The "Bookmarks" window will open.



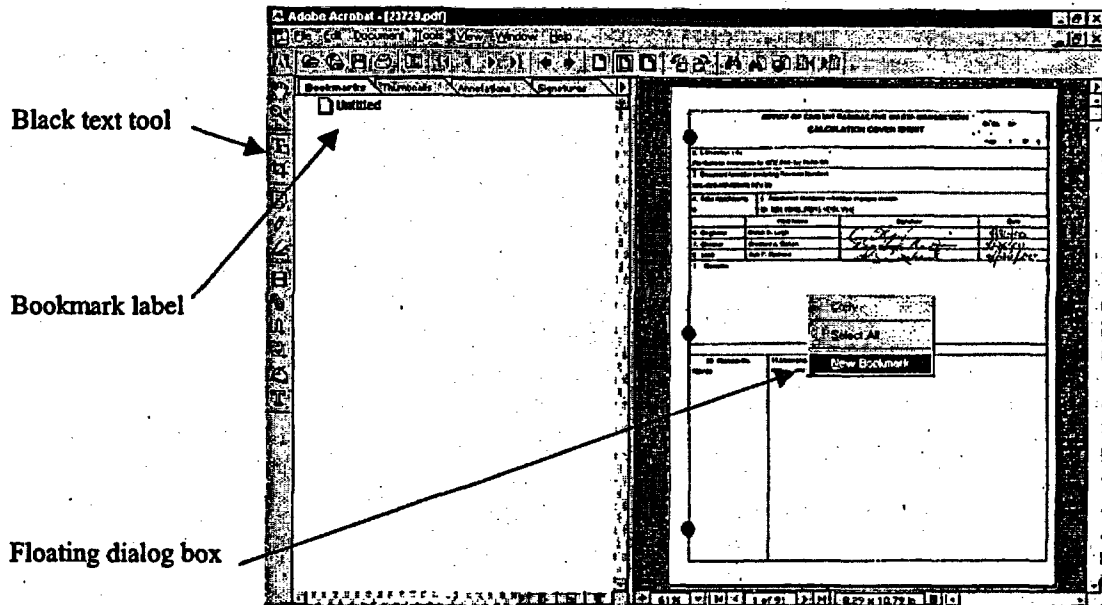
- c) Select the black text tool from the button menu.

Note: The button bars appears here on the top and side. Button bars can be moved anywhere on the working screen as the operator so desires.

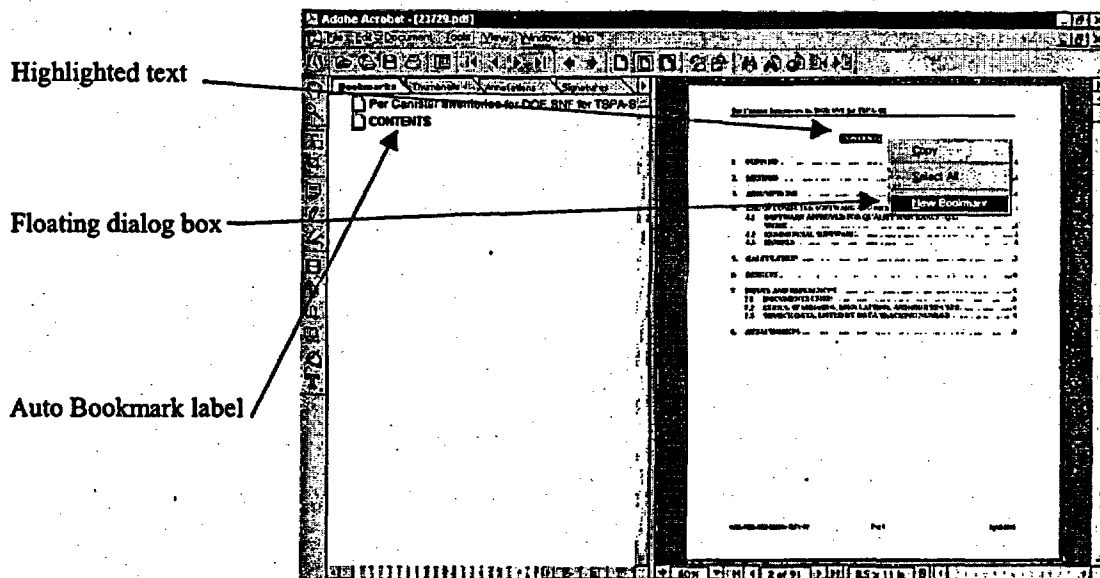
d) With the black text tool selected place cursor on text to be used for the bookmark label.

Note: Text on a scan page cannot be select without running "Paper Capture" first. Go to section on "How to Page Capture."

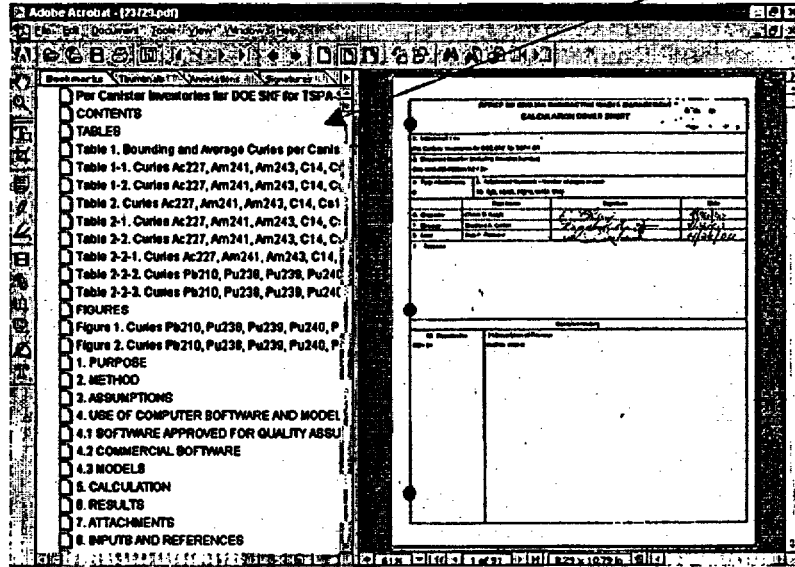
e) Bookmarking can still be achieved on a scanned page by selecting the black text tool, placing it on the page and right mouse click. When the floating dialog box appears select New Bookmark.



f) For scanned page type-in the title of the document for the first bookmark. If using highlighted text the bookmark label will appear in the "Bookmarks" window automatically.



g) Continue for each heading in the document. Include header numbering, signature pages, revision history, summary, disclaimers, acronyms, tables, figures, references and appendices/indexes.



h) Indent the bookmarks by dragging and dropping into place within the bookmark structure.

- g) the middle). Select blue (all bookmarks and links, within the document, must be blue).
- h) Select the **Link Tool** from the vertical toolbar. Pressing the left mouse button, drag a tight box
- i) around the selected text. A dialogue box will appear. Select **Invisible Rectangle** in the **Type** drop-down
- j) menu. Scroll down to the correct page where the text should link to (i.e. If my selected text is
- k) **Appendix A**, scroll down to the actual **Appendix A**. This will allow the user to simply click on the
- l) **Appendix A** link and be transported to the actual **Appendix A** page). Select **Set Link** to create the
- m) **hypertext link**.
- n) Create the **hypertext links** for the title of the document, the content page of the document, the first
- o) level sections inside that content page, all figures, all tables, and a link to the appendix.
- p) **NOTE: Critical documents receive special treatment and may require additional links. Check with Sandi**
- q) **Moore.**
- r) **Scan signature, ECN pages, Blues Sheet or any other pages with hand written notes. (Get approval for hand written pages before scanning.)**
- s) **Merge all pdfs associated to procedure/document.**
- t) **Verify pdf against the hard copy**
- u) **Bookmark all documents. (Do not bookmark plans/procedures.)**
- v) **Load the pdf onto the FTP Sever, with the exception of procedures.**
- w) **Create a OPDD cover page (splash page)**
- x) **Make copies for Master file, RTN (Q procedure only), CSR, original document to records.**

Use temperature as the independent variable to define interpolation functions, check interpolation values against Incropera and DeWitt (1996, p.846)

Saturated Vapor Pressure

$$P_{\text{sat}}(T) := \text{linterp}\left[\left(A^{<0>}\right), A^{<1>}, \frac{T}{K}\right] \cdot \text{bar}$$

$$P_{\text{sat}}(342\text{K}) = 0.298 \cdot \text{bar} \quad (\text{check})$$

$$T := 273.15\text{K}, 274.15\text{K}.. 373.15\text{K} \quad (0\text{ }^\circ\text{C to } 100\text{ }^\circ\text{C})$$

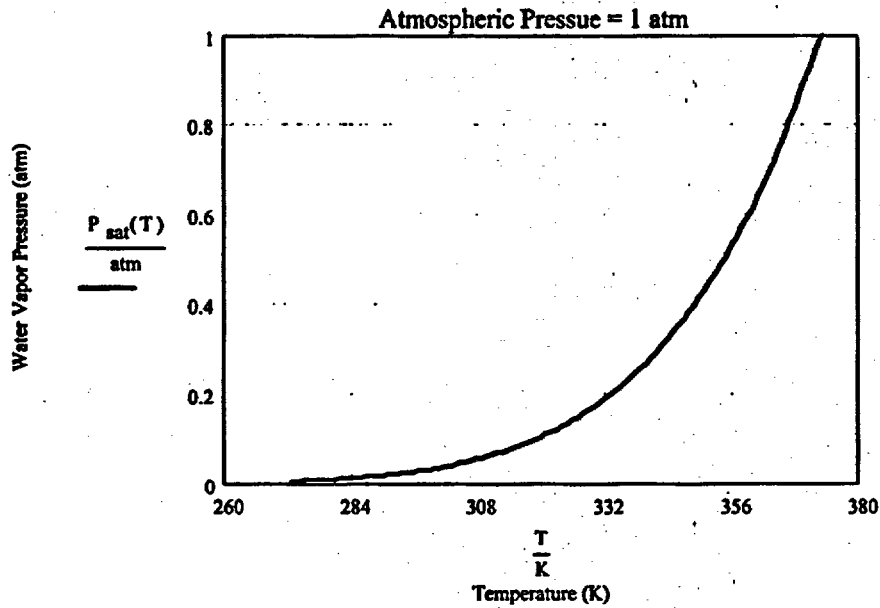


Figure III-1 P_{sat} as a function of temperature

Specific Volume of Liquid Water and Water Vapor

$$v_w(T) := \text{linterp}\left[\left(A^{<0>}\right), A^{<2>}, \frac{T}{K}\right] \cdot 10^{-3} \frac{\text{m}^3}{\text{kg}}$$

$$v_v(T) := \text{linterp}\left[\left(A^{<0>}\right), A^{<3>}, \frac{T}{K}\right] \frac{\text{m}^3}{\text{kg}}$$

$$v_w(342\text{-K}) = 1.022 \times 10^{-3} \text{ m}^3 \text{ kg}^{-1} \quad (\text{check})$$

$$v_v(342\text{-K}) = 5.317 \text{ m}^3 \text{ kg}^{-1} \quad (\text{check})$$

Absolute Viscosity of Liquid Water

$$\mu_w(T) := \text{linterp}\left[A^{(0)}, A^{(4)}, \frac{T}{K}\right] \cdot 10^{-6} \cdot \text{N} \cdot \frac{\text{s}}{\text{m}^2}$$

$$\mu_w(342\text{-K}) = 4.076 \times 10^{-4} \text{ N} \cdot \frac{\text{s}}{\text{m}^2} \quad (\text{check})$$

Calculate density of liquid water and water vapor

$$\rho_w(T) := \frac{1}{v_w(T)}$$

$$\rho_v(T) := \frac{1}{v_v(T)}$$

Define other Constants

$$\lambda := 10^{-10} \cdot \text{m}$$

$$\text{Angstrom} := 10^{-10} \cdot \text{m} \quad R := 461.8 \cdot \frac{\text{J}}{\text{kg} \cdot \text{K}}$$

$$B := 25 \cdot \text{mm} \quad (\text{CRWMS M\&O 2000g})$$

Define atmospheric pressure for analysis

$$P := 1.0 \cdot \text{atm}$$

Input free water diffusion coefficient at standard condition

$$D_o := 2.13 \cdot 10^{-5} \cdot \frac{\text{m}^2}{\text{s}} \quad (\text{Ho, 1997, p.2665})$$

Calculate binary diffusivity as a function of temperature
(Equation 6.37)

$$D_{AB}(T) := D_o \cdot \left(\frac{1.013 \cdot 10^5 \cdot \text{Pa}}{P} \right) \cdot \left(\frac{T}{273.15 \cdot \text{K}} \right)^{1.8}$$

Calculate adsorptive film thickness on horizontal surface (Rearranged from Eq. 6.26)

$$\delta(RH) := \frac{-\lambda}{\ln(RH)} \quad RH := 0.20, 0.21.. 0.99$$

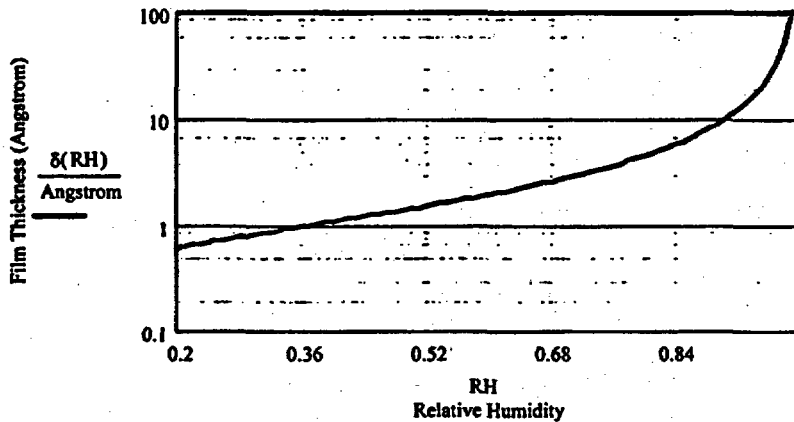


Figure III-2 Film Thickness as a Function of Relative Humidity without the impacts of gravity and hydrostatic pressure

Spot check the validity of Equation 6.44 by comparing film thicknesses on vertical and horizontal walls.

Rationale: On vertical walls, the thickening of film due to gravity is minimal when x is small, so that the film thickness shall be close to that on horizontal surface. Set $x = 1$ mm; relative humidity = 98% and temperature = 60 °C for the calculation.

$$x := 1 \text{ mm}$$

$$RH := 0.98 \quad T := 60 \text{ K} + 273.15 \text{ K}$$

Estimated film thickness

$$\delta(0.98) = 49.49831645 \text{ Angstrom} \quad (\text{Film thickness on horizontal surface})$$

$$\delta := 49.4983162674 \text{ Angstrom} \quad (\text{guess value for solving Equation 6.44})$$

Solve Equation (6.44)

$$f(x, \delta, RH, T) := \text{root} \left[\left[\int_0^\delta \left(\frac{\delta^3 - \frac{B}{2} \delta^2}{\frac{-\lambda}{e^\delta} - RH} \right) d\delta \right] \cdot 10^{12} - \left[\frac{\mu_w(T) \cdot D_{AB}(T) \cdot P_{\text{sat}}(T) \cdot x}{\rho_w(T) \cdot g \cdot (\rho_w(T) - \rho_v(T)) \cdot R \cdot T} \right] \cdot 10^{12}, \delta \right]$$

$$f(x, \delta, RH, T) = 49.498328 \text{ Angstrom}$$

The film thickness $f(x, \delta, RH, T) = 49.498328$ Angstrom on a vertical wall at $x = 1$ mm essentially equals to $\delta = 49.49831645$ Angstrom on a horizontal surface. (Check)

Calculate film thickness, mass and volumetric flow rates, and average velocity at the bottom of the internal structural reinforcement beams (vertical wall at $x = 90$ mm) using the temperature and relative humidity histories for drip shield after 1,500 years from the Thermohydrologic Model (Section 6.3, Figure 6-34 for the L4C4 location, 56 MUT/acre, mean infiltration, 0% seepage).

Mass Flow Rate (Equation 6.35)

$$M(x, \delta, RH, T) := \frac{\rho_w(T) \cdot g (\rho_w(T) - \rho_v(T)) \cdot f(x, \delta, RH, T)^3}{3 \cdot \mu_w(T)}$$

Calculate Volumetric Flow Rate from the Mass Flow Rate

$$V(x, \delta, RH, T) := \frac{M(x, \delta, RH, T)}{\rho_w(T)}$$

Average Velocity (Equation 6.45)

$$U(x, \delta, RH, T) := \frac{g (\rho_w(T) - \rho_v(T)) \cdot f(x, \delta, RH, T)^2}{\mu_w(T)} \cdot \frac{1}{3}$$

Input the temperature and RH histories for drip shield

Table III-2 Drip Shield Temperature and Relative Humidity Histories (Figure 6-34, 0% seepage)

TEDS :=	{	1500 94.2	}	RHDS :=	{	1500 0.960
		2000 87.8				2000 0.971
		3000 78.1				3000 0.978
		4000 72.0				4000 0.980
		5000 66.4				5000 0.981
		7000 58.3				7000 0.983
		10000 50.2				10000 0.985
		30000 30.5				30000 0.99
		1000000 21.5				1000000 0.999

$x := 90 \text{ mm}$ (flow distance at bottom of internal structural reinforcement beam)

$i := 0..8$

$$\delta_{\text{guess}}(\text{RH}, T) := \frac{-\lambda}{\ln(\text{RH})} - 1.01 \quad (\text{guess values for solving Equation 6.44})$$

$$\text{Film}_i := f(x, \delta_{\text{guess}}(\text{RHDS}_{i,1}, \text{TEDS}_{i,1} \cdot \text{K} + 273.15\text{K}), \text{RHDS}_{i,1}, \text{TEDS}_{i,1} \cdot \text{K} + 273.15\text{K})$$

$$\text{Mass}_i := M(x, \text{Film}_i, \text{RHDS}_{i,1}, \text{TEDS}_{i,1} \cdot \text{K} + 273.15\text{K})$$

$$\text{Volume}_i := V(x, \text{Film}_i, \text{RHDS}_{i,1}, \text{TEDS}_{i,1} \cdot \text{K} + 273.15\text{K})$$

$$\text{Velocity}_i := U(x, \text{Film}_i, \text{RHDS}_{i,1}, \text{TEDS}_{i,1} \cdot \text{K} + 273.15\text{K})$$

Results

Plot temperature vs. relative humidity at Drip Shield

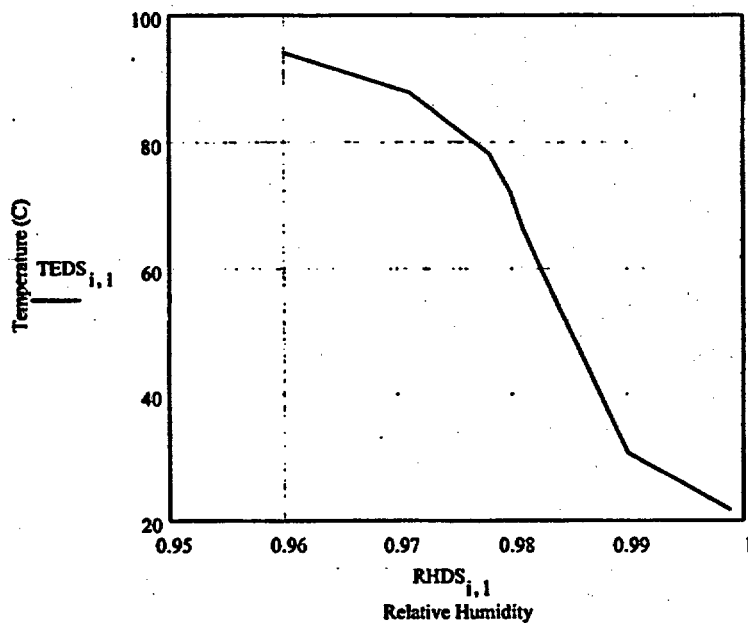


Figure III-3 Temperature vs. Relative Humidity at Drip Shield

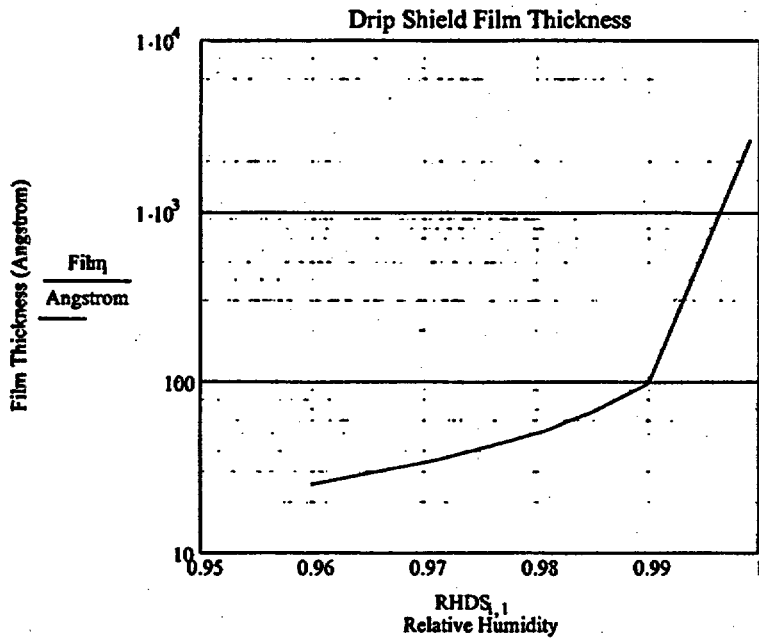


Figure III-4 Film Thickness as a Function of Relative Humidity

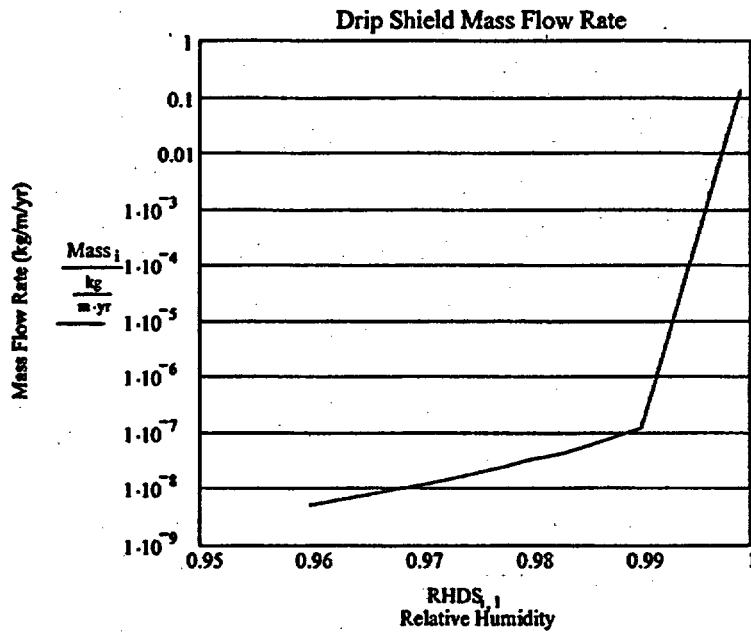


Figure III-5 Mass Flow Rate as a Function of Relative Humidity

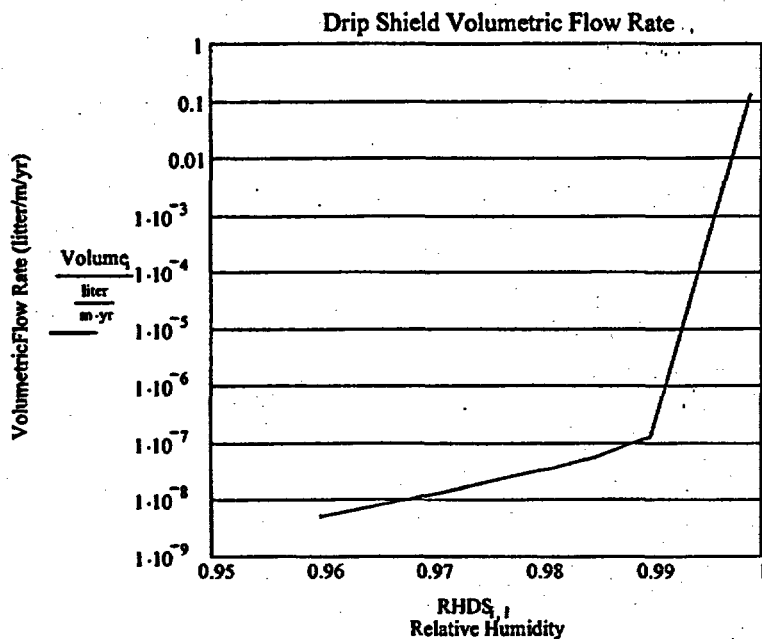


Figure III-6 Volumetric Flow Rate as a Function of Relative Humidity

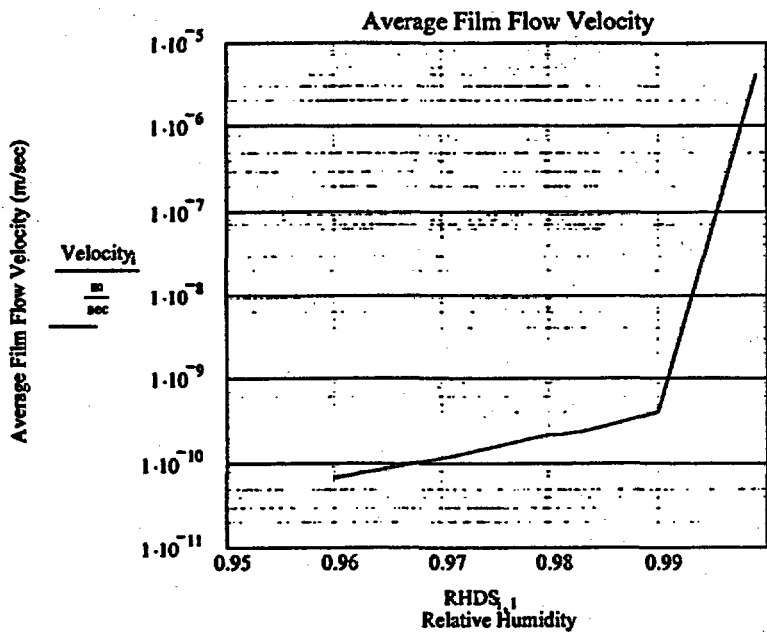


Figure III-7 Average Velocity as a Function of Relative Humidity

The Figures above show that as temperature drops, relative humidity rises in the drift that creates a stronger driving force for the adsorptive condensation. As a result, the film thickness, flow rate and average velocity increase.

ATTACHMENT IV
Verification of Software Routine COVER V1.1

VERIFICATION OF SOFTWARE ROUTINE COVER V1.1

ROUTINE IDENTIFICATION

Cover Version 1.1. Initial issue of routine. This routine was developed using MatLAB v5.3.0.1083 (R11). The source code for this routine is *cover.m*. All the files are provided in attached CD in Attachment XVI).

It should be noted that repository layout parameters, which include the footprint as discussed in Section 1.3 represents the repository design in effect at the time this model was under development. The parameters are the best available information for modeling purpose. As the design of the repository is advanced, parameter changes will be evaluated for their effect upon the models during future revisions.

ROUTINE PURPOSE AND VALIDATION

The purpose of this routine is to develop a block model of the repository from information contained in *dft1.dat* (Attachment XI), which is listed in Table IV-2. The output of this routine contains the edges of the block model in the file *shapel.dat* (Attachment XI) which is listed in Table IV-1. The resulting repository block model is intended to have a similar area to the original layout. The block model is used to develop infiltration rates over the repository footprint. Range of validation: this routine is limited to developing a block model from information in the file *shapel.dat* (Attachment XI). Validation is achieved by verifying that the objective of the code (i.e., similar footprint area) was achieved. The area outlined in *dft1.dat* (Attachment XI) is calculated and compared to the area contained in the block model (*shapel.dat*).

Table IV-1. Area of Repository Block Model

Location ID	Easting	Northing	Equation I-1
A	171368.06	235822.06	4303909
B	170422.51	235872.29	-121804376
C	170343.91	234392.62	-125402076
D	170205.80	234399.95	-195258392
E	170083.53	232098.24	-196365687
F	170221.63	232090.90	-28610852
G	170204.16	231762.08	-32257943
H	171149.71	231711.85	347432200
A	171368.06	235822.06	352179357
Total Area:			4216139

The exact area of a solid by coordinates is found by the following equation:

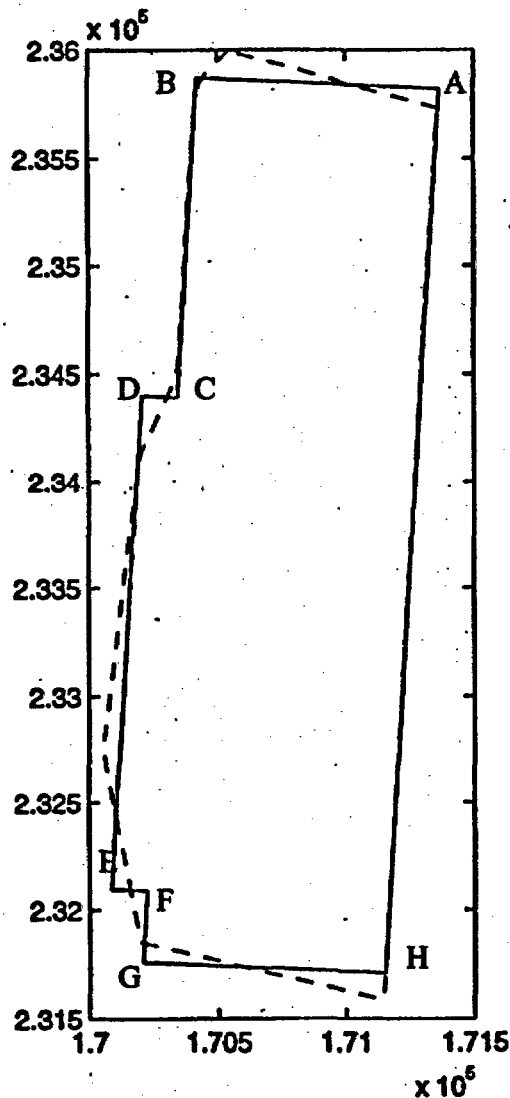
$$Area = \frac{1}{2} [x_1(y_2 - y_n) + x_2(y_3 - y_1) + \dots + x_n(y_1 - y_{n-1})] \quad (\text{Eq. IV-1})$$

where:

Area -area enclosed by coordinates
x -x coordinate

y -y coordinate
n -last point of figure
Source: (Hartman, H. L. 1992, p. A-37)

The routine is verified by finding the area of the repository using Equation IV-1 and visual inspection of the original and derived boundaries of the repository. The routine predicted an area of 4,216,139 ft² (see Table IV-1), and the actual area is 4,310,041 ft² (see Table IV-2). This is an error of less than three percent. This documents the accuracy of the output of this routine. The visual inspection result is presented in Figure IV-1. As indicated in Figure IV-1, the derived boundary closely follows the original boundary.



Note: The dotted line is from the drift endpoints in the file dft1.dat (Attachment XI) and the solid line is from the file shape1.dat (Attachment XI).

Figure IV-1. Repository and Repository Block Model

Table IV-2. Calculation of Actual Area of Repository (unit in ft²)

East Boundary		West Boundary		Calculation Using Equation I-1		
Northing	Easting	Northing	Easting	East pts	West pts	
235997.80	170544.61	235732.05	171362.51	19825811	26327279	
235964.55	170515.90	235690.53	171359.24	-8505333	10680821	
235898.04	170458.47	235607.39	171353.01	-12019879	14298552	
235823.52	170425.70	235523.64	171348.62	-13295761	14349590	
235742.01	170414.44	235439.90	171344.23	-14059191	14348366	
235658.52	170409.28	235356.16	171339.84	-14227471	14347998	
235575.03	170404.11	235272.42	171335.46	-14227039	14348488	
235491.54	170398.95	235188.67	171331.07	-14226608	14348120	
235408.05	170393.78	235104.93	171326.68	-14226177	14346896	
235324.56	170388.62	235021.19	171322.29	-14225746	14346529	
235241.07	170383.45	234937.45	171317.90	-14238945	14347018	
235157.42	170378.77	234853.70	171313.51	-14259851	14346650	
235073.68	170374.38	234769.96	171309.12	-14267151	14345426	
234989.94	170369.99	234686.22	171304.73	-14267635	14345058	
234906.19	170365.60	234602.48	171300.35	-14267267	14345548	
234822.45	170361.21	234518.73	171295.96	-14266048	14345180	
234738.71	170356.83	234434.99	171291.57	-14265681	14343956	
234654.97	170352.44	234351.25	171287.18	-14266165	14343588	
234571.22	170348.05	234267.51	171282.79	-14120150	14344077	
234489.19	170338.41	234183.76	171278.40	-13495061	14343710	
234412.77	170311.48	234100.02	171274.01	-12918977	14342486	
234337.48	170281.06	234016.28	171269.62	-12819610	14342118	
234262.20	170250.64	233932.54	171265.24	-12817319	14342608	
234186.91	170220.23	233848.79	171260.85	-12985250	14342240	
234109.63	170195.95	233765.05	171256.46	-13568021	14341016	
234027.47	170186.69	233681.31	171252.07	-13998706	14340648	
233945.12	170178.03	233597.57	171247.68	-14015012	14341137	
233862.76	170169.37	233513.82	171243.29	-14014298	14340769	
233780.41	170160.72	233430.08	171238.90	-14013586	14339545	
233698.05	170152.06	233346.34	171234.51	-14013724	14339178	
233615.69	170143.41	233262.60	171230.13	-14012161	14339667	
233533.34	170134.75	233178.85	171225.74	-14011447	14339300	
233450.98	170126.10	233095.11	171221.35	-14010735	14338076	
233368.63	170117.44	233011.37	171216.96	-14010022	14337708	
233286.27	170108.78	232927.63	171212.57	-14010159	14338197	
233203.91	170100.13	232843.88	171208.18	-14008596	14337829	
233121.56	170091.47	232760.14	171203.79	-14007883	14336605	
233039.20	170082.82	232676.40	171199.40	-14007171	14336238	
232956.85	170074.16	232592.66	171195.02	-14006457	14335871	
232874.49	170065.50	232508.92	171190.63	-14006595	14336359	
232792.13	170056.85	232425.17	171186.24	-14317086	14335992	
232706.11	170059.48	232341.43	171181.85	-14949079	14334768	
232616.32	170073.70	232257.69	171177.46	-15270918	14334401	
232526.53	170087.93	232173.95	171173.07	-15272195	14334889	
232436.74	170102.15	232090.20	171168.68	-15273472	14334521	
232346.95	170116.37	232006.46	171164.29	-15274749	14333298	
232257.16	170130.59	231922.72	171159.91	-15276026	14332931	
232167.37	170144.81	231838.98	171155.52	-15277302	14333419	
232077.58	170159.03	231755.23	171151.13	-15277729	14333051	
231987.80	170173.25	231671.49	171146.74	-15279005	14331828	
231898.01	170187.47	231587.75	171142.35	-11461275	10748595	
231853.11	170194.58	231545.88	171140.16	-29965309	-22706876	
				SUM:	-7.09E+08	713361262
					Total Area:	4310040.8

ATTACHMENT V
Calculation of the Coordinates of the Chimney Locations

CALCULATION OF THE COORDINATES OF THE CHIMNEY LOCATIONS

The repository block model developed in Attachment IV, shapel.dat (see Figure IV-1), is divided into 31 sections. The block model is composed of a rectangle with a smaller rectangle attached to the southern half of the west boundary of the repository. The 31 sections of the block model are derived by dividing the block model into 4 columns with seven rows, plus one additional column (3 rows) in the extension on the southwest side of the repository. The location for the center of each chimney is presented in Figure V-1. The process of calculating the coordinates for the 31 chimney locations is described in this Attachment. All the files are provided in attached CD in Attachment XVI.

The coordinates for the 31 chimney locations derived from the repository boundary corner points (shapel.dat) were calculated based on transformation of the coordinate system (See Figure V-1). The calculation was included in the Microsoft EXCEL 97 spreadsheet file *repository_shape V1.0.xls* (Attachment XI). The six steps used in the calculation are described below.

Step 1: calculate the coordinate of the origin (Point O in Figure V-1) for the transformed coordinate system (X'Y' in Figure V-1).

The coordinate of Point O (X_0, Y_0) was calculated as the intersection point of line GH and line DE. The coordinate of Point O was calculated as Easting of 170,066.1 and Northing of 231,769.4.

Step 2: calculate the angle α for the rotation of the coordinate system (see Figure V-1).

Angle α was calculated based on the coordinates of Point G (X_G, Y_G) and Point H (X_H, Y_H) using the equation:

$$\alpha = \alpha \tan \left[\frac{(Y_H - Y_G)}{(X_H - X_G)} \right]$$

The angle was calculated as -3.04° .

Step 3: obtain the transformed coordinates for the repository boundary corner points based on the coordinate transformation equation.

The transformed coordinates for the repository boundary corner points were obtained based on the following equation:

$$\begin{bmatrix} x' \\ y' \end{bmatrix} = \begin{bmatrix} \cos \alpha & \sin \alpha \\ -\sin \alpha & \cos \alpha \end{bmatrix} \cdot \begin{bmatrix} x - x_0 \\ y - y_0 \end{bmatrix}$$

The transformed coordinates are tabulated in Table V-1.

Step 4: calculate the spacings between the chimney locations.

The spacings between the chimney location were calculated as follows:

$$S_{x'1} = L_{GH} / 4$$

$$S_{x'2} = L_{OH} / 5$$

$$S_y = L_{HA} / 7$$

where

$S_{x'1}$ is the spacing along X' axis for Rows 1, 2, 3 and 7 (L1, L2, L3, and L7, see Figure V-1).

$S_{x'2}$ is the spacing along X' axis for Rows 4, 5 and 6 (L4, L5, and L7, see Figure V-1).

S_y is the spacing along Y' axis for all Rows (L1 to L7, see Figure V-1).

Step 5: calculate the coordinates (in X'Y' coordinate system) for all the chimney locations.

The coordinates for all the chimney locations were calculated based on the spacings obtained in Step 4. The coordinates in X'Y' are presented in Table V-2.

Step 6: obtain the coordinates (in original coordinate system) for all the chimney locations based on the coordinate transformation equation.

The original coordinates for the chimney locations were transformed based on the following equation:

$$\begin{bmatrix} x \\ y \end{bmatrix} = \begin{bmatrix} \cos\alpha & -\sin\alpha \\ \sin\alpha & \cos\alpha \end{bmatrix} \cdot \begin{bmatrix} x' \\ y' \end{bmatrix} + \begin{bmatrix} x_0 \\ y_0 \end{bmatrix}$$

The calculated coordinates for all the chimney locations tabulated in Table V-3. The coordinates are included in an ASCII text file *column.data* (Attachment XI).

Table V-1. Repository Boundary Corner Points Coordinates in X'Y' Coordinate System

Location ID	x'	y'
A	1085.2	4116.0
B	138.3	4116.0
C	138.3	2634.2
D	0.0	2634.2
E	0.0	329.3
F	138.3	329.3
G	138.3	0.0
H	1085.2	0.0

Table V-2. Coordinates of Chimney Locations in X'Y' Coordinate System

Chimney Location ID	x'	y'
17c4	256.7	294.0
17c3	493.4	294.0
17c2	730.1	294.0
17c1	966.8	294.0
16c5	108.5	882.0
16c4	325.6	882.0
16c3	542.6	882.0
16c2	759.6	882.0
16c1	976.7	882.0
15c5	108.5	1470.0
15c4	325.6	1470.0
15c3	542.6	1470.0
15c2	759.6	1470.0
15c1	976.7	1470.0
14c5	108.5	2058.0
14c4	325.6	2058.0
14c3	542.6	2058.0
14c2	759.6	2058.0
14c1	976.7	2058.0
13c4	256.7	2646.0
13c3	493.4	2646.0
13c2	730.1	2646.0
13c1	966.8	2646.0
12c4	256.7	3234.0
12c3	493.4	3234.0
12c2	730.1	3234.0
12c1	966.8	3234.0
11c4	256.7	3822.0
11c3	493.4	3822.0
11c2	730.1	3822.0
11c1	966.8	3822.0

Table V-3. Coordinates of the Chimney Locations

Chimney Location ID	Easting	Northing
17c4	170338.0	232049.4
17c3	170574.3	232036.8
17c2	170810.7	232024.3
17c1	171047.1	232011.7
16c5	170221.2	232644.4
16c4	170437.9	232632.9
16c3	170654.7	232621.4
16c2	170871.4	232609.9
16c1	171088.1	232598.4
15c5	170252.4	233231.6
15c4	170469.1	233220.1
15c3	170685.9	233208.6
15c2	170902.6	233197.1
15c1	171119.3	233185.5
14c5	170283.6	233818.8
14c4	170500.3	233807.3
14c3	170717.1	233795.7
14c2	170933.8	233784.2
14c1	171150.5	233772.7
13c4	170462.7	234398.1
13c3	170699.1	234385.5
13c2	170935.5	234373.0
13c1	171171.9	234360.4
12c4	170493.9	234985.3
12c3	170730.3	234972.7
12c2	170966.7	234960.1
12c1	171203.1	234947.6
11c4	170525.1	235572.4
11c3	170761.5	235559.9
11c2	170997.9	235547.3
11c1	171234.3	235534.8

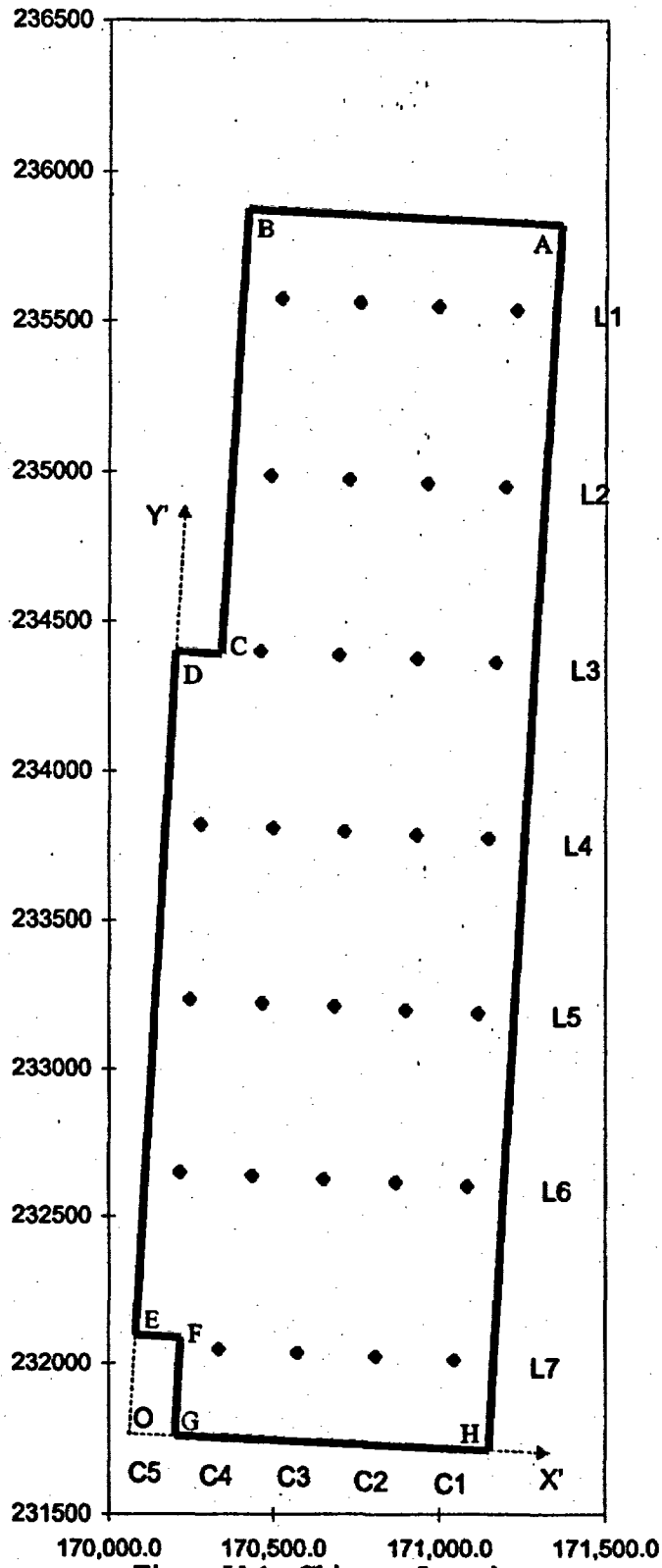


Figure V-1. Chimney Locations

ATTACHMENT VI
Verification of Software Routine CHIM_SURF_TP V1.0

VERIFICATION OF SOFTWARE ROUTINE CHIM_SURF_TP V1.0

ROUTINE IDENTIFICATION

Chim_Surf_TP V1.0, Initial issue of routine. The routine was developed and compiled using Fortran Version 77 SC4.2. The source code is *chim_surf_TP.f*. All the files are provided in attached CD in Attachment XVI.

ROUTINE PURPOSE AND VALIDATION

The purpose of this routine is to calculate the temperature and pressure at a given location using the inverse distance cubed method (For appropriateness of using the inverse distance cubed method, refer to Isaaks and Srivastava 1989, p.258). The specific input files used for this calculation are: *tspa99_primary_mesh*, which is a renaming of *UZ99_3_3D.mesh* (see Figure 3-1), *bcs_99.dat*, and *column.data* (Attachment XI). The inverse distance cubed function is:

$$V = \frac{\sum_{i=1}^n V_i \cdot \frac{1}{d_i^3}}{\sum_{i=1}^n \frac{1}{d_i^3}} \quad (\text{Eq. VI-1})$$

where:

- V -Value of interest at a given point
- V_i -Value at point i, d_i meters away
- d_i -Plan distance between points.
- n -Number of points in data set

Documentation of the accuracy of this routine is in the form of a test case. The test case is the interpolation of temperature at an arbitrary location (170000N, 230000E) given five temperatures at various locations. The hand calculation that verifies the accuracy of the test case is in Table VI-1. Due to the reduction in file size and format minor changes were made to *chim_surf_TP V1.0* in order to execute the test case. The modified source code (*chim_surf_bc_tst.f*) is in Attachment XI and is used to execute the test case for *chim_surf_TP.f*. The input file for the test case is *chim_test* and the output file is *chim_out* (Attachment XI).

Table VI-1. Calculation of Temperature Using Inverse Distance Method

Northing	Easting	1/(distance ³)	Temperature	T _i / (distance ³)
169398.601	236623.643	3.39908E-12	14.27	4.85048E-11
172705.438	230904.031	4.30854E-11	18.62	8.0225E-10
168909.656	233244.625	2.49348E-11	17.00	4.23892E-10
171465.906	237975.359	1.87545E-12	16.89	3.16763E-11
172320.452	237217.733	2.29468E-12	17.53	4.02258E-11
	1/d ³ Sum:	7.55894E-11	T _i /d ³ Sum:	1.34655E-09
Estimated Temperature (T _i /d ³ Sum / 1/d ³ Sum):				17.8140

Note: The Northings and Eastings were randomly selected from *UZ99_3_3D.mesh* (Attachment XI).
 The Temperatures were randomly selected from *bcs_99.dat* (Attachment XI).
 The distance is between each point and the reference location.

The test case was run and the predicted temperature is 17.8140 °C (Attachment XI, file *chim_out*). This documents the accuracy of this routine for predicting temperature and pressure at given points.

ATTACHMENT VII
Verification of Software Routine COLUMNINFILTRATION V1.1

VERIFICATION OF SOFTWARE ROUTINE COLUMNINFILTRATION V1.1

ROUTINE IDENTIFICATION

ColumnInfiltration V1.1. Initial issue of routine. This routine was developed and compiled using C++ vsc4.2. The source code for this routine is *columninfiltration.c*. All files are provided in attached CD in Attachment XVI.

ROUTINE PURPOSE AND VALIDATION

The purpose of this routine is to calculate the infiltration at a given location using Gaussian interpolation method (For appropriateness of using Gaussian interpolation method, refer to Isaaks and Srivastava 1989, p.208 Kitanidis 1997, p.54). The specific files used for this calculation are: *GlacialI.NV*, *Glacialm.NV*, *Glacialu.NV* (Attachment XI). The Gaussian weighting function is:

$$I = \sum_{i=1}^n I_i \cdot W_i \quad (\text{Eq. VII-1})$$

where

$$W = e^{-\left[\left(\frac{D}{\text{Scale}}\right)^2\right]} \quad (\text{Eq. VII-2})$$

where I = Interpolated infiltration
I_i = Value at point i, d meters away
D_i = Plan distance between points.
n = Number of points in data set
W = Calculated weight assigned to each value (W=W_i)
Scale = Effective radius of influence (Scale = 20ft).

Documentation of the accuracy of this routine is in the form of a test case. The test case involves the interpolation of the infiltration rate at an arbitrary reference location (242000N, 168000E) given infiltration rates at five various points. The input files for the test case are *columninfiltration_tst.NV* and *columninfiltration_tst.dat* (Attachment XI). The output file from this test case is *columninfiltration_tst.out* (Attachment XI). The hand calculation that verifies the accuracy of the test case is in Table VII-1.

Table VII-1. Calculation of Infiltration Using the Gaussian Method

Northing	Easting	Weight	Infiltration	$W_i * Infiltration_i$
168192.021	242645.935	1.300E-79	1.94718	2.532E-79
168222.029	242645.830	9.530E-82	1.23309	1.17517E-81
168252.037	242645.725	3.399E-84	0.00	0
168282.045	242645.621	5.899E-87	0.45	2.67267E-87
168312.053	242645.516	4.981E-90	0.54	2.68959E-90
	Weight Sum:	1.30968E-79	W * Infiltration Sum:	2.54331E-79
Estimated Temperature (W * Infiltration Sum / Weight Sum):				1.941933

Note: The Northings, Eastings, and infiltration rates were selected from *Glacial.NV* (Attachment XI).
The weight is found using Equation VII-2.

The test case was run and the predicted infiltration rate is 1.941933 (Attachment XI-*columninfiltration_tst.out*). This documents the accuracy of this routine for predicting infiltration rates at given points.

ATTACHMENT VIII
Verification of Software Routine RME6 V1.1

VERIFICATION OF SOFTWARE ROUTINE RME6 V1.1

ROUTINE IDENTIFICATION

rme6 V1.1. Initial issue of routine. This routine was developed and compiled using C++ vsc4.2. The source code for this routine is *rme6.c*. All files are provided in attached CD in Attachment XVI.

ROUTINE PURPOSE AND VALIDATION

The purpose of this routine is to reformat and combine the files *tspa99_primary_mesh* and *UZ99_3.grd* (Attachment XI) to a format that is readable to YMESH V 1.53. As shown in Figure 3-1, *tspa99_primary_mesh* is a renaming of *UZ99_3_3D.mesh*. The output of this routine is the file *LBL99-YMESH* (Attachment XI). This routine is verified by visually inspecting the file *LBL99-YMESH* file. The upper block of *LBL99-YMESH* is essentially the same as the mesh file *tspa99_primary_mesh* with the format modified. The lower block of *LBL99-YMESH* is the repetition of the vertices file *UZ99_3.grd* with modified format.

ATTACHMENT IX
Calculation of the Normalized Infiltration Rates

CALCULATION OF THE NORMALIZED INFILTRATION RATES

The calculated infiltration rate in the modeled repository is different from the average infiltration rate in the actual repository. To offset this difference, the infiltration rates at the 31 locations are normalized (Table IX-1). The normalized infiltration rate is the product of the estimated infiltration rate and a normalization factor. The normalization factor is the quotient of the average normalized infiltration and the actual infiltration. The average normalized infiltration is the average of the estimated infiltration at the 31 block element locations (Attachment XI, *.out). The average actual infiltration is included in the output from ConvertCoords V1.1 (files: *Glaciall_convert*, *Glacialm_convert*, *Glacialu_convert*). All files are provided in attached CD in Attachment XVI.

Table IX-1. Interpolated and Normalized Infiltration Rates

	Interpolated Glacial			Normalized Glacial		
	Low	Mean	Hi	Low	Mean	Hi
I7c4	0.278	3.684	7.090	0.392	5.211	10.031
I7c3	1.511	13.020	24.530	2.131	18.418	34.705
I7c2	1.731	15.849	29.967	2.442	22.420	42.398
I7c1	0.848	4.958	9.067	1.196	7.013	12.829
I6c5	7.645	21.725	35.804	10.785	30.732	50.657
I6c4	1.476	33.842	66.208	2.082	47.872	93.674
I6c3	2.623	11.716	20.810	3.700	16.574	29.442
I6c2	1.824	7.766	13.708	2.573	10.986	19.395
I6c1	1.617	10.660	19.702	2.281	15.079	27.875
I5c5	6.474	21.117	35.760	9.134	29.872	50.594
I5c4	2.157	42.583	83.009	3.043	60.237	117.443
I5c3	4.065	14.103	24.140	5.735	19.949	34.154
I5c2	3.804	19.155	34.708	5.085	27.097	49.103
I5c1	0.084	0.577	1.071	0.118	0.816	1.515
I4c5	2.538	14.289	26.043	3.577	20.214	36.847
I4c4	1.412	29.690	57.967	1.992	41.998	82.014
I4c3	3.915	27.330	50.745	5.523	38.660	71.795
I4c2	1.910	19.740	37.570	2.694	27.923	53.155
I4c1	2.349	13.348	24.346	3.314	18.881	34.446
I3c4	3.505	45.970	88.435	4.944	65.028	125.120
I3c3	0.636	2.965	5.293	0.897	4.194	7.489
I3c2	0.163	0.899	1.634	0.230	1.271	2.312
I3c1	1.269	19.091	36.912	1.791	27.005	52.224
I2c4	6.417	41.445	76.473	9.052	58.627	108.195
I2c3	2.955	44.655	86.354	4.169	63.168	122.176
I2c2	0.054	16.541	33.029	0.076	23.399	46.730
I2c1	0.092	0.518	0.944	0.130	0.733	1.336
I1c4	0.174	13.472	26.770	0.245	19.057	37.875
I1c3	1.702	22.932	44.162	2.400	32.439	62.482
I1c2	0.390	1.506	2.622	0.550	2.130	3.709
I1c1	0.189	9.560	18.931	0.266	13.523	26.784
Avg Int.	2.116	17.571	33.026	2.985	24.856	46.726
Actual Avg	2.985	24.856	46.726	2.985	24.856	46.726

(Normalized value)=(Interpolated value * Actual avg/Avg of interpolated values)

Avg. Int. = Average of Interpolated values, or the average of each column.

Actual Avg = actual average of infiltration values that occur within the repository footprint. This value is included in the output files from *ConvertCoords V1.1*.

ATTACHMENT X

Hydrologic and Thermal Properties of the Overton Sand

ATTACHMENT X. HYDROLOGIC AND THERMAL PROPERTIES OF THE OVERTON SAND

This attachment presents an analysis of the estimated flow properties for the Overton Sand

X.1 Grain Size Distribution

The Overton sand is described as a fine to medium sand. The hydrologic and geotechnical properties for the Overton Sand are taken from Particle Size Data, Water Retention Data, and Hydraulic Conductivity Data for Overton Sand Used In The Water Diversion Model AMR (DTN: MO9912EBSPWR28.001) for two samples sieved between 0.1 and 1.0 mm. The grain size distribution curve for Overton Sand from sieve analysis is presented in Figure X-1. The hydrological and thermal properties for this sand are presented below.

X.2 Dry Bulk Density and Porosity

The estimated solid density of the backfill material is 2.7 g/cm^3 corresponding to a bulk density of 1.59 g/cm^3 as calculated below. The grain density of the Overton Sand is 2.7 g/cm^3 which falls within a range of grain densities of from 2.50 to 2.80 for quartz (Winterkorn and Fang 1975, p.79).

The emplaced porosity for the Overton Sand is estimated to be 0.41. The porosity is taken as the average volumetric moisture content for the first and second Overton Sand samples near saturation from Tempe Cell or pressure cell tests. These data sets are illustrated in Figures X-1 and X-2.

Using the soil phase convention of setting the volume of the solids (V_s) equal to 1.0 cm^3 , the total volume (V_t) equals the volume of the voids (V_v) and the solids (V_s).

$$V_t = V_v + V_s \quad (\text{Eq. X-1})$$

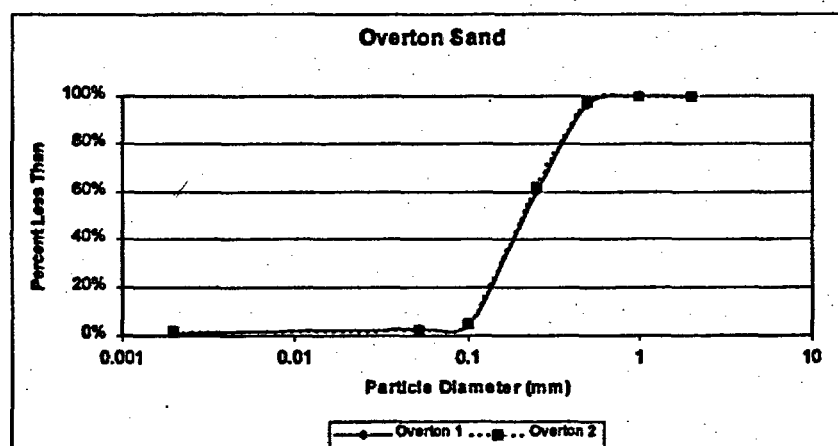


Figure X-1. Grain Size Distribution for Overton Sand

The porosity (ϕ) is defined as the volume of the voids divided by the total volume:

$$\phi = V_v/V_t \quad (\text{Eq. X-2})$$

$$V_v = 0.41V_t \quad (\text{Eq. X-3})$$

Solving for V_v :

$$V_v = 0.41 (V_v+1.0)$$

$$V_v = 0.41/(1-0.41) = 0.695 \quad (\text{Eq. X-4})$$

The dry bulk density (ρ) is defined as:

$$\rho = G_s V_s/V_t \quad (\text{Eq. X-5})$$

The dry bulk density is calculated as:

$$\rho = 2.7 (1.0)/(0.695+1.0) = 1.59 \text{ g/cm}^3 \quad (\text{Eq. X-6})$$

X.3 Moisture Retention

Moisture retention measurements were performed on the Overton Sand using two methods. These include the Unsaturated Flow Apparatus (UFA) measurements (CRWMS M&O 1996, Appendix C) and Tempe Cell or pressure cell measurements (Jury et al. 1991, p.62).

The UFA mainly consists of an ultracentrifuge in which a soil sample is subject to centrifugal force. The volumetric moisture content (θ) as a function of the moisture potential (ψ) as discussed subsequently below can be determined by allowing the sample to drain until the moisture potential equals the centrifugal force per unit area divided by the unit weight in a state of equilibrium. The volumetric moisture content (θ) is determined gravimetrically using the bulk density of the sample.

The UFA represents an efficient method for testing fine-grained soils at higher moisture potential (ψ). For low moisture potentials, the Tempe Cell or pressure cell method was used (Jury et al. 1991, p.62). The Tempe Cell consists of an airtight chamber with a freely draining, water saturated, porous ceramic plate on the bottom. The chamber is pressurized, which induces flow out of the sample through the porous cup. At equilibrium, flow through the tube is changed to zero and the moisture potential (ψ) can be calculated from the change in pressure. The volumetric moisture content is again determined gravimetrically.

Note that in the following discussion that moisture potential is a suction potential, and the convention is adopted for flow analysis that the moisture potential (ψ) is negative. The moisture retention and hydraulic conductivity relationships presented subsequently are functions of the absolute value of moisture potential (ψ).

The moisture retention data obtained from the two methods can be plotted and a curve fitting performed for the retention model based upon the van Genuchten two-parameter model $m=1-1/n$ (Fetter 1993, p.172).

The moisture potential (capillary pressure divided by weight density) versus moisture content relation is defined by:

$$\theta(\alpha, n, \theta_s, \theta_r, \psi) = \left[1 + (|\psi\alpha|)^n \right]^{-m} (\theta_s - \theta_r) + \theta_r \quad (\text{Eq. X-7})$$

For the two-parameter model, $m = 1-1/n$ (Fetter 1993, p.172). Substituting this value of (m) into Equation (X-7) gives:

$$\theta(\alpha, n, \theta_s, \theta_r, \psi) = \left[1 + (|\psi\alpha|)^n \right]^{-1\left(1-\frac{1}{n}\right)} (\theta_s - \theta_r) + \theta_r \quad (\text{Eq. X-8})$$

The van Genuchten curve-fitting parameters (θ_r , α_b , and n_b) were determined by fitting a curve to the retention data for the first Overton Sand sample using the *Microsoft Excel 97* equation solver. The saturated moisture content (θ_s) was determined from the Tempe Cell measurements as discussed above. The first Overton sand sample from the UFA measurements was used for curve fitting. For low volumetric moisture contents associated with high potential (greater than 360 cm), the first and second Overton Sand samples provided similar results. Also, the UFA measurements are more appropriate at the higher moisture potential. Figure X-2 presents Equation (X-8) along with the UFA and Tempe Cell data for Overton sand.

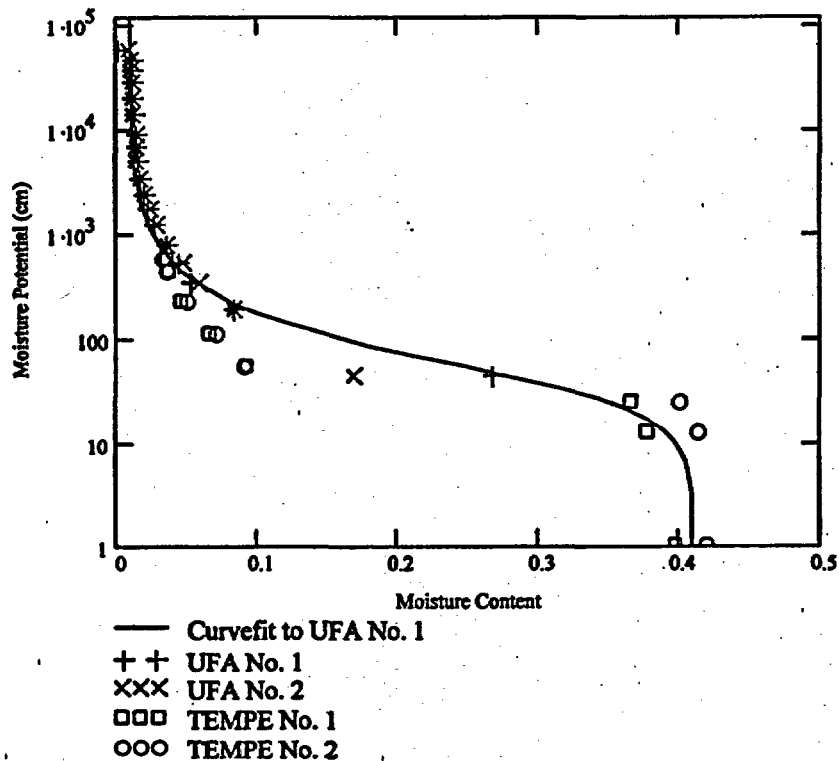


Figure X-2. Moisture Retention Relationship for Backfill Material

A *Microsoft Excel 97* spreadsheet calculation using the *Microsoft Excel 97* Equation Solver is used to optimize the model parameters by fitting the closed-form mathematical expression in Equation (X-8) to the retention data. The estimated results from the curve-fitting process for the Overton Sand are given below. Note that the units of measurement for moisture potential in the UFA testing are presented in units of bars as a suction pressure while the moisture potential for engineering analysis is in cm:

$$\begin{aligned}\theta_r &= 0.01 \\ \alpha_b &= 0.03 \text{ (1/cm)} \\ n_b &= 1.986\end{aligned}$$

To convert α_r to (1/Pa) divide by the density of water (1.0 gm/cm³) times the acceleration of gravity:

$$0.027\text{cm}^{-1} \cdot \frac{1}{1.0 \frac{\text{gm}}{\text{cm}^3} \cdot 981 \frac{\text{cm}}{\text{sec}^2}} = 2.752 \times 10^{-4} \frac{1}{\text{P}}$$

From the definition of van Genuchten m ($m=1-1/n$) given above:

$$1 - \frac{1}{1.986} = 0.5$$

The residual saturation equals the residual moisture content divided by the porosity ($0.01/0.41$) = 0.024. The saturated saturation is by definition.

X.4 Intrinsic Permeability

The unsaturated flow properties data for sand were measured from UFA measurements as discussed subsequently. The saturated hydraulic conductivity of the Overton Sand (K_s) is estimated to be 0.014 cm/sec by extrapolation of the unsaturated hydraulic conductivity versus volumetric moisture content θ relationship at the value of the saturated volumetric moisture content (θ_s) or porosity (ϕ). The saturated hydraulic conductivity (Figure X-3), corresponds to an approximate intrinsic permeability of 1.4×10^{-7} cm² or 1.4×10^{-11} m².

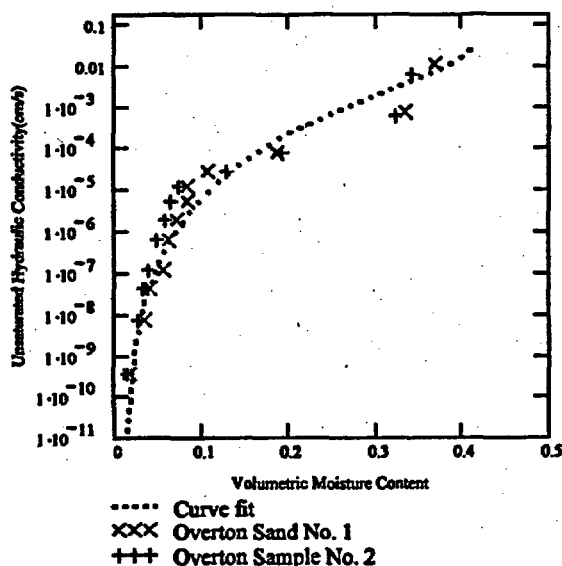


Figure X-3. Relationship of Volumetric Moisture Content to Unsaturated Hydraulic Conductivity for Backfill

X.5 Relative Permeability

The UFA test apparatus described above is equipped with a constant ultra low flow pump that provides fluid to the sample through a rotating seal assembly and microdispersal system. This system can be used to determine the relationship between the unsaturated hydraulic conductivity

(K_u) and volumetric moisture content through a direct application of Darcy's Law (CRWMS M&O 1996, Appendix C). Samples are spun at a constant rate to define the hydraulic gradient in the core. A constant flux is applied to the top of the core. The change in water content to carry the applied flux (flow rates to 0.001 ml/hr) at the applied gradient is measured. The unsaturated hydraulic conductivity can be determined from the ratio of the flow rate to the centrifugal force per unit volume (CRWMS M&O 1996, p.C-2).

The relationship of the unsaturated hydraulic conductivity with volumetric moisture content is given by (Jury et al. 1991, p.109):

$$K(\theta) = K_s \left(\frac{\theta - \theta_r}{\theta_s - \theta_r} \right)^{\frac{1}{2}} \left[1 - \left[1 - \left(\frac{\theta - \theta_r}{\theta_s - \theta_r} \right)^{\frac{1}{1-n}} \right]^{\left(1 - \frac{1}{n} \right)} \right]^2 \quad (\text{Eq. X-9})$$

This relationship is plotted against measured data for the first and second Overton Sand samples in Figure X-3.

The wetting-phase relative permeability as a function of moisture potential for this model is restated from Fetter (1993, p.182). The unsaturated hydraulic conductivity (wetting-phase relative permeability times saturated hydraulic conductivity) as a function of moisture potential is given below.

$$K(\alpha, n, \psi, K_s) = K_s \frac{\left[1 - (\alpha \psi)^{n-1} \left[1 + (\alpha \psi)^n \right]^{\left(-1 + \frac{1}{n} \right)} \right]^2}{\left[1 + (\alpha \psi)^n \right]^{\left[\frac{1}{2} - \frac{1}{(2n)} \right]}} \quad (\text{Eq. X-10})$$

The relative permeability function scales the saturated conductivity (K_s) to allow the unsaturated hydraulic conductivity function to be determined. Equation (X-10) with van Genuchten parameters is used to plot the relationship for Overton Sand as shown in Figure X-4.

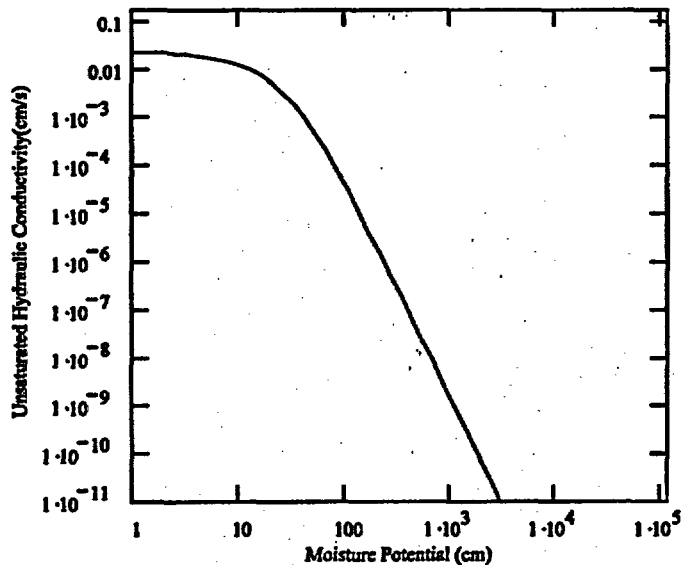


Figure X-4. Unsaturated Hydraulic Conductivity versus Moisture Potential for Overton Sand

X.6 Overton Sand Thermal Properties

Thermal conductivity (K_t) is a strong function of water content (Jury et al. 1991, p.183). For dry sand, the thermal conductivity at 20 °C is about 0.33 W/m-°K (Lide and Frederikse 1997, p. 12 – 199). Jury et al. (1991, p.179) presents a value for the specific heat (C_p) of a coarse quartz sand of 0.19 cal/(g °K) . Converting the units from cal/g/°K to J/ (kg °K) gives

$$C_p = 0.19 \frac{\text{cal}}{\text{g} \cdot \text{K}}$$

$$C_p = 795.42 \frac{\text{J}}{\text{kg} \cdot \text{K}}$$

The calculated value for C_p is 795.492 J/(kg°K) for the Overton Sand. The thermal emissivity of the Overton Sand is assumed to be equal to the emissivity for quartz on a rough surface, i.e., 0.93 (Holman 1997, p.649).

ATTACHMENT XI
Computer Files for Water Drainage Model

This attachment provides a list of computer files for the water drainage model. The files listed in Table XI-1 are contained on the CD in Attachment XVI.

Table XI-1. List of Computer Files

File Name	Directory	Brief description	
Glaciall.inf	Source Data	Infiltration Input File for Glacial Lower Bound	
Glacialm.inf		Infiltration Input File for Glacial Mean	
Glacialu.inf		Infiltration Input File for Glacial Upper Bound	
bcs_99.dat		Pressure and Temperature Boundary Condition Files	
Dft1.dat		Repository Drifts End Points Coordinates	
UZ99_3_3D.mesh		UZ Model mesh File	
tspa99_primary_mesh		Renaming of UZ99_3_3D.mesh	
UZ99_3.grd		UZ Model Grid File	
Glaciall.NV		Intermediate Data Files	Converted Infiltration Data File for Glacial Lower Bound
Glacialm.NV	Converted Infiltration Data File for Glacial Mean		
Glacialu.NV	Converted Infiltration Data File for Glacial Upper Bound		
Glaciall.out	Interpolated Infiltration at Chimneys for Glacial Lower Bound		
Glacialm.out	Interpolated Infiltration at Chimneys for Glacial Mean		
Glacialu.out	Interpolated Infiltration at Chimneys for Glacial Upper Bound		
Glaciall_convert	Actual Average Infiltration for Glacial Lower Bound		
Glacialm_convert	Actual Average Infiltration for Glacial Mean		
Glacialu_convert	Actual Average Infiltration for Glacial Upper Bound		
outpt	Pressure and Temperature at Ground Surface		
outpt_wt	Intermediate Data Files	Pressure and Temperature at Water Table	
shape1.dat		Block Model Corner Points Coordinates	
Column.data		Coordinates for the 31 Chimney Locations	
L4c4.dat		Coordinate for the L4C4 Chimney	
LBL99-YMESH		Combined Files from UZ99_3.grd and UZ99_3_3D.mesh	
L4c4.col.units		Stratigraphic Column for the L4C4 Chimney	
repository_shape V1.0.xls		Calculation of the Coordinates of the Chimney Locations	
Cover.m		Source Code for Cover V1.1	
Chim_Surf_TP.f		Source Code for Chim_Surf_TP V1.1	
Columninfiltration.c		Source Code for Columninfiltration V1.1	
rme6.c	Source Code for Rme6 V1.1		
Chim_Surf_bc_tst.f	Software Routine Source Codes and Verification Files	Modified Source Code for Chim_Surf_TP V1.1 for Verification	
Chim_test		Verification Input File for Chim_Surf_TP V1.1	
Chim_out		Verification output File for Chim_Surf_TP V1.1	
columninfiltration_tst.dat		Verification Input File for Columninfiltration V1.1	
columninfiltration_tst.NV		Verification Input File for Columninfiltration V1.1	
columninfiltration_tst.out		Verification output File for Columninfiltration V1.1	
1.in		NUFT Inputs	Input File for Case 1
5.in			Input File for Case 2
9.in			Input File for Case 3
dkm-afc-NBS-WDR			Material Properties File for the NBS
dkm-afc-NBS-Rev10-WDR	Material Properties File for the EBS		
vtough.pkg	NUFT Accepted Data File		
1.f.EBS.ext	NUFT Outputs		Fracture Output File for Case 1
1.m.EBS.ext		Matrix Output File for Case 1	
5.f.ext		Fracture Output File for Case 2	
5.m.ext		Matrix Output File for Case 2	
9.f.ext		Fracture Output File for Case 3	
9.m.ext		Matrix Output File for Case 3	

Table XI-1. List of Computer Files (Continued)

File Name	Directory	Brief description
Case1_Flux V1.0.mcd	Processed Outputs	Flow rate through the Invert for Case 1
Case899.1_Flux V1.0.mcd		Flow rate through the invert for Case 3
Case1 V1.0.mcd		Travel time through the invert for Case 1
Case9 V1.0.mcd		Travel time through the invert for Case 3
Summary of travel time calculation V1.0.xls		Average pore water velocity through the invert for various cases

ATTACHMENT XII
Comparison of NUFT Flux Rates with a Closed Form Solution
for Flow near a Cylindrical Inclusion

COMPARISON OF NUFT FLUX RATES WITH A CLOSED FORM SOLUTION FOR FLOW NEAR A CYLINDRICAL INCLUSION

XII.1 PURPOSE

The results of the NUFT calculations can be compared with a closed form solution for a single backfill. In this calculation, a closed form solution for the focusing effect of the backfilled drift is used. The calculation uses potential or field theory and is based upon a cylindrical geometry, and follows the example presented by Phillips (1991, pp.67-69) for flow and reactions in permeable rocks.

The following calculation compares the results of two analyses. These analyses include the (1) closed form calculation based upon a cylindrical inclusion and a (2) two dimensional NUFT analysis for the base case (Section 6.2.5) based upon the active fracture concept for the water distribution and removal model. The following presents the calculation method used for the closed form solution, constitutive properties for the backfill, and surrounding rock media, the flux distribution across the repository drift horizon, and a comparison with the NUFT calculations.

XII.2 CALCULATION METHOD FOR THE CLOSED FORM SOLUTION

In this calculation, a closed form solution for the focusing effect of the backfilled drift is used. The calculation uses potential or field theory (Assumption 5.11) and is based upon a cylindrical geometry. The calculation follows the example presented by (Phillips 1991, pp.67-69) for flow and reactions in permeable rocks.

XII.2.1 Closed Form Solution and Boundary Conditions

From Phillips (1991, pp.67-69), a solution is presented for a spherical inclusion in a uniform flow field. A solution is developed below for a cylindrical geometry that corresponds to a backfilled tunnel. The solution presented satisfies the steady state flow Laplace equation presented by Phillips (1991, Equation 3.8.1, pp.50 and 67). Consider the solution for a cylindrical geometry. The Laplace Operator for a cylindrical geometry for steady state flow (Sokolnikoff and Redheffer 1966, p. 417) is given by:

$$\text{del}^2 (u) = \frac{1}{r} \frac{d}{dr} \left(r \frac{d}{dr} u \right) + \frac{1}{r^2} \frac{d^2}{d\theta^2} u + \frac{d^2}{dz^2} u \quad (\text{XII-1})$$

where

u = Field function,

r = Radius,

θ = Angle, and

z = Vertical coordinate.

Note that $\text{del}^2 = \nabla^2$

From Phillips (1991, p.50), Laplace's Equation is satisfied for steady state flow:

$$\text{del}^2 (u) = 0 \quad (\text{XII-2})$$

Writing the Laplace Equation for two dimensional flow and noting that u is equivalent to pressure ($u=p$) for flow in a porous media:

$$\text{del}^2 (p) = \frac{1}{r} \frac{d}{dr} \left(r \frac{d}{dr} p \right) + \frac{1}{r^2} \frac{d^2}{d\theta^2} p + \frac{d^2}{dz^2} p \quad (\text{XII-3})$$

Noting that for a two dimensional problem flow equals zero in the z direction,

$$\frac{d^2}{dz^2} p = 0 \quad (\text{XII-4})$$

$$\frac{d^2}{dr^2} p + \left(\frac{1}{r} \frac{d}{dr} p + \frac{1}{r^2} \frac{d^2}{d\theta^2} p \right) = 0 \quad (\text{XII-5})$$

The above equation is subject to the same conditions as the spherical inclusion (Phillips 1991, p.68):

$$p_o = p_i \quad r=a \quad (\text{XII-6})$$

$$k_i \frac{d}{dr} p_i = k_o \frac{d}{dr} p_o \quad r=a \quad (\text{XII-7})$$

p_o approaches $-\omega x$ or $-\omega r \cos(\theta)$ as r approaches infinity

(XII-8)

where

p = Pressure,

r = Radius,

θ = Angle,

p_i = Internal pressure,

p_o = External pressure,

k_i = Permeability of the inclusion,

k_o = Permeability of the surrounding media,

ω = Field variable for a uniform flow field, and

x = Coordinate in the direction of the flow field.

In Bear (1988, p.270) a definition for a well posed problem is provided. These include:

- (a) The flow domain is defined at large distances from the inclusion with flow in the vertical direction,
- (b) The flow problem can be stated mathematically by means of a dependent variable which in the present case is the pressure p ,
- (c) A partial differential equation can be specified for the dependent variable p , and
- (d) The pressure p can be defined at infinity.

As Bear (1988, p.271) states that for a well posed problem a solution exists that is unique and that continuously depends on the data. Therefore, if a solution is found that satisfies partial differential equation (Equation XII-5) subject to the boundary conditions (Equation XII-6) through (Equation XII-8); the solution is unique to the problem. The solution presented by Phillips (1991, p.68) is expressible in spherical harmonics with two directions of curvature. Expressing a solution with one direction of curvature, p_i and p_o are obtained:

$$p_i = -\omega \cdot \frac{2 \cdot k_o}{k_i + k_o} \cdot r \cdot \cos(\theta) \quad r \leq a$$

(XII-9)

$$p_o = -\omega \cdot \left[1 - \frac{(k_i - k_o) \cdot a^2}{k_i + k_o \cdot r^2} \right] \cdot r \cdot \cos(\theta) \quad r \geq a$$

(XII-10)

XII.2.2 Pressure Boundary Condition at the Radius of the Inclusion

Check the pressure boundary condition at $r = a$. The pressure p_i from (XII-9) is given by:

$$p_i = -\omega \cdot \frac{2 \cdot k_o}{k_i + k_o} \cdot a \cdot \cos(\theta) \quad (\text{XII-11})$$

The pressure boundary condition from (XII-10) is given by:

$$p_o = -\omega \cdot \left[1 - \frac{(k_i - k_o) \cdot a^2}{k_i + k_o \cdot a^2} \right] \cdot a \cdot \cos(\theta) \quad (\text{XII-12})$$

which, after simplifying becomes:

$$p_o = -2 \cdot \omega \cdot \frac{k_o}{(k_i + k_o)} \cdot a \cdot \cos(\theta) \quad (\text{XII-13})$$

The pressure at the boundary of the emplacement drift is satisfied ($p_o = p_i$) from the two relations (XII-11) and (XII-13).

XII.2.3 Gradient Boundary Condition at the Radius of the Inclusion

Check the gradient boundary condition at $r = a$. Considering the interior of the room, applying Darcy's Law to the left side of the expression from Equation (XII-7):

$$k_i \cdot \frac{d}{dr} p_i \quad (\text{XII-14})$$

Substitute the expression on the right side of Equation XII-9 into Equation XII-14 yields:

$$k_i \cdot \left[\frac{d}{dr} \left(-\omega \cdot \frac{2 \cdot k_o}{k_i + k_o} \cdot r \cdot \cos(\theta) \right) \right] \quad (\text{XII-15})$$

Taking the derivative to Equation XII-15 with respect to r and obtaining:

$$-2 \cdot k_i \omega \cdot \frac{k_o}{(k_i + k_o)} \cdot \cos(\theta) \quad (\text{XII-16})$$

Apply the Darcy's Law for the exterior, and substitute in the expression on the right side of Equation XII-10 in similar fashion:

$$k_o \cdot \frac{d}{dr} \left[-\omega \cdot \left[1 - \frac{(k_i - k_o) \cdot a^2}{k_i + k_o \cdot r^2} \right] \cdot r \cdot \cos(\theta) \right] \quad (\text{XII-17})$$

Taking the derivative to Equation XII-17 with respect to r and obtaining:

$$k_o \cdot \left[-2 \cdot \omega \cdot \frac{(k_i - k_o) \cdot a^2}{(k_i + k_o) \cdot r^2} \cdot \cos(\theta) - \omega \cdot \left[1 - \frac{(k_i - k_o) \cdot a^2}{(k_i + k_o) \cdot r^2} \right] \cdot \cos(\theta) \right] \quad (\text{XII-18})$$

Simplify the expression and substitute $r = a$ at the boundary:

$$k_o \cdot \left[\omega \cdot \cos(\theta) \cdot \frac{(-a^2 \cdot k_i + a^2 \cdot k_o - r^2 \cdot k_i - r^2 \cdot k_o)}{[(k_i + k_o) \cdot r^2]} \right] \quad (\text{XII-19})$$

Simplifying yields the expression:

$$-2 \cdot k_i \omega \cdot \frac{k_o}{(k_i + k_o)} \cdot \cos(\theta) \quad (\text{XII-20})$$

The flux boundary condition in Equation XII-20 agrees with gradient boundary condition in Equation XII-16.

XII.2.4 Solution to the Partial Differential Equation Within the Drift

Check the solution to the partial differential equation inside the emplacement drift. Substituting the right side of Equation XII-9 into left side of Equation XII-5 yields the expression:

$$\left. \frac{d^2}{dr^2} \left(-\omega \cdot \frac{2 \cdot k_o}{k_i + k_o} \cdot r \cdot \cos(\theta) \right) + \left[\frac{1}{r} \cdot \frac{d}{dr} \left(-\omega \cdot \frac{2 \cdot k_o}{k_i + k_o} \cdot r \cdot \cos(\theta) \right) + \frac{1}{r^2} \cdot \frac{d^2}{d\theta^2} \left(-\omega \cdot \frac{2 \cdot k_o}{k_i + k_o} \cdot r \cdot \cos(\theta) \right) \right] \right\} \quad (\text{XII-21})$$

Evaluate the first term in the above expression by differentiating with respect to r twice:

$$\frac{d^2}{dr^2} \left(-\omega \cdot \frac{2 \cdot k_o}{k_i + k_o} \cdot r \cdot \cos(\theta) \right) = 0 \quad (\text{XII-22})$$

Evaluate the second term in Equation XII-21 by differentiating with respect to r once:

$$\frac{1}{r} \cdot \frac{d}{dr} \left(-\omega \cdot \frac{2 \cdot k_o}{k_i + k_o} \cdot r \cdot \cos(\theta) \right) = \frac{-2}{r} \cdot \omega \cdot \frac{k_o}{(k_i + k_o)} \cdot \cos(\theta) \quad (\text{XII-23})$$

Evaluate the third term in Equation XII-21 by differentiating with respect to θ twice

$$\frac{1}{r^2} \cdot \frac{d^2}{d\theta^2} \left(-\omega \cdot \frac{2 \cdot k_o}{k_i + k_o} \cdot r \cdot \cos(\theta) \right) = \frac{2}{r} \cdot \omega \cdot \frac{k_o}{(k_i + k_o)} \cdot \cos(\theta) \quad (\text{XII-24})$$

Zero is obtained by adding the right-hand side of Equations XII-22 through XII-24:

$$0 + \frac{-2}{r} \cdot \omega \cdot \frac{k_o}{(k_i + k_o)} \cdot \cos(\theta) + \frac{2}{r} \cdot \omega \cdot \frac{k_o}{(k_i + k_o)} \cdot \cos(\theta) = 0 \quad (\text{XII-25})$$

The solution for pressure inside the drift satisfies the Partial Differential Equation (PDE) (Equation XII-5).

XII.2.5 Solution to the Partial Differential Equation Outside the Drift

Check the solution to the PDE outside the inclusion. Substituting the right hand side of Equation XII-10 into Equation XII-5, the following expression is obtained:

$$\begin{aligned} & \frac{d^2}{dr^2} \left[-\omega \cdot \left[1 - \frac{(k_i - k_o) \cdot a^2}{k_i + k_o} \cdot \frac{a^2}{r^2} \right] \cdot r \cdot \cos(\theta) \right] + \frac{1}{r} \left[\frac{d}{dr} \left[-\omega \cdot \left[1 - \frac{(k_i - k_o) \cdot a^2}{k_i + k_o} \cdot \frac{a^2}{r^2} \right] \cdot r \cdot \cos(\theta) \right] \right] \dots \\ & + \frac{1}{r^2} \frac{d^2}{d\theta^2} \left[-\omega \cdot \left[1 - \frac{(k_i - k_o) \cdot a^2}{k_i + k_o} \cdot \frac{a^2}{r^2} \right] \cdot r \cdot \cos(\theta) \right] \end{aligned} \quad \text{(XII-26)}$$

Note that the symbol "... " signifies continuation of the expression on the next line.

Evaluate the first term in Equation XII-26 by differentiating the expression with respect to r twice:

$$\frac{d^2}{dr^2} \left[-\omega \cdot \left[1 - \frac{(k_i - k_o) \cdot a^2}{k_i + k_o} \cdot \frac{a^2}{r^2} \right] \cdot r \cdot \cos(\theta) \right] = 2 \cdot \omega \cdot \frac{(k_i - k_o) \cdot a^2}{(k_i + k_o) \cdot r^3} \cdot \cos(\theta) \quad \text{(XII-27)}$$

Evaluate the second term in Equation XII-26 by differentiating the expression with respect to r once:

$$\frac{1}{r} \left[\frac{d}{dr} \left[-\omega \cdot \left[1 - \frac{(k_i - k_o) \cdot a^2}{k_i + k_o} \cdot \frac{a^2}{r^2} \right] \cdot r \cdot \cos(\theta) \right] \right] = \frac{-1}{r^3} \cdot \omega \cdot \cos(\theta) \cdot \frac{[a^2 \cdot (k_i - k_o) + r^2 \cdot (k_i + k_o)]}{(k_i + k_o)} \quad \text{(XII-28)}$$

The expression above simplifies to:

$$\frac{-1}{r^3} \cdot \omega \cdot \cos(\theta) \cdot a^2 \cdot \frac{(k_i - k_o)}{(k_i + k_o)} - \frac{1}{r} \cdot \omega \cdot \cos(\theta) \cdot (1)$$

(XII-29)

Evaluate the third term in Equation XII-26 by differentiating the expression with respect to θ twice:

$$\frac{1}{r^2} \cdot \frac{d^2}{d\theta^2} \left[-\omega \cdot \left[1 - \frac{(k_i - k_o) \cdot a^2}{k_i + k_o \cdot r^2} \right] \cdot r \cdot \cos(\theta) \right] = \frac{1}{r} \cdot \omega \cdot \left[1 - \frac{(k_i - k_o) \cdot a^2}{(k_i + k_o) \cdot r^2} \right] \cdot \cos(\theta)$$

(XII-30)

This expression simplifies to:

$$\frac{1}{r} \cdot (\omega \cdot \cos(\theta)) - \frac{(k_i - k_o)}{(k_i + k_o)} \cdot \frac{a^2}{r^3} \cdot \omega \cdot \cos(\theta)$$

(XII-31)

Combining Equations XII-27, XII-29, and XII-31:

$$2 \cdot \omega \cdot \frac{(k_i - k_o)}{(k_i + k_o)} \cdot \frac{a^2}{r^3} \cdot \cos(\theta) + \left[\frac{-1}{r^3} \cdot \omega \cdot \cos(\theta) \cdot a^2 \cdot \frac{(k_i - k_o)}{(k_i + k_o)} - \frac{1}{r} \cdot \omega \cdot \cos(\theta) \cdot (1) \right] \dots$$

$$+ \frac{1}{r} \cdot (\omega \cdot \cos(\theta)) - \frac{(k_i - k_o)}{(k_i + k_o)} \cdot \frac{a^2}{r^3} \cdot \omega \cdot \cos(\theta)$$

(XII-32)

All the terms presented above cancel out, and the Laplace Equation (Equation XII-5) is satisfied. The solution (Equation XII-5) for the potential function outside the inclusion satisfies the PDE.

IX2.6 Development of the Focusing Ratio

Phillips (1991, p.68) develops focusing ratio for a spherical inclusion from the solution of the problem for a spherical inclusion. The following discussion develops a focusing ratio for a cylindrical inclusion. Consider the solution for the internal pressure from Equation XII-9. Substituting $x = r \cos(\theta)$, and Equation XII-9 into Darcy's Law gives the expression:

$$k_o \cdot \frac{d}{dx}(\omega \cdot x) \quad (\text{XII-33})$$

Take the derivative with respect to x and noting that $x = r \cos(\theta)$:

$$\frac{d}{dx} p_i = -\omega \cdot \frac{2 \cdot k_o}{k_i + k_o} \quad (\text{XII-34})$$

The water flux in the emplacement drift is given by substituting the expression on the right hand side of Equation IX-34 into Equation XII-14:

$$k_i \left(\frac{d}{dx} p_i \right) = k_i \left(\frac{-\omega \cdot 2 \cdot k_o}{k_i + k_o} \right) \quad (\text{XII-35})$$

Consider the solution for the farfield pressure in Equation XII-10:

$$p_o = -\omega \cdot \left[1 - \frac{(k_i - k_o) \cdot a^2}{k_i + k_o \cdot r^2} \right] \cdot r \cdot \cos(\theta) \quad (\text{XII-36})$$

Taking the derivative with respect to x for Equation XII-35:

$$k_o \cdot -\omega \quad (\text{XII-37})$$

The ratio of the fluxes is then:

$$\frac{(k_i) \cdot \left(\frac{-\omega \cdot 2 \cdot k_o}{k_i + k_o} \right)}{(k_o \cdot -\omega)} \quad (\text{XII-38})$$

Which simplifies to:

$$2 \cdot \frac{k_i}{(k_i + k_o)} \quad \text{(XII-39)}$$

This formula can be used to bound the flow through the backfill and the effects of percolation rate at the repository horizon. Figure XII-1 presents relationship for the focusing ratio for the cylindrical inclusion (Equation XII-39) as a function of the ratio of the conductivities (k_i/k_o). This solution is compared to the solution presented by Phillips (1991, p.69) for a spherical inclusion. For low (k_i/k_o) ratios, the focusing ratio is small while for large ratios, the focusing ratio approaches three for the spherical case and two for the cylindrical case.

XII.3 Constitutive Properties for the Backfill and Surrounding Rock Media

The moisture potential versus unsaturated hydraulic conductivity for the surrounding tuff is used to determine the moisture potential or moisture potential over the range of infiltration rates under the assumption that the percolation rate under steady state conditions equals the unsaturated hydraulic conductivity (Section 5.12). Steady state conditions are defined as the conditions in which the flow rate is constant or is not changing with time.

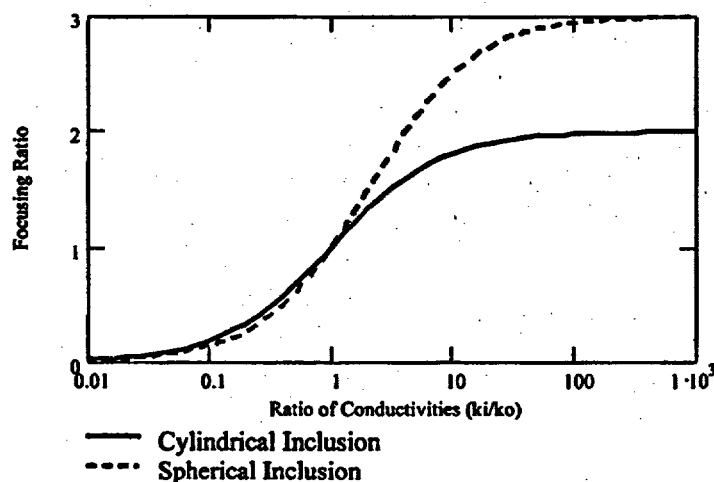


Figure XII-1. The Focusing Ratio or Velocity Ratio for a Sphere of Permeability k_i in a Matrix of Permeability k_o

The van Genuchten constitutive relation given by Fetter (1993, p.182) for the unsaturated hydraulic conductivity for the several media are presented in Figure XII-2. The van Genuchten constitutive relation for the unsaturated hydraulic conductivity at ambient temperature is given by:

$$K(\alpha, n, \psi, K_s) := K_s \frac{\left[\frac{e}{1 - (|\alpha \cdot \psi|)^{(n-1)} \cdot [1 + (|\alpha \cdot \psi|)^n]^{-1 + \frac{1}{n}}} \right]^2}{\left[\frac{e}{1 + (|\alpha \cdot \psi|)^n} \right]^{\frac{1}{2} \cdot \frac{1}{(2 \cdot n)}}} \quad (\text{XII-40})$$

For the active fracture model at the repository horizon, the constitutive relation as a function of saturation S_e is given by:

$$K_{af}(S_e, \gamma, m) := S_e^{\frac{(1+\gamma)}{2}} \cdot \left[1 - \left[1 - S_e^{\frac{(1-\gamma)}{m}} \right]^m \right]^2 \cdot K_f \quad (\text{IX-41})$$

For the active fracture model, for the retention relationship for the active fracture model is given by:

$$P_c(S_e, \alpha, \gamma, m) := \frac{1}{\alpha} \cdot \left[S_e^{\frac{(\gamma-1)}{m}} - 1 \right]^{\frac{1}{(m-1)}} \quad (\text{IX-42})$$

Equations XII-41 and XII-42 can be combined together resulting in the relationship of K_{af} as function of the capillary pressure.

For a deep water table in an isotropic medium, the seepage flux downwards establishes a moisture potential equilibrium level in which (Jury et al. 1991, p.127):

$$J_w = -K(\theta) \quad (\text{XII-43})$$

This can be expressed through the unsaturated hydraulic conductivity relationship (Equation XII-40):

$$J_w = -K(\psi) \quad (\text{XII-44})$$

Equation XII-44 can be applied to estimate the moisture potential within the surrounding media. In the water distribution and removal model for the glacial climate for the column chimney 14c4, the estimated seepage flux (J_w) is 42 mm per year ($1.331 \cdot 10^{-6}$ kg/(m²-sec) (Section 6.2.5). This estimated seepage rate corresponded to an unsaturated hydraulic conductivity of $1.3 \cdot 10^{-7}$ cm/s with the moisture potential of 42 cm (4100 Pa).

XII.4 FLUX DISTRIBUTION ACROSS THE REPOSITORY DRIFT HORIZON

The following analysis develops the flux distribution across the repository drift horizon for comparison to the NUFT calculations in Section XII.5. If Darcy's Law is applied to the closed form solution at the mid plane of the inclusion, expressions for the flow focusing can be derived in which the unsaturated hydraulic conductivities are estimated from Figure XII-2 for a particular percolation rate. Within the entry, the flux is uniform, and equals the value given by Equation XII-35. The following analysis develops the solution outside the inclusion ($r \geq a$) through use of the closed form solution from Equation XII-9.

Equation XII-9 presents the solution in cylindrical coordinates. The following analysis develops the gradient in the x direction using a coordinate transformation from cylindrical coordinates to rectangular coordinates. The chain rule is invoked the flux distribution.

From the *CRC Standard Mathematical Tables* (Beyer 1987, p.205), the coordinate transformation is given by

$$\theta = \text{atan}\left(\frac{y}{x}\right) \quad r = \sqrt{x^2 + y^2} \tag{XII-45}$$

Define a variable u for application of the chain rule:

$$u = \frac{y}{x} \tag{XII-46}$$

Take the derivative of u with respect to x:

$$\frac{d}{dx} u = \frac{-y}{x^2} \tag{XII-47}$$

Consider the inverse tangent function:

$$\theta = \text{atan}(u) \tag{XII-48}$$

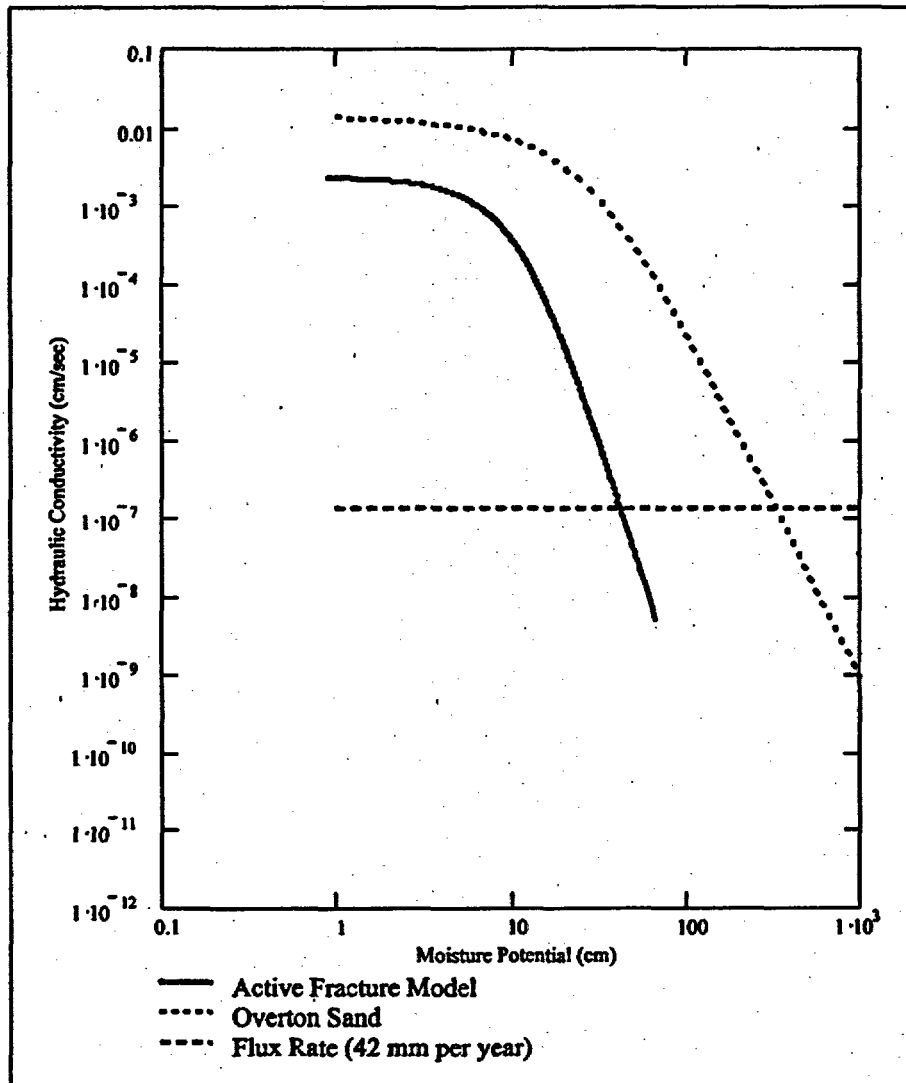


Figure XII-2. Constitutive Properties for the Active Fracture Model, and the Overton Sand

From the *CRC Standard Mathematical Tables* (Beyer 1987, p.31), the derivative is given by

$$\frac{d}{dx} \theta = \frac{1}{1+u^2} \frac{d}{dx} u \quad (\text{XII-49})$$

Applying the chain rule, the following derivative is obtained:

$$\frac{d}{dx} \theta = \frac{-y}{(x^2 + y^2)} \quad (\text{XII-50})$$

Take the derivative with respect to the radius:

$$r = \sqrt{x^2 + y^2} \quad (\text{XII-51})$$

$$\frac{d}{dx} r = \frac{1}{(x^2 + y^2)^{\frac{1}{2}}} \cdot x \quad (\text{XII-52})$$

For the case inside the inclusion, the derivative is trivial from Equation XII-9:

$$\frac{d}{dx} p_i = -\omega \cdot \frac{2 \cdot k_o}{k_i + k_o} \cdot 1 \quad (\text{XII-53})$$

For the case outside the inclusion using the chain rule

$$\frac{d}{dx} p_o = -\omega \left[1 + \frac{(k_i - k_o) \cdot a^2}{(k_i + k_o) \cdot r^2} \right] \cdot \frac{x}{\sqrt{x^2 + y^2}} \cdot \cos(\theta) - \omega \left[r - \frac{(k_i - k_o) \cdot a^2}{k_i + k_o} \cdot \frac{1}{r} \right] \cdot \sin(\theta) \cdot \frac{-y}{(x^2 + y^2)} \quad (\text{XII-54})$$

Substitute the definitions for $\sin(\theta)$ and $\cos(\theta)$

$$\frac{d}{dx} p_o = -\omega \left[1 + \frac{(k_i - k_o) \cdot a^2}{(k_i + k_o) \cdot r^2} \right] \cdot \frac{x}{\sqrt{x^2 + y^2}} \cdot \frac{x}{r} - \omega \left[r - \frac{(k_i - k_o) \cdot a^2}{k_i + k_o} \cdot \frac{1}{r} \right] \cdot \frac{-y}{r} \cdot \frac{-y}{(x^2 + y^2)} \quad (\text{XII-55})$$

Simplifying the expression:

$$\frac{d}{dx} p_o = -\omega \left[1 + \frac{(k_i - k_o)}{(k_i + k_o)} \cdot \frac{a^2}{r^2} \right] \cdot \frac{x^2}{r^2} - \omega \left[1 - \frac{(k_i - k_o)}{k_i + k_o} \cdot \frac{a^2}{r^2} \right] \cdot \frac{y^2}{r^2}$$

(XII-56)

Noting that $x = 0$ along the drift centerline:

$$\frac{d}{dx} p_o = -\omega \left[1 - \frac{(k_i - k_o)}{k_i + k_o} \cdot \frac{a^2}{r^2} \right] \cdot \frac{y^2}{r^2}$$

(XII-57)

Applying Darcy's Law Inside the inclusion, the flux is

$$-\omega \cdot \frac{2 \cdot k_o}{k_i + k_o} \cdot k_i$$

(XII-58)

Applying Darcy's Law outside the inclusion along the y axis

$$k_o \cdot \omega \left[1 - \frac{(k_i - k_o)}{k_i + k_o} \cdot \frac{a^2}{r^2} \right] \cdot \frac{y^2}{r^2}$$

(XII-59)

XII.5 COMPARISON WITH NUFT CALCULATIONS

These expressions can be compared to the results of NUFT calculations from the water drainage model for the Overton sand with 42 mm per year percolation rate. From Figure XII-2, the ratio of the unsaturated hydraulic conductivities of the Overton sand to the active fracture hydraulic conductivity is approximately a factor 3700. From Equation XII-53, the ratio of fluxes nearly equals the theoretical maximum ratio of 2. The flux distributions are compared in Figure XII-3. The calculations are in qualitative agreement in showing an increase in flux within the drift, and a decrease in flux rate outside the drift.

Note that within the drift, the drip shield acts to exclude water, which increases the flux in the drip lobe that forms adjacent to the drip shield. The maximum flux rate from the water distribution model is 145 mm per year ($4.6 \cdot 10^{-6}$ kg/(m²-sec)). The peak flux rate from the simple ratio of the diameters of the drift diameter to the drip shield is approximately 200 mm per year.

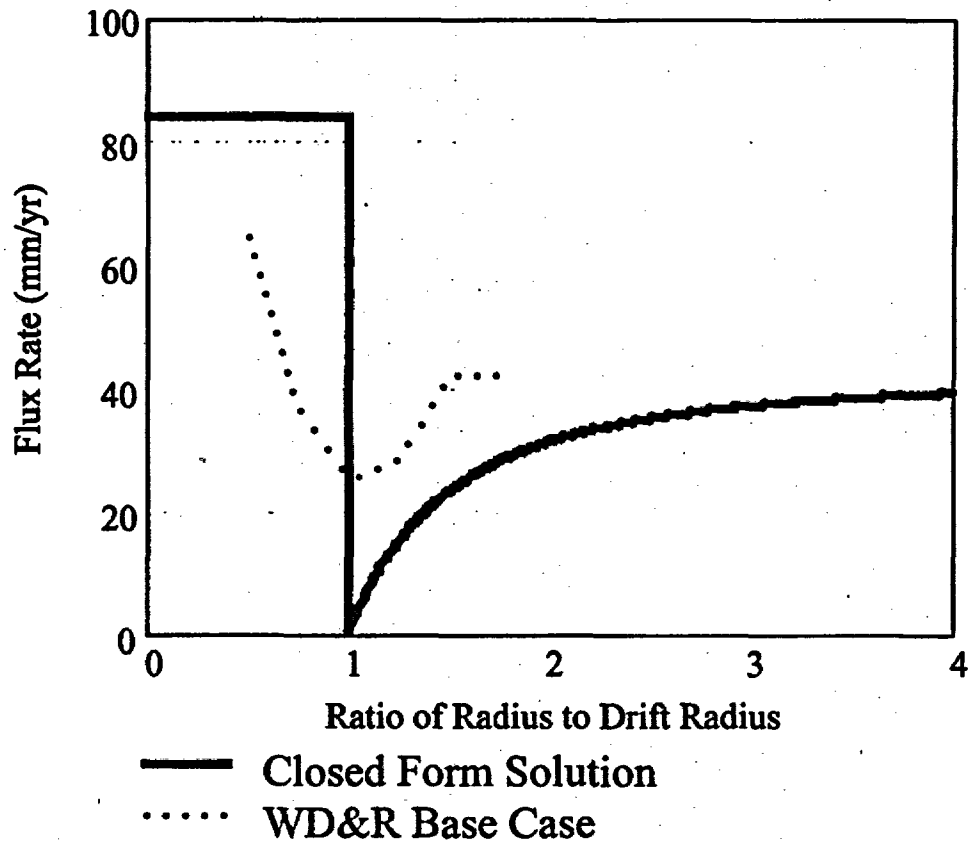


Figure XII-3. Comparison of the NUFT Calculations to the Closed Form Solution

XII.6 CONCLUSIONS

Comparisons were made between the NUFT calculations for the base case and a closed form solution for steady state flow for a fine Overton sand backfill. The unsaturated hydraulic conductivity for the backfill was compared to the unsaturated hydraulic conductivity for the active fracture model. It was found that the Overton sand unsaturated hydraulic conductivity is a factor of 3700 higher than the surrounding host rock at a percolation rate of 42 mm per year. The NUFT model predicts that the flux rate through the backfill will be higher than percolation rate through the host rock by some factor ranging from 1.5 to 5 affected by flow exclusion of the drip shield. These results are in general agreement with the results of hand calculations based upon a closed form solution for flow in and around a cylindrical inclusion.

ATTACHMENT XIII
Verification of EXCEL 97 MACRO expand

**ATTACHMENT XIII.
VERIFICATION OF EXCEL 97 MACRO expand**

XIII.1 Macro Identification

Macro name: expand. The macro runs under Microsoft Excel 97 SR-2. This macro resides in the Excel spreadsheet files "wdrdsc.xls" and "wdrdscu.xls" in attached CD (Attachment XVI) under the "dscondensation" directory.

XIII.2 Macro Purpose and Validation

The purpose of the macro is to interpolate linearly the values of vapor pressure and temperature from a steam table. The steam table is obtained from Himmelblau (1996) for temperature (T) versus saturated vapor pressure (Vp) data at every 2 Fahrenheit-degree intervals (approximately 1.11 degrees Centigrade). The macro expand is used to interpolate the T vs. Vp data at approximately 0.1-degree-centigrade intervals.

Microsoft Excel 97 Macro "expand" is listed as follows:

Sub.expand()

Dim i As Integer, i1 As Integer, i2 As Integer, i3 As Integer, ik As Integer

'Dim ic1 As Integer, ic2 As Integer, ic3 As Integer, ic4 As Integer

'Dim flag As Integer

Dim temp0 As Single, pres0 As Single, temp1 As Single, temp2 As Single

Dim dt As Single, dp As Single

ik = 2

For i = 1 To 72

For j = 1 To 10

temp0 = ActiveSheet.Cells(4 + i, 1).Value

pres0 = ActiveSheet.Cells(4 + i, 2).Value

temp1 = ActiveSheet.Cells(4 + i + 1, 1).Value

pres1 = ActiveSheet.Cells(4 + i + 1, 2).Value

dt = (temp1 - temp0) / 10

dp = (pres1 - pres0) / 10

```
il = 4 + (i - 1) * 10 + j
```

```
ActiveSheet.Cells(il, 11).Value = temp0 + (j - 1) * dt
```

```
ActiveSheet.Cells(il, 12).Value = pres0 + (j - 1) * dp
```

```
Next j
```

```
Next i
```

```
End Sub
```

Comparison of the results (original steam table curve and the "expand" calculated curve) is shown in Figure XIII-1. The plot shows that the two curves overlapping each other and are identical.

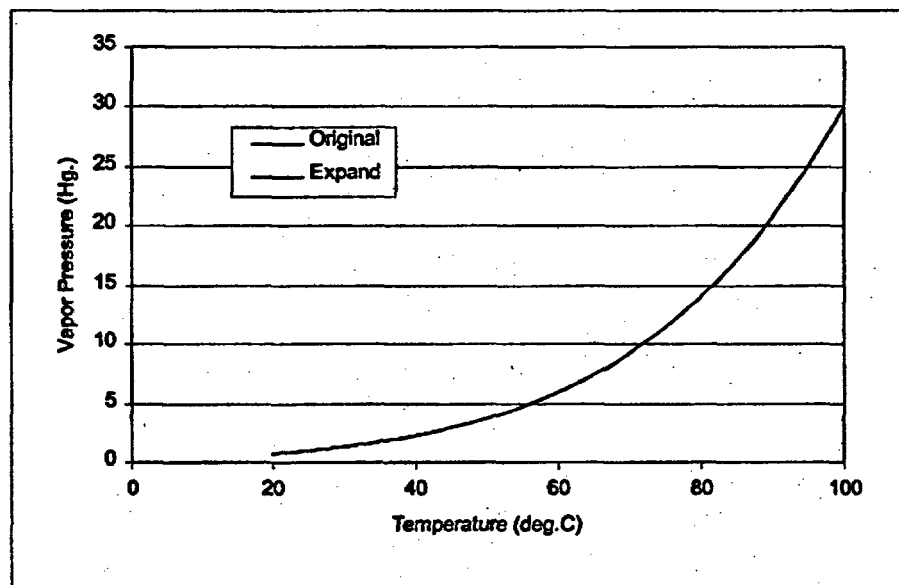


Figure XIII-1. Comparison of the Original and "expand" Temperature-Vapor Pressure Relationships.

ATTACHMENT XIV.

Hydrologic and Thermal Properties of the Invert

Attachment XIV. Hydrologic and Thermal Properties of the invert

Crushed tuff is selected for the invert (Section 4.1.2.4) to provide geochemical compatibility with the surrounding host rock. The basis for the selection of the crushed is that the material provides diffusion-barrier performance when transport from the waste package to the rock floor is diffusion dominated. This could occur if a waste package is breached but the protecting drip shield is intact, so that the invert ballast material immediately below the drip shield is unsaturated and protected from advective flow from other engineered barrier components.

Crushed welded tuff sieved between 2.0 and 4.75 mm has been selected for pilot testing and the properties are described below for this material. The final design may require a different size distribution or material type, or both.

XIV.1 Bulk Density and Porosity

The invert material is crushed tuff from the Tptpl lithostratigraphic unit which is part of the TSw2 thermal/mechanical unit (CRWMS M&O 2000v, p.13). The Repository Host Horizon is located mainly in the TSw2 unit. The invert material hydrological properties are presently unavailable for the Tptpl formation. Properties for Tptpmn are used in this analysis. It is valid to substitute the Tptpmn properties in place of Tptpl values because they are both part of the TSw2 thermal/mechanical unit (CRWMS M&O 2000v, p.13).

The U.S. Geological Survey measured the bulk density, water retention, and unsaturated hydraulic conductivity. These properties were measured in conjunction with the UFA measurements as described subsequently. The hydrologic and geotechnical properties for the crushed tuff are taken from U. S. Geological Survey (USGS) testing entitled *Water Retention and Unsaturated Hydraulic Conductivity Measurements for Various Size Fractions of Crushed, Sieved, Welded Tuff Samples Measured Using a Centrifuge* (DTN: GS980808312242.015). These are data sets as illustrated in Figures XIV-1 and XIV-2.

For materials sieved between 2.00 and 4.75 mm, used for hydraulic conductivity measurements, the measured dry bulk density was 1.15 g/cm³ (DTN: GS980808312242.015) as calculated below. The grain density is 2.53 gm/cm³. Calculate the porosity using the soil phase convention of setting the volume of the solids (V_s) equal to 1.0 cm³, developing a formula for the bulk density, and then calculating the volume of the voids. The dry bulk density (ρ) is defined as:

$$\rho = G_s V_s / V_t \quad (\text{XIV-1})$$

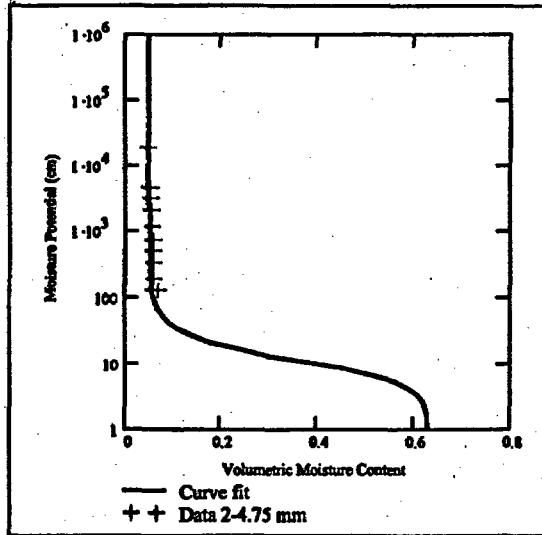


Figure XIV-1. Moisture Retention Relationship for the Invert

where

- ρ = Dry bulk mass density (g/cm^3)
 G_s = Specific gravity of solids
 V_s = Solids volume (cm^3)
 V_t = Total volume (cm^3)

Substituting in for the total volume which is equal to the volume of the solids and volume of the voids ($V_t = V_s + V_v$):

$$\rho = G_s V_s / (V_s + V_v) \quad (\text{XIV-2})$$

where

- V_v = Void volume (cm^3)

Substituting in the values for G_s , ρ , and V_s :

$$1.15 \text{ cm}^3 = 2.53 \text{ gm}/\text{cm}^3 (1.0 \text{ cm}^3) / (1.0 \text{ cm}^3 + V_v) \quad (\text{XIV-3})$$

Solve for V_v :

$$V_v = (2.53/1.15 - 1.0) \text{ cm}^3 \quad (\text{XIV-4})$$

$$V_v = 1.200 \text{ cm}^3 \quad (\text{XIV-5})$$

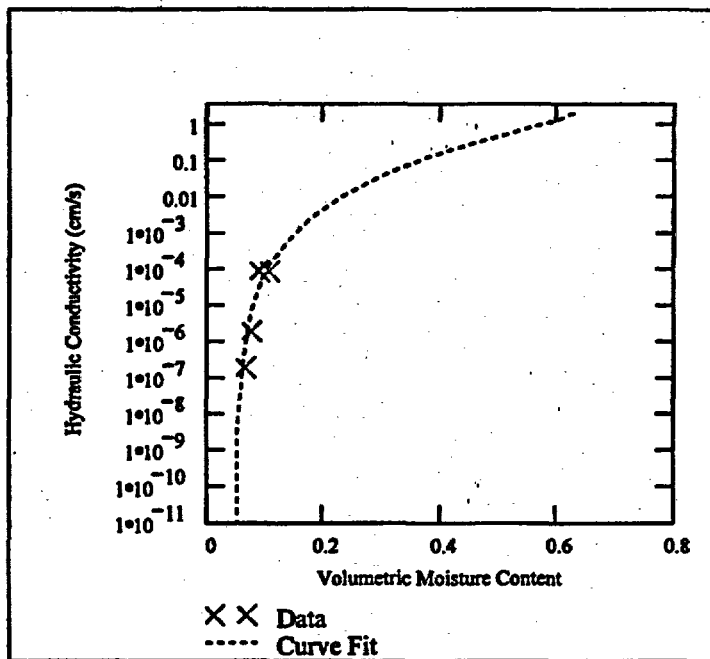


Figure XIV-2. Unsaturated Hydraulic Conductivity versus Volumetric Moisture Content for the Invert

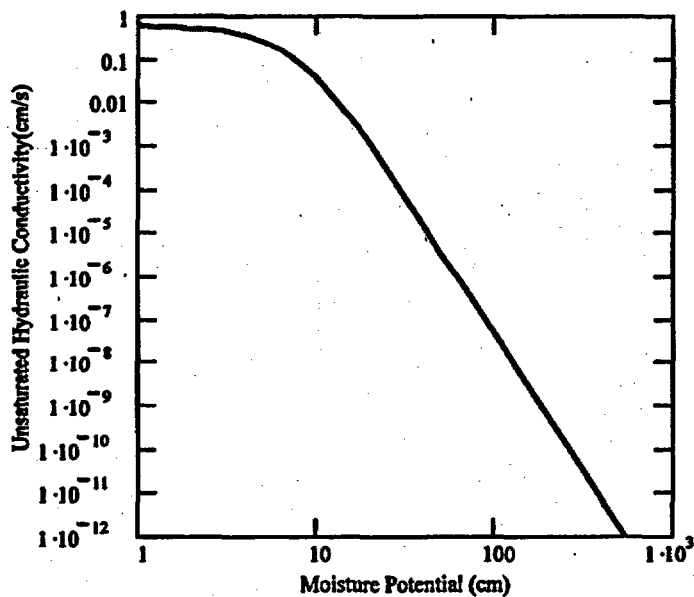


Figure XIV-3. Unsaturated Hydraulic Conductivity versus Moisture Potential for the Invert

Solve for the porosity (ϕ)

$$\phi = 1.209/(1.0+1.209) = 0.55$$

(XIV-6)

XIV.2 Moisture Retention

Moisture retention measurements were performed on the crushed tuff using the Unsaturated Flow Apparatus (UFA) measurements (CRWMS M&O 1996, Appendix C).

The UFA consists of an ultracentrifuge with a constant ultra low flow pump that provides fluid to the sample through a rotating seal assembly and microdispersal system. The volumetric moisture content (θ) as a function of the moisture potential (ψ) can be determined by allowing the sample to drain until the moisture potential equals the centrifugal force per unit area divided by the unit weight in a state of equilibrium. The sample is then weighed to determine the volumetric moisture content (θ).

The moisture retention data obtained from the two methods can be plotted and a curve fitting performed for the retention model based upon the Van Genuchten two-parameter model ($m=1-1/n$) (Fetter 1993 p.172). Define the moisture potential (capillary pressure divided by weight density) versus moisture content relation:

$$\theta = \left[1 + (\psi \cdot \alpha)^n \right]^m \cdot (\theta_s - \theta_r) + \theta_r$$

(XIV-7)

where

- n = van Genuchten curve-fitting parameter
- m = van Genuchten curve-fitting parameter
- α = van Genuchten or exponential curve-fitting parameters (cm^{-1})
- θ = Volumetric moisture content
- θ_i = Volumetric moisture content for the i th component of a soil
- θ_r = Residual volumetric moisture content
- θ_s = Saturated volumetric moisture content and
- ψ = Moisture potential (cm)

Substituting the value of (m) into Equation (XIV-7) for the two-parameter model, gives

$$\theta = \left[1 + (\psi \cdot \alpha)^n \right]^{1-\frac{1}{n}} \cdot (\theta_s - \theta_r) + \theta_r$$

(XIV-8)

A *Microsoft Excel 97* spreadsheet calculation using the *Microsoft Excel 97* equation solver is used to optimize the model parameters by fitting the closed-form mathematical expression in Equation (XIV-8) to the retention data (Tables XIV-1, and XIV-2). These Excel files are saved as "TableXIV_1.xls" and "TableXIV_2.xls" under drainage directory in attached CD (Attachment XVI). The estimated curve-fitting parameters (Table XIV) are

$$\theta_r = 0.05$$

$$\alpha_i = 0.12 \text{ (1/cm)}$$

$$n_i = 2.75$$

Figure XIV-1 (DTN: GS980808312242.015) presents Equation (XIV-9) with the UFA data for the invert.

- To convert α_r to (1/Pa) divide by the density of water (1.0 gm/cm^3) times the acceleration of gravity:

$$0.12 \text{ cm}^{-1} \cdot \frac{1}{1.0 \frac{\text{gm}}{\text{cm}^3} \cdot 981 \frac{\text{cm}}{\text{sec}^2}} = 1.223 \times 10^{-3} \frac{1}{\text{Pa}}$$

- From the definition of van Genuchten m ($m=1-1/n$) given above:

$$1 - \frac{1}{2.75} = 0.64$$

- The residual saturation equals the residual moisture content divided by the porosity ($0.05/0.545$) = 0.092. The satiated saturation is by definition.

Note that the measurements were performed near the residual moisture saturation. To establish the curve at higher moisture contents, the volumetric moisture content at saturation was estimated from the porosity. The volumetric moisture content θ_s equals the porosity of 0.63 which corresponds to the loose state. It should be noted that while the UFA testing was performed on the crushed tuff in a loose state ($\phi = 0.63$) than what would be anticipated in the repository ($\phi = 0.55$) allowing for consolidation over time, the moisture retention scaled to the saturation level would not be significantly different.

An alternate calculation was performed with the combined retention and unsaturated hydraulic conductivity data for the crushed tuff. The RETC program (van Genuchten et al. 1991) was used to optimize model parameters by fitting a closed form solution to the two-parameter relations (α_i , n_i) presented above. Attachment XV presents the results of this analysis which is in agreement with the EXCEL spreadsheet program using the Solver routine presented above.

XIV.3 Intrinsic Permeability

The saturated hydraulic conductivity (K_s) of the invert is estimated from the RETC curve fitting analysis presented in Attachment XV using the combined UFA unsaturated hydraulic conductivity (K_u) to moisture potential (ψ) and retention measurements. The calculated value from the RETC analysis is 0.60 cm/sec. This value corresponds to an approximate intrinsic permeability conversion value of $6.0 \times 10^{-6} \text{ cm}^2$ or $6.0 \times 10^{-6} \text{ m}^2$ (Freeze and Cherry, p.29).

Table XIV-1 van Genuchten Curve Fit Parameter Results for the Invert

Moisture Content at Saturation (θ_s)	0.63		
Residual Moisture Content (θ_r)	0.05		
a	117.00 bars ⁻¹	0.12 cm ⁻¹	
n	2.75		
m	0.64		
Sum of Residuals	5.25E-04		

Note that the parameters are calculated using the EXCEL Equation Solver based upon the sum of the residuals as given above from Table XIV-2.

Table XIV-2 Retention Analysis Results for the Invert

Volumetric Moisture Content	Moisture Potential (bars)	Predicted Moisture Content	Residuals
0.068	0.121	0.057	1.29E-04
0.059	0.174	0.054	2.52E-05
0.058	0.309	0.052	3.49E-05
0.057	0.483	0.051	3.03E-05
0.056	0.696	0.051	2.24E-05
0.055	1.090	0.051	1.51E-05
0.053	1.930	0.051	3.83E-06
0.052	3.020	0.051	9.60E-07
0.050	4.350	0.051	1.02E-06
0.045	17.400	0.051	3.60E-05
0.060	0.121	0.057	1.14E-05
0.060	0.174	0.054	3.63E-05
0.059	0.309	0.052	4.77E-05
0.058	0.483	0.051	4.23E-05
0.058	0.696	0.051	4.54E-05
0.056	1.090	0.051	2.38E-05
0.054	1.930	0.051	8.74E-06
0.054	3.020	0.051	8.88E-06
0.052	4.350	0.051	9.79E-07
0.047	17.400	0.051	1.60E-05

Note: Volumetric moisture content and moisture potential are obtained from DTN GS980808312242.015 for Crushed Tuff Equation (XIV-8) is used for calculating the predicted moisture content.

Residuals are calculated as the square of the difference between the actual volumetric moisture content and the predicted moisture content.

XIV.4 Relative Permeability

The UFA test apparatus described above can be used to determine the relationship between the unsaturated hydraulic conductivity (K_u) and volumetric moisture content through a direct application of Darcy's Law (CRWMS M&O 1996, Appendix C). By measuring the flow rates to 0.001 ml/hr and measuring the effluent collected from the sample in a volumetrically calibrated chamber that determines volumetric moisture content (θ), the unsaturated hydraulic conductivity can be determined from the ratio of the flow rate to the centrifugal force per unit volume (CRWMS M&O 1996, p. C-2).

The relationship of the unsaturated hydraulic conductivity with volumetric moisture content is given by (Jury et al. 1991, p.109):

$$K(\theta) = K_s \cdot \left(\frac{\theta - \theta_r}{\theta_s - \theta_r} \right)^{\frac{1}{2}} \cdot \left[1 - \left[1 - \left(\frac{\theta - \theta_r}{\theta_s - \theta_r} \right)^{\frac{1}{1-n}} \right]^{\left(\frac{1-n}{n} \right)^2} \right]$$

(XIV-9)

where

K_s = Saturated hydraulic conductivity (cm/sec)

The relative permeability function scales the saturated conductivity (K_s) to allow the unsaturated hydraulic conductivity function to be determined. Equation (XIV-10) with Van Genuchten parameters is used to plot the relationship crushed tuff as shown in Figure XIV-2.

The wetting-phase relative permeability as a function of moisture potential for this model is restated from Fetter (1993 p.182) and illustrated in Figure XIV-3. The unsaturated hydraulic conductivity (wetting-phase relative permeability times saturated hydraulic conductivity) as a function of moisture potential is given below.

$$K(\psi) = K_s \cdot \frac{\left[1 - (\alpha \cdot \psi)^{(n-1)} \cdot \left[1 + (\alpha \cdot \psi)^n \right]^{\left(-1 + \frac{1}{n} \right)} \right]^2}{\left[1 + (\alpha \cdot \psi)^n \right]^{\left[\frac{1}{2} \frac{1}{(2-n)} \right]}}$$

(XIV-10)

The relative permeability function scales the saturated conductivity (K_s) to allow the unsaturated hydraulic conductivity function to be determined. Equation (XIV-10) with Van Genuchten

parameters (Section XIV.3) is used to plot the relationship for crushed as shown in Figure XIV-3.

XIV.5 Thermal Properties

Thermal properties for the invert that were used for the backfill case were initially identified. For dry crushed tuff, the thermal conductivity is about 0.58 to 0.74 W/m-°K, or an average value of 0.66 W/(m-°K) (Ryder et al. 1996, p.5-3). This value is similar to the dry sand thermal conductivity reported by de Marsily (1986, p.281) of 0.4-0.8 W/(m-°K).

The rock grain specific heat for crushed tuff is estimated to be 948 J/(kg*°K). The specific heat for the crushed tuff with a porosity of 0.55 and a bulk density of 1.15 g/cm³ equals the specific heat of the grains since specific heat capacity depends on mass which is independent of volume. The volumetric heat (C_p) equals the specific heat (C_s) 948 J/(kg °K) times the bulk density (ρ) 1.15 g/cm³. The thermal emissivity of the invert is assumed equal to the emissivity for quartz on a rough surface 0.93 (Holman 1997, p. 649).

Additional measurements (DTN: GS0000483351030.003) of geotechnical and thermal properties have been performed to characterize the thermal properties of crushed tuff as discussed in CRWMS M&O 2000q, Item 2). Also, it includes measurements of thermal properties of oven dry samples of crushed tuff using the Thermolink Probe. This device uses a dual-probe, short-duration, heat pulse technique to simultaneously measure the volumetric specific heat and thermal diffusivities of granular materials. The measurements were performed for a "fine" crushed tuff, and "4-10" Crushed Tuff. The average properties are summarized below for oven dry conditions at ambient temperature.

Additional physical properties measurements for the "4-10" Crushed Tuff (DTN: GS000683351030.006) were conducted according to the American Society for Testing and Materials Standard C1252 entitled "Standard Test Methods for Uncompacted Void Content of Fine Aggregate (as Influenced by Particle Shape, Surface Texture, and Grading)." Twenty five samples were tested. These tests showed the average porosity was 50.26 ± 0.93 % with a corresponding dry bulk density of 1.26 ± 0.03 gm/cm³. If this dry bulk density is applied to the measured volumetric specific heat for 4-10 Crushed Tuff, the calculated value for specific heat capacity is 740. J/(kg*K).

**Table XIV-3. Summary of Thermolink Results for Crushed Tuff
(DTN: GS000483351030.003)**

Material	Volumetric Specific Heat (J/cm ³ /°K)	Thermal Conductivity (W/m ² /K)	Thermal Diffusivity (mm ² /s)	Temperature (°C)
4-10 Crushed Tuff	0.930 ± 0.074	0.16 ± 0.01	0.175 ± 0.013	17.3 ± 1.1
Fine Crushed Tuff Group 1	0.919 ± 0.061	0.14 ± 0.01	0.152 ± 0.004	23.8 ± 2.4
Fine Crushed Tuff Group 2	0.971 ± 0.036	0.15 ± 0.01	0.158 ± 0.007	20.1 ± 2.3

Note that measurements made on specific heat capacity for intact tuff show a strong temperature dependence. Information is presented by Brodsky et al. (1997, p.53) show that the specific heat capacity for TSw2 tuff is approximately 810 J/(kg*K) at a temperature of 60 C.

A review of models to predict thermal conductivity is presented by SEA (CRWMS M&O 2000q, pp.13-17). Crane et al. (1977) compared a number of models to the results of experimental studies. SEA's literature review suggested that two models provided somewhat better correlations. These included the model developed by Willhite, Kunii and Smith (1962), and the Dietz model. The Dietz model is a Fourier model for thermal conductivity of a packed bed. The Dietz model considered a special case of the packed bed-hexagonal array of touching spheres. However, it was found that the resulting expression for the effective bed conductivity was only a weak function of bed geometry, allowing the expression to be applied to a variety of packings.

These models were evaluated by comparing the predicted values for thermal conductivity on a separate and independent set of data developed by Saxena et al. 1986. Saxena et al. 1986 performed thermal conductivity measurements on porous materials. Measurements of effective thermal conductivity of these materials were made using three different experimental methods via the thermal probe method. The thermal probe method reported by Saxena et al. consisted of a line heat source method in which a steel hypodermic needle of length 10 cm and outer diameter 0.125 cm is used as the source and sensor for temperature.

The measured data are regressed against the predicted data and illustrated in Figure XIV-4. The plot shows the ratio of the thermal conductivity to the continuous or gas phase thermal conductivity for measured data and predicted values for the Dietz Model. The Dietz model was found to produce a better result for this data. The Dietz Model is given by (CRWMS M&O 2000q, p.20):

$$\lambda_d(\lambda_g, \lambda_s) = 1.14 \cdot \lambda_g \cdot \left(\frac{\lambda_s}{\lambda_g}\right)^{\frac{1}{2}} \cdot \frac{\frac{1}{2} \cdot K0 \left[\left(\frac{40 \cdot \lambda_g}{\lambda_s}\right)^{\frac{1}{2}}\right]}{K1 \left[\left(\frac{40 \cdot \lambda_g}{\lambda_s}\right)^{\frac{1}{2}}\right]}$$

(XIV-11)

where

λ_g = Thermal conductivity of the gas phase,

λ_d = Thermal conductivity of the solids phase,

K0 = Zeroth order modified Bessel function of the second kind, and

K1 = First order modified Bessel function of the second kind.

The results of the analysis on the Saxena et al (1986) data over a range of porosities are presented in Figure XIV-4. Also, this figure shows a data point for crushed tuff using the grain thermal conductivity for TSw34 as discussed below. Note that the analysis shows some degree of variation that may be attributable to the higher porosity. CRWMS M&O 2000q, p.20, reports that good agreement was obtained for void fractions between 0.38 to 0.49.

The Dietz model (Equation XIV-11) can be applied to measured data for crushed tuff (TSw4) performed by the YMP. The value for the solids phase thermal conductivity for welded tuff is given by Table 4-5, of this report, as 1.56 W/(m*K). Considering the air thermal conductivity is given by Chapman (1974, p.593) as 0.026 W/(m*K) at 60 °C, the calculated value for thermal conductivity of crushed tuff is predicted to be 0.15 W/(m*K) which compares reasonably well with the measured values presented in Table XIV-3.

The Dietz model can be used to predict the thermal conductivity under saturated conditions by substituting the value of thermal conductivity for water into Equation (XIV-11). Considering the water thermal conductivity given by Chapman (1974, p. 586) at 60C, the value is 0.65 W/(m*K). Substituting in this value in Eq. (XIV-11) yields a value for thermal conductivity under saturated conditions of 1.03 W/(m*K).

The volumetric heat capacity under saturated conditions may be estimated by simple volumetric averaging. According to Jury et al. (1991, p. 179):

$$C_c = X_s \cdot C_s + X_w \cdot C_w + \sum_{j=1}^N X_{s_j} \cdot C_{s_j}$$

(Eq. XIV-12)

Where

C_c = Average volumetric heat capacity
 X_a = Void fraction of air
 X_w = Void fraction of water
 X_{sj} = Void fraction of the jth solids component
 C_a = Heat capacity per unit volume of the air
 C_w = Heat capacity per unit volume of the water, and
 C_{sj} = Heat capacity per unit volume of the jth solids component.

Note that NUFT will calculate the volume averaged specific heat capacity based upon the volume fractions and their respective volumetric heats for the solids, water, and air. The following calculation is provided for reference, and illustrates how specific heat, and thermal diffusivity would change when the degree of saturation is increased from zero to one.

Calculate the volumetric heat capacity for air. From Chapman (1974, p.593), the properties of air at 60 C (140 F) are given by:

$$C_{p_a} = 0.2409 \cdot \frac{\text{BTU}}{\text{lb} \cdot \text{R}} \quad \rho_a = 0.06614 \cdot \frac{\text{lb}}{\text{ft}^3}$$

Converting to the SI system of units:

$$C_{p_a} = 1009 \cdot \frac{\text{J}}{\text{kg} \cdot \text{K}} \quad \rho_a = 1.059 \cdot \frac{\text{kg}}{\text{m}^3}$$

Calculate the volumetric heat capacity for air:

$$C_a = C_{p_a} \cdot \rho_a \quad C_a = 1069.0 \cdot \frac{\text{J}}{\text{m}^3 \cdot \text{K}}$$

Calculate the volumetric capacity of the tuff from Equation (XIV-12) by considering 4-10 crushed tuff that has a volumetric heat capacity of 0.930 J/(cm³ K) for TSw4 (Table XIV-3) and an air void fraction of 0.51:

$$9.30 \cdot 10^5 = C_a \cdot X_a + (1 - X_a) \cdot C_s$$

(XIV-13)

Solving for C_s , the value of $1.89 \cdot 10^6$ J/(m³ K) is obtained which is approximately twice the value for the porous crushed tuff since as noted by Jury et al. (1991, p.180), the volumetric heat capacity of air is small.

Consider now the properties of water. From Chapman (1974 p.586) at a temperature of 60C (140 F):

$$C_{p_w} = 0.998 \cdot \frac{\text{BTU}}{\text{lb} \cdot \text{R}} \quad \rho_w = 61.39 \cdot \frac{\text{lb}}{\text{ft}^3}$$

Converting to SI units:

$$C_{p_w} = 4178 \cdot \frac{\text{J}}{\text{kg} \cdot \text{K}} \quad \rho_w = 983.373 \cdot \frac{\text{kg}}{\text{m}^3}$$

The calculated volumetric heat capacity for water (C_w) is $4.11 \cdot 10^6 \text{ J}/(\text{m}^3 \text{ K})$. Substituting in Equation (XIV-13), the volumetric heat capacity under saturated conditions is given by:

$$X_w \cdot C_w + (1 - X_w) \cdot C_s = 3.01 \cdot 10^6 \cdot \frac{\text{J}}{\text{m}^3 \cdot \text{K}}$$

The volumetric heat capacity is increased by an approximate factor of three. The mass density under saturated conditions is calculated from the dry density of $1.26 \text{ gm}/\text{cm}^3$ using the standard soil mechanics convention of setting the volume of the solids to 1 cm^3 . Solving for the volume of voids:

$$V_v = \frac{\phi}{1 - \phi}$$

(XIV-14)

The total volume is 2.01 cm^3 . Calculate the weight of solids (W_s) based upon the dry density of $1.26 \text{ gm}/\text{cm}^3$:

$$W_s = 1.26 \cdot \frac{\text{gm}}{\text{cm}^3} \cdot 2.01 \cdot \text{cm}^3 = 2.54 \cdot \text{gm}$$

Calculate the weight of the water equal the mass density of the water times the void volume:

$$W_w = 0.983 \cdot \frac{\text{gm}}{\text{cm}^3} \cdot 1.01 \cdot \text{cm}^3 = 0.99 \text{ gm}$$

Calculate the saturated unit density:

$$\rho_s = \frac{W_s + W_w}{V_t}$$

(XIV-15)

$$\rho_s = \frac{2.54 \cdot \text{gm} + 1.01 \cdot \text{gm}}{2.01 \cdot \text{cm}^3} = 1.76 \cdot \frac{\text{gm}}{\text{cm}^3}$$

The mass specific heat capacity may also be expressed as (Jury et al. 1991, p.179):

$$C = \rho C_p \quad (\text{XIV-16})$$

Solving for C_p under saturated conditions, the calculated value for C_p is $1.71 \cdot 10^3 \text{ J/(kg}\cdot\text{K)}$.

The thermal diffusivity under saturated conditions is estimated from the thermal diffusivity relationship (Jury et al. 1991, p. 178):

$$\alpha = \lambda / C \quad \text{Eq. (XIV-17)}$$

The calculated thermal diffusivity under saturated conditions is $0.34 \text{ mm}^2/\text{s}$. In comparing this thermal diffusivity to the dry case, the thermal diffusivity is increased by a factor of 2.

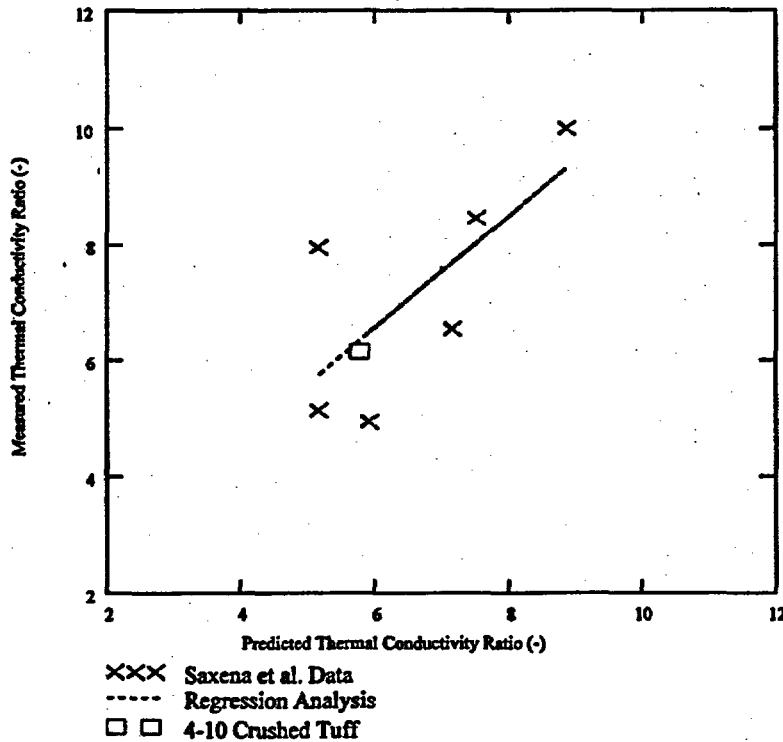


Figure XIV-4 Comparison of Experimental Results with Calculated Thermal Conductivity for the Dietz Model

ATTACHMENT XV

RETC Analysis for the Crushed Tuff Invert

**ATTACHMENT XV
RETC ANALYSIS FOR THE CRUSHED TUFF INVERT**

```

*
* ANALYSIS OF SOIL HYDRAULIC PROPERTIES
*
* 2-4.75 Crushed Tuff (Ttpmn)
*
* MUALEM-BASED RESTRICTION, M=1-1/N
* SIMULTANEOUS FIT OF RETENTION AND CONDUCTIVITY DATA
* MTYPE= 3 METHOD= 1
* Inputs or observed data are from DTN: GS980808312242.015
* for crushed tuff *
* See van Genuchten et al. 1991 for definition of variables and
* output

```

INITIAL VALUES OF THE COEFFICIENTS

NO	NAME	INITIAL VALUE	INDEX
1	WCR	.0300	1
2	WCS	.6320	0
3	Alpha	.5000	1
4	n	5.0000	1
5	m	.8000	0
6	l	.5000	0
7	Ksat	.0001	1

OBSERVED DATA (DTN: GS980808312242.015)

OBS. NO.	PRESSURE HEAD	WATER CONTENT	WEIGHTING COEFFICIENT
1	177.000	.0590	1.0000
2	315.000	.0580	1.0000
3	493.000	.0570	1.0000
4	709.000	.0560	1.0000
5	1110.000	.0550	1.0000
6	1970.000	.0530	1.0000
7	3080.000	.0520	1.0000
8	4430.000	.0500	1.0000
9	17700.000	.0450	1.0000
10	123.000	.0600	1.0000
11	177.000	.0600	1.0000
12	315.000	.0590	1.0000
13	493.000	.0580	1.0000
14	709.000	.0580	1.0000
15	1110.000	.0560	1.0000
16	1970.000	.0540	1.0000
17	3080.000	.0540	1.0000
18	4430.000	.0520	1.0000
19	17700.000	.0470	1.0000

	WATER CONTENT	CONDUCTIVITY	WEIGHTING COEFFICIENT
20	.1090	.4280E-04	1.0000
21	.0920	.4280E-05	1.0000
22	.0760	.1070E-05	1.0000
23	.0660	.1190E-06	1.0000

WEIGHTING COEFFICIENTS

=====

W1= 1.00000 W2=***** W12=*****

NIT	SSQ	WCR	Alpha	n	Ksat
0	.05014	.0300	.5000	5.0000	.0001
1	.05014	.0300	.0983	5.0030	.0001
2	.04964	.0301	.0286	5.6822	.0002
3	.02339	.0416	.0153	5.7738	.0094
4	.00492	.0541	.0151	7.0152	.0309
5	.00231	.0560	.0160	7.4612	.0416
6	.00219	.0571	.0178	7.1658	.0467
7	.00213	.0575	.0196	6.7883	.0513
8	.00208	.0576	.0213	6.4247	.0558
9	.00204	.0576	.0228	6.0987	.0604
51	.00104	.0559	.1160	2.7445	.6032

CORRELATION MATRIX

=====

	WCR	Alpha	n	Ksat
	1	2	3	4
1	1.0000			
2	-.1460	1.0000		
3	.4623	-.8219	1.0000	
4	-.3835	.8414	-.9958	1.0000

RSQUARED FOR REGRESSION OF OBSERVED VS FITTED VALUES = .99592182

=====

NONLINEAR LEAST-SQUARES ANALYSIS: FINAL RESULTS

=====

VARIABLE	VALUE	S.E. COEFF.	T-VALUE	95% CONFIDENCE LIMITS	
				LOWER	UPPER
WCR	.05589	.00203	27.47	.0516	.0602
Alpha	.11596	.13196	.88	-.1602	.3922
n	2.74449	.70882	3.87	1.2608	4.2282
Ksat	.60316	.77320	.78	-1.0152	2.2216

OBSERVED AND FITTED DATA

=====

NO	P	LOG-P	WC-OBS	WC-FIT	WC-DEV
1	.1770E+03	2.2480	.0590	.0589	.0001

2	.3150E+03	2.4983	.0580	.0570	.0010
3	.4930E+03	2.6928	.0570	.0564	.0006
4	.7090E+03	2.8506	.0560	.0562	-.0002
5	.1110E+04	3.0453	.0550	.0560	-.0010
6	.1970E+04	3.2945	.0530	.0559	-.0029
7	.3080E+04	3.4886	.0520	.0559	-.0039
8	.4430E+04	3.6464	.0500	.0559	-.0059
9	.1770E+05	4.2480	.0450	.0559	-.0109
10	.1230E+03	2.0899	.0600	.0615	-.0015
11	.1770E+03	2.2480	.0600	.0589	.0011
12	.3150E+03	2.4983	.0590	.0570	.0020
13	.4930E+03	2.6928	.0580	.0564	.0016
14	.7090E+03	2.8506	.0580	.0562	.0018
15	.1110E+04	3.0453	.0560	.0560	.0000
16	.1970E+04	3.2945	.0540	.0559	-.0019
17	.3080E+04	3.4886	.0540	.0559	-.0019
18	.4430E+04	3.6464	.0520	.0559	-.0039
19	.1770E+05	4.2480	.0470	.0559	-.0089

	WC	K-OBS	K-FIT	K-DEV	LOGK-OBS	LOGK-FIT
20	.1090	.4280E-04	.4124E-04	.1565E-05	-4.3686	-4.3847
21	.0920	.4280E-05	.1006E-04	-.5779E-05	-5.3686	-4.9974
22	.0760	.1070E-05	.1187E-05	-.1166E-06	-5.9706	-5.9257
23	.0660	.1190E-06	.9651E-07	.2249E-07	-6.9245	-7.0154

SUM OF SQUARES OF OBSERVED VERSUS FITTED VALUES

	UNWEIGHTED	WEIGHTED
RETENTION DATA	.00030	.00030
COND/DIFF DATA	.00000	.00074
ALL DATA	.00030	.00104

SOIL HYDRAULIC PROPERTIES (MTYPE = 3)

WC	P	LOGP	COND	LOGK	DIF	LOGD
.0589	.1756E+03	2.244	.1151E-08	-8.939	.3861E-04	-4.413
.0619	.1180E+03	2.072	.1441E-07	-7.841	.1625E-03	-3.789
.0679	.7926E+02	1.899	.1806E-06	-6.743	.6851E-03	-3.164
.0799	.5318E+02	1.726	.2265E-05	-5.645	.2896E-02	-2.538
.0919	.4206E+02	1.624	.9956E-05	-5.002	.6753E-02	-2.170
.1039	.3557E+02	1.551	.2850E-04	-4.545	.1235E-01	-1.908
.1159	.3120E+02	1.494	.6450E-04	-4.190	.1979E-01	-1.704
.1279	.2800E+02	1.447	.1259E-03	-3.900	.2916E-01	-1.535
.1399	.2554E+02	1.407	.2217E-03	-3.654	.4058E-01	-1.392
.1519	.2355E+02	1.372	.3622E-03	-3.441	.5416E-01	-1.266
.1639	.2191E+02	1.341	.5592E-03	-3.252	.7004E-01	-1.155
.1759	.2052E+02	1.312	.8252E-03	-3.083	.8837E-01	-1.054
.1879	.1932E+02	1.286	.1174E-02	-2.930	.1093E+00	-.961
.1999	.1827E+02	1.262	.1622E-02	-2.790	.1330E+00	-.876
.2119	.1735E+02	1.239	.2185E-02	-2.660	.1597E+00	-.797
.2239	.1651E+02	1.218	.2882E-02	-2.540	.1896E+00	-.722
.2359	.1576E+02	1.198	.3731E-02	-2.428	.2230E+00	-.652
.2479	.1507E+02	1.178	.4755E-02	-2.323	.2602E+00	-.585
.2599	.1444E+02	1.160	.5976E-02	-2.224	.3014E+00	-.521
.2719	.1386E+02	1.142	.7419E-02	-2.130	.3471E+00	-.460

.2839	.1332E+02	1.124	.9112E-02	-2.040	.3976E+00	-.401
.2959	.1281E+02	1.108	.1108E-01	-1.955	.4534E+00	-.343
.3079	.1234E+02	1.091	.1336E-01	-1.674	.5152E+00	-.288
.3199	.1189E+02	1.075	.1598E-01	-1.796	.5834E+00	-.234
.3319	.1146E+02	1.059	.1898E-01	-1.722	.6588E+00	-.181
.3439	.1105E+02	1.043	.2241E-01	-1.650	.7422E+00	-.129
.3559	.1066E+02	1.028	.2629E-01	-1.580	.8346E+00	-.079
.3680	.1029E+02	1.012	.3068E-01	-1.513	.9371E+00	-.028
.3800	.9929E+01	.997	.3564E-01	-1.448	.1051E+01	.022
.3920	.9580E+01	.981	.4121E-01	-1.385	.1178E+01	.071
.4040	.9242E+01	.966	.4747E-01	-1.324	.1320E+01	.121
.4160	.8913E+01	.950	.5447E-01	-1.264	.1479E+01	.170
.4280	.8590E+01	.934	.6231E-01	-1.205	.1658E+01	.220
.4400	.8273E+01	.918	.7105E-01	-1.148	.1860E+01	.270
.4520	.7961E+01	.901	.8081E-01	-1.093	.2090E+01	.320
.4640	.7652E+01	.884	.9169E-01	-1.038	.2354E+01	.372
.4760	.7344E+01	.866	.1038E+00	-.984	.2657E+01	.424
.4880	.7037E+01	.847	.1173E+00	-.931	.3009E+01	.478
.5000	.6728E+01	.828	.1324E+00	-.878	.3422E+01	.534
.5120	.6416E+01	.807	.1493E+00	-.826	.3914E+01	.593
.5240	.6098E+01	.785	.1681E+00	-.774	.4505E+01	.654
.5360	.5772E+01	.761	.1893E+00	-.723	.5232E+01	.719
.5480	.5433E+01	.735	.2132E+00	-.671	.6144E+01	.788
.5600	.5078E+01	.706	.2403E+00	-.619	.7324E+01	.865
.5720	.4699E+01	.672	.2713E+00	-.567	.8911E+01	.950
.5840	.4285E+01	.632	.3072E+00	-.513	.1117E+02	1.048
.5960	.3818E+01	.582	.3496E+00	-.456	.1467E+02	1.167
.6080	.3260E+01	.513	.4013E+00	-.396	.2097E+02	1.322
.6200	.2507E+01	.399	.4691E+00	-.329	.3668E+02	1.564
.6260	.1938E+01	.287	.5154E+00	-.288	.6146E+02	1.789
.6320	.0000E+00		.6032E+00	-.220		

END OF PROBLEM

OFFICE OF CIVILIAN RADIOACTIVE WASTE MANAGEMENT

1. QA: QA

SPECIAL INSTRUCTION SHEET

Page: 1 of: 1

Complete Only Applicable Items

ok
2-14-01
wjc

This is a placeholder page for records that cannot be scanned or microfilmed

2. Record Date
01/23/2001

3. Accession Number

ATT-10 MRL-20010214-0031

4. Author Name(s)
YUEYING DENG

5. Author Organization
N/A

6. Title
WATER DISTRIBUTION AND REMOVAL MODEL

7. Document Number(s)
ANL-EBS-MD-000032

8. Version
REV 01

9. Document Type
DATA

10. Medium
CD-ROM

11. Access Control Code
PUB

12. Traceability Designator
DC #26386

13. Comments *SPECIAL PROCESS # 2-11-01*
~~THIS IS A ONE-OF-A-KIND DOCUMENT~~ DUE TO THE CD-ROM ENCLOSED AS PART OF ATTACHMENT I, AND CAN BE LOCATED THROUGH THE RPC

DC# 26386

OFFICE OF CIVILIAN RADIOACTIVE WASTE MANAGEMENT
ELECTRONIC SOURCE FILE VERIFICATION

QA: N/A

1. DOCUMENT TITLE:
and *Q# 12/01/00*
Water Distribution and Removal Model

2. DOCUMENT IDENTIFIER:

ANL-EBS-MD-000032

3. REVISION DESIGNATOR:

REV. 01

ELECTRONIC SOURCE FILE INFORMATION

4. ELECTRONIC SOURCE FILE NAME WITH FILE EXTENSION PROVIDED BY THE SOFTWARE:

wd&r_rev01.doc

5. DATE LAST MODIFIED:

12/01/00

6. ELECTRONIC SOURCE FILE APPLICATION:
(I.E., EXCEL, WORD, CORELDRAW)

Micorsoft Word

7. FILE SIZE IN KILOBYTES:

7,336kb

8. FILE LINKAGE INSTRUCTIONS/INFORMATION:

N/A

9. FILE CUSTODIAN: (I.E., DC, OR DC APPROVED CUSTODIAN)

DC

10. FILE LOCATION FOR DC APPROVED CUSTODIAN: (I.E., SERVER, DIRECTORY)

Attached CD

11. PRINTER SPECIFICATION (I.E., HP4SI) INCLUDING POSTSCRIPT INFORMATION (I.E., PRINTER DRIVER) AND PRINTING PAGE SETUP: (I.E., LANDSCAPE, 11 X 17 PAPER)

HP CLJ 8500-PCL on \\Ymnts3\t617ghp8500

12. COMPUTING PLATFORM USED: (I.E., SUN)

PC

13. OPERATING EQUIPMENT USED: (I.E., UNIX, SOLARIS)

Windows 95

14. ADDITIONAL HARDWARE/SOFTWARE REQUIREMENT USED TO CREATE FILE(S):

NONE

15. ACCESS RESTRICTIONS: (IF ANY)

NONE

COMMENTS/SPECIAL INSTRUCTIONS

16.
NONE

CERTIFICATION

17. NAME (Print and Sign)

Randolph L. Schreiner

Randolph L. Schreiner

18. DATE:

12/01/2000

19. ORGANIZATION:

Subsurface Facilities

20. DEPARTMENT:

Process Modeling

21. LOCATION/MAILSTOP:

1020E/MS423

22. PHONE:

(702)295-4443

DC USE ONLY

23. DATE RECEIVED:

01/19/2001

24. DATE REVIEWED:

02/07/2001

25. DATE FILES TRANSFERRED:

1/22/2001

26. NAME (Print and Sign):

Marina Blackwell *Marina Blackwell*

27. DATE:

02/07/2001

ATTACHMENT XVI

Attached Compact Disk (CD)

Compact Disk:

A compact disk is provided in attachment to contain all the electronic files used in this report. The CD is arranged in four directories: (1) diversion; (2) drainage; (3) thermohydro; and (4) dscondensation. A file named "directory_listing.doc" is saved in the root directory to identify each individual file per model.

The electronic files developed for the WD&R model are listed in the following:

Folder	Dates and Times	File Size
\diversion		
crevice_flow_f.mcd	9/11/00 11:57AM	14kb
crevice_flow_p.mcd	10/5/00 12:27 PM	16kb
adsoptive_film.mcd	10/9/00 1:17 PM	40kb
properties.prn	7/28/00 12:00PM	1kb
\drainage		
Glaciall.inf	9/15/99 5:02PM	2,219kb
Glacialm.inf	9/15/99 5:05PM	2,219kb
Glacialu.inf	9/15/99 5:05PM	2,219kb
bcs_99.dat	10/21/99 12:35PM	274kb
Dft1.dat	11/28/99 10:40PM	5kb
UZ99_3_3D.mesh	09/09/99 1:53PM	28,037kb
UZ99_3.grd	09/09/99 1:52PM	873kb
Glaciall.NV	09/23/99 2:29PM	7,022kb
Glacialm.NV	09/23/99 2:29PM	7,022kb
Glacialu.NV	09/23/99 2:30PM	7,022kb
Glaciall.out	11/23/99 9:38AM	1kb
Glacialm.out	11/23/99 9:38AM	1kb
Glacialu.out	11/23/99 9:39AM	1kb
Glaciall_convert	12/08/99 10:14AM	1kb
Glacialm_convert	12/08/99 10:14AM	1kb
Glacialu_convert	12/08/99 10:14AM	1kb
Outpt	11/30/99 1:18PM	2kb
outpt_wt	11/30/99 1:20PM	2kb
shape1.dat	10/27/99 1:46AM	1kb
Column.data	10/12/99 2:09PM	1kb
L4c4.dat	12/08/99 10:13AM	1kb
LBL99-YMESH	10/08/99 10:37AM	16,350kb
L4c4.col.units	12/08/99 10:13AM	2kb
repository_shape V1.0.xls	12/09/99 9:36AM	34kb
Cover.m	10/12/99 2:57PM	3kb

Chim_Surf_TP.f	10/12/99 8:08AM	3kb
ColumnInfiltration.c	10/12/99 2:09PM	5kb
rme6.c	10/08/99 11:19AM	10kb
Chim_Surf_bc_tst.f	11/27/99 12:48PM	2kb
Chim_test	11/27/99 12:43PM	5kb
Chim_out	11/27/99 12:44PM	1kb
columnInfiltration_tst.dat	11/22/99 11:56AM	1kb
columnInfiltration_tst.NV	11/22/99 11:56AM	1kb
columnInfiltration_tst.out	11/22/99 11:56AM	1kb
1.in	11/05/99 10:09AM	26kb
5.in	11/05/99 10:09AM	28kb
9.in	11/05/99 10:09 AM	27kb
dkm-afc-NBS-WDR	11/11/99 10:50AM	55kb
dkm-afc-EBS_Rev10-WDR	11/11/99 10:50AM	9kb
vtough.pkg	10/22/99 3:35PM	3kb
1.f.EBS.ext	12/20/99 4:08PM	675kb
1.m.EBS.ext	12/20/99 4:08PM	672kb
5.f.ext	12/20/99 4:59PM	1,540kb
5.m.ext	12/20/99 4:59 PM	1,537kb
9.f.ext	12/20/99 5:14PM	2,214kb
9.m.ext	12/20/99 5:17PM	1,872kb
Case1_Flux V1.0.mcd	01/18/00 11:08AM	7kb
Case899.1_Flux V1.0.mcd	01/18/00 10:52AM	17kb
Case1 V1.0.mcd	12/28/99 10:21AM	124kb
Case9 V1.0.mcd	12/28/99 02:53PM	124kb
Summary of travel time calculation V1.0.xls	01/03/00 3:37PM	23kb
\dscondensation		
repos_to_Nvcentral	08/16/00 09:47AM	17kb
wdrdsc.xls	10/18/00 02:47PM	317kb
wdrdscu.xls	09/15/00 01:33PM	220kb
\thermohydro		
non_isothermal_seepage.tar.gz	10/10/00 04:01PM	301,734kb
consisting of the following:		
LDTH-SDT-0.3Qheat-50y_vent-20		
directory_listing		
dkm-afc-1Dds-mc-li-00		
dkm-afc-1Dds-mc-mi-00		
dkm-afc-1Dds-mc-ui-00		
dkm-afc-EBS_Rev21		
enthalpyWater34Low.nft		

enthalpyWater34Med.nft
enthalpyWater34Upp.nft
enthalpyWater56Low.nft
enthalpyWater56Med.nft
enthalpyWater56Upp.nft
fluxOutput00
infiltration.xls
14c1-LDTH34-5pt.xz
14c1-LDTH34-inv-5pt.xz
14c1-LDTH34-li-inv.03.f.EBS.ext
14c1-LDTH34-li-inv.03.in
14c1-LDTH34-li-inv.03.m.EBS.ext
14c1-LDTH34-li-inv.30.f.EBS.ext
14c1-LDTH34-li-inv.30.in
14c1-LDTH34-li-inv.30.m.EBS.ext
14c1-LDTH34-li.00.f.EBS.ext
14c1-LDTH34-li.00.in
14c1-LDTH34-li.00.m.EBS.ext
14c1-LDTH34-li.03.f.EBS.ext
14c1-LDTH34-li.03.in
14c1-LDTH34-li.03.m.EBS.ext
14c1-LDTH34-li.30.f.EBS.ext
14c1-LDTH34-li.30.in
14c1-LDTH34-li.30.m.EBS.ext
14c1-LDTH34-mi-inv.03.f.EBS.ext
14c1-LDTH34-mi-inv.03.in
14c1-LDTH34-mi-inv.03.m.EBS.ext
14c1-LDTH34-mi-inv.30.f.EBS.ext
14c1-LDTH34-mi-inv.30.in
14c1-LDTH34-mi-inv.30.m.EBS.ext
14c1-LDTH34-mi.00.f.EBS.ext
14c1-LDTH34-mi.00.in
14c1-LDTH34-mi.00.m.EBS.ext
14c1-LDTH34-mi.03.f.EBS.ext
14c1-LDTH34-mi.03.in
14c1-LDTH34-mi.03.m.EBS.ext
14c1-LDTH34-mi.30.f.EBS.ext
14c1-LDTH34-mi.30.in
14c1-LDTH34-mi.30.m.EBS.ext
14c1-LDTH34-ui-inv.03.f.EBS.ext
14c1-LDTH34-ui-inv.03.in
14c1-LDTH34-ui-inv.03.m.EBS.ext
14c1-LDTH34-ui-inv.30.f.EBS.ext
14c1-LDTH34-ui-inv.30.in
14c1-LDTH34-ui-inv.30.m.EBS.ext
14c1-LDTH34-ui.00.f.EBS.ext

14c1-LDTH34-ui.00.in
14c1-LDTH34-ui.00.m.EBS.ext
14c1-LDTH34-ui.03.f.EBS.ext
14c1-LDTH34-ui.03.in
14c1-LDTH34-ui.03.m.EBS.ext
14c1-LDTH34-ui.30.f.EBS.ext
14c1-LDTH34-ui.30.in
14c1-LDTH34-ui.30.m.EBS.ext
14c4-LDTH56-5pt.xz
14c4-LDTH56-inv-5pt.xz
14c4-LDTH56-li-inv.03.f.EBS.ext
14c4-LDTH56-li-inv.03.in
14c4-LDTH56-li-inv.03.m.EBS.ext
14c4-LDTH56-li-inv.30.f.EBS.ext
14c4-LDTH56-li-inv.30.in
14c4-LDTH56-li-inv.30.m.EBS.ext
14c4-LDTH56-li.00.f.EBS.ext
14c4-LDTH56-li.00.in
14c4-LDTH56-li.00.m.EBS.ext
14c4-LDTH56-li.03.f.EBS.ext
14c4-LDTH56-li.03.in
14c4-LDTH56-li.03.m.EBS.ext
14c4-LDTH56-li.30.f.EBS.ext
14c4-LDTH56-li.30.in
14c4-LDTH56-li.30.m.EBS.ext
14c4-LDTH56-mi-inv.03.f.EBS.ext
14c4-LDTH56-mi-inv.03.in
14c4-LDTH56-mi-inv.03.m.EBS.ext
14c4-LDTH56-mi-inv.30.f.EBS.ext
14c4-LDTH56-mi-inv.30.in
14c4-LDTH56-mi-inv.30.m.EBS.ext
14c4-LDTH56-mi.00.f.EBS.ext
14c4-LDTH56-mi.00.in
14c4-LDTH56-mi.00.m.EBS.ext
14c4-LDTH56-mi.03.f.EBS.ext
14c4-LDTH56-mi.03.in
14c4-LDTH56-mi.03.m.EBS.ext
14c4-LDTH56-mi.30.f.EBS.ext
14c4-LDTH56-mi.30.in
14c4-LDTH56-mi.30.m.EBS.ext
14c4-LDTH56-ui-inv.03.f.EBS.ext
14c4-LDTH56-ui-inv.03.in
14c4-LDTH56-ui-inv.03.m.EBS.ext
14c4-LDTH56-ui-inv.30.f.EBS.ext
14c4-LDTH56-ui-inv.30.in
14c4-LDTH56-ui-inv.30.m.EBS.ext

14c4-LDTH56-ui.00.f.EBS.ext
14c4-LDTH56-ui.00.in
14c4-LDTH56-ui.00.m.EBS.ext
14c4-LDTH56-ui.03.f.EBS.ext
14c4-LDTH56-ui.03.in
14c4-LDTH56-ui.03.m.EBS.ext
14c4-LDTH56-ui.30.f.EBS.ext
14c4-LDTH56-ui.30.in
14c4-LDTH56-ui.30.m.EBS.ext
modprop_dr-20
output.times-34-20
output.times-34-20a
output.times-56-20a
run_control_param_LDTH-v09